

# SOLID SPONGES AS SUPPORT FOR HETEROGENEOUS CATALYSTS IN GAS-PHASE REACTIONS

Vom Fachbereich Produktionstechnik  
der  
UNIVERSITÄT BREMEN

zur Erlangung des Grades  
Doktor-Ingenieur  
genehmigte

Dissertation

von  
Lars Kiewidt, M. Sc.

Gutachter: Prof. Dr.-Ing. Jorg Thöming  
Prof. Dr.-Ing. Robert Güttel (Universität Ulm)

Tag der mündlichen Prüfung: 7. Dezember 2017



# Zusammenfassung

Feste Schwämme, häufig auch als offenzellige Schäume bezeichnet, kombinieren auf Grund ihrer hohen Porosität und ihrer kontinuierlichen festen Phase große spezifische Oberflächen, geringe Druckverluste und herausragende Wärmetransporteigenschaften. Zusätzlich ermöglichen sie als beschichtete Monolithen die weitgehende Entkopplung katalytischer Aktivität und Selektivität, welche durch das Material und die Struktur der Beschichtung beeinflusst werden, von Wärme-, Stoff- und Impulstransport innerhalb des Reaktors, welcher vornehmlich durch die Morphologie des Katalysatorträgers beeinflusst werden. Daher ist der Einsatz fester Schwämme als monolithische Katalysatorträger besonders für endo- und exotherme Prozesse vielversprechend.

Bei der Auswahl geeigneter Porositäten und Fensterdurchmesser für feste Schwämme hinsichtlich hoher Katalysatordichten, geringer Druckverluste und hoher effektiver Wärmeleitfähigkeiten müssen jedoch Kompromisse hingenommen werden. Des Weiteren wurden feste Schwämme bisher lediglich im Labormaßstab als Katalysatorträger eingesetzt und mit konventionellen Packungen aus Pellets verglichen. Daher ist unklar, ob feste Schwämme gegenüber Packungen aus Pellets auch im Produktionsmaßstab konkurrenzfähig sind.

Ziel dieser Arbeit ist es daher, die Zielkonflikte in der Gestaltung katalytischer Schwämme quantitativ zu erforschen und darauf aufbauend Gestaltungsrichtlinien für katalytische Schwämme abzuleiten. Weiterhin soll untersucht werden, ob und unter welchen Bedingungen katalytische Schwämme im Produktionsmaßstab gegenüber konventionellen Packungen aus Pellets konkurrenzfähig sind und welche potentiellen Vorteile sie bieten.

Dafür wird ein mehrskaliges pseudo-homogenes 2-d Reaktormodell entwickelt und implementiert, welches speziell auf aktuelle Transportmodelle für feste Schwämme zurückgreift. Mit Hilfe von Experimenten zur Methanisierung von Kohlenstoffdioxid in einem polytrop betriebenen Laborreaktor ( $\varnothing 25$  mm) wird das Modell validiert. Um die Zielkonflikte bei der Gestaltung katalytischer Schwämme zu untersuchen, wurde eine Mehrkriterienoptimierung mit Hilfe eines genetischen Algorithmus durchgeführt und vielversprechende Kombinationen von Porositäten und Fensterdurchmessern identifiziert. Diese wurden anschließend in einer Fallstudie zur Methanisierung von Kohlenstoffdioxid im Rahmen einer Power-to-Gas-Anlage im Produktionsmaßstab mit konventionellen Packungen aus Pellets hinsichtlich Raumzeitausbeute, Druckverlust und Temperaturanstieg verglichen. Darüber hinaus wurden gradierte Schwämme mit diskreten Schichten unterschiedlicher Porosität in radialer Richtung vorgestellt und untersucht, um die bestehenden Zielkonflikte in der Gestaltung katalytischer Schwämme zumindest teilweise aufzulösen.

Die Analyse der Zielkonflikte in der Gestaltung katalytischer Schwämme zeigt, dass Schwämme einen Fensterdurchmesser unterhalb 1 mm aufweisen sollten, um hohe Katalysatordichten und somit hohe Raumzeitausbeuten (mehrere  $100 \text{ kg m}^{-3} \text{ h}^{-1}$ ) zu ermöglichen.

Die Porosität sollte möglichst hoch, jedoch derart gewählt werden, dass ein thermischer Runaway bei exothermen Reaktionen verhindert wird. Trotz der kleinen Fensterdurchmesser ist der resultierende Druckverlust auf Grund der vergleichsweise hohen Porosität auch noch für mittlere bis hohe Durchsätze tolerierbar. Des Weiteren sollte die Wärmeleitfähigkeit des Materials möglichst hoch sein, um die Vorteile der kontinuierlichen festen Phase auszunutzen.

Im Vergleich zu Packungen aus Pellets sind die derart gestalteten katalytischen Schwämme für die Methanisierung von Kohlenstoffdioxid durchaus konkurrenzfähig. Insbesondere erlauben sie auf Grund des hohen Anteils an Wärmeleitung im Feststoff einen stabilen Betrieb bei geringen Durchsätzen. Somit bieten katalytische Schwämme im Vergleich zu Schüttungen eine größere Flexibilität bezüglich des Durchsatzes, was speziell für den dynamischen Betrieb von Power-to-Gas-Anlagen von Vorteil ist. Zusätzlich kann der Druckverlust und der maximale Temperaturanstieg durch den Einsatz gradiertter Schwämme mit maßgeschneiderten radialen Porositäten im Vergleich zu Schwämmen mit gleichförmig verteilter Porosität um bis zu 26 % bzw. 46 % reduziert werden. Gleichzeitig sinkt die erzielte Raumzeitausbeute um lediglich 5 %. Durch eine gezielte Strukturierung kann die Leistung katalytischer Schwämme demnach noch weiter gesteigert werden.

Die Ergebnisse dieser Arbeit zeigen, dass feste Schwämme im Speziellen und monolithische Katalysatorträger im Allgemeinen auch im Produktionsmaßstab konkurrenzfähig zu konventionellen Packungen aus Pellets sind. Zudem erlauben sie einen stabilen Betrieb über einen weiten Bereich an Durchsätzen und sind somit besonders für die Anwendung in der Chemischen Energiespeicherung, wie z.B. einer Power-to-Gas-Anlage, geeignet. Des Weiteren zeigen die vorgestellten gradierten Schwämme das Potential von maßgeschneiderter monolithischer Katalysatorträger hinsichtlich einer weiteren Prozessintensivierung auf. Die vorgestellten Ansätze und Ergebnisse sind somit ein wichtiger Grundstein für die weitere Entwicklung monolithischer Katalysatorträger hin zum Produktionsmaßstab und ein erster Schritt in Richtung maßgeschneiderter Katalysatorträger, die durch hochentwickeltes Katalysatordesign und additive Fertigung ideal an die Bedürfnisse des Prozesses angepasst sind.

# Abstract

As a result of their high porosity and their continuous solid phase, solid sponges, also called open-cell foams, combine large specific surface areas, low pressure losses, and excellent heat transport properties. In addition, coated solid sponges allow to decouple catalytic activity and selectivity, which are influenced by the catalytic coat, from heat, mass, and momentum transport, which are mainly influenced by the morphology of the support, to a large extent. Thus, solid sponges are promising monolithic catalyst supports for either endo- or exothermic processes. Nevertheless, tradeoffs regarding the choice of the porosity and window diameter of solid sponges with respect to high bulk catalyst densities, low pressure losses, and high effective thermal conductivities remain unsolved. In addition, solid sponges have so far only been applied as catalyst supports at the lab scale. Consequently, their performance compared to conventional packed beds of pellets at the production scale is still unknown.

In order to obtain a more complete picture of the potential of solid sponges as monolithic catalyst supports, the tradeoffs regarding the design of solid sponges should be explored and quantified to deduce design guidelines. Further, it should be investigated whether solid sponges are competitive at the production scale.

Therefore, a 2-d pseudo-homogeneous multi-scale reactor model using state-of-the-art transport models for solid sponges is developed and implemented. The model is validated against polytropic lab-scale experiments in a fixed-bed reactor for the methanation of carbon dioxide. To explore the design tradeoffs of solid sponges, a multi-objective optimization problem is solved using a genetic algorithm, and promising combinations of the sponges' porosity and window diameter are identified. In a case study regarding the production-scale methanation of carbon dioxide for Power-to-Gas storage of surplus renewable electricity, selected sponge designs are compared to conventional packed beds of pellets with respect to space-time yield, pressure loss, and temperature increase. Furthermore, graded sponges with discrete porosity layers in the radial direction are presented as a concept to partially resolve the existing design tradeoffs of solid sponges.

The solution of the multi-objective optimization problem reveals that catalytic sponges should exhibit small window diameters below 1 mm to provide large specific surface areas and thus to obtain high space-time yields of several  $100 \text{ kg m}^{-3} \text{ h}^{-1}$ . The porosity should be carefully adjusted to provide a sufficiently large thermal conductivity to prevent thermal runaway in case of exothermic reactions. Although small window diameters are used, the high porosity of solid sponges still permits tolerable pressure losses. In addition, the solid thermal conductivity of catalytic sponges should be high to take full advantage of the continuous solid phase. In comparison to conventional packed beds of pellets, the selected catalytic sponge designs yield competitive performance. In particular, they allow

stable operation at low throughputs and thus provide flexibility regarding varying flow rates, which are expected for Power-to-Gas methanation units. Moreover, tailored graded sponges with discrete layers of different porosity in the radial direction allow to partially resolve the existing design tradeoffs of catalytic sponges. For the considered case, the graded sponges lead to a reduction of the pressure loss and the temperature increase by 26 % and 46 %, respectively, while the space-time yield decreases only by 5 % compared to uniform sponges.

In conclusion, the results of this study show that catalytic sponges in particular and monolithic catalyst supports in general allow competitive designs at the production scale. In addition, they enable stable operation over a wide range of flow rates and are thus ideally suited for Chemical Energy Storage applications such as Power-to-Gas. The prediction of graded sponges with discrete porosity layers in the radial direction demonstrates the potential of monolithic catalyst supports with specifically tailored morphology. Consequently, the presented approach represents a first step towards tailored monolithic catalysts that combine advanced catalyst design and additive manufacturing to produce the next generation of monolithic catalyst supports for chemical synthesis that are ideally adapted to the process requirements.

# Acknowledgement

As this is the last section I am writing for this thesis, I will take a moment to recall the last four years, which had been a time of hard work, scientific and personal achievements, but also of turning points and frustration. Thus, I would like to take the chance to give thought to the people who accompanied and supported me during this period.

First of all, I thank Prof. Dr.-Ing. Jorg Thöming, not only for his supervision and for reviewing this thesis, but also for his efforts to organize funding for my project, his honest curiosity and interest in my work, and most important, for his on-point and always encouraging advices regarding my scientific and personal development.

I also thank Prof. Dr.-Ing. Robert Güttel for his upright interest in my work, his time to review this thesis, and his valuable advices during several meetings at summer schools and conferences.

Further, I express my gratitude to the German Research Foundation (DFG) and the research training group MIMENIMA which provided funding for my thesis to a large extent and enabled me to present me and my work at national and international conferences. I also give my thanks to all the project leaders and peers, who still are or had been involved in the research training group, for intense but fruitful discussions during many scientific discourses and progress reports, uncomplicated access to their labs, and for sharing their ideas.

Especially, I thank Dr. Michael Baune for his encouraging support and his creative and quick fixes for many challenges that came up in the lab.

A special thanks also goes to my former peers in the research training group Miriam Schubert, Gerd Mikolajczyk, and Li Huang who provided their knowledge and skills regarding catalyst synthesis and coating,  $\mu$ CT analysis, and MRI measurements.

A special shoutout also goes to my peer Georg Pesch for many scientific discussions, chit chat, and his company during long weekends in the office.

In addition to my peers from the research training group, I also want to thank the current and former members of the Chemical Engineering – Recovery and Recycling group at the Center for Environmental Research and Sustainable Technology, who made my time in the group productive, creative, and enjoyable. In particular, I thank Jürgen Ulpts for the design and construction of the lab-scale reactor, and our successful cooperation in the field of *operando* concentration mapping using MRI.

I also thank the numerous students, namely Anna Becker, Ingmar Bösing, Jonas Wentrup, Maximilian Waack, Matthias Niemeyer, and Philipp Bruck, who either helped out in the lab or did their Bachelor and Master theses with me, for their curiosity and their commitment to the project.

Besides the people I met in my professional life, I also want to gratefully thank my family, especially my parents, who enabled me to get an excellent education and who always make me feel welcome very when I come home.

Finally, I say thank you to you, Katharina. You gave up a lot of common quality time, especially during the exciting last weeks of this thesis, and you always motivated me to go on in times of frustration and disappointment. Thank you!

# Contents

<b>1</b>	<b>Introduction</b>	<b>1</b>
1.1	Catalysis and solid catalysts . . . . .	1
1.2	Monolithic catalyst supports . . . . .	2
1.3	Objectives of this thesis . . . . .	4
1.4	Structure of this thesis . . . . .	5
<b>2</b>	<b>Technological and Scientific Background</b>	<b>7</b>
2.1	Chemical Energy Storage . . . . .	7
2.2	Methanation . . . . .	10
2.2.1	General introduction . . . . .	10
2.2.2	Thermodynamic analysis . . . . .	10
2.2.3	Catalysts and kinetic models . . . . .	13
2.2.4	Reactor concepts . . . . .	17
2.2.5	Current and future challenges . . . . .	18
2.3	Solid sponges . . . . .	19
2.3.1	General introduction . . . . .	19
2.3.2	Morphology and geometrical characterization . . . . .	19
2.3.3	Pressure loss along solid sponges . . . . .	24
2.3.4	Heat transport in solid sponges . . . . .	26
2.3.5	Mass transport in solid sponges . . . . .	40
2.3.6	Heat and mass transfer in solid sponges . . . . .	41
2.3.7	Global sensitivity analysis of transport in solid sponges . . . . .	44
2.3.8	Detailed simulations of fluid flow, heat, and mass transport in solid sponges . . . . .	46
2.3.9	Solid sponges as catalyst supports . . . . .	48
2.3.10	Additive manufacturing of monolithic catalyst supports – a recent trend . . . . .	53
2.3.11	Summary and concluding remarks . . . . .	55
<b>3</b>	<b>Catalysts, Reactor Setups, and Experimental Methods</b>	<b>57</b>
3.1	Morphological characterization of the investigated solid sponges . . . . .	57
3.2	Synthesis, application, and characterization of the catalytic coating . . . . .	61
3.2.1	Catalyst synthesis and coating procedure . . . . .	61
3.2.2	Characterization of the catalyst and the catalytic layer . . . . .	61
3.3	Determination of kinetic parameters . . . . .	64

3.3.1	Reactor setup, experimental procedure, and data evaluation . . . . .	64
3.3.2	Determination of the pre-exponential factors and activation energies	67
3.4	Polytropic CO <sub>2</sub> -methanation experiments . . . . .	71
3.4.1	Reactor setup . . . . .	71
3.4.2	Experimental procedure and data evaluation . . . . .	74
<b>4</b>	<b>Fixed-Bed Reactor Model</b>	<b>77</b>
4.1	Introduction to reactor models . . . . .	77
4.2	General description of the implemented reactor model . . . . .	77
4.3	Description of the reactor-scale model . . . . .	78
4.3.1	Heat, mass, and momentum balances . . . . .	78
4.3.2	Flow models . . . . .	80
4.3.3	Initial and boundary conditions . . . . .	81
4.3.4	Numerical approach and solution procedure . . . . .	82
4.3.5	Simplified steady-state reactor model without axial dispersion . . . . .	82
4.4	Description of the catalyst-scale model . . . . .	83
4.4.1	Heat, mass, and momentum balances . . . . .	83
4.4.2	Flux models . . . . .	84
4.4.3	Boundary conditions and solution of the catalyst-scale model . . . . .	85
4.4.4	Calculation of the effectiveness factor . . . . .	86
4.4.5	Simplified models to approximate the effectiveness factor . . . . .	86
<b>5</b>	<b>Results and Discussion</b>	<b>91</b>
5.1	Validation of the implemented reactor model . . . . .	91
5.1.1	Stability of the catalyst during polytropic operation and reproducibility of the lab-scale fixed-bed reactor experiments . . . . .	91
5.1.2	Comparison of simulated and measured axial temperature profiles during CO <sub>2</sub> -methanation . . . . .	92
5.1.3	Model validation against operando Magnetic Resonance Spectroscopy Imaging measurements . . . . .	101
5.2	Performance of catalytic sponges during methanation of carbon dioxide at production scale . . . . .	103
5.2.1	Scale-up analysis of catalytic sponges for CO <sub>2</sub> -methanation . . . . .	103
5.2.2	Analysis of tradeoffs in the design of catalytic sponges . . . . .	109
5.2.3	Comparison of catalytic sponges and packed beds of pellets for CO <sub>2</sub> -methanation at production scale . . . . .	115
5.3	Catalytic sponges with radially graded porosity . . . . .	121
5.3.1	Modeling graded sponges . . . . .	121
5.3.2	Calculation and analysis of tailored porosity profiles . . . . .	124
<b>6</b>	<b>Conclusions and Outlook</b>	<b>131</b>
6.1	Summary of the current state of catalytic Sponges and monolithic catalyst supports . . . . .	131
6.2	Outlook on the future of monolithic catalyst supports . . . . .	133

<b>Appendix</b>	137
<b>A Additional Validation Results</b>	137
<b>B Additional Simulation Results</b>	143
<b>C Additional Experimental Details</b>	145
<b>D Computational Fluid Dynamics: Velocity distribution in solid sponges</b>	149
<b>E Calculation of Gas-Phase Equilibria</b>	153
<b>F Calculation of Pure Species, Mixture, and Reaction Properties</b>	157
<b>G Collection of Solid Sponge Morphological Properties</b>	161
<b>Notation</b>	165
<b>References</b>	173



## 1.1 Catalysis and solid catalysts

Catalysis is of tremendous importance for the chemical industry and modern societies alike since it enables efficient conversion of raw materials, reduces pollution and waste, and allows the production of essential chemicals. Among the most prominent applications of catalysis are the Haber-Bosch process to produce ammonia as base material for artificial fertilizers, fluid catalytic cracking of crude oil into transportation fuels and light hydrocarbons, and the catalytic treatment of poisonous gases and pollutants in exhaust gas of power plants and automobiles. Today, 85%–90% of all processes in the chemical industry make use of catalysts [42, 135]. Even more, every single molecule of current transportation fuels has probably been in contact with a catalyst at least once during production [42]. In 2014, catalysts worth \$17.2 billion in total were traded worldwide and estimates are that the catalyst market continues to grow annually around 5%–6% on average [135]. With a fraction of 80%, solid or heterogeneous catalysts make up most of the catalyst market, followed by homogeneous catalysts (15%–17%), and biocatalysts (3%–5%) [42, 135]. The great success of catalysts is mainly based on the value they add to their various products. The total value of chemicals and fuels which are produced using a catalyst is estimated to be at least 100 times higher than the one of the global catalyst market itself [42, 135]. Consequently, nearly 80% of the total added value created in the chemical industry is produced by catalysts. Moreover, experts estimate that around 20% of the global economy depend directly on the catalyst industry [135].

Solid catalysts consist of an active component, usually a metal, that is typically deposited on an oxidic support with large specific surface area (several  $100 \text{ m}^2 \text{ g}^{-1}$ ) to stabilize the nanometer-sized metal clusters. For technological applications catalysts are shaped into mesoporous pellets or extrudates, which are then filled into several reactor tubes to create a random bed of loosely packed catalyst pellets. The milli- or centimeter-sized pellets allow a better handling of the catalysts. In addition, they influence heat, mass, and momentum transport in the reactor. Small pellets for example lead to a higher pressure loss along the catalyst bed than larger pellets, and are thus not applicable in large scale industrial reactors with high throughputs.

de Jong [42] reviewed the development of the production of solid catalysts from natural materials at the end of the 19th century, over specially synthesized materials used in the 20th century, to nanostructured materials developed at the beginning of the 21st century. From 1940 to 2010 for instance, the advances in surface and material science led not only to an increase of the selectivity of modern catalysts (see Fig. 1.1 b), but also to a 30-fold increase of the space-time yield (see Fig. 1.1 a). Although the data shown here is only for Fischer-Tropsch catalysts, it can be expected that the same trend is true for other catalysts as well. Consequently, in order to utilize the full potential of modern catalysts, significant heat and mass fluxes have to be managed in modern chemical reactors, especially in case

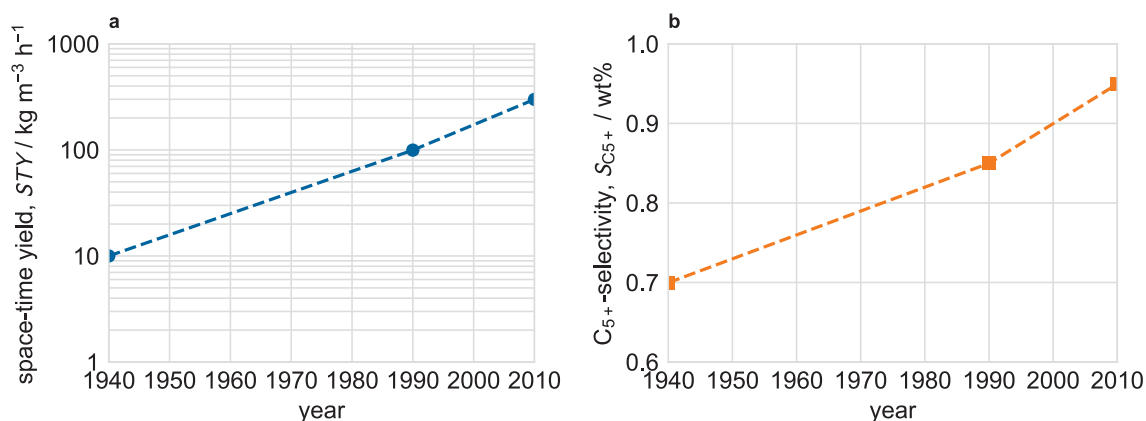


**FIG. 1.1.** Development of space-time-yield  $STY$  (a) and  $C_5+$ -selectivity  $S_{C_5+}$  (b) of Fischer-Tropsch catalysts in the past. Data compiled by de Jong [42, p. 3].

of exo- and endothermic processes. Even though advances in heat and mass transport were made along the development of modern catalysts, many current catalytic processes in the chemical industry are still limited by either heat or mass transport. As a consequence, chemical engineers started to investigate *monolithic, structured catalyst supports* for chemical reactors because of their promising heat and mass transport properties.

## 1.2 Monolithic catalyst supports

In contrast to pellets, which are much smaller than the reactor tube, monolithic catalyst supports exhibit the same diameter as the reactor tube. Typical monolithic catalyst supports are honeycombs and solid sponges (see Fig. 1.2, honeycombs not shown). Although honeycombs are already applied commercially for exhaust gas treatment in automobiles and power plants, the application of honeycombs and solid sponges as monolithic catalyst supports in the chemical industry is still in a conceptual phase of development with first proof-of-principles at the lab scale. Because of their too low surface area for catalysis (usually  $1 \text{ m}^2 \text{ g}^{-1}$ – $5 \text{ m}^2 \text{ g}^{-1}$ ), monolithic catalyst supports are covered with a micrometer-sized layer of a washcoat with large specific surface area (typically several  $100 \text{ m}^2 \text{ g}^{-1}$ ), which is subsequently impregnated with the active catalytic material (see Govender and



**FIG. 1.2.** Examples of catalyst supports in heterogeneous catalysis. Background: solid mullite sponges ( $\varnothing 25 \text{ mm} \times 25 \text{ mm}$ ) with decreasing window size from left to right; foreground: alumina pellets ( $\varnothing 3.1 \text{ mm} \times 5.1 \text{ mm}$ ).

Friedrich [93] and Kraushaar-Czarnetzki and Müller [157]). Alternatively, the application of the coating and its impregnation can be achieved in one step by mixing the active compound into the washcoat slurry prior to the dip-coating procedure.

The high porosities of solid sponges and the regular geometry of honeycombs provide low pressure losses along the catalyst bed. Furthermore, monolithic catalyst supports allow high heat transport rates via thermal conduction in the continuous solid phase. Compared to honeycombs, sponges exhibit larger specific surface areas and also allow radial fluid flow and increased mixing which improves interfacial heat and mass transfer between the fluid and solid phase. The main advantage of monolithic catalyst supports, however, is the decoupling of catalytic activity and selectivity, which is controlled by the mesoporous washcoat, and heat and mass transport, which are predominantly controlled by the morphology of the support—a strategy that, according to Twigg and Richardson [282], has been successfully applied in automotive catalysis for decades and is now adopted for chemical reactors. More recently, Gascon et al. [81], Güttel [102], and Güttel and Turek [104] reestablished the concept of decoupling and optimizing catalytic activity and heat and mass transport in structured reactors, and outlined the potential of structuring catalysts on the micro-, meso-, and macroscale for process intensification, or as Kreutzer et al. [158] concluded: “Taking complete control over the shape of the voids between the catalytically active material automatically introduces new independent length scales that allow decoupling of intra-particle phenomena from extra-particle phenomena.” (Kreutzer et al. [158], p. 117).

Figure 1.3 illustrates the concept of decoupling catalytic activity and selectivity, and heat and mass transport using monolithic catalyst supports. For packed beds, the material, the micro- and mesostructure, and the shape of the catalyst pellets influence catalytic activity, selectivity, and efficiency, as well as pressure loss, heat and mass transfer, and heat and mass transport in the packed bed. In the case of coated monoliths, the catalytic washcoat controls catalytic activity, selectivity, and efficiency, while the support mainly influences pressure loss, interfacial heat and mass transfer, and heat and mass transport. The advantage of decoupling the catalytic and the heat and mass transport properties becomes evident when taking a closer look at heat transport and the thermal conductivity. Because the pellets need to provide a high porosity and a large (inner) surface area to yield catalytic activity, their relative density is only between 30 % and 50 %. Consequently, the effective thermal conductivity of a single pellet is also only 30 % and 50 % of the material thermal conductivity, if a linear relation between the relative density and the effective thermal conductivity of an individual pellet is assumed. In case of coated monoliths, the washcoat exhibits a low relative density to yield catalytic activity, while the support has a high relative density of 85 %–95 % (see Dietrich et al. [49]), and thus a high thermal conductivity. Consequently coated monoliths allow to combine high catalytic activity and high thermal conductivities. In addition, different materials for the support could be chosen, e. g., metals, to further boost the thermal conductivity of the catalyst. Therefore, “conductive structured catalysts (...) offer unparalleled potential for engineering the heat management in catalytic reactors for non-adiabatic processes.”, (Tronconi et al. [278], p. 62).

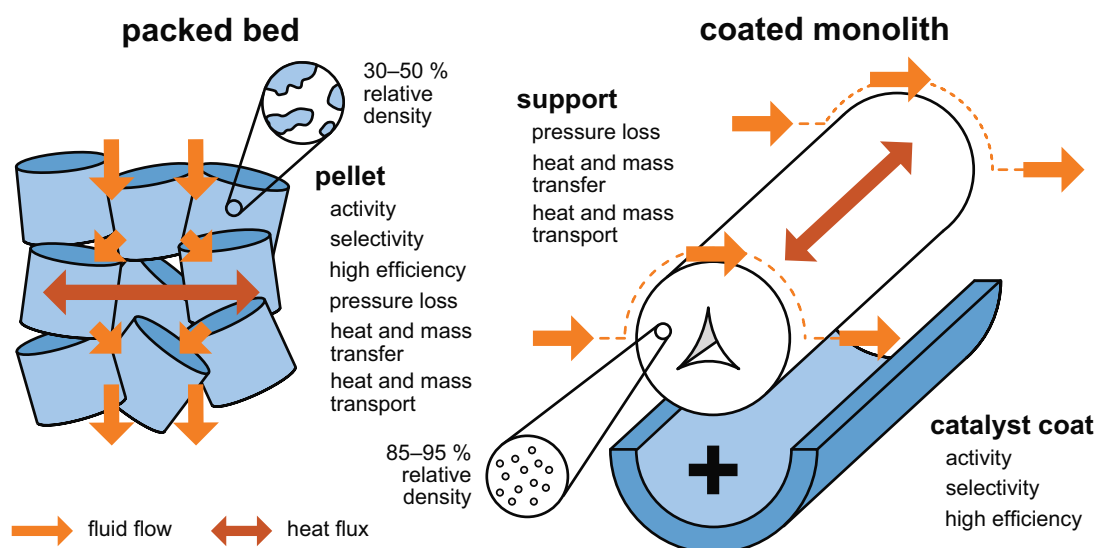


**FIG. 1.3.** Conceptual illustration of packed beds and coated monoliths, here a solid sponge, as catalyst supports. While the shape and the micro- and mesostructure of the pellet influence not only the catalytic activity and efficiency, they also influence pressure loss, interfacial heat and mass transfer, and heat and mass transport within in the packed bed significantly. For coated monoliths, the catalytic activity and efficiency is mainly controlled by the mesoporous catalyst coat, while pressure loss, interfacial heat and mass transfer, and heat and mass transport are predominantly influenced by the morphology of the support. Thus, catalytic activity and heat and mass transport are to a large extent decoupled and can be tuned independently.

### 1.3 Objectives of this thesis

Although the tradeoffs between catalytic performance and heat and mass transport are resolved to a large extent by using coated monolithic catalyst supports, tradeoffs regarding the design of catalytic sponges towards high bulk catalyst densities (catalyst mass per unit reactor volume), low pressure losses, and high effective thermal conductivities remain unsolved. Figure 1.4 illustrates the trilemma regarding the design of catalytic sponges with respect to their porosity and window diameter. In order to reach high bulk catalyst densities, sponges should provide large specific surface areas and thus small window diameters. In contrast, low pressure losses require large window diameters and high porosities. Finally, low porosities, i. e., high relative densities, lead to high thermal conductivities, which are vital to control the temperature in endo- and exothermic processes.

Therefore, the objectives of this thesis are:

1. the implementation and validation of a 2-d multi-scale fixed-bed reactor model for catalytic sponges;
2. the analysis of tradeoffs regarding the design of catalytic sponges using multi-objective optimization and the deduction of design guidelines for catalytic sponges in gas-phase reactions, and
3. the introduction and evaluation of graded sponges with tailored radial porosity profiles as a potential method to resolve the existing design tradeoffs.

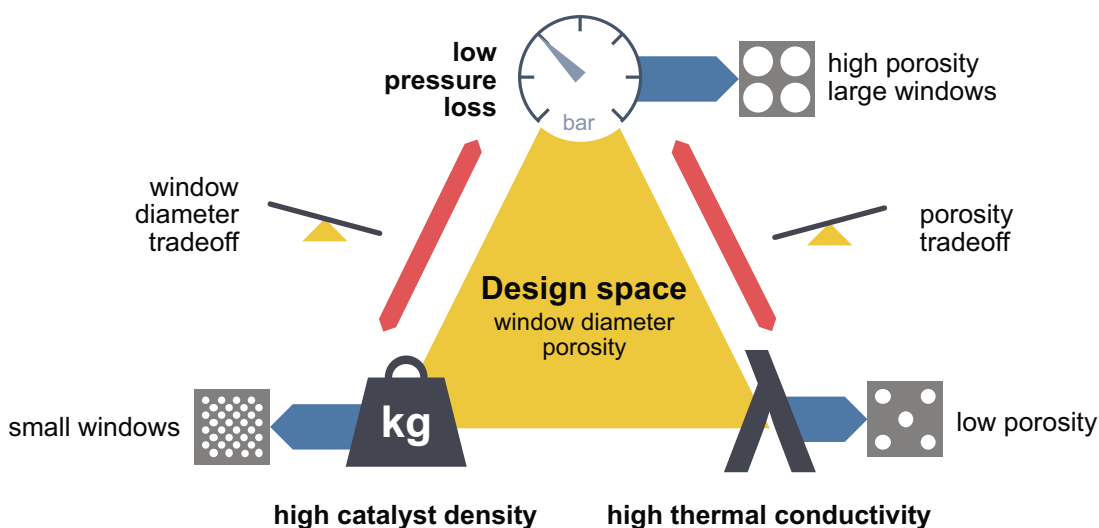


**FIG. 1.4.** Trilemma of the choice of the porosity and the window diameter of catalytic sponges with respect to high bulk catalyst densities (catalyst mass per unit reactor volume), low pressure losses, and high effective thermal conductivities. Because of the conflicting structural requirements (low vs. high porosities and small vs. large window diameters), a tradeoff between high bulk catalyst densities, low pressure losses, and high effective thermal conductivities is inevitable.

In this work, the methanation of carbon dioxide is chosen as a representative exothermic gas-phase process because it can be operated at low to moderate pressures in the lab and yields a simple product spectrum that can easily be analyzed using conventional gas chromatography. In addition, its successful application in Chemical Energy Storage (CES) demands the development of distributed small to medium scale methanation units that might benefit considerably from efficient catalytic sponges. Nevertheless, it is expected that the results of this work regarding the design of catalytic sponges can readily be extrapolated to other gas-phase catalytic processes such as methanol synthesis. The latter, however, requires high pressures and is thus elaborate to operate in a fixed-bed reactor at the lab scale.

## 1.4 Structure of this thesis

After a general introduction to catalysis, monolithic catalyst supports, and the design tradeoffs of solid sponges in this chapter, the technological and scientific background regarding Chemical Energy Storage, methanation, and in particular regarding solid sponges is thoroughly reviewed in Chapter 2. In addition to the presentation of the available models to describe heat, mass, and momentum transport in solid sponges, comparisons of solid sponges and packed beds of pellets are presented, and conclusions regarding the application of solid sponges as catalyst support are drawn. Furthermore, the current state of development of catalytic sponges and related monolithic catalyst supports, such as 3-d printed structures, is presented and analyzed.

In Chapter 3, the materials and experimental setups applied in this work to obtain original data for model validation are presented. In addition, the kinetic parameters of an in-house synthesized methanation catalyst are presented in this chapter.

The heart of this work is the development and implementation of a 2-d multi-scale reactor model for catalytic sponges based on state-of-the-art constitutive models, which is presented in detail in Chapter 4.

In Chapter 5, the implemented reactor model is validated against original experimental data obtained from conventional lab-scale experiments and from *in-situ* Magnetic Resonance Imaging measurements. Further, a scale-up study on the methanation of carbon dioxide over catalytic sponges is presented before the tradeoffs regarding the design of catalytic sponges are explored using an evolutionary multi-objective optimization algorithm. The optimization results are the foundation for a case study comparing catalytic sponges and conventional packed beds of pellets for the methanation of carbon dioxide at production scale. In addition, tailored graded monolithic sponges with radially varying porosity are presented and their potential regarding process intensification is outlined.

Finally, the results obtained in this work are summarized and discussed in Chapter 6, and explicit recommendations for future research are given.

#### **A remark on units**

Throughout this work units from the International System (SI) are used. Thus, if not explicitly stated otherwise, all equations have to be evaluated using SI units to obtain correct results. Nevertheless, numerical values are often given in more practical units, such as mm instead of m. In addition, the non-SI units °C and bar are frequently used for temperature and pressure because they not only provide a more practical approach for experimental results and operating conditions, but are also standard in the chemical engineering community. Moreover, the conversion of °C ( $0\text{ °C} = 273.15\text{ K}$ ,  $\Delta T/\text{K} = \Delta T/\text{°C}$ ) and bar ( $1\text{ bar} = 1 \cdot 10^5\text{ Pa}$ ) to their SI counterparts is trivial. Further, a temperature of 273.15 K and a pressure of 1.013 25 bar are used as normal conditions, also abbreviated NTP.

## 2.1 Chemical Energy Storage

The rejection of nuclear power after the incident at the Fukushima Dai-ichi nuclear power plant in 2011 [270], limited fossil resources, such as crude oil, coal, and natural gas, and most critical, a rising carbon dioxide concentration in the earth's atmosphere and the related effects of global warming induced societies worldwide to increase the share of renewable energies in their energy system (see Schlögl [256]). The Umweltbundesamt (UBA), Germany's Federal Environmental Agency, for instance reports a 50 % relative increase of the contribution of renewable energies to the total power production from 20.3 % in 2011 to 31.7 % in 2016 [287]. Furthermore, the UBA aims at 100 % renewable energy in the electricity sector in 2050 [286]. The numbers not only indicate the rise of renewable energies, but also that the current technology is capable to produce enough renewable energy to cover a considerable amount of the total energy consumption of a large G7 country.

The major drawback of renewable energies, such as wind and solar power, however, is their fluctuating nature (see for example Schlögl [256]). Consequently, differences between production and demand either lead to shortages of electricity (production < demand), or overcapacities (production > demand) that ultimately lead to negative electricity prices for the producers. In addition, the discrepancies between production and demand are even more likely to occur if renewable energy makes up most of the total energy production.

Although periodic cycles, such as the day-night cycle and the summer-winter cycle can be estimated and possibly compensated by conventional power plants, other cycles such as cloud coverage or weak winds are less predictable. Furthermore, conventional power plants are presumably to sluggish to quickly react to short-term fluctuations. Consequently, the successful incorporation of renewable energies is only possible if short- and long-term storage of renewable energy is available to compensate the differences between fluctuating production and demand [256].

In order to appropriately store surplus renewable electricity, different storage technologies from batteries for short-term storage of moderate amounts of energy (up to 1 MWh for several days) to long-term storage of chemical energy carriers (up to 1 TWh for months and years) should be applied [259]. Pumped hydro is also able to store large amounts of energy for long periods, however, its availability strongly depends on geographical aspects (height difference). Thus, the storage of surplus renewable electricity in chemical energy carriers such as methane (substitute natural gas, SNG) or liquid fuels, summarized as Chemical Energy Storages (CES) or Power-to-X (PtX, where X stands for the energy carrier), is the only option for regionally independent long-term storage of large amounts of energy [101, 259].

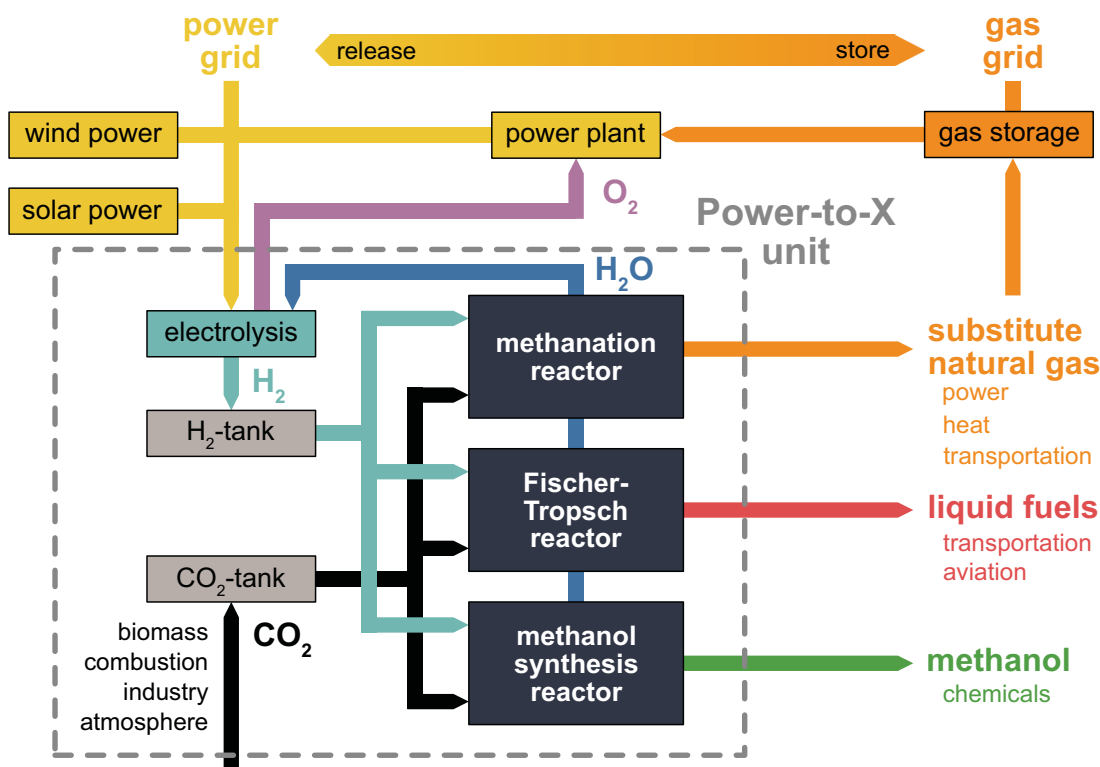


**FIG. 2.1.** Simplified Power-to-X (PtX) concept to store excess renewable energy, such as wind and solar power, in substitute natural gas (SNG) for later power generation or heating, in liquid fuels for transportation and aviation, and in methanol for production of various chemicals. In addition, hydrogen could be used directly as energy carrier. For the Fischer-Tropsch synthesis, carbon dioxide must probably be reduced to carbon monoxide first. Adapted and extended from Sterner and Stadler [269, p. 416].

A simplified PtX concept is illustrated in Fig. 2.1. If possible, wind and solar power plants feed electricity directly into the power grid. If production however is larger than the current electricity demand, the surplus renewable electricity is used to produce hydrogen (H<sub>2</sub>) via electrolysis. Although hydrogen is an excellent energy carrier (33.3 kWh kg<sup>-1</sup> at 1 bar, see [259]), the infrastructure for storage, distribution, and usage has yet to be built from scratch. Consequently, hydrogen is further converted catalytically together with carbon dioxide (CO<sub>2</sub>) to produce SNG (Power-to-Gas, PtG), liquid fuels (Power-to-Liquid, PtL), or methanol as base chemical (also PtL). In addition, hydrogen could be used to reduce carbon dioxide by producing syngas via the reverse water-gas-shift reaction (Power-to-Syngas, Pt-Syngas) (see Sternberg and Bardow [268]). Syngas is a H<sub>2</sub>/CO-mixture that is the main feed of many processes in the chemical industry. Thus, not only surplus renewable electricity would be stored, but carbon dioxide emissions would also be reduced. The carbon dioxide could be provided from biomass, combustion, industrial processes (cement industry), or even from the atmosphere (see for instance Climeworks AG [37]).

In contrast to hydrogen, the infrastructure to store, distribute, and use SNG is readily available worldwide. Hence, SNG produced via methanation of carbon dioxide can be fed to the existing gas grid, and reconverted into electricity (Power-to-Power, PtP) during periods of low availability of renewable energies. In addition, it can be used for heating or as fuel for transportation.

Liquid fuels via Fischer-Tropsch synthesis (FTS) on the other hand will most likely not be used to produce electricity, but to drive the mobility sector that still relies on liquid fuels. Thus, as long as internal combustion engines dominate the transportation sector, PtL is an option to increase the share of renewable energies and thus partly decarbonize the mobility sector. In addition, because of their unmatched volumetric energy density (liquid fuels:  $10 \text{ kWh L}^{-1}$ ; SNG:  $0.1 \text{ kWh L}^{-1}$  [259]), liquid fuels based on renewable energies are also a promising alternative for aviation.

Another option is the conversion of hydrogen and carbon dioxide to methanol (also PtL) that can not only be used in the transportation sector, but is also a relevant platform chemical from which other important chemicals can be synthesized.

Sternberg and Bardow [267, 268] compared the different storage strategies regarding their environmental impact. Accordingly, PtG has the potential to reduce the emission of carbon dioxide and equivalent greenhouse gases by about  $48 \text{ g kWh}^{-1}$  if it replaces the utilization of natural gas. A comparable value ( $72 \text{ g kWh}^{-1}$ ) was recently reported by Uusitalo et al. [288]. For comparison, Sternberg and Bardow [268] calculated a value of  $100 \text{ g kWh}^{-1}$  for the Pt-Syngas route, and Uusitalo et al. [288] report a cut of  $144 \text{ g kWh}^{-1}$  for methanol production if conventional processes were substituted one to one.

In their comprehensive study, Ausfelder et al. [7] estimated that 2.3 TWh surplus renewable electricity have to be stored in Germany in 2032. Based on the current technology, they determined the efficiency of PtP based on SNG to about 25%. Hence, electricity from PtP will cost approximately 4–5 times as much as electricity produced from natural gas in existing power plants (PtP:  $22.7 \text{ ct kWh}^{-1}$ ; conventional:  $4 \text{ ct kWh}^{-1}$  [7]). Jürgensen et al. [136], Kopp et al. [151], Schiebahn et al. [248], and Thema et al. [277] got to the same conclusion based on their economical analysis of PtG technologies. If however the share of renewable energies in the energy system increases to reduce carbon dioxide emissions, PtX is inevitable or as Thema et al. put it: “There is a dilemma which needs to be resolved: from an economical point of view, power-to-gas is a prospective required technology which is not worthwhile to operate today mainly because of an unsuitable framework. To reach the technically required power-to-gas capacity at the right point of time, we have to start building up the necessary infrastructure now.” (Thema et al. [277], p. 399).

Thus, PtG via methanation of carbon dioxide may not be the ideal solution for storage of renewable electricity and the decarbonization of the energy sector, but it can rely on an existing infrastructure and is thus a promising option for a transition period from an energy system dominated by fossil fuels to an energy system that mostly relies on renewable resources. Moreover, PtX allows to connect the energy, the transportation, the heat, and the chemical sector, and thus the formation of a more flexible and robust energy system.

From a reaction engineering and reactor design point of view, PtX is challenging because it demands decentralized small to medium scale catalytic reactor units that are efficient, tolerate fluctuating loads, and provide low complexity to be operated, probably autonomously, in remote regions. Thus, existing reactor concepts, which were so far streamlined to centralized large-scale production (economies of scale), have to be rethought and adapted, and new catalysts, supports, and reactor designs have to be developed to enable the successful incorporation of renewable energies into the energy system.

## 2.2 Methanation

### 2.2.1 General introduction

The methanation of carbon monoxide and carbon dioxide, Eqns. (2.1) and (2.2), over nickel catalysts was first described by Sabatier and Baptiste [240] in 1902:



$$\Delta_{\text{R}}G_{298} = -142 \text{ kJ mol}^{-1}$$



$$\Delta_{\text{R}}G_{298} = -113 \text{ kJ mol}^{-1}$$

Since then, it has been mostly applied to remove small amounts of carbon monoxide in hydrogen-rich feeds for ammonia synthesis, and later for fuel cell applications [156, 208]. Comprehensive reviews on methanation were recently presented by Kopyscinski et al. [152] and Rösner et al. [238]. Accordingly, methanation of stoichiometric feeds was first discussed during the oil crisis in the 1970ties to convert large amounts of coal to SNG. Nevertheless, only few applications reached a commercial level. Today, methanation is discussed again as a promising process to decrease the dependency on finite fossil resources, and to utilize carbon dioxide and thus reduce greenhouse gas emissions. Whereas researchers and engineers in Europe mainly work on small to medium scale methanation of carbon dioxide to incorporate renewable energies into the energy system and to reduce carbon dioxide emissions (see Section 2.1, pp. 7 ff.), efforts in China mainly focus on the large-scale conversion of coal to SNG. In the upcoming sections, fundamentals of methanation regarding favorable thermodynamics, catalysts and kinetics, and reactor design are reviewed and current and future challenges are discussed.

### 2.2.2 Thermodynamic analysis

Both, the methanation of carbon monoxide and carbon dioxide are strongly exothermic and exhibit a strong reduction in volume by 50 % and 40 %, respectively, as the reaction proceeds. Thus, following Le Chatelier's principle, low temperatures and high pressures are favorable from a thermodynamic point of view to obtain high methane yields. In addition to the two methanation reactions, several other chemical reactions between the participating species are possible (see Tab. 2.1) [80, 171, 202, 273]. The interplay between the different reactions forms a complex gas-solid system. Thus, numerical methods are usually applied to calculate the equilibrium mole fractions to subsequently choose favorable operating windows regarding temperature, pressure, and feed ratio. The most comprehensive thermodynamic analysis of the methanation process so far was conducted by Gao et al. [80].

Figure 2.2 shows the equilibrium mole fractions of carbon dioxide (a), methane (b), carbon monoxide (c), and solid carbon (d) for different temperatures and feed ratios at 1 bar and 10 bar, which were calculated in this work using a Gibbs-free-energy minimization method (see Appendix E, p. 153 ff. for a detailed description of the method). For the calculations,

**TAB. 2.1.** Summary of the most relevant chemical reactions for the methanation of carbon oxides compiled from [80, 171, 202, 273].

No.	Name	Reaction	Heat of reaction at 298.15 K kJ mol <sup>-1</sup>
1	carbon monoxide methanation	$\text{CO} + 3\text{H}_2 \rightleftharpoons \text{CH}_4 + \text{H}_2\text{O}$	-206
2	carbon dioxide methanation	$\text{CO}_2 + 4\text{H}_2 \rightleftharpoons \text{CH}_4 + 2\text{H}_2\text{O}$	-165
3	methane dry-reforming	$\text{CO}_2 + \text{CH}_4 \rightleftharpoons 2\text{CO} + 2\text{H}_2$	+247
4	reverse water-gas-shift	$\text{CO}_2 + \text{H}_2 \rightleftharpoons \text{CO} + \text{H}_2\text{O}$	+41
5	Boudouard reaction	$2\text{CO} \rightleftharpoons \text{C} + \text{CO}_2$	-172
6	methane cracking	$\text{CH}_4 \rightleftharpoons \text{C} + 2\text{H}_2$	+75
7	carbon monoxide reduction	$\text{CO} + \text{H}_2 \rightleftharpoons \text{C} + \text{H}_2\text{O}$	-131
8	carbon dioxide reduction	$\text{CO}_2 + 2\text{H}_2 \rightleftharpoons \text{C} + 2\text{H}_2\text{O}$	-90
9	chain growth	$\text{CO} + 2\text{H}_2 \rightleftharpoons -\text{CH}_2- + \text{H}_2\text{O}$	-150
10	chain growth	$\text{CO}_2 + 3\text{H}_2 \rightleftharpoons -\text{CH}_2- + 2\text{H}_2\text{O}$	-110

only hydrogen and carbon dioxide were considered in the feed, and the Peng-Robinson cubic equation of state (EOS) [216] was applied.

The carbon dioxide mole fraction clearly decreases with increasing feed ratio and approaches zero at the stoichiometric feed ratio of 4, indicating complete conversion of carbon

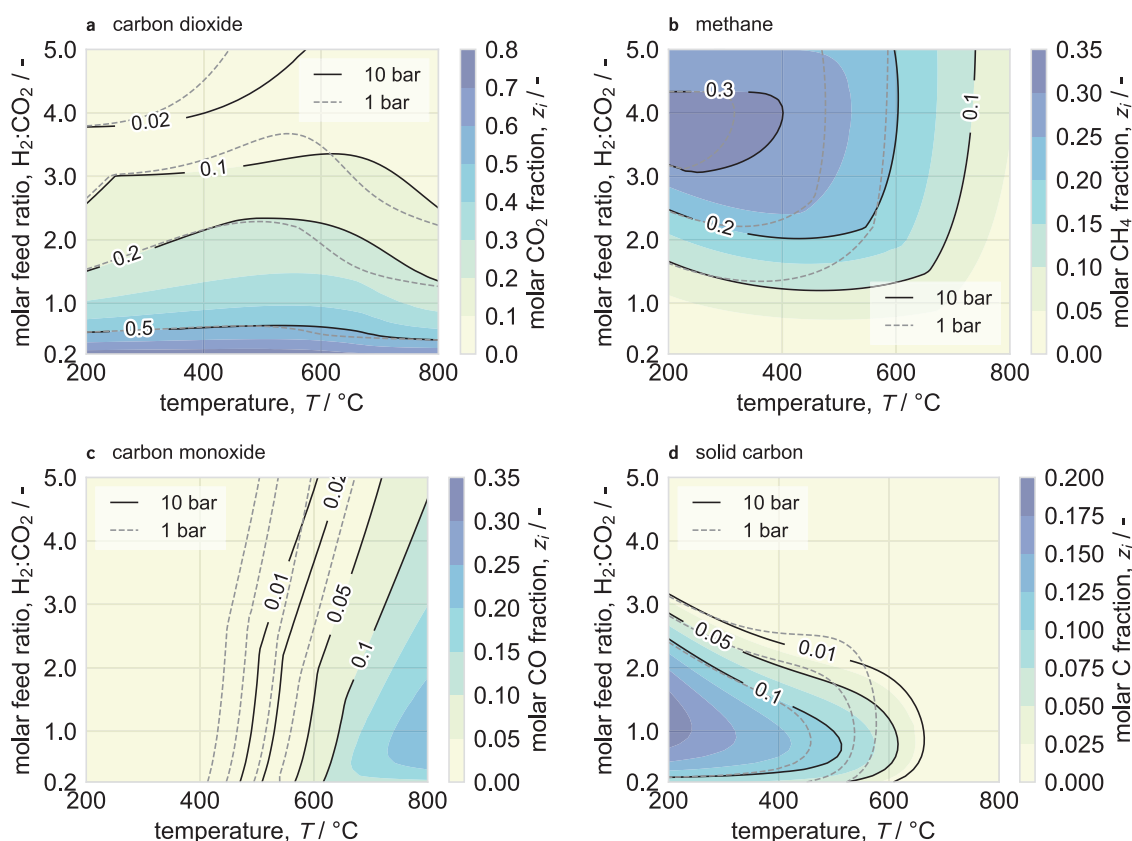


**FIG. 2.2.** Equilibrium mole fractions of carbon dioxide (a), methane (b), carbon monoxide (c), and solid carbon (d) depending on temperature and H<sub>2</sub>/CO<sub>2</sub> ratio for a pressure of 10 bar. The grey dashed lines indicate the same isolevels for 1 bar.

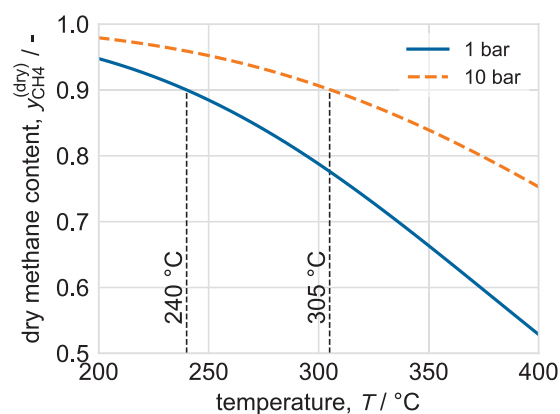


**FIG. 2.3.** Equilibrium dry mole fraction of methane, i. e., water was completely removed, depending on temperature for pressures of 1 bar and 10 bar.

dioxide (see Fig. 2.2 a). At a stoichiometric feed ratio of 4, the carbon dioxide mole fraction increases significantly for temperatures above 400 °C because the reverse reaction limits the conversion of carbon dioxide into methane. For temperatures above 600 °C, the carbon dioxide mole fraction decreases again because of carbon monoxide formation (see Fig. 2.2 c).

In order to obtain high methane yields at an operating pressure of 10 bar, temperatures below 400 °C and a feed ratio close to 4 should be maintained (see Fig. 2.2 b). At 1 bar, the maximum temperature for a methane mole fraction of 0.3 decreases from 400 °C to 300 °C because of the strong volume contraction of the methanation reaction, Eq. (2.2) (see grey dashed lines in Fig. 2.2 b). Consequently, high pressure should be applied for the methanation process. Nevertheless, for small- to medium-scale methanation of carbon dioxide within PtG, pressures around 10 bar are reasonable as the local gas distribution grid is operated at around 8 bar (see Osman et al. [204]). In addition, low pressures allow a more dynamic operation of the methanation unit.

Carbon monoxide is produced from carbon dioxide and hydrogen at high temperatures via the reverse water-gas shift reaction (see Fig. 2.2 c and reaction 4 in Tab. 2.1). At a feed ratio of 4, the carbon monoxide mole fraction is around 1 vol% at 575 °C. For feed ratios around 1, 1 vol% carbon monoxide are already encountered at 500 °C. Although the formation of carbon monoxide can be disregarded from a thermodynamic viewpoint, carbon monoxide can also be formed at the surface of the catalyst at lower temperatures via dissociative adsorption of carbon dioxide. If the adsorbed carbon dioxide is not further reduced to solid carbon, it can desorb into the gas phase.

Although solid carbon presumably plays a vital role in the methanation of carbon dioxide, it does not accumulate on the surface of the catalyst at feed ratios of 4 because of the excess of hydrogen according to thermodynamics (see Fig. 2.2 d). Below feed ratios of 3, however, the formation of considerable amounts of surface carbon is thermodynamically favorable. During methanation, feed ratios of 3 and below could be encountered in the mesopores of the catalyst because pore diffusion affects carbon dioxide more than hydrogen. Thus, the H<sub>2</sub>/CO<sub>2</sub> ratio might change within the catalyst and cause formation of solid carbon, which leads to deactivation of the catalyst. Gao et al. [80], however, point out that the formation

of water vapor during the methanation helps to prevent solid carbon accumulation on the catalyst surface.

For efficient operation of a PtG unit, downstream post-processing of the produced methane should be reduced to a minimum. Thus, after the condensation of water, the dry methane content should be above 90 vol% or even 95 vol% for direct injection in the local natural gas grid (see Osman et al. [204]). In order to achieve such high methane contents in the dry product gas, the temperature at the outlet of the catalyst should therefore not exceed 305 °C and 250 °C at 10 bar to reach 90 vol% and 95 vol% methane, respectively (see Fig. 2.3). The temperature limits serve as guidelines for the maximum cooling temperature in case of cooled fixed-bed reactors.

### 2.2.3 Catalysts and kinetic models

From a thermodynamic point of view, the methanation of carbon monoxide and carbon dioxide are both not only exothermic but also exergonic, and thus would proceed spontaneously. Nevertheless, both reactions are kinetically limited and demand the use of catalysts to obtain acceptable reaction rates for technological applications. The reduction of carbon dioxide to methane for example, requires the transfer of eight electrons (see Thampi et al. [275]). Typical methanation catalysts are the group VIII metals (see Vance and Bartholomew [290] and Weatherbee and Bartholomew [298, 299]) such as ruthenium (Ru, [30, 112, 133, 179, 257]), iron (Fe, [225]), nickel (Ni, [1, 44, 78, 154, 173, 175, 177, 182, 196, 257, 299, 308, 315]), and cobalt (Co, [258]). Mills and Steffgen [191] reported the following order regarding the activity of the metals for carbon dioxide methanation: Ru > Fe > Ni > Co. Regarding methane selectivity the proposed order is: Ni > Co > Fe > Ru. Consequently, based on today's knowledge, nickel is the catalyst of choice, especially for technological applications, as it provides the best compromise between methane selectivity and activity, and is also affordable. Typical support materials are Al<sub>2</sub>O<sub>3</sub>, SiO<sub>2</sub>, and TiO<sub>2</sub>.

Because of the low possibility of carbon formation on the surface of the catalyst during methanation of carbon dioxide, Rösch et al. [238] concluded that sulfur poisoning and thermal sintering above 500 °C are the main deactivation mechanisms for methanation catalysts. For high-temperature methanation in adiabatic reactors, however, catalysts with improved stability regarding thermal sintering up to 700 °C were developed (see Nguyen et al. [199]). In case of dynamic methanation in PtG units, the formation of nickel carbonyls below 200 °C can additionally lead to catalyst deactivation during startup and shutdown (see Rösch et al. [238]).

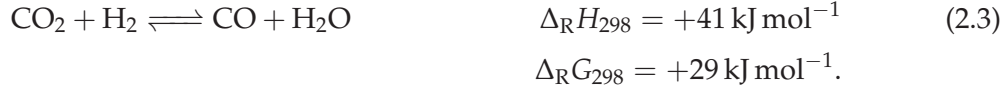
While the choice of nickel as catalyst is rather obvious, the mechanism of the methanation of carbon oxides over nickel catalysts is not fully understood. Till now, two different routes have emerged (see Miao et al. [190] and Rösch et al. [238]). First, a *dissociative* mechanism which assumes that carbon dioxide dissociates at the metal-support interface to adsorbed CO\* that is subsequently reduced to surface carbon, C\*, and finally converted to CH<sub>4</sub> following the steps of carbon monoxide methanation [66, 77, 147, 154, 214, 299, 315]. Second, an *associative* mechanism which proposes that carbon dioxide adsorbs non-dissociatively at the support and is then converted to formate species [6, 207, 250, 303]. CO is thus not an intermediate according to the associative mechanism. Although the available

data suggest that the dissociative mechanism is more likely for methanation of carbon dioxide, the rate-determining step (RDS) has not been clearly identified (see Rönsch et al. [238]). Weatherbee and Bartholomew [299] proposed that the dissociation of adsorbed  $\text{CO}^*$  is the RDS for temperatures below  $300^\circ\text{C}$ , while Klose and Baerns [147] denied that  $\text{CO}^*$  dissociation is the RDS below  $284^\circ\text{C}$ . In contrast, Sehested et al. [261] suggested that  $\text{CO}^*$  dissociation is the RDS between  $270^\circ\text{C}$  and  $400^\circ\text{C}$ . Consequently, detailed mechanisms for the methanation of carbon monoxide and carbon dioxide have not been presented yet.

Nevertheless, several kinetic models for the methanation of carbon oxides based on Langmuir-Hinshelwood-Hougen-Watson rate equations were presented in the past to enable simulations of methanation reactors. Among the available kinetic models, the ones of Koschany et al. [154], Xu and Froment [308], and Zhang et al. [315] are most interesting for reactor simulations as they were obtained under technologically relevant conditions.

### Xu and Froment (1989) kinetic model

The model of Xu and Froment [308] is most frequently applied in simulation studies on methanation. Originally Xu and Froment [308] developed the model for the methane steam reforming process, which is the reverse reaction of the methanation of carbon oxides. Nevertheless, they also conducted experiments for the methanation of carbon dioxide which were taken into consideration for the model discrimination. In addition to the two methanation reactions, Eqns. (2.1) and (2.2), they also considered the reverse water-gas-shift reaction in their model:



The final rate equations for the three reactions are:

$$r_1^{(m)} = \frac{-\frac{k_{m,1}}{p_{\text{H}_2}^{2.5}} \left( p_{\text{CH}_4} p_{\text{H}_2\text{O}} - p_{\text{H}_2}^3 p_{\text{CO}_2} K_{p,1}^{(\text{eq})} \right)}{\left( 1 + K_{\text{CO}} p_{\text{CO}} + K_{\text{H}_2} p_{\text{H}_2} + K_{\text{H}_2\text{O}} \frac{p_{\text{H}_2\text{O}}}{p_{\text{H}_2}} \right)^2}, \quad (2.4a)$$

$$r_2^{(m)} = \frac{-\frac{k_{m,2}}{p_{\text{H}_2}^{3.5}} \left( p_{\text{CH}_4} p_{\text{H}_2\text{O}}^2 - p_{\text{H}_2}^4 p_{\text{CO}_2} K_{p,2}^{(\text{eq})} \right)}{\left( 1 + K_{\text{CO}} p_{\text{CO}} + K_{\text{H}_2} p_{\text{H}_2} + K_{\text{H}_2\text{O}} \frac{p_{\text{H}_2\text{O}}}{p_{\text{H}_2}} \right)^2}, \quad (2.4b)$$

$$r_3^{(m)} = \frac{-\frac{k_{m,3}}{p_{\text{H}_2}} \left( p_{\text{CO}} p_{\text{H}_2\text{O}} - p_{\text{H}_2} p_{\text{CO}_2} K_{p,3}^{(\text{eq})} \right)}{\left( 1 + K_{\text{CO}} p_{\text{CO}} + K_{\text{H}_2} p_{\text{H}_2} + K_{\text{H}_2\text{O}} \frac{p_{\text{H}_2\text{O}}}{p_{\text{H}_2}} \right)^2}. \quad (2.4c)$$

Herein,  $p_i$  are the partial pressures of species  $i$ ,  $k_{m,j}$  are the specific rate coefficients of reaction  $j$  per unit catalyst mass,  $K_i$  are the adsorption constants of species  $i$ , and  $K_{p,j}^{(\text{eq})}$  are the equilibrium constants for reaction  $j$  in the pressure formulation. The latter were calculated using van't Hoff's law in this work (see Appendix F.3, pp. 158 f.). Although Xu and Froment [308] set up the model for steam reforming of methane, the rate equations are here written to provide the reaction rates of the forward equation, i. e., methanation.

The specific rate coefficients  $k_{m,j}$  and the adsorption constants  $K_i$  were calculated using Arrhenius law:

$$k_{m,j} = k_{m,j}^{(\text{inf})} \exp \left\{ -\frac{E_{a,j}}{R_u T} \right\}, \quad (2.5a)$$

$$K_i = K_i^{(\text{inf})} \exp \left\{ -\frac{\Delta H_i}{R_u T} \right\}. \quad (2.5b)$$

The values of the pre-exponential factors  $k_{m,j}^{(\text{inf})}$  and  $K_i^{(\text{inf})}$ , and of the activation energies  $E_{a,j}$  and adsorption enthalpies  $\Delta H_i$ , as well as the type of catalyst and the operating conditions are summarized in Tab. 2.2, p. 16.

### Zhang et al. (2013) kinetic model

In contrast to Xu and Froment [308], Zhang et al. [315] considered only the methanation of carbon monoxide, Eq. (2.1), and the reverse water-gas-shift reaction, Eq. (2.3). Thus, the methanation of carbon dioxide proceeds over carbon monoxide formation via the reverse water-gas-shift reaction, followed by the methanation of carbon monoxide. For the methanation of carbon monoxide, Zhang et al. [315] adopted the model of Klose and Baerns [147] and complemented it with the model of Xu and Froment [308] for the reverse water-gas-shift reaction:

$$r_1^{(m)} = \frac{k_{m,1} K_C K_H^2 p_{H_2} p_{CO}^{0.5} \left( 1 - \frac{p_{CH_4} p_{H_2O}}{p_{CO} p_{H_2}^3 K_{p,1}^{(\text{eq})}} \right)}{\left( 1 + K_C p_{CO}^{0.5} + K_{H_2} p_{H_2}^{0.5} \right)^3} \quad (2.6a)$$

$$r_3^{(m)} = \frac{-\frac{k_{m,3}}{p_{H_2}} \left( p_{CO} p_{H_2O} - p_{H_2} p_{CO_2} K_{p,3}^{(\text{eq})} \right)}{\left( 1 + K_{CO} p_{CO} + K_{H_2} p_{H_2} + K_{H_2O} \frac{p_{H_2O}}{p_{H_2}} \right)^2} \quad (2.6b)$$

Originally, Zhang et al. [315] did not include the reverse reaction in their model. Later, Rönsch et al. [237] reviewed several kinetic models for the methanation process and added the reverse reaction. The final kinetic parameters are listed in Tab. 2.2, p. 16.

### Koschany et al. (2016) kinetic model

The most recent model for the methanation of carbon dioxide was presented by Koschany et al. [154], who followed the approach of Weatherbee and Bartholomew [299], however, investigated the intrinsic kinetics under technologically relevant conditions. Based on the small amounts of carbon monoxide below 350 °C in equilibrium, they disregarded the formation of carbon monoxide in their model. Thus, the methanation of carbon dioxide was considered as only reaction:

$$r_2^{(m)} = \frac{k_{m,2} p_{H_2}^{0.5} p_{CO_2}^{0.5} \left( 1 - \frac{p_{CH_4} p_{H_2O}^2}{p_{CO_2} p_{H_2}^4 K_{p,2}^{(\text{eq})}} \right)}{\left( 1 + K_{OH} \frac{p_{H_2O}}{p_{H_2}^{0.5}} + K_{H_2} p_{H_2}^{0.5} + K_{\text{mix}} p_{CO_2}^{0.5} \right)^2}. \quad (2.7)$$

Again, the operating conditions and the kinetic parameters of the model are summarized in Tab. 2.2, p. 16.

**TAB. 2.2.** Summary of operation conditions and kinetic parameters of technologically relevant rate equations for CO<sub>2</sub>- and CO-methanation over supported Ni-catalysts. All parameters were converted to SI units. Thus the partial pressures have to be in Pa to correctly evaluate the kinetic models.

Study	Parameter	Value	Unit	
Xu and Froment [308] • 15 wt% Ni/MgAl <sub>2</sub> O <sub>4</sub> • 300 °C–400 °C • 3 bar–10 bar • H <sub>2</sub> /CO <sub>2</sub> =0.5–1	$k_{m,1}^{(inf)}$	$4.546 \cdot 10^{17}$	$\text{mol Pa}^{0.5} \text{kg}_{\text{cat}}^{-1} \text{s}^{-1}$	
	$k_{m,2}^{(inf)}$	$1.098 \cdot 10^{17}$	$\text{mol Pa}^{0.5} \text{kg}_{\text{cat}}^{-1} \text{s}^{-1}$	
	$k_{m,3}^{(inf)}$	6.652	$\text{mol Pa}^{-1} \text{kg}_{\text{cat}}^{-1} \text{s}^{-1}$	
	$E_{a,1}$	240.1	$\text{kJ mol}^{-1}$	
	$E_{a,2}$	243.9	$\text{kJ mol}^{-1}$	
	$E_{a,3}$	67.1	$\text{kJ mol}^{-1}$	
	$K_{\text{CO}}^{(inf)}$	$8.23 \cdot 10^{-10}$	$\text{Pa}^{-1}$	
	$K_{\text{H}_2}^{(inf)}$	$6.12 \cdot 10^{-14}$	$\text{Pa}^{-1}$	
	$K_{\text{CH}_4}^{(inf)}$	$6.65 \cdot 10^{-9}$	$\text{Pa}^{-1}$	
	$K_{\text{H}_2\text{O}}^{(inf)}$	$1.77 \cdot 10^5$	-	
	$\Delta H_{\text{CO}}$	-70.65	$\text{kJ mol}^{-1}$	
	$\Delta H_{\text{H}_2}$	-82.90	$\text{kJ mol}^{-1}$	
	$\Delta H_{\text{CH}_4}$	-38.28	$\text{kJ mol}^{-1}$	
	$\Delta H_{\text{H}_2\text{O}}$	88.68	$\text{kJ mol}^{-1}$	
	Zhang et al. [315] • 50 wt% Ni/Al <sub>2</sub> O <sub>3</sub> • 250 °C–360 °C • 1 bar–5 bar • H <sub>2</sub> /CO=1.95–3	$k_{m,1}^{(inf)}$	$1.944 \cdot 10^{10}$	$\text{mol kg}_{\text{cat}}^{-1} \text{s}^{-1}$
		$k_{m,3}^{(inf)}$	$2.175 \cdot 10^1$	$\text{mol Pa}^{-1} \text{kg}_{\text{cat}}^{-1} \text{s}^{-1}$
$E_{a,1}$		103	$\text{kJ mol}^{-1}$	
$E_{a,3}$		62	$\text{kJ mol}^{-1}$	
$K_{\text{C}}^{(inf)}$		$1.834 \cdot 10^{-4}$	$\text{Pa}^{-0.5}$	
$K_{\text{H}}^{(inf)}$		$5.060 \cdot 10^{-5}$	$\text{Pa}^{-0.5}$	
$K_{\text{CO}}^{(inf)}$		$8.23 \cdot 10^{-10}$	$\text{Pa}^{-1}$	
$K_{\text{H}_2}^{(inf)}$		$6.12 \cdot 10^{-14}$	$\text{Pa}^{-1}$	
$K_{\text{CH}_4}^{(inf)}$		$6.65 \cdot 10^{-9}$	$\text{Pa}^{-1}$	
$K_{\text{H}_2\text{O}}^{(inf)}$		$1.77 \cdot 10^5$	-	
$\Delta H_{\text{C}}$		-42.00	$\text{kJ mol}^{-1}$	
$\Delta H_{\text{H}}$		-16.00	$\text{kJ mol}^{-1}$	
$\Delta H_{\text{CO}}$		-70.65	$\text{kJ mol}^{-1}$	
$\Delta H_{\text{H}_2}$		-82.90	$\text{kJ mol}^{-1}$	
$\Delta H_{\text{CH}_4}$		-38.28	$\text{kJ mol}^{-1}$	
$\Delta H_{\text{H}_2\text{O}}$		88.68	$\text{kJ mol}^{-1}$	
Koschany et al. [154] • 19 wt% Ni/Al <sub>2</sub> O <sub>3</sub> • 180 °C–340 °C • 1 bar–15 bar • H <sub>2</sub> /CO <sub>2</sub> =0.25–8	$k_{m,2}^{(inf)}$	$6.813 \cdot 10^1$	$\text{mol Pa}^{-1} \text{kg}^{-1} \text{s}^{-1}$	
	$E_{a,2}$	77.5	$\text{kJ mol}^{-1}$	
	$K_{\text{OH}}^{(inf)}$	$2.092 \cdot 10^{-1}$	$\text{Pa}^{-0.5}$	
	$K_{\text{H}_2}^{(inf)}$	$3.63 \cdot 10^{-4}$	$\text{Pa}^{-0.5}$	
	$K_{\text{mix}}^{(inf)}$	$3.188 \cdot 10^{-4}$	$\text{Pa}^{-0.5}$	
	$\Delta H_{\text{OH}}$	22.4	$\text{kJ mol}^{-1}$	
	$\Delta H_{\text{H}_2}$	-6.2	$\text{kJ mol}^{-1}$	
	$\Delta H_{\text{mix}}$	-10.0	$\text{kJ mol}^{-1}$	

Based on a comparison of the several kinetic models for the methanation of carbon dioxide, Rönsch et al. [237] concluded that the original kinetic model of Xu and Froment [308] is not suitable for methanation simulations as it underpredicts the activity of state-of-the-art methanation catalysts. Instead, they suggest to use the model of Zhang et al. [315] because it is able to predict the reaction rates of commercial catalysts and includes the formation of carbon monoxide via the reverse water-gas-shift reaction. The model of Koschany et al. [154], will certainly be used in future simulation studies because of its clear derivation and its solid experimental foundation. A comparison between the different kinetic models is presented in Section 3.3.2, pp. 67 ff.

## 2.2.4 Reactor concepts

The methanation technology developed in the 1970ties was recently reviewed and discussed in detail by Götz et al. [92], Kopyscinski et al. [152], and Rönsch et al. [238]. Accordingly, the still commercially available methanation units (Air Liquide, formerly Lurgi; British Gas, now Johnson Matthey, 1973; Haldor Topsoe, 1978) consist of two to four adiabatic fixed-bed reactors with interstage cooling and product recycle to solve the dilemma between kinetic limitations at low temperatures and thermodynamic limitations at high temperatures. The reactors were originally designed for methanation of carbon monoxide, but can be adjusted for the methanation of carbon dioxide.

With the revival of carbon dioxide methanation for PtG units, new reactor concepts were developed and brought to pilot scale in the last years. Bailera et al. [12] recently presented a comprehensive review of existing and planned pilot and production plants for the methanation of carbon oxides. The so far largest operational plant is the Audi e-gas plant in Werlte, Germany. It allows an electricity input of 6 MW and produces at most  $325 \text{ Nm}^3 \text{ h}^{-1}$  SNG with an efficiency of 54 % (see Osman et al. [204] and Rieke [236]). The methanation of the undiluted hydrogen and carbon dioxide feed takes place in a cooled multi-tubular fixed-bed reactor. Because of temperatures up to  $500 \text{ }^\circ\text{C}$ , a molten salt bath is used as cooling medium. The reactor itself was developed by Outotec and MAN.

In addition to the development of demonstration plants, researchers investigated different reactor types to improve the methanation process. Ohya et al. [203] and Schlereth and Hinrichsen [255] suggested a membrane reactor to either remove water vapor from the reactor to remove thermodynamic limitations, or to distribute the carbon dioxide feed along the reactor axis to control the local heat release. Belimov et al. [15] and Görke et al. [90] developed microreactors that allow to effectively remove the reaction heat because of the high surface-to-volume ratio of the mm-size channels. Fukuhara et al. [79], Schlereth et al. [254], and Sudiro et al. [272] investigated the use of structured, honeycomb-type catalyst supports to improve heat transport within cooled fixed-bed reactors. The potential of the structured catalyst supports at a production scale, however, was not investigated.

In their theoretical study, Kiewidt and Thöming [144] used the Semenov number

$$Se = \underbrace{\frac{D_t^2}{24\lambda_{\text{rad}}^{\text{(eff)}}}}_{\text{thermal design}} \underbrace{\frac{\eta\rho_{\text{cat}}^{(\text{bulk})}r^{(\text{m})}(-\Delta_{\text{R}}H)}{T_{\text{in}}}}_{\text{operation and process conditions}} \frac{E_a}{R_u T_{\text{in}}} = \frac{\text{heat production rate}}{\text{cooling rate}} \quad (2.8)$$

to predict and analyze optimal temperature profiles in polytropic single-stage fixed-bed reactors for CO<sub>2</sub>-methanation. They demonstrated that the optimal Semenov number, and thus the optimal temperature profile, can be obtained by tuning the heat transport in the catalytic bed. In comparison to isothermal ( $Se \rightarrow 0$ ) and adiabatic reactors ( $Se \rightarrow \infty$ ), the optimal temperature profile in polytropic reactors ( $0 \leq Se < \infty$ ) ideally balances kinetic and thermodynamic limitations and hence leads to up to a twofold increase of the achievable methane yield for single passes.

Götz et al. [91] investigated the application of a three-phase reactor that allows isothermal operation because of the high thermal conductivity of the used liquids. The nickel catalyst is dispersed within the liquid in form of small particles, and hydrogen and carbon dioxide are dispersed in form of small bubbles. Because of the low solubility of the gases in the liquid, however, three-phase methanation reactors exhibit a much lower space-time yield than two-phase fixed-bed reactors, which limits their potential for decentralized small to medium scale PtG units. Furthermore, biological methanation at temperatures between 40 °C and 70 °C was reviewed by Götz et al. [92]. Although biological methanation tolerates a higher level of impurities in the feed, it is limited by low reaction rates and thus requires large reactors. In addition, it is mostly operated in continuously-stirred tank reactors (CSTR) which do not allow high methane contents because of backmixing.

## 2.2.5 Current and future challenges

Although first PtG demonstration plants have been launched in recent years, there are still major challenges to overcome. The existing reactor concepts need to be adjusted to small- to medium-scale production. This implies the removal of reactor stages and the reduction of product gas recycles (see Rönsch et al. [238]). Neubert et al. [197] stated that successful decentralized PtG demands the solution of the trilemma between high conversion rates (high temperatures), high methane contents (low temperatures), and a low complexity of the process.

Probably one of the most difficult challenges for PtG is the dynamic operation of catalytic reactors to adjust the storage process to the fluctuating nature of renewable energies. With first studies appearing now (see for example [74, 103, 123, 167, 181, 183]), dynamic operation of fixed-bed reactors requires more research to understand and control the mechanisms at the involved time scales.

Along the improvements of process technology, advances on the more fundamental aspects of methanation are required. In particular, the mechanistic processes of methanation at the catalyst surface need to be clarified in order to understand the conversion under steady and transient conditions. In addition, more research on the deactivation of methanation catalysts, in particular regarding thermal sintering and poisoning because of impurities in the feed, is required.

## 2.3 Solid sponges

### 2.3.1 General introduction

Today, solid ceramic sponges, sometimes called open-cell foams, are mass-produced for foundry applications and are commercially available on the market in different geometries, materials ( $\text{Al}_2\text{O}_3$ ,  $\text{SiO}_2$ ,  $\text{ZrO}_2$ ,  $\text{TiO}_2$ , and  $\text{SiC}$ ), porosities, and pore densities [3, 4, 234, 271]. Because of their thermal and chemical stability, ceramic sponges are widely used as flow regularisers and filters in metal casting to remove impurities from the melt. The main production procedure is the so-called Schwarzwaldler [260] process, a replica procedure in which a polyurethane (PU) template is coated with a ceramic suspension. Afterwards, the coated PU template is dried and sintered at high temperatures to form a solid ceramic sample. During the sintering process, the PU evaporates and thus creates pores within the struts of the ceramic sponge. A detailed review about the manufacturing of solid sponges and the replica procedure, as well as about other manufacturing routes such as direct foaming, is for example given by Studart et al. [271].

In the last 10–20 years, chemical engineers were attracted by the sponges' high porosities, large specific surface areas, and promising heat and mass transport properties. Consequently, they investigated them regarding their potential for process intensification as porous burners for flame stabilisation [35, 52–54], heat exchangers [26], particle filters in exhaust gas treatment [318, 319], transparent supports in photoreactors for biomass production [31, 32, 132], and in particular as supports for heterogeneous catalysts [36, 55, 61, 63, 72, 73, 95, 96, 162, 164, 169, 170, 174, 176, 192–194, 200, 206, 209, 212, 213, 215, 223, 233–235, 239, 246, 252, 301] (see Sect. 2.3.9, pp. 48 ff., for a detailed review of catalytic applications). Especially in the field of catalysis, metallic sponges made of aluminum, FeCrAlloy®, and copper [5, 19, 20, 85, 86, 278] were investigated alongside ceramic sponges to increase the thermal conductivity of catalyst supports.

In the following sections, the morphology, characterization, pressure loss, heat and mass transport, interfacial heat and mass transfer, and applications of sponges as catalyst supports are thoroughly reviewed and discussed regarding their potential for process intensification in the field of catalysis.

### 2.3.2 Morphology and geometrical characterization

Solid sponges are an irregular, continuous network of solid struts that surround three-dimensional cells (see dashed circle in Fig. 2.4 a). The cells are connected by windows that allow fluid flow and lateral mixing in all spatial directions. If the replica method is used for production, the struts are usually hollow because of the evaporation of the PU template (see Fig. 2.4 b). Depending on the amount of solid used during production, the struts exhibit a circular, triangular, or concave-triangular cross section (see for example Inayat et al. [125]).

On the market, solid sponges are usually characterized by their pore density measured in number of pores per linear inch (ppi), which typically ranges from 10 ppi–100 ppi, and their nominal porosity  $\varepsilon_n$ , typically between 0.7–0.95. The pore density, however, does not distinguish between cells and windows and thus does not allow to calculate the actual size of the cells or windows. In addition, the provided pore density usually refers to the

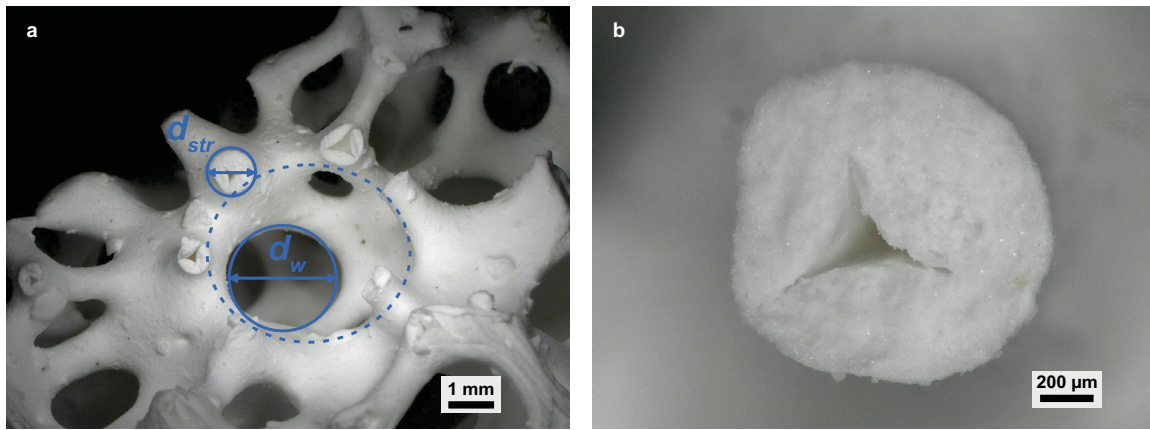


**FIG. 2.4.** Microscopic image of a 20 ppi mullite sponge indicating the area-equivalent window and strut diameters  $d_w$  and  $d_s$ , and a single cell (dashed circle) (a), and example of a hollow strut with circular cross section (b).

PU template, and coating and shrinkage during sintering affect the size of the windows. Therefore, the average window diameter  $d_w$  and the average strut diameter  $d_s$  (both area-equivalent circle) are used in chemical engineering for a more accurate characterization of solid sponges. Likewise, the nominal porosity is only an approximation of the actual porosity of solid sponges. Instead, the open porosity  $\varepsilon_o$ , that does solely take into account the voids that are available for fluid flow, and the total porosity  $\varepsilon_t$ , that includes the voids within the hollow struts, are used. Because of its effect on the flow through solid sponges, the open porosity is often called hydrodynamic porosity  $\varepsilon_h$ .

Typical values of the average window diameter and open porosity range from approximately 0.2 mm–3 mm and 0.7–0.98, respectively (see Fig. 2.5). While ceramic sponges typically exhibit open porosities between 0.7 and 0.9 (see Fig. 2.5 a), metal sponges exhibit open porosities above 0.9 (see Fig. 2.5 b). For open porosities below 0.8, a lower bound for the window diameter is observable (see dashed line in Fig. 2.5 a). Other than that, no correlation between the window diameter and the open porosity is deducible.

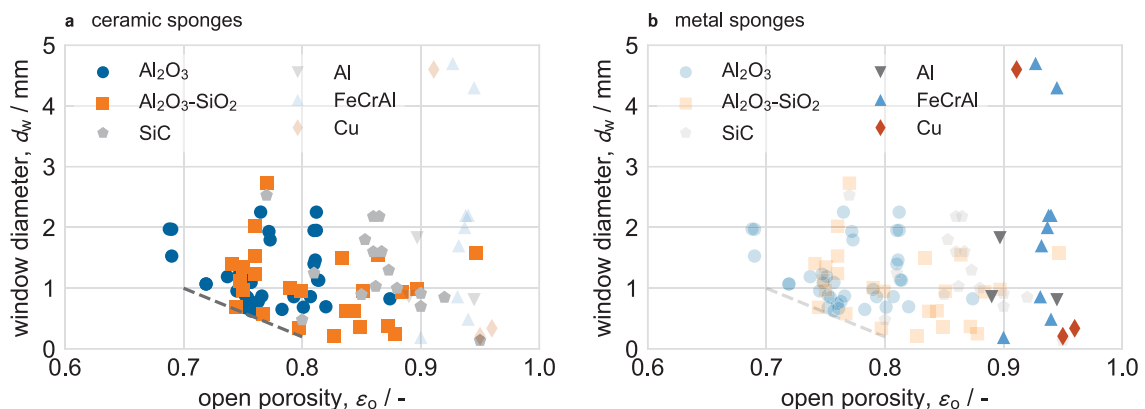


**FIG. 2.5.** Summary of reported open porosities and corresponding average window diameters of ceramic sponges (a) and metal sponges (b). In total, 92 data points are included (see Tab. G.1 in Appendix G, pp. 161 ff.). The dashed line indicates an apparent lower bound of the window diameter for open porosities below 0.8.

### Measurement of the window and strut diameter

The distribution of the window and strut diameter can be determined from microscopic images [33, 51, 98, 99, 125] (see Fig. 2.4). Nevertheless, a large number of measurements has to be conducted to accurately deduce the average diameter and its standard deviation because the window and strut diameter vary significantly within a single sample. This is particularly true for the struts as their diameter is usually larger close to a node where several struts meet than in the middle of the strut (see Fig. 4 b in [125]). Furthermore, only windows and struts that are located in the outer regions of the sponge are accessible with incident light microscopy, unless the sample is cut in several slices and thus destroyed. In addition, windows and struts that are not parallel to the observation plane lead to a systematic underestimation of both quantities. Thus, care has to be taken when selecting the windows and struts during the measurement.

### Measurement of the total and open porosity

The total and open porosity can be determined with a combination of gravimetric analysis, mercury intrusion, and helium pycnometry [125, 129] by using the following equations:

$$\varepsilon_t = 1 - \frac{\rho_{\text{bulk}}}{\rho_{\text{app}}} \quad (2.9a)$$

$$\varepsilon_o = 1 - \frac{\rho_{\text{bulk}}}{\rho_{\text{env}}}. \quad (2.9b)$$

The bulk, solid, and skeletal densities are:

$$\rho_{\text{bulk}} = \frac{m_{\text{sample}}}{V_{\text{bulk}}}, \quad (2.10a)$$

$$\rho_{\text{app}} = \frac{m_{\text{sample}}}{V_{\text{app}}}, \quad (2.10b)$$

$$\rho_{\text{env}} = \frac{m_{\text{sample}}}{V_{\text{app}} + V_{\text{strut-cavities}}}, \quad (2.10c)$$

where  $m_{\text{sample}}$  is the mass of the sponge,  $V_{\text{bulk}}$  is the volume of the (cylindrical) sample,  $V_{\text{app}}$  is the solid volume obtained from helium pycnometry, and  $V_{\text{strut-cavities}}$  is the gas volume inside the hollow struts obtained from mercury intrusion. Figure 2.6 shows an illustration of the definitions of the different densities of solid sponges. The mass and volume of the sample can easily be measured using a standard lab scale and standard calliper.

### Volume imaging techniques

An alternative to the above mentioned conventional approaches to determine the porosities and window diameters of solid sponges, are volume imaging techniques such as X-ray absorption micro computer tomography ( $\mu$ CT) and Magnetic Resonance Imaging (MRI), which have been used increasingly in the last years to characterize solid sponges [46, 51, 99, 125, 129, 180]. By combining several hundreds of 2-d slices (reconstruction),  $\mu$ CT and MRI allow the creation of a 3-d computer model of a sponge from which the open and closed porosity, the distributions of the window and strut diameter, and particularly the specific surface area can be calculated. Thus, volume imaging methods not only provide a full characterization with a single measurement, but also allow to take into account windows

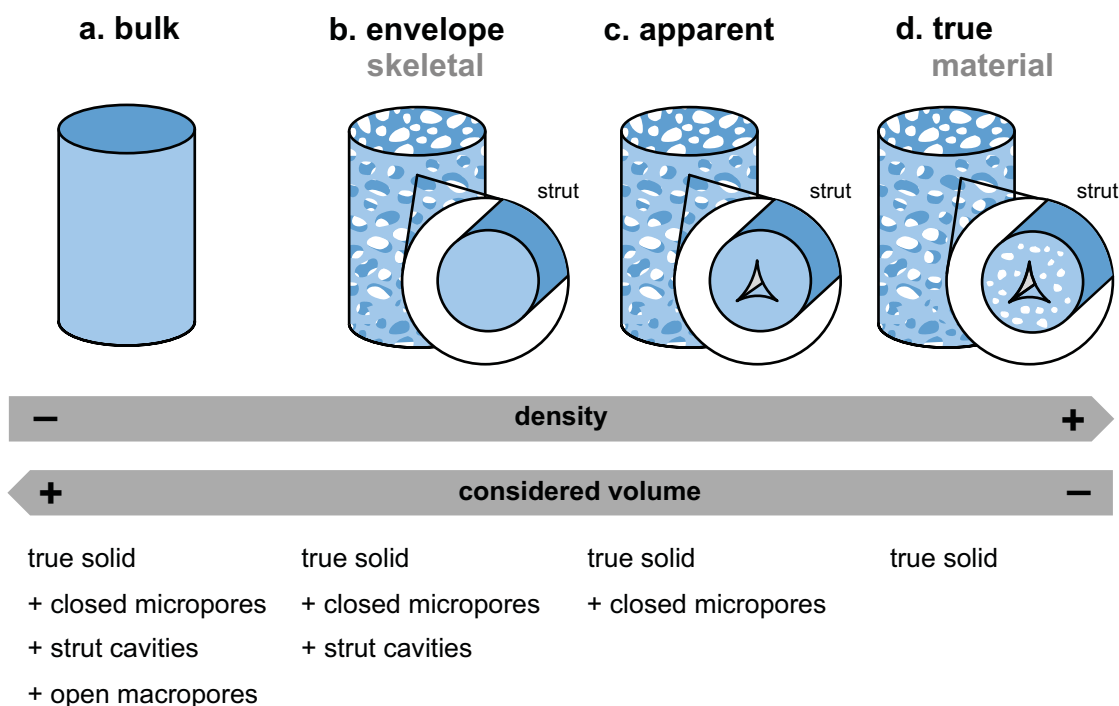


**FIG. 2.6.** Illustration of the definition of the bulk, the envelope or skeletal, the apparent, and the true or material density of solid sponges used in this work. While the solid mass is equal for all stages, the considered volume changes in each stage. The same approach can be adopted for packed beds of pellets, or for mesoporous catalyst coats. For conventional catalyst coats, however, the envelope density and the bulk density are equal because of the absence of a superimposed macroporous structure.

and struts in the inner regions of the sponge that are not accessible with light microscopy. In addition, volume imaging techniques enable the measurement of the specific surface area of sponges. Nitrogen adsorption, which is typically applied to measure specific surface areas, is not usable for solid sponges as it will overdetermine the specific surface area because of surface roughness and the consideration of the inner surface of the struts that is usually not of interest for chemical engineering applications.

In comparison, the spatial resolution of both,  $\mu$ CT and MRI, ranges from 10  $\mu\text{m}$ –100  $\mu\text{m}$  (isotropic voxel size) depending on the setup and the measurement procedure, and is thus sufficient for most solid sponges in chemical engineering. For MRI, however, the sponges have to be completely filled with a MRI-active liquid to obtain high spatial resolutions because the ceramic material itself is not visible in MRI [99]. During this step, gas bubbles might be trapped inside the cells of the sponge and thus corrupt the measurements. Therefore, if possible,  $\mu$ CT is preferable over MRI regarding the geometric characterization of ceramic sponges.

A detailed comparison of the values obtained from MRI, light microscopy, and gravimetric analysis, including recommendations regarding the evaluation of volume imaging data, was given by Große et al. [99]. They demonstrated that the average window diameter and the open porosity obtained with volume imaging techniques match well with the data obtained from conventional methods. Despite their advantages, volume imaging methods

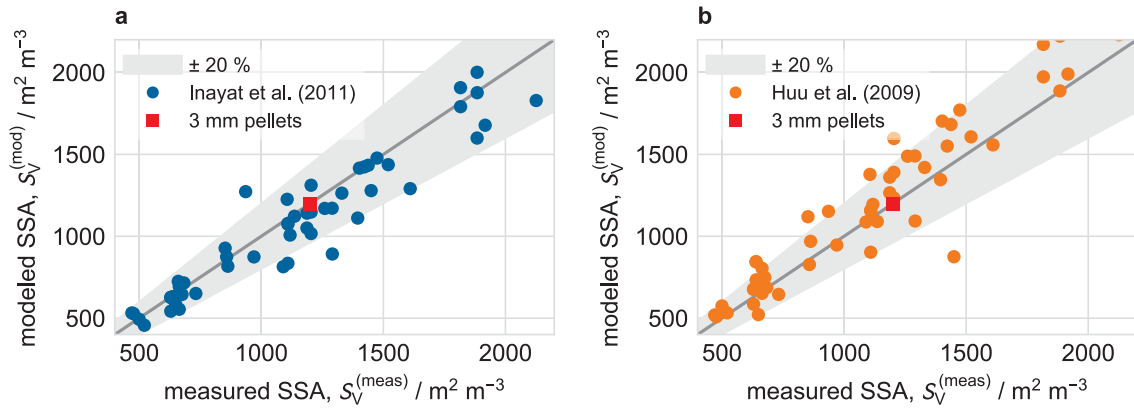


**FIG. 2.7.** Comparison of measured and calculated specific surface areas using the model of Inayat et al. [125] (a), and the one of Huu et al. [119] (b). The data points were extracted from studies that explicitly report the average window diameter, the open porosity, and the specific surface area [19, 51, 98, 99, 129, 192, 296] (see Tab. G.1 in Appendix G, pp. 161 ff.).

require expensive hardware, considerable computing power and memory to handle large data sets (several GB per individual sample), and expert knowledge to evaluate the data.

### Unit cell models

Alongside experimental methods, researchers developed models based on cubic [65, 163], tetrakaidecahedral [33, 125], Weaire–Phelan [98, 222], and pentagonal dodecahedron [119] unit cells to calculate the strut diameter and the specific surface area from known porosities and window diameters. Inayat et al. [125] built on the tetrakaidecahedral unit cell model and explicitly considered the strut cross section in their model. They demonstrated that the adjusted model provides a more accurate estimation of the specific surface area in comparison to experimental data than the models of Buciuman and Kraushaar-Czarnetzki [33], Grosse et al. [98], and Huu et al. [119]. In contrast to Grosse et al. [98], they additionally removed the necessity of an empirical constant.

Figure 2.7 shows a comparison of calculated specific surface areas using the models of Inayat et al. [125] (Fig. 2.7 a) and Huu et al. [112] (Fig. 2.7 b), and experimental data of more than 50 individual samples taken from studies that explicitly report measured values of the average window diameter, the open porosity, and the specific surface area [19, 51, 98, 99, 129, 192, 296] (see Tab. G.1 in Appendix G, pp. 161 ff.). The tetrakaidecahedral model of Inayat et al. [125] calculates the specific surface area accurately within 20% for 90% of the samples, while the pentagonal dodecahedron model (fat cylindrical struts) of Huu et al. [119] achieves the same accuracy only for 80% of the samples. Moreover, Huu’s model requires the solution of a nonlinear implicit equation.

Using the model of Inayat et al. [125], the strut diameter can be calculated by

$$d_s = \frac{C_s d_w \sqrt{(1 - \varepsilon_0)}}{1 - 0.971 \sqrt{(1 - \varepsilon_0)}}, \quad (2.11)$$

and the specific surface area by

$$S_V = \frac{C_s C_S}{d_s} (1 - \varepsilon_o). \quad (2.12)$$

The constants  $C_S$  and  $C_s$  are *analytically* derived from the tetradecehedral unit cell model and geometric considerations. They depend on the strut cross section:

$$C_s = \begin{cases} 0.6164 & \text{for circular struts} \\ 0.5338 & \text{for triangular struts} \\ 0.5338 & \text{for concave-triangular struts} \end{cases} \quad (2.13)$$

and

$$C_S = \begin{cases} 4.867 & \text{for circular struts} \\ 5.620 & \text{for triangular struts} \\ 6.490 & \text{for concave-triangular struts.} \end{cases} \quad (2.14)$$

From the numerical values one can deduce that sponges with triangular and concave-triangular struts exhibit slightly thinner struts and larger specific surfaces areas.

Using a cubic unit cell, the product  $C_S C_s$  would be exactly 4 [65, 163]. Thus, the cubic unit cell model significantly underpredicts the specific surface area of solid sponges. The equation for the specific surface area, Eq. 2.12, is also analogous to the expression for the specific surface area of a packed bed of spherical pellets. For pellets the product  $C_S C_s$  is exactly 6, and the characteristic diameter is the pellet diameter  $D_p$ . For a typical application in heterogeneous catalysis, the pellet diameter is approximately three times larger than the strut diameter ( $D_p = 3 \text{ mm}$ ,  $d_s = 1 \text{ mm}$ ), while the porosity of the packed bed is two times lower than the open porosity of the sponge ( $\varepsilon_{\text{bed}} = 0.4$ ,  $\varepsilon_o = 0.8$ ). Thus, in typical applications, sponges exhibit comparable specific surface areas at much higher porosities as conventional packed beds of pellets (see also Fig. 2.7).

### 2.3.3 Pressure loss along solid sponges

The pressure loss along solid sponges has been investigated intensively in the scientific literature. First studies were already conducted in the early 1990s for example by Schlegel et al. [253]. 15 years later, in 2008, Edouard et al. [57] reviewed several at that time state-of-the-art empirical correlations based on the Darcy-Forchheimer equation,

$$\frac{dp}{dz} = -\frac{\mu_f}{K} v_{\text{sup}} - \frac{\rho_f}{c_F} v_{\text{sup}}^2. \quad (2.15)$$

The permeability  $K$  and the Forchheimer-coefficient  $c_F$  were obtained by integrating Eq. (2.15) and fitting the resulting pressure loss to experimental data. Edouard et al. [57] found that most existing models for the pressure loss along solid sponges show deviations up to 100 % compared to experimental data. As a conclusion, they proposed to use the model of Lacroix et al. [163] who used Eq. (2.15) and the well-known expressions for the permeability and the Forchheimer coefficient from the Ergun equation [62],

$$K = \frac{\varepsilon_o^3 D_p^2}{150 (1 - \varepsilon_o)^2}, \quad (2.16a)$$

$$c_F = \frac{\varepsilon_o^3 D_p}{1.75 (1 - \varepsilon_o)}, \quad (2.16b)$$

together with an effective pellet diameter (equivalent specific surface area) obtained from the cubic unit cell model,

$$D_p = D_p^{(\text{eff})} = \frac{3}{2} d_s. \quad (2.17)$$

Although the cubic unit cell is only a simplification of the real cell morphology encountered in solid sponges, the deviations between predictions and experimental data regarding the pressure loss were at most 30 %.

Later, Dietrich et al. [51] started from the definition of the well-known friction factor and derived the following expressions for the permeability and the Forchheimer coefficient of solid sponges:

$$K = \frac{\varepsilon_o d_h}{A}, \quad (2.18a)$$

$$c_F = \frac{\varepsilon_o^2 d_h}{B}, \quad (2.18b)$$

with

$$d_h = \frac{4\varepsilon_o}{S_V} \quad (2.19)$$

being the hydraulic diameter. The empirical constants  $A = 110$  and  $B = 1.45$  were determined by integration of Eq. (2.15) and subsequent fitting of the pressure loss to experimental data for a wide range of open porosities (0.75–0.85), window diameters (0.63 mm–2.3 mm), materials ( $\text{Al}_2\text{O}_3\text{-SiO}_2$ ,  $\text{Al}_2\text{O}_3$ , OBSiC), and velocities ( $\leq 9 \text{ m s}^{-1}$ ). The deviations between predictions and experimental data were at most 20 %.

Recently, Inayat et al. [126] derived a universal model for the pressure loss along solid sponges that does not rely on empirical parameters. In addition, it takes into consideration the cross section of the struts using the tetracaidecahedral unit cell model of the same authors [125]. The corresponding equations for the permeability, the Forchheimer coefficient, and the sponge tortuosity  $\tau_{\text{spg}}$ , which accounts for the tortuous flow pattern in the sponges, are:

$$K = \frac{\varepsilon_o d_h^2}{32 \tau_{\text{spg}}^2}, \quad (2.20a)$$

$$c_F = \frac{\varepsilon_o^2 d_h}{2 \tau_{\text{spg}}^3}, \quad (2.20b)$$

$$\tau_{\text{spg}} = 1 + \frac{S_V d_w}{4\varepsilon_o} = 1 + \frac{d_w}{d_h}. \quad (2.20c)$$

The authors tested their equation against published experimental data for the pressure loss along solid sponges and reported deviations below 10 % for a wide range of geometric

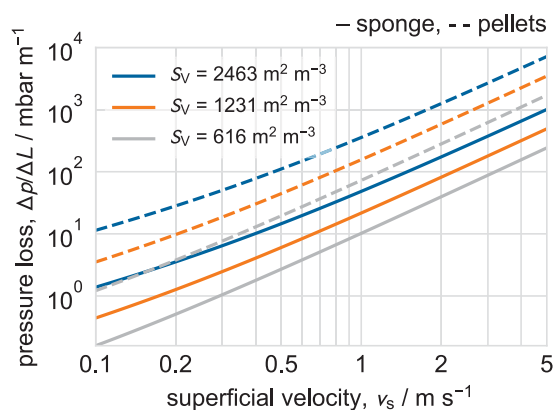


**FIG. 2.8.** Comparison of the pressure loss along solid sponges and packed beds of pellets for equivalent specific surface areas calculated with the models of Inayat et al. [126] and Ergun [62]. The (open) porosities of the sponge and pellet bed are 0.8 and 0.4, respectively. The window diameters of the sponges are 0.5 mm, 1 mm and 2 mm; the corresponding pellet diameters (equivalent specific surface area) are 1.5 mm, 2.9 mm and 5.8 mm.

sponge parameters. Independently, Woudberg and Du Plessis [307] also derived an analytical model for the pressure loss along solid sponges based on a representative unit cell. Their model, however, was only able to calculate the permeability and the Forchheimer coefficient within 15%–25% accuracy. Thus, the model of Inayat et al. [126] currently provides the most accurate prediction of the pressure loss along solid sponges.

In comparison to packed beds of pellets, the pressure loss along solid sponges is approximately eight times lower for equivalent specific surface areas over a wide range of superficial fluid velocities because of the much higher porosities (see Fig. 2.8 and [51]). Hence, solid sponges could possibly intensify processes that are operated at low feed pressures or high throughputs. If solely pressure loss is crucial, however, honeycombs provide a better option because they offer even lower pressure losses than solid sponges because of their regular morphology. In addition, usually a compromise between low pressure loss and high bulk catalyst density has to be made in catalytic applications.

### 2.3.4 Heat transport in solid sponges

Promising heat transport is one of the key drivers for research on solid sponges as catalyst support. Especially in monolithic applications in which the sponge diameter is equal to the reactor tube diameter, the continuous solid network of sponges allows high heat fluxes via thermal conduction, in particular for well conducting materials such as silicon carbide (SiC), aluminum (Al), and copper (Cu).

Heat transport in solid sponges, and in porous media in general, can be modeled using either (pseudo)-heterogeneous [46, 85] or pseudo-homogeneous approaches [19, 70, 296] (see Fig. 2.9). The (pseudo)-heterogeneous approaches distinguish between the solid and fluid phase regarding temperature and thermal conductivity, and thus require individual energy balance equations for the fluid and the solid phase. The balance equations are coupled by the transfer of thermal energy at the surface of the solid phase, characterized by heat transfer coefficient  $\alpha$  that depends on fluid velocity and the geometrical properties of

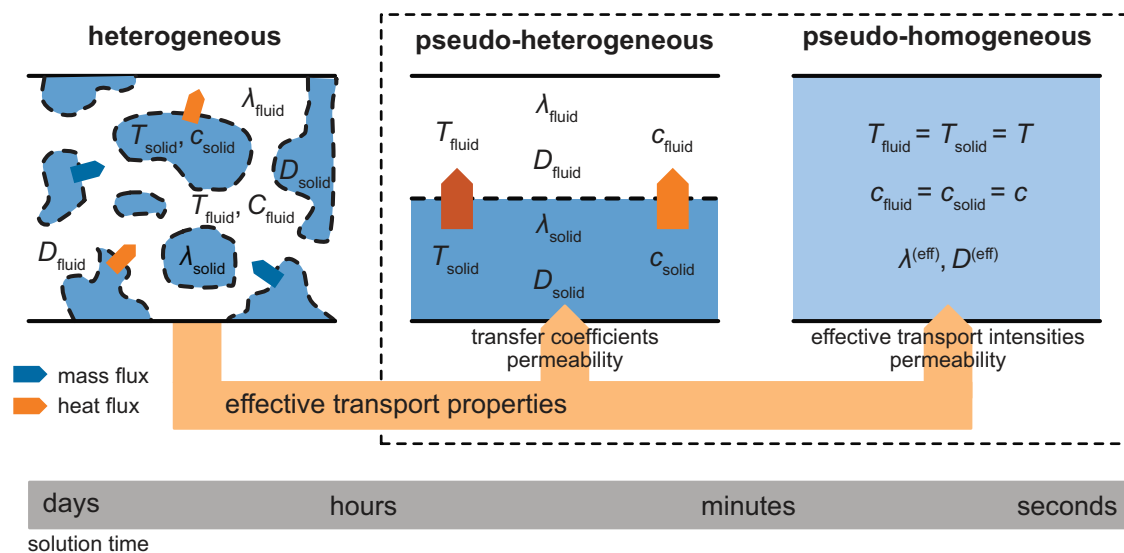


**FIG. 2.9.** Illustration of the main approaches to model heat and mass transport in porous media. Heterogeneous and pseudo-heterogeneous models treat the fluid and solid phase separately while pseudo-homogeneous models combine both phases into a single effective phase with effective transport intensities. Thus, interfacial temperature and concentration gradients are not considered in the pseudo-homogeneous model. The necessary effective transport properties (pseudo-homogeneous models) and transfer coefficients (pseudo-heterogeneous models) are either deduced from simulations with heterogeneous models, or from experiments.

the sponge. In contrast to the pseudo-heterogeneous approach, the fully heterogeneous approach also considers the local morphology of the solid phase. Usually the detailed velocity field in the fluid phase is also taken into account. Consequently, heat transport in the fluid and the solid phase, and heat transfer between the fluid and solid phase are simulated using fundamental principles. Hence, no effective thermal conductivities and heat transfer coefficients are required. Instead, fully heterogeneous models can be used to deduce models for the effective thermal conductivity and the heat transfer coefficient.

In contrast, the pseudo-homogeneous approach combines the solid and fluid phase into a single homogeneous phase with a single (average) temperature and an *effective thermal conductivity* (ETC). Thus, only a single energy balance has to be considered. Because of the combination of two phases, however, homogeneous models are not valid universally but only for the considered morphologies and combinations of solids and fluids.

In pseudo-homogeneous models, the dependency of the effective thermal conductivity on the solid and fluid thermal conductivities, the geometrical properties of the sponge, and possible fluid flow is usually obtained by fitting calculated spatial temperature profiles to measured ones. Some researchers [20, 296] also consider a wall heat transfer coefficient  $\alpha_w$  as second fitting parameter. This approach, however, is questionable for solid sponges because it was originally developed for randomly packed beds in which the open porosity close to the wall increases to approximately 0.94, and thus heat transfer from the fluid to the reactor wall is dominated by convection. For solid sponges, however, the open porosity remains constant over the whole cross section, and thus the wall heat transfer coefficient strongly depends on the contact between the sponge and the reactor wall [296]. In

addition, Mülheims et al. [193] demonstrated that an almost ideal thermal contact ( $\alpha_w \rightarrow \infty$ ) between the sponge and the reactor wall can be achieved by wrapping the sponges with a carbon foil with high thermal conductivity. Moreover, Razza et al. [231] showed with detailed Computational Fluid Dynamic (CFD) simulation of conjugate heat transport in solid sponges, that an ideal thermal contact between the sponge and the reactor wall can be assumed if approximately 20 % of the sponge struts are in contact with the wall. Therefore, it is not necessary to apply the wall heat transfer coefficient  $\alpha_w$  in the case of solid sponges if a good thermal contact between the sponges and the wall are guaranteed.

In pseudo-heterogeneous models the main fitting parameter is the heat transfer coefficient. Although the pseudo-heterogeneous approach resembles the physics of heat transport in solid sponges more accurately, pseudo-homogeneous approaches are mostly used to model heat transport because they require less mathematical and computational efforts (see solution time scale in Fig. 2.9). In addition, pseudo-heterogeneous approaches require the measurement of the solid temperature distribution which is experimentally difficult for solid sponges. As a workaround for solid materials with high thermal conductivities, the solid temperature is assumed uniform and then included as a fitting parameter together with the heat transfer coefficient (see for example Giani et al. [85]).

Prior to a discussion of available models for heat transport in solid sponges, a review of the solid thermal conductivity, sometimes called material thermal conductivity, and its measurement is presented. Heat transfer between the fluid and the solid phase using pseudo-heterogeneous models is discussed in Sect. 2.3.6, pp. 41 ff.

### Determining the material thermal conductivity of solid sponges

The material or solid thermal conductivity  $\lambda_s$  and the specific heat capacity  $c_{p,s}$  play an important role for heat transport in catalytic sponges. Although tabulated values for both quantities are available for various ceramics (see for example [242]) and metals, the manufacturing process and the resulting microstructure of solid sponges strongly influence the material properties. Thus, the solid thermal conductivity and the specific heat capacity have to be determined experimentally.

Dietrich et al. [49] were the first to measure the material thermal conductivity of solid sponges. They crushed ceramic sponges, sieved and milled the resulting powder, and pressed it into small discs ( $\varnothing 10 \text{ mm} \times 2 \text{ mm}$ ) with pressures up to 400 MPa. Afterwards, they sintered the discs to match their porosity and grain size distribution to the one of the original struts of the investigated sponges. Finally, the material thermal diffusivity  $a_s = \lambda_s / (\rho_s c_{p,s})$  of the discs was measured using the established laser-flash technique [130, 210]. The experiments were later successfully repeated by Wallenstein et al. [296]. Recently, Fishedick et al. [69] built on Dietrich's approach and particularly extended the measurements to temperatures up to 1000 °C (see Fig. 2.10).

While the thermal conductivity of mullite ( $\text{Al}_2\text{O}_3\text{-SiO}_2$ ) and oxygen-bonded silicon carbide (OBSiC) remains almost constant around  $3 \text{ W m}^{-1} \text{ K}^{-1}$  and  $7 \text{ W m}^{-1} \text{ K}^{-1}$  between 100 °C–1000 °C, the thermal conductivity of pure alumina ( $\text{Al}_2\text{O}_3$ ) decreases exponentially from  $23 \text{ W m}^{-1} \text{ K}^{-1}$  at 100 °C to about  $5 \text{ W m}^{-1} \text{ K}^{-1}$  at 1000 °C. In the relevant temperature range for methanation between 200 °C–500 °C (grey region in Fig. 2.10), the average values

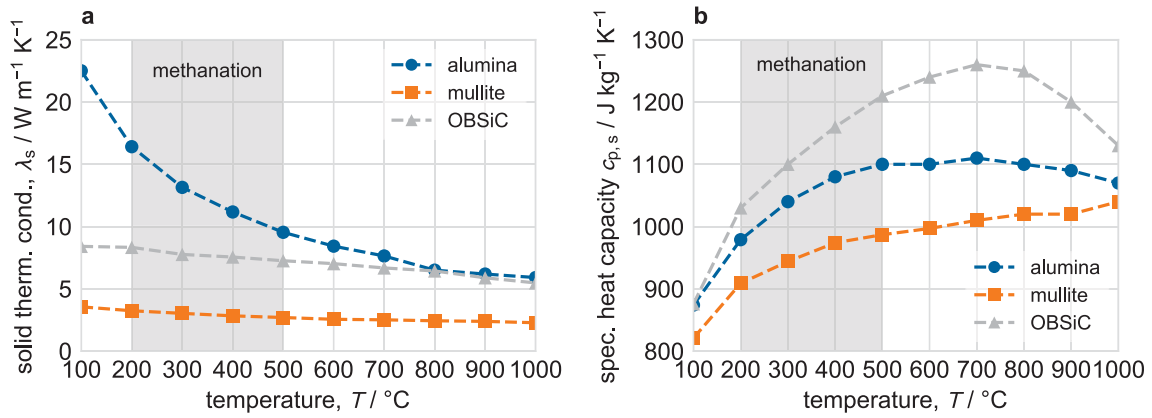


**FIG. 2.10.** Measured thermal conductivities (a) and specific heat capacities (b) from Fishedick et al. [69] for pure alumina, mullite, and OBSiC over a wide temperature range. The average thermal conductivities between 200 °C and 500 °C (grey area) are 12.4 W m<sup>-1</sup> K<sup>-1</sup>, 3.0 W m<sup>-1</sup> K<sup>-1</sup>, and 7.7 W m<sup>-1</sup> K<sup>-1</sup> for pure alumina, mullite, and OBSiC.

are in decreasing order 12.4 W m<sup>-1</sup> K<sup>-1</sup> for pure alumina, 7.7 W m<sup>-1</sup> K<sup>-1</sup> for OBSiC, and 3 W m<sup>-1</sup> K<sup>-1</sup> for mullite.

In comparison, the results of Fishedick et al. [69] fit well to the values reported by Dietrich et al. [49] and Wallenstein et al. [296] for pure alumina and mullite sponges if the different temperatures and the practically constant thermal conductivity of mullite are taken into account (see Tab. 2.3). In addition, the values for alumina agree with the reference values given in [242]. For OBSiC, the reported values are less consistent. Nevertheless, the values reported by Dietrich et al. [49] and Fishedick et al. [69] (8.1 W m<sup>-1</sup> K<sup>-1</sup> and 7.7 W m<sup>-1</sup> K<sup>-1</sup>) and the ones of Wallenstein et al. [296] and Salmang and Scholze [242] (15 W m<sup>-1</sup> K<sup>-1</sup> and 16 W m<sup>-1</sup> K<sup>-1</sup>) match pairwise considering the weak influence of the temperature on the material thermal conductivity for OBSiC. A possible reason for the large deviation of the reported values might be a different microstructure or composition of the investigated OBSiC.

**TAB. 2.3.** Summary of measured solid thermal conductivities available in literature for typical ceramic materials and different temperatures.

Reference	Temperature °C	Thermal conductivity W m <sup>-1</sup> K <sup>-1</sup>				
		Al <sub>2</sub> O <sub>3</sub> ·SiO <sub>2</sub> <sup>a</sup>	Al <sub>2</sub> O <sub>3</sub> <sup>b</sup>	OBSiC <sup>c</sup>	SSiC <sup>d</sup>	SiSiC <sup>e</sup>
Dietrich et al. [49]	25	4.4	25.9	8.1	-	-
Wallenstein et al. [296]	25–50	3.4	26.8	15	-	60
Fishedick et al. [69]	100	3.6	22.5	8.6	-	-
	200–500 <sup>f</sup>	3	12.4	7.7	-	-
Munro [195]	20	-	-	-	114	-
	500	-	-	-	55	-
Salmang and Scholze [242]	100	-	25	-	-	-
	600	-	-	16	50	60

<sup>a</sup> mullite    <sup>b</sup> pure alumina    <sup>c</sup> oxygen-bonded silicon carbide    <sup>d</sup> sintered silicon carbide  
<sup>e</sup> silicon-infiltrated silicon carbide    <sup>f</sup> averaged values

The thermal conductivity of sponges made of sintered silicon carbide (SSiC) and especially of silicon-infiltrated silicon carbide (SiSiC) has not yet been investigated as thoroughly as the one of other ceramic materials. Wallenstein et al. [296] measured a value of  $60 \text{ W m}^{-1} \text{ K}^{-1}$  for SiSiC at room temperature. The same value is given in [242], however, at  $600^\circ\text{C}$ . For SSiC, a thermal conductivity of  $50 \text{ W m}^{-1} \text{ K}^{-1}$  at  $600^\circ\text{C}$  can be found in [242], which is consistent with the value measured by Munro [195] for SSiC with a relative density of 98 % and at slightly lower temperature ( $500^\circ\text{C}$ ). In addition, the results of Munro [195] indicate that the thermal conductivity of SSiC decreases significantly with increasing temperature ( $114 \text{ W m}^{-1} \text{ K}^{-1}$  at  $20^\circ\text{C}$  and  $55 \text{ W m}^{-1} \text{ K}^{-1}$  at  $500^\circ\text{C}$ ). Gräf et al. [95] and Mühlheims and Kraushaar-Czarnetzki [192] assumed a thermal conductivity of  $120 \text{ W m}^{-1} \text{ K}^{-1}$  for technical SiC based on manufacturer information. The value is consistent with the one of Munro [195] at room temperature, and thus far below the required temperatures for most heterogeneous catalysts. Therefore, such a high thermal conductivity of SSiC can probably not be achieved during operation.

In summary, the material thermal conductivity of solid sponges increases in the following order from  $3 \text{ W m}^{-1} \text{ K}^{-1}$  to  $60 \text{ W m}^{-1} \text{ K}^{-1}$ : mullite < OBSiC < alumina < SSiC < SiSiC. For comparison, Bianchi et al. [19] report a value of  $218 \text{ W m}^{-1} \text{ K}^{-1}$  for an aluminum alloy (Al-6101 T6) over a wide range of temperatures, and Aghaei et al. [5] give a value of  $370 \text{ W m}^{-1} \text{ K}^{-1}$  for copper (Cu) at  $300^\circ\text{C}$ . A more in depth discussion about the differences between ceramic and metallic sponges is presented in the next section.

In contrast to the material thermal conductivity, the differences in the material specific heat capacity between  $200^\circ\text{C}$ – $500^\circ\text{C}$  among ceramic materials are less pronounced (see Fig. 2.10 b). The average values are in decreasing order  $1277 \text{ J kg}^{-1} \text{ K}^{-1}$  for OBSiC,  $1054 \text{ J kg}^{-1} \text{ K}^{-1}$  for pure alumina, and  $956 \text{ J kg}^{-1} \text{ K}^{-1}$  for mullite. Consequently, for transient processes such as reactor startup or operation with fluctuating throughput, the influence of the sponge material on the heat capacity of the reactor setup is presumably small, especially because of the high porosity of solid sponges.

### Pseudo-homogeneous models for heat transport in solid sponges

Using the homogeneous approach, the effective thermal conductivity  $\lambda^{(\text{eff})}$  or ETC, in the flow (axial) and transversal (lateral, radial) direction, is generally divided into a stagnant contribution  $\lambda_{\text{stg}}^{(\text{eff})}$  (no fluid flow) and a dispersive contribution  $\lambda_{\text{disp}}^{(\text{eff})}$ , that takes into account the effect of hydrodynamic dispersion:

$$\lambda_{\text{ax}}^{(\text{eff})} = \lambda_{\text{stg}}^{(\text{eff})} + \lambda_{\text{disp,ax}}^{(\text{eff})} \quad (2.21a)$$

$$\lambda_{\text{rad}}^{(\text{eff})} = \lambda_{\text{stg}}^{(\text{eff})} + \lambda_{\text{disp,rad}}^{(\text{eff})} \quad (2.21b)$$

The stagnant ETC is usually equal in all directions because of the isotropic morphology of solid sponges. If thermal radiation is considered in the model, the stagnant ETC is further split into a conductive part  $\lambda_{\text{cond}}^{(\text{eff})}$  that solely describes heat transport by thermal conduction, and a radiative part  $\lambda_{\text{ray}}^{(\text{eff})}$ , that describes heat transport by thermal radiation:

$$\lambda_{\text{stg}}^{(\text{eff})} = \lambda_{\text{cond}}^{(\text{eff})} + \lambda_{\text{ray}}^{(\text{eff})} \quad (2.22)$$

**TAB. 2.4.** Summary of studies investigating the effective radial and axial thermal conductivities of solid sponges including fluid flow using a pseudo-homogeneous approach.

Study	Direction	Solids	Fluids	Temperature $T / ^\circ\text{C}$	Window diameter $d_w / \text{mm}$	Total porosity $\epsilon_t$	Superficial velocity <sup>a</sup> $v_{\text{sup}} / \text{m s}^{-1}$	Conductivity ratio $\lambda_s / \lambda_f$	Péclet number $Pe_w^b$	Accuracy
Fishedick et al. [70] <sup>c</sup> Fishedick et al. [69] <sup>c</sup>	radial	Al <sub>2</sub> O <sub>3</sub> Al <sub>2</sub> O <sub>3</sub> -SiO <sub>2</sub> OBSiC SiSiC	air	100–800	0.45–4.3	0.75–0.88	1–3	4–1935	0–455	±30%
Gräf et al. [95] <sup>d</sup> Gräf [94] <sup>d</sup>	radial axial	Al <sub>2</sub> O <sub>3</sub> Al <sub>2</sub> O <sub>3</sub> -SiO <sub>2</sub>	H <sub>2</sub> C <sub>6</sub> H <sub>6</sub>	170–250	2.73–4.46 <sup>f</sup>	0.81–0.86	0.16–0.32	16–106	2–9	n.a.
Wallenstein et al. [296]	radial	Al <sub>2</sub> O <sub>3</sub> Al <sub>2</sub> O <sub>3</sub> -SiO <sub>2</sub> OBSiC SiSiC	air	25–50	0.98–2.53	0.75–0.85 <sup>g</sup>	0.6–3	130–2308	0–350	±10%
Bianchi et al. [19] <sup>c</sup>	radial	FeCrAlloy® Al-6101	N <sub>2</sub> He	100–500	0.81–2.2	0.89–0.95	0.4–0.95	53–7267	0–320	±25%
Dietrich [50]	radial	Al <sub>2</sub> O <sub>3</sub> Al <sub>2</sub> O <sub>3</sub> -SiO <sub>2</sub> OBSiC	air	25–100	0.63–2.25	0.74–0.85	0.4–2.5	130–996	0–103	±25%
Edouard et al. [59] <sup>e</sup>	radial	SSiC	air	25–100	1	0.88 <sup>h</sup>	0.02–0.32	258–578	0.6–15	n.a.
Dietrich et al. [48]	axial	Al <sub>2</sub> O <sub>3</sub> Al <sub>2</sub> O <sub>3</sub> -SiO <sub>2</sub> OBSiC	air	25–100	0.63–2.25	0.74–0.85	0.1–1	130–996	0–260	±40%

<sup>a</sup> at normal conditions (NTP, 273.15 K, 1.01325 bar). <sup>b</sup> definition based on fluid properties and window diameter for comparison ( $Pe_w = \rho_f c_p v_{\text{sup}} d_w / \lambda_f$ )  
<sup>c</sup> includes radiation using the Rosseland approximation (see Dietrich et al. [47]) <sup>d</sup> parameters deduced during exothermal chemical reaction (benzene hydrogenation) <sup>e</sup> only a single sample investigated <sup>f</sup> only hydraulic diameters reported <sup>g</sup> only nominal porosities reported  
<sup>h</sup> only open porosity reported

The main differences between the available homogeneous models for heat transport in solid sponges [19, 48, 50, 59, 70, 94, 95, 296] are the choice of the model for the stagnant ETC, the choice of the characteristic length and the velocity in the dispersive part, and the ranges of investigated parameters (see Tab. 2.4).

### Stagnant effective thermal conductivity

The conductive part of the effective stagnant thermal conductivity  $\lambda_{\text{cond}}^{(\text{eff})}$  has been studied intensively over the last years. Numerous scientists developed analytical, asymptotic, and semi-empiric expressions based on either unit cells or real sponges [17, 76, 159–161, 186–188, 205, 310, 313]. Recently, Ranut [229] presented a very comprehensive review about these models for the ETC of aluminum sponges with porosities above 0.88. Some of the expressions, however, require the knowledge of geometrical parameters that are difficult to measure, such as the size of the nodes where the struts meet or the length of the struts [159, 310].

Consequently, in the engineering community empirical models that only require the knowledge of measurable properties, such as the open porosity and the window diameter, are preferred. One of the most encountered models for the stagnant ETC is the modified Krischer model (see [49, 69]), also called plate model, which is a weighted sum of the upper and lower asymptotic bound for the effective thermal conductivity of porous media:

$$\lambda_{\text{cond}}^{(\text{eff})} = b\lambda_{\text{serial}}^{(\text{eff})} + (1 - b)\lambda_{\text{parallel}}^{(\text{eff})} \quad (2.23a)$$

$$\lambda_{\text{serial}}^{(\text{eff})} = \left( \frac{\varepsilon_t}{\lambda_f} + \frac{1 - \varepsilon_t}{\lambda_s} \right)^{-1} \quad (2.23b)$$

$$\lambda_{\text{parallel}}^{(\text{eff})} = \varepsilon_t\lambda_f + (1 - \varepsilon_t)\lambda_s \quad (2.23c)$$

The weight parameter  $b$  is usually determined empirically from experimental data. For ceramic sponges filled with air (see Tab. 2.4), the values of Wallenstein et al. [296] ( $b = 0.63$ ), Edouard et al. [59] ( $b = 0.65$ ), and Dietrich et al. [49] ( $b = 0.51$ ) are in good agreement. Bhattacharya et al. [17] also determined  $b = 0.63$ , however, for metallic sponges. Fishedick et al. [69] obtained  $b = 0.48$ , probably because they also measured at high temperatures where the thermal conductivity ratio  $\lambda_s/\lambda_f$  is low, and the contribution of the fluid thermal conductivity is thus larger than at low temperatures.

Another popular model to describe the conductive part of the stagnant ETC is Lemlich's model [166]:

$$\lambda_{\text{cond}}^{(\text{eff})} = \frac{1 - \varepsilon_t}{f_L} \lambda_s. \quad (2.24)$$

In contrast to the modified Krischer model, the Lemlich model does not take the fluid thermal conductivity  $\lambda_f$  into consideration. Thus, it is only valid for  $\lambda_f \ll \lambda_s$  or very low porosities. Although the condition of negligible fluid conductivity is usually true for air, it has to be checked for liquids and hydrogen-rich mixtures such as syngas ( $\text{H}_2/\text{CO}$  mixture). The Lemlich model was applied by Bianchi et al. [19] who used Lemlich's originally proposed value  $f_L = 3$  to describe conductive heat transport in metal sponges. The factor 3 was recently confirmed for metal sponges by Aghaei et al. [5].

Gräf et al. [95] also used Lemlich's expression to describe the conductive part of the stagnant ETC for ceramic sponges. Based on their measurements they determined  $f_L = 5.2$ . In addition, they deduced  $f_L = 3.4$  for aluminum sponges reported in literature. In comparison, their results agree well with other studies for mullite sponges [49, 296] and aluminum sponges [5, 19]. Nevertheless, their values for alumina sponges are significantly lower than the ones reported by Dietrich et al. [49], Fishedick et al. [69], and Wallenstein et al. [296]. A possible explanation for the deviation is the assumption of a too high solid thermal conductivity for alumina between 170 °C–250 °C. Instead of approximately  $16 \text{ W m}^{-1} \text{ K}^{-1}$  (see Fig. 2.10 a), they assumed a value of  $26 \text{ W m}^{-1} \text{ K}^{-1}$  measured by Wallenstein et al. [296] at room temperature. Consequently, the factor  $f_L$  was overdetermined during the fitting procedure. A quick estimation using the corrected value for the solid thermal conductivity also yields  $f_L \approx 3$ .

At high temperatures, heat transport by thermal radiation has to be considered alongside thermal conduction. From the selected homogeneous models that also consider fluid flow, only the ones of Bianchi et al. [19] and Fishedick et al. [69] take into account thermal radiation. If it is not considered explicitly, the contribution of thermal radiation is lumped into the contribution of thermal conduction, and thus might artificially increase the influence of thermal conduction at high temperatures.

Thermal radiation is typically modelled using the Rosseland approximation (see [47]),

$$\lambda_{\text{ray}}^{(\text{eff})} = \frac{16\sigma_B T^3}{3E_r}, \quad (2.25)$$

with the Stefan-Boltzmann constant  $\sigma_B = 5.67 \cdot 10^{-8} \text{ W m}^{-2} \text{ K}^{-4}$ , and the Rosseland extinction coefficient  $E_r$ . The Rosseland approximation was originally developed for opaque systems. Because of high pore densities, however, the mean free path for thermal radiation in solid sponges is short. Consequently, solid sponges can be treated as quasi-opaque systems and the application of the Rosseland approximation is justified (see [47]). The extinction can be interpreted as the inverse penetration thickness of thermal radiation. It depends on the geometrical and material properties of the solid sponge. Bianchi et al. [19] use the following parameterization for the Rosseland extinction coefficient in their homogeneous model:

$$E_r = C_R \frac{(1 - \varepsilon_0)^{1/2}}{d_c} \quad (2.26)$$

with the cell diameter  $d_c$  and  $C_R = 2.65$  for metallic sponges. Fishedick et al. [69] used in principle the same form for the extinction coefficient, however, they chose the window diameter  $d_w$  as characteristic length and an exponent of  $1/3$  instead of  $1/2$  in the numerator:

$$E_r = C_R \frac{(1 - \varepsilon_0)^{1/3}}{d_w}. \quad (2.27)$$

For ceramic sponges ( $\text{Al}_2\text{O}_3$ ,  $\text{Al}_2\text{O}_3\text{-SiO}_2$ ,  $\text{OBSiC}$ ,  $\text{SSiC}$ ), Fishedick et al. [69] found  $C_R = 1.3$  which is significantly lower than the value obtained by Bianchi et al. [19]. Taking into account the choice of the window diameter ( $d_c \approx 2.3d_w$ , see [126]), however, both models yield comparable values for the extinction coefficient.

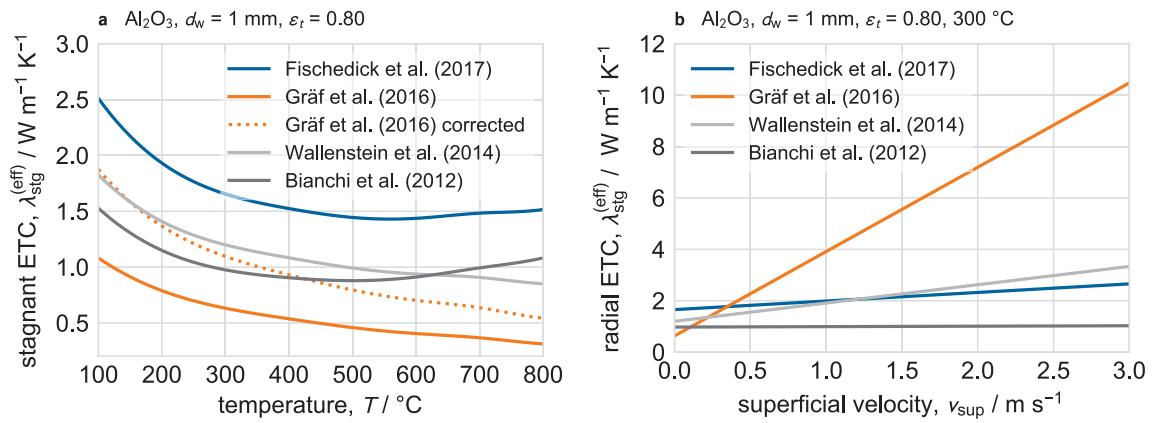


**FIG. 2.11.** Comparison of the stagnant ETC (a) and the radial ETC (b) calculated with the models of Bianchi et al. [19], Fishedick et al. [70], Gräf et al. [95], and Wallenstein et al. [296] for a  $\text{Al}_2\text{O}_3$  sponge with window diameter of 1 mm and total porosity of 0.8. The fluid used for the calculations was a 4:1  $\text{H}_2/\text{CO}_2$  mixture at 10 bar.

Figure 2.11 a shows a comparison of the stagnant ETC of an alumina sponge with an average window diameter of 1 mm and a total porosity of 0.8, calculated with the models of Fishedick et al. [69], Gräf et al. [95], Wallenstein et al. [296], and Bianchi et al. [19]. All models except for the one of Gräf et al. [95] provide consistent estimations for the stagnant ETC taking into consideration their accuracies (see Tab. 2.4). If however the above mentioned correction is applied to the model of Gräf et al. [95], i. e., using  $f_L = 3$  instead of  $f_L = 5.2$ , it also yields comparable values of the stagnant ETC. The model of Fishedick et al. [69] consistently predicts the highest values of the stagnant ETC because they also included high temperatures in their measurements and thus considered the increased fluid thermal conductivities at high temperatures. For all models the stagnant ETC decreases with increasing temperatures up to  $400\text{ }^\circ\text{C}$  because of the decreasing solid thermal conductivity of alumina (see Fig. 2.10 a). For temperatures above  $400\text{ }^\circ\text{C}$  the stagnant ETC keeps decreasing according to the models of Gräf et al. [95] and Wallenstein et al. [296], while it slowly increases according to the models of Fishedick et al. [69] and Bianchi et al. [19]. The increase of the stagnant ETC is due to thermal radiation, which is considered in the latter models, and that compensates the decrease of the solid thermal conductivity at high temperatures. In addition, the relative increase of the stagnant ETC due to thermal radiation is comparable in both models because of the comparable models for the extinction coefficient  $E_r$ .

In summary, the model of Fishedick et al. [69] is probably most suitable for calculations of solid sponges as catalyst supports because it covers a wide ranges of ceramic materials, geometrical properties, and process conditions. In particular, it includes low thermal conductivity ratios ( $\lambda_s/\lambda_f \geq 4$ ) and temperatures up to  $800\text{ }^\circ\text{C}$ , and is thus applicable for fluid mixtures with high thermal conductivity such as syngas, and high temperature applications. Consequently, the following discussion about the conductive and radiative contribution to the stagnant ETC is based on the values calculated with the model of Fishedick et al. [69].

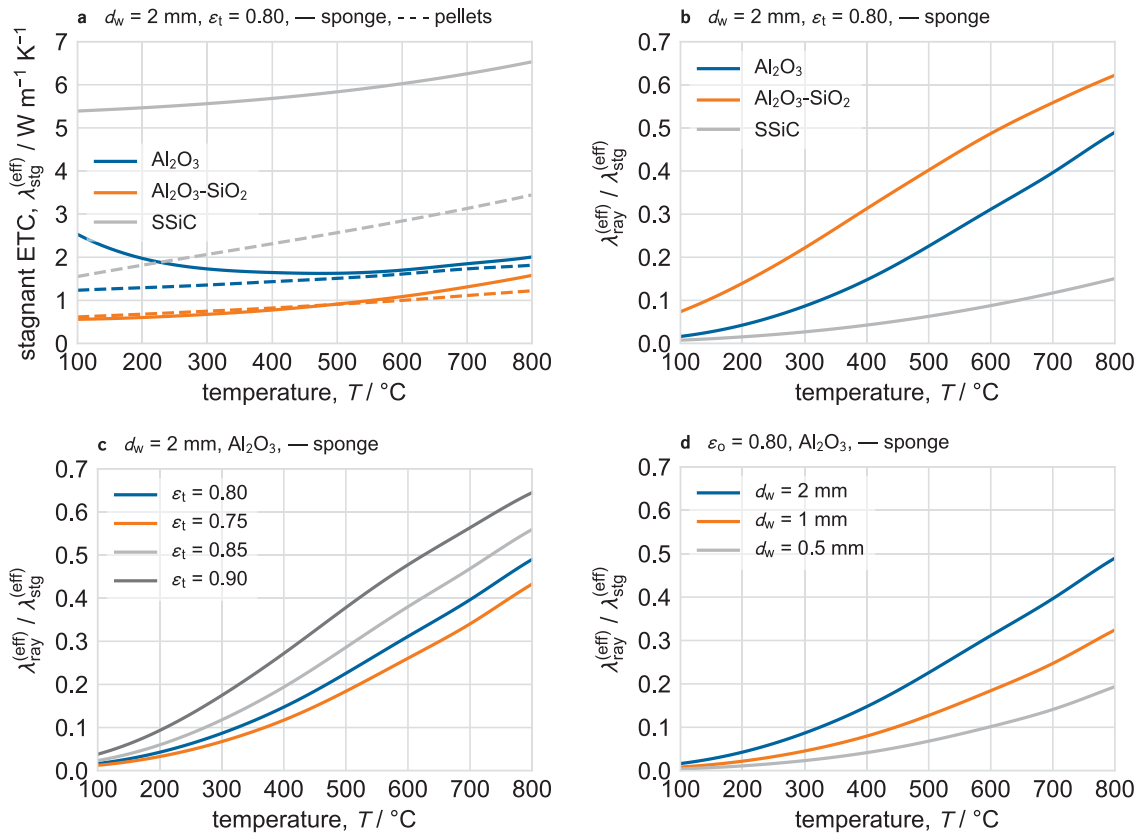


**FIG. 2.12.** Analysis of the stagnant effective thermal conductivity calculated with the model of Fishedick et al. [69]: (a) influence of temperature on the absolute stagnant effective thermal conductivity; (b) relative contribution of radiative heat transport; (c) and (d) influence of total porosity and window diameter on the relative contribution of radiative heat transport for Al<sub>2</sub>O<sub>3</sub>. The fluid used for the calculations was a 4:1 H<sub>2</sub>/CO<sub>2</sub> mixture at 10 bar.

Figure 2.12 a shows the stagnant ETC of ceramic sponges with  $d_w = 2$  mm and  $\varepsilon_t = 0.80$  over a wide range of temperatures. Obviously the stagnant ETC increases with increasing solid thermal conductivity. As explained above the stagnant ETC of alumina sponges decreases for temperatures below 400 °C because of the decreasing solid thermal conductivity and the dominance of thermal conduction within the solid. Above 400 °C it increases again because of increasing heat transport via thermal radiation. For mullite, the solid thermal conductivity remains relatively constant over the whole temperature range (see Fig. 2.10 a), and the stagnant ETC thus increases monotonically with increasing temperature because of thermal radiation. The same is true for the sponge made out of SSiC here because a constant solid thermal conductivity of 50 W m<sup>-1</sup> K<sup>-1</sup> over the whole temperature range is assumed due to lack of reliable data.

In comparison to packed beds of pellets, mullite sponges exhibit almost the same stagnant ETC over the whole range of the considered temperature, however, at a much higher porosity (sponge, 0.8; packed bed, 0.4; see Fig. 2.12 a). A similar comparison is also observable in case of alumina for temperatures above 400 °C. At lower temperatures, however, the stagnant ETC of alumina sponges is considerably higher than the one of packed beds of alumina pellets because of the dominance of thermal conduction within

the continuous solid phase and the higher solid thermal conductivity of alumina at lower temperatures. Consequently, it can be concluded that for the considered total porosity of 0.8, a solid thermal conductivity of at least  $10 \text{ W m}^{-1} \text{ K}^{-1}$  (see Fig. 2.10 a,  $400 \text{ }^\circ\text{C}$ ) is necessary in order to obtain a higher stagnant ETC for solid sponges than for packed beds of pellets. The full potential of solid sponges regarding heat transport, however, unfolds if materials with high solid thermal conductivities, such as SSiC ( $50 \text{ W m}^{-1} \text{ K}^{-1}$ ), are used. At  $300 \text{ }^\circ\text{C}$  for example, the stagnant ETC of a packed bed of SSiC pellets is approximately  $2 \text{ W m}^{-1} \text{ K}^{-1}$ . In case of SSiC sponges, the stagnant ETC is around  $5.5 \text{ W m}^{-1} \text{ K}^{-1}$ , and thus around 2.75 times higher than for the packed bed of pellets.

The relative contribution of thermal radiation to the stagnant ETC,  $\lambda_{\text{ray}}^{(\text{eff})} / \lambda_{\text{stg}}^{(\text{eff})}$ , is shown in Fig. 2.12 b. In general, the amount of radiative heat transport increases with increasing temperature. For materials with high thermal conductivity, however, the absolute contribution of thermal radiation to the stagnant ETC is significantly lower than the one for materials with low thermal conductivity. While thermal radiation makes up less than 10% of the stagnant ETC, and thus can possibly be disregarded, up to  $600 \text{ }^\circ\text{C}$  for a SSiC sponge, it contributes around 10% to the stagnant ETC of a mullite sponge already at  $100 \text{ }^\circ\text{C}$ .

Figure 2.12 c shows the influence of the total porosity on the relative contribution of the stagnant ETC for an alumina sponge. Independent of the total porosity, the relative contribution of thermal radiation increases with the same slope at high temperatures. The absolute value of the relative contribution of thermal radiation, however, decreases with the total porosity because of the increase of the conductive contribution. Consequently, the influence of the total porosity on the relative contribution of thermal radiation is mainly due to the changing contribution of solid conduction.

Finally, Fig. 2.12 d shows the influence of the window diameter on the relative contribution of thermal radiation. In contrast to the total porosity, the window diameter clearly influences the relative contribution of thermal radiation as the latter increases with different slopes for increasing temperature. For small window diameters ( $d_w = 0.5 \text{ mm}$ ), the relative contribution of thermal radiation increases only slightly to 0.2 at  $800 \text{ }^\circ\text{C}$ , while it increases to approximately 0.5 at  $800 \text{ }^\circ\text{C}$  for large window diameters ( $d_w = 2 \text{ mm}$ ) because fewer struts block the radiation path at low pore densities or large window diameters (see [47, 70]).

To sum up, if a high stagnant ETC is required the application of a solid material with high thermal conductivity, such as SSiC, is necessary. Furthermore, the total porosity should be low and the window diameter large to increase the path of thermal radiation. Large window diameters, however, lead to small specific surface areas and thus to low catalyst densities.

Ultimately, the conclusion of maximal solid thermal conductivity would lead to the choice of metals that outperform ceramic materials regarding thermal conductivity by at least one order of magnitude. Because of their high porosities larger 0.9 (see Fig. 2.5, p. 20), however, metallic sponges exhibit comparable values for the stagnant ETC as typical SSiC sponges. Bianchi et al. [19], for example, report a stagnant ETC of  $7.8 \text{ W m}^{-1} \text{ K}^{-1}$  for an aluminum (Al) sponge with a total porosity of 0.89; Aghaei et al. [5] determined a stagnant ETC of  $4.5 \text{ W m}^{-1} \text{ K}^{-1}$  for a copper (Cu) sponge with total porosity of 0.96. Thus,

metal sponges do not provide a significant boost of the stagnant ETC compared to SSiC as long as the total porosity is larger than 0.9. In addition, thermal expansion of metals is usually much larger (approx.  $25 \cdot 10^{-6} \text{ K}^{-1}$  for Al at  $300 \text{ }^\circ\text{C}$  [108]) than for ceramics (approx.  $4 \cdot 10^{-6} \text{ K}^{-1}$  for SSiC at  $300 \text{ }^\circ\text{C}$  [195]), which might lead to cracks or even loss of the catalyst coating during heat up or dynamic operation.

### Effective dispersive thermal conductivity

The dispersive contribution to the ETC in either the axial or radial (lateral) direction is usually described by a characteristic Péclet number  $Pe_{\text{char}}$  and the dispersion coefficients  $K_{\text{ax}}$  and  $K_{\text{rad}}$ :

$$\lambda_{\text{disp,ax}}^{(\text{eff})} = \frac{\rho_f c_{p,f} d_{\text{char}} v_{\text{char}}}{K_{\text{ax}}} = \frac{1}{K_{\text{ax}}} Pe_{\text{char}} \lambda_f, \quad (2.28a)$$

$$\lambda_{\text{disp,rad}}^{(\text{eff})} = \frac{\rho_f c_{p,f} d_{\text{char}} v_{\text{char}}}{K_{\text{rad}}} = \frac{1}{K_{\text{rad}}} Pe_{\text{char}} \lambda_f \quad (2.28b)$$

Again, the main difference between various pseudo-homogeneous models [19, 48, 50, 59, 70, 94, 95, 296] for the dispersive contribution to the *radial* ETC are the choices of the characteristic velocity  $v_{\text{char}}$  and the characteristic diameter  $d_{\text{char}}$ , the fitted value of the radial dispersion coefficient  $K_{\text{rad}}$ , and range of the investigated parameters (see Tab. 2.4). While Bianchi et al. [19], Edouard et al. [57], and Fishedick et al. [70] used the superficial velocity  $v_{\text{sup}}$ , Dietrich [50], Gräf et al. [95], and Wallenstein et al. [296] used the intrinsic velocity  $v_{\text{sup}}/\varepsilon_0$ . The choice of the characteristic diameter is less consistent among the models: Fishedick et al. [70] defined a mixing length based on a flow model of Bauer and Schlünder [14]; similarly, Wallenstein et al. [296] defined a mixing length as the sum of the strut and window diameter, including an empirical fitting factor to account for the shape of the struts; Dietrich [50] and Gräf et al. [95] made use of the hydraulic diameter in their models; Edouard et al. [57] simply used the cell diameter, and Bianchi et al. [19] used the square root of the permeability. Consequently, because of the inconsistencies, only the model of Fishedick et al. [70] is here presented in detail as it includes a physically sound flow model and covers the widest range of parameters and temperatures and is thus most suited for calculations of catalyst supports.

Based on the flow models for the mixing length of Bauer and Schlünder [14], Fishedick et al. [70] developed a model for the mixing length during forced convection in solid sponges. They applied a Kelvin unit cell model and took into account three different flow paths: first, flow around the whole Kelvin unit cell, second, flow around the struts, and third, flow straight through adjacent windows of the Kelvin unit cell. Their expression for the characteristic mixing length  $d_{\text{mix}}$  reads

$$d_{\text{mix}} = \frac{1.428 d_w}{\varepsilon_t} F_1 + \frac{\varepsilon_t - \varepsilon_0}{\varepsilon_t} \left( \frac{3l_s}{2d_s} \right)^{1/3} d_s F_2 + \frac{\varepsilon_0 - 0.476}{\varepsilon_t} \sqrt{2} d_w F_3, \quad (2.29)$$

with

$$F_1 = 2.37 (1 - S_V d_s)^2, \quad F_2 = 2.48 (1 - S_V d_s)^2, \quad F_3 = 3.87 (1 - S_V d_s)^2. \quad (2.30)$$

The numerical coefficients in equations (2.30) were obtained by fitting a pseudo-homogeneous model to measured fluid temperature distributions. For the radial dispersion coefficient, they used  $K_{\text{rad}} = 8$  based on a theoretical analysis.

A comparison of the radial ETC as a function of the fluid velocity calculated with the models of Fishedick et al. [69], Gräf et al. [95], Wallenstein et al. [296], and Bianchi et al. [19] is shown in Fig. 2.11 b, p. 34, for an alumina sponge with an average window diameter of 1 mm and a total porosity of 0.8. The models of Fishedick et al. [70] and Wallenstein et al. [296] provide similar values for the radial ETC. The model of Bianchi et al. [19] gives a constant value for the whole velocity range because they solely considered metallic sponges with high thermal conductivity in their model. Thus, thermal conduction is the predominant heat transport mechanism, even at high flow rates, and dispersive heat transport contributes only by a negligible amount to the total radial ETC. Contrary, the model of Gräf et al. [95] exhibits a strong dependency of the radial ETC on the fluid velocity. Among the compared studies, however, Gräf et al. [95] obtained their experimental data from *operando* temperature measurements during the exothermic hydrogenation of benzene, and thus they were limited to low flow rates at the lab scale in order to maintain a certain residence time. Consequently, the contribution of radial dispersive ETC might be negligible under their conditions so that the radial dispersion coefficient could not be determined accurately.

Fig. 2.13 a shows a comparison of the effective radial ETC of solid sponges (solid lines) and packed beds (dashed lines) for different materials and fluid velocities. The radial ETCs were calculated with the models of Fishedick et al. [70] for the sponges, and with the well-established models of Winterberg and Tsotsas [280, 281, 305] for the packed beds of pellets with an open porosity of 0.4 and a particle size of 3 mm. In general, the radial ETC of sponges is much less dependent on the fluid velocity than the one of packed beds because of the continuous solid phase and the higher porosities, and thus lower hydrodynamic dispersion. Consequently, the predominant heat transport mechanism in solid sponges is thermal conduction in the solid phase [70, 95, 296]. Therefore, an increase of the solid thermal conductivity has a more pronounced effect on the radial ETC of sponges than on the radial ETC of a packed bed of the same material. For poor thermal conductors such as mullite ( $\text{Al}_2\text{O}_3 \cdot \text{SiO}_2$ ), the radial ETC of a packed bed is in most cases higher than the one of a solid sponge because of the high contribution of radial dispersion in the packed bed. For a SSiC sponge with a total porosity of 0.8, the radial ETC of the sponge is significantly higher than the one of the packed bed up to fluid velocities of  $1.5 \text{ m s}^{-1}$ . At higher fluid velocities, the radial ETC of the packed bed exceeds the one of the solid sponge because of the dominance of hydrodynamic dispersion.

The relative increase of the radial ETC through hydrodynamic dispersion with increasing fluid velocity is shown in Fig. 2.13 b. Because the radial ETC is here normalized with the stagnant ETC, all curves converge at a fluid velocity of  $0 \text{ m s}^{-1}$ . Again, the relative increase of the radial ETC is consistently higher for packed beds than for sponges. For both structures, solid sponges and packed beds, the relative increase of the radial ETC with increasing fluid velocity is less pronounced at high thermal conductivities (compare  $\text{Al}_2\text{O}_3 \cdot \text{SiO}_2$  and SSiC) because of increased heat transport via thermal conduction.

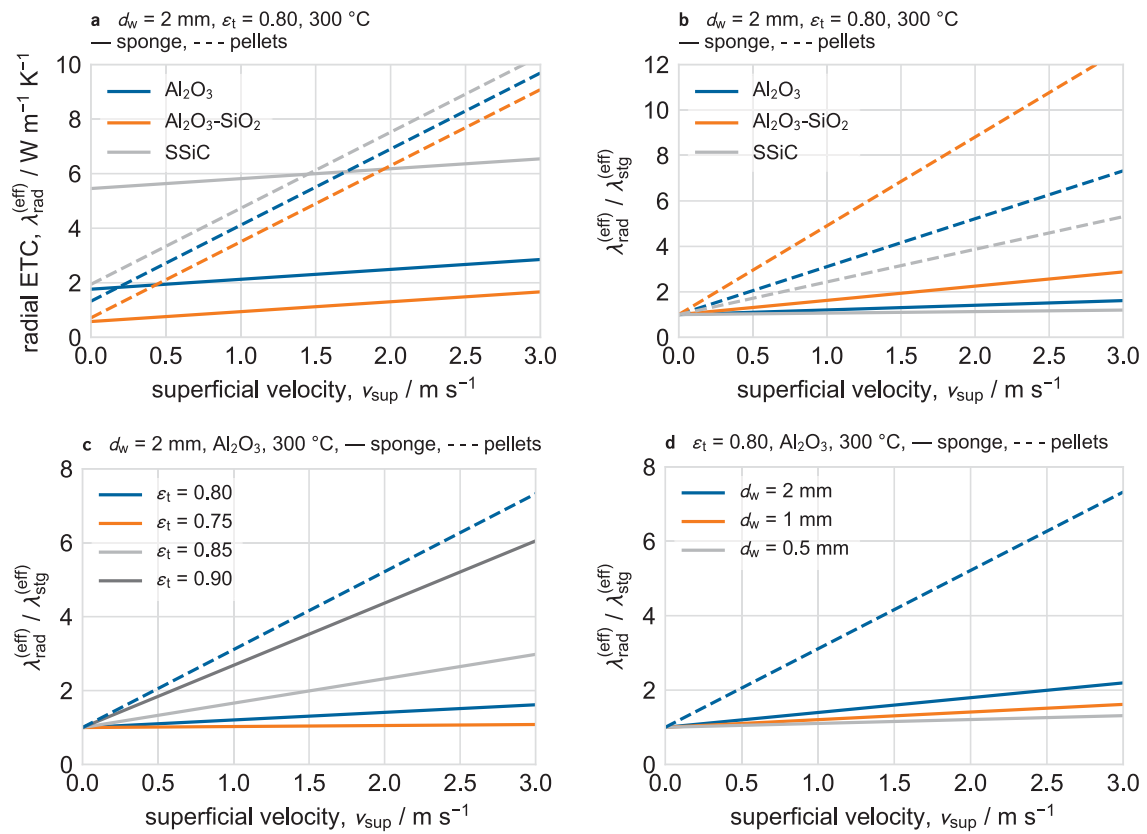


**FIG. 2.13.** Analysis of the dispersive part of the radial effective thermal conductivity of solid sponges calculated with the model of Fishedick et al. [70] (solid lines). For comparison, the dashed lines show the radial ETC of packed beds of pellets with an open porosity of 0.4 and a pellet size of 3 mm, calculated with the established models of Winterberg and Tsotsas [280, 281, 305]: (a) influence of superficial velocity on the absolute radial effective thermal conductivity; (b) relative contribution of dispersive heat transport to the total radial effective thermal conductivity; (c) and (d) influence of total porosity and window diameter on the relative contribution of dispersive heat transport. The material of the sponge and pellets was  $\text{Al}_2\text{O}_3$ . The fluid used for the calculations was a 4:1  $\text{H}_2/\text{CO}_2$  mixture at 10 bar and  $300^\circ\text{C}$ .

The same explanation is true for the influence of the total porosity on the relative increase of the ETC with increasing fluid velocity for an alumina sponge (see Fig. 2.13 c). At high total porosities, heat transport via thermal conduction in the solid phase is low, and thus the relative increase of the ETC with increasing fluid velocity is higher than at low total porosities. At the upper bound of the total porosity for typical sponges, 0.9, the relative increase of the radial ETC of a solid sponge is comparable to the one of a packed bed with an open porosity of 0.4 and a pellet diameter of 3 mm.

In contrast, the influence of the window diameter on the relative increase of the radial ETC with increasing fluid velocity is much lower than the one of the total porosity (see Fig. 2.13 d). With increasing window diameter, the contribution of the radial dispersive ETC to the total radial ETC increases as well because of the larger mixing length. Consequently, hydrodynamic dispersion transports thermal energy over a larger distance and thus adds more to the total radial ETC. Compared to the effect of the porosity, the effect of the window diameter on the dispersive contribution of the radial ETC is small.

In summary, thermal conduction through the continuous solid phase is the dominant heat transport mechanism in monolithic solid sponges. Therefore, the radial ETC of solid sponges is much less dependent on the fluid velocity at low to moderate total porosities than the one of packed beds. At high total porosities, the radial ETC of solid sponges and packed beds exhibit almost the same relative increase with increasing velocity. Regarding their application as monolithic catalyst support, solid sponges thus allow effective heat transport at low flow rates and a robust behavior against varying flow rates, if solid sponges with higher thermal conductivities than that of  $\text{Al}_2\text{O}_3$  are used. For temperatures lower than  $400\text{ }^\circ\text{C}$ , however,  $\text{Al}_2\text{O}_3$  solid sponges are superior to packed beds again because of the higher solid thermal conductivity at low temperatures.

The dispersive ETC in the *axial* direction has not been studied extensively yet. Only Dietrich et al. [48] and Gräf et al. [95] provided models for the axial dispersive ETC. Both studies used Eq. (2.28) with the intrinsic velocity  $v_{\text{sup}}/\varepsilon_0$  and the hydraulic diameter  $d_h$  as characteristic velocity and diameter, respectively. While Dietrich et al. [48] determined  $K_{\text{ax}} = 1.19$  for ceramic materials ( $\text{Al}_2\text{O}_3\text{-SiO}_2$ ,  $\text{SiO}_2$ ,  $\text{OBSiC}$ ) and air flow up to  $100\text{ }^\circ\text{C}$  and  $1\text{ m s}^{-1}$ , Gräf et al. [95] obtained  $K_{\text{ax}} = 4$  during benzene hydrogenation over mullite and alumina sponges at  $250\text{ }^\circ\text{C}$ .

Nevertheless, the data on axial dispersion in monolithic sponges is still too scarce to deduce general dependencies from both models. In addition, Dietrich et al. [48] give an accuracy of only  $\pm 40\%$  for their correlation. Moreover, the role of axial dispersion in catalytic sponges is still unclear. For packed beds, axial dispersion of heat can usually be neglected because the loose contact between the individual pellets only allows for axial heat transport by convection. In contrast, thermal conduction in the continuous solid phase of monolithic sponges is basically unaffected by convective heat transport. Thus, thermal conduction in the axial direction will have some influence on the heat transport in and against the flow direction, particularly for materials with high thermal conductivities. Therefore, the application of a pseudo-homogeneous approach is probably not sufficient to accurately describe axial heat transport in solid sponges. In most applications of solid sponges as catalyst supports, however, several sponges are stacked to form the catalyst bed. Thus, thermal conduction in the axial direction is severely limited at the bounds of the individual samples [95]. Therefore, more research on the axial heat transport in stacked solid sponges is necessary to clarify its effect on temperature distributions in catalytic sponge packings.

### 2.3.5 Mass transport in solid sponges

In contrast to heat transport, the continuous solid phase of solid sponges does not contribute to mass transport. Consequently, mass transport in solid sponges has not been investigated intensively yet, neither in the axial nor in the radial direction.

Habisreuther et al. [105], Saber et al. [241], and Zürcher et al. [319] investigated axial mass transport in solid sponges using conventional tracer experiments, however, they did not correlate the obtained axial effective dispersion coefficients (EDC) with the geometrical properties of the sponges and the fluid properties. Mass transport in the radial direction was studied by Benz et al. [16], Hackert et al. [106], and Pereira et al. [219] using

a point-wise injection of a tracer (methane or smoke) at the inlet and a moveable probe or laser-induced imaging methods at the outlet. Hutter et al. [115] used a combination of particle image velocimetry (PIV) and laser-induced fluorescence (LIF) to map velocity and concentration fields behind solid metal sponges. Although, the experimental data scatters, all studies agree that the radial EDC,  $D_{\text{rad}}^{(\text{eff})}$ , is proportional to  $v_{\text{sup}}d_{\text{char}}$ , and that the stagnant contribution, i. e., molar diffusion in the voids of the sponge is negligible for most applications.

In addition, Gräf et al. [95] performed a small sensitivity analysis using a pseudo-homogeneous reactor model to simulate temperature and concentration fields during benzene hydrogenation. They found that increasing the radial and axial EDC by a factor of 2 or 5 does neither influence the simulated axial and radial temperature profiles nor the simulated conversion.

Consequently, in this work the axial and radial mass dispersion coefficients,  $D_{\text{ax},i}^{(\text{eff})}$  and  $D_{\text{rad},i}^{(\text{eff})}$  are estimated using the analogy between heat and mass transport and the models of Dietrich et al. [48] and Fishedick et al. [70] for the dispersive contributions to the axial and radial ETC:

$$D_{\text{ax},i}^{(\text{eff})} \approx \varepsilon_o D_{\text{mol},i} + \frac{v_{\text{sup}} d_{\text{h}}}{1.19 \varepsilon_o}, \quad (2.31\text{a})$$

$$D_{\text{rad},i}^{(\text{eff})} \approx \varepsilon_o D_{\text{mol},i} + \frac{v_{\text{sup}} d_{\text{mix}}}{8}, \quad (2.31\text{b})$$

with the hydraulic diameter  $d_{\text{h}}$ , and the mixing length  $d_{\text{mix}}$  from equations (2.29) and (2.30).

In addition to two-phase mass transport, first studies on three-phase mass transport (solid-gas-liquid) have been presented by Edouard et al. [58], Grosse and Kind [100], Lévêque et al. [168], and Voltolina et al. [295].

### 2.3.6 Heat and mass transfer in solid sponges

In contrast, to the determination of heat and mass transport which allows the use of homogeneous models, the investigation of heat and mass transfer from the fluid to the solid phase and vice versa requires the use of (pseudo)-heterogeneous approaches to distinguish between the fluid and the solid temperature. Thus, heat transfer has not been studied as intensively as effective heat transport yet.

#### Heat transfer

Models for the heat transfer coefficient  $\alpha$  are usually written in dimensionless expressions of the form

$$Nu = C_{\text{h}} Re^{m_{\text{h}}} Pr^{\frac{1}{3}}. \quad (2.32)$$

The coefficients  $C_{\text{h}}$  and  $m_{\text{h}}$  are either estimated using experimental data [46, 85, 86, 97, 129], or derived from unit cell approaches [82, 119]. The dimensionless groups are defined as

$$Nu = \frac{\alpha d_{\text{char}}}{\lambda_{\text{f}}}, \quad Re = \frac{\rho_{\text{f}} v_{\text{sup}} d_{\text{char}}}{\mu_{\text{f}}}, \quad Pr = \frac{\mu_{\text{f}} c_{\text{p},\text{f}}}{\lambda_{\text{f}}}, \quad (2.33)$$

with  $d_{\text{char}}$  being some characteristic length, for example the strut diameter  $d_s$ . Moreover, the Reynolds number is sometimes defined with the interstitial velocity  $v = v_{\text{sup}}/\varepsilon_o$  instead of the superficial velocity  $v_{\text{sup}}$  (see for example [46]).

Giani et al. [85] determined heat transfer in FeCrAlloy® and copper sponges with a nominal porosity of 0.95 and window diameters from 2 mm–4.7 mm. They determined  $C_h = 1.2$  and  $m_h = 0.43$  by fitting a pseudo-heterogeneous model to their experimental results for  $20 \leq Re \leq 240$ . The solid temperature was assumed to be uniform because of the high thermal conductivity of the sponges. Later, Groppi et al. [97] refined the correlation using the maximal velocity in the definition of the Reynolds number and found  $C_h = 1.0$ .

In contrast to Giani et al. [85], Dietrich [46] explicitly measured the solid temperature by contacting thin thermocouples ( $\varnothing 0.5$  mm) to the sponge surface using a highly conductive paste. They considered ceramic materials ( $\text{Al}_2\text{O}_3$ ,  $\text{Al}_2\text{O}_3\text{-SiO}_2$ , OBSiC), window diameters of 0.69 mm–2.3 mm, and nominal porosities of 0.75–0.88. They proposed  $C_h = 0.57C_{\text{Re}}C_{\text{geo}}$  and  $m_m = 0.67$  with

$$C_{\text{Re}} = \left( \frac{Re + 1}{Re + 1000} \right)^{0.25} \quad (2.34a)$$

$$C_{\text{geo}} = \left( \frac{d_h/(d_s + d_w)}{1.626} \right)^{1.5}. \quad (2.34b)$$

The coefficient  $C_{\text{geo}}$  takes into account the geometrical properties of the sponges. Moreover, Dietrich [46] used the hydraulic diameter  $d_h$  as characteristic length and defined the Reynolds number with the intrinsic velocity. Although the correlation is valid for a wide range of Reynolds numbers ( $50 \leq Re \leq 1400$ ), it only describes the experimental data within an accuracy of  $\pm 40\%$ . Nevertheless, Meinicke et al. [185] could partly confirm Dietrich's correlation regarding the overall trend and absolute values using scale-resolved Computational Fluid Dynamics (CFD) simulations.

### Mass transfer

Mass transfer between the fluid and solid phase is typically described in analogy to heat transfer. The resulting correlations for the dimensionless mass transfer coefficients  $\beta_i$  (Sherwood numbers) exhibit the same form as Eq. (2.32),

$$Sh = C_m Re^{m_m} Sc^{\frac{1}{3}}. \quad (2.35)$$

The Sherwood and Schmidt numbers are defined as

$$Sh = \frac{\beta_i d_{\text{char}}}{D_{\text{mol},i}}, \quad Sc = \frac{\mu_f}{\rho_f D_{\text{mol},i}}. \quad (2.36)$$

In addition to their heat transfer investigations, Giani et al. [86] and later Groppi et al. [97] measured mass transfer coefficients during oxidation of carbon monoxide (CO). Using the same sponges as in their heat transfer study, they proposed  $C_m = 0.91$  and  $m_m = 0.43$  ( $15 \leq Re \leq 200$ ) based on the definition of the dimensionless groups with the strut diameter and the maximal intrinsic velocity. By comparing their correlations for heat and mass

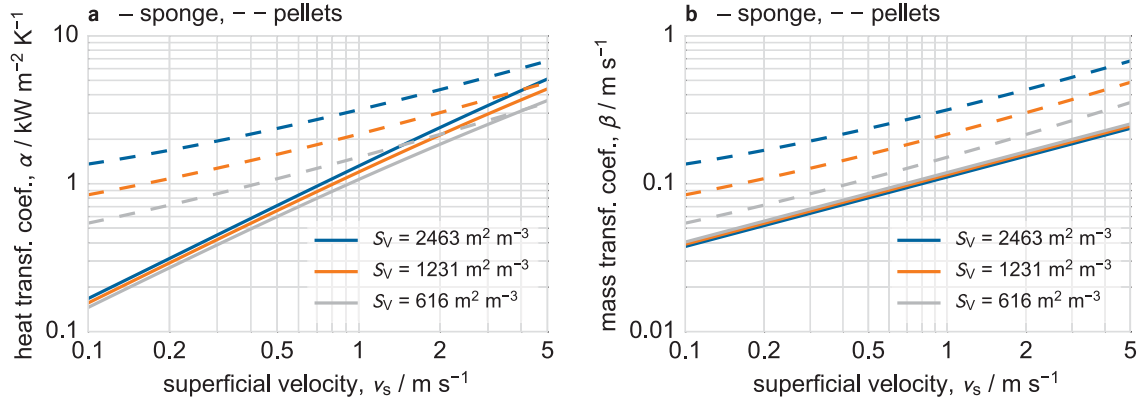


**FIG. 2.14.** Comparison of heat (a) and mass (b) transfer coefficients in solid sponges and packed beds of pellets for different specific surface areas calculated with the models of Dietrich [46] (heat transfer) and Incera Garrido et al. [129] (mass transfer). The (open) porosities of the sponge and pellet bed are 0.8 and 0.4, respectively. The window diameters of the sponges are 0.5 mm, 1 mm and 2 mm; the corresponding pellet diameters (equivalent specific surface area) are 1.5 mm, 2.9 mm and 5.8 mm. The fluid used for the calculations was a 4:1 H<sub>2</sub>/CO<sub>2</sub> mixture at 10 bar and 250 °C.

transfer, they could show that the Chilton-Colburn analogy ( $Nu/Pr^{1/3} = Sh/Sc^{1/3}$ ) is also applicable for solid sponges.

Incera Garrido et al. [129] also used CO oxidation to determine mass transfer coefficients in solid sponges (Al<sub>2</sub>O<sub>3</sub>, stainless steel;  $d_w = 0.69$  mm–2.3 mm;  $\varepsilon_n = 0.75$ –0.85). Their coefficients are  $C_m = C_{geo}$  and  $m_m = 0.47$  for  $7 \leq Re \leq 1100$ , based on the sum of the window and strut diameter as characteristic length. With the introduction of the geometry factor

$$C_{geo} = \left( \frac{d_w + d_s}{1 \text{ mm}} \right)^{0.58} \varepsilon_o^{0.44}. \quad (2.37)$$

they could describe the observed mass transfer coefficients within a 95 % confidence interval. Later, the same authors [128] extended their work to anisotropic sponges by using the semi-diameters  $a$ ,  $b$ , and  $c$  of the elliptic sponge cells in the calculation of the geometry factor resulting in

$$C_{geo} = 0.81 \left( \frac{a^2}{bc} \right)^{0.84} \varepsilon_o^{0.43}. \quad (2.38)$$

### Comparison of solid sponges and packed beds of pellets regarding interfacial heat and mass transfer

In comparison with packed beds, sponges exhibit lower heat transfer coefficients  $\alpha$  at equivalent specific surface areas, especially at low fluid velocities (see Fig. 2.14 a, values determined with Dietrich’s model [46]). Nevertheless, according to Dietrich [46], the heat transfer coefficients in sponges increase faster with increasing velocity than the one in packed beds. At superficial velocities of  $1 \text{ m s}^{-1}$ , heat transfer in sponges is comparable to the one in packed beds for small specific surface areas of  $616 \text{ m}^2 \text{ m}^{-3}$ . The main reason for the lower heat transfer is probably the much lower hydrodynamic dispersion in solid sponges than in packed beds. In addition, the window diameter and the porosity do not affect heat transfer in solid sponges significantly.

The comparison of the mass transfer coefficients  $\beta$  between solid sponges and packed beds of pellets is similar to the comparison of the heat transfer coefficient (see Fig. 2.14 b, values determined with Incerra Garrido's isotropic model [129]). In general, the calculated heat transfer coefficients in solid sponges are lower than the ones in packed beds. The dependency on the velocity, however, is less pronounced in the model of Incerra Garrido et al. [129]. Nevertheless, the window diameter and porosities of the sponges have almost no influence on the mass transfer coefficients.

In conclusion, heat and mass transfer coefficients are on average 2–2.5 times lower in solid sponges than in packed beds of pellets because of less hydrodynamic dispersion and radial mixing. Recalling, however, that the pressure loss along solid sponges is approximately 8 times lower than the one along packed beds, solid sponges show a better tradeoff regarding heat and mass transfer and pressure loss. This is consistent with the measurements of Patcas et al. [213] who compared the performance of packed beds, sponges, and honeycombs during CO-oxidation.

### 2.3.7 Global sensitivity analysis of transport in solid sponges

Based on the review of the available models, it becomes evident that heat and mass transport, pressure loss, and heat and mass transfer in solid sponges can be influenced by carefully adjusting the material, the porosity, and the window size. To find out the most sensitive parameters, and to indicate the tradeoffs between heat and mass transport, pressure loss, and heat and mass transfer, a global sensitivity analysis has been conducted as part of this work using a variance decomposition technique (Sobol method). In contrast to local sensitivities, global sensitivity indices provide a measure of the sensitivity of a quantity on a certain parameter over the whole design space and thus allow a more general analysis. Therefore, several thousand parameter combinations are considered. A detailed description of the technique and illustrative examples are given by Saltelli et al. [243–245] and Zhang et al. [316].

Figure 2.15 shows the results of the global sensitivity analysis in terms of the total sensitivity indices of the radial ETC (a), the radial EDC (b), the pressure loss per unit length (c), and the heat transfer coefficient (d). The used fixed parameters, and the bounds of the design space are summarized in Tab. 2.5. The total sensitivity indices can be interpreted as the relative fraction of the variation of a certain quantity, e. g., the radial ETC, that can be attributed to variations in a specific parameter, e. g., the open porosity. The ranges of the parameters are chosen to represent typical ceramic sponges and operating conditions in heterogeneous catalysis. A summary of the parameter ranges and the fixed parameters is given in Tab. 2.5.

As mentioned in the previous sections, the solid thermal conductivity is the most relevant parameter to change the radial ETC (see Fig. 2.15 a). The sensitivities of the open porosity, the window size, and the fluid velocity, however, are only slightly lower. Consequently, any adjustments of the sponge morphology will likely affect the radial ETC. In addition, the sum of the total sensitivity indices clearly exceeds one (1.37) indicating strong second-order interactions between the parameters. For instance, high solid thermal conductivities and low open porosities lead to extraordinarily high values of the radial ETC. The fluid thermal

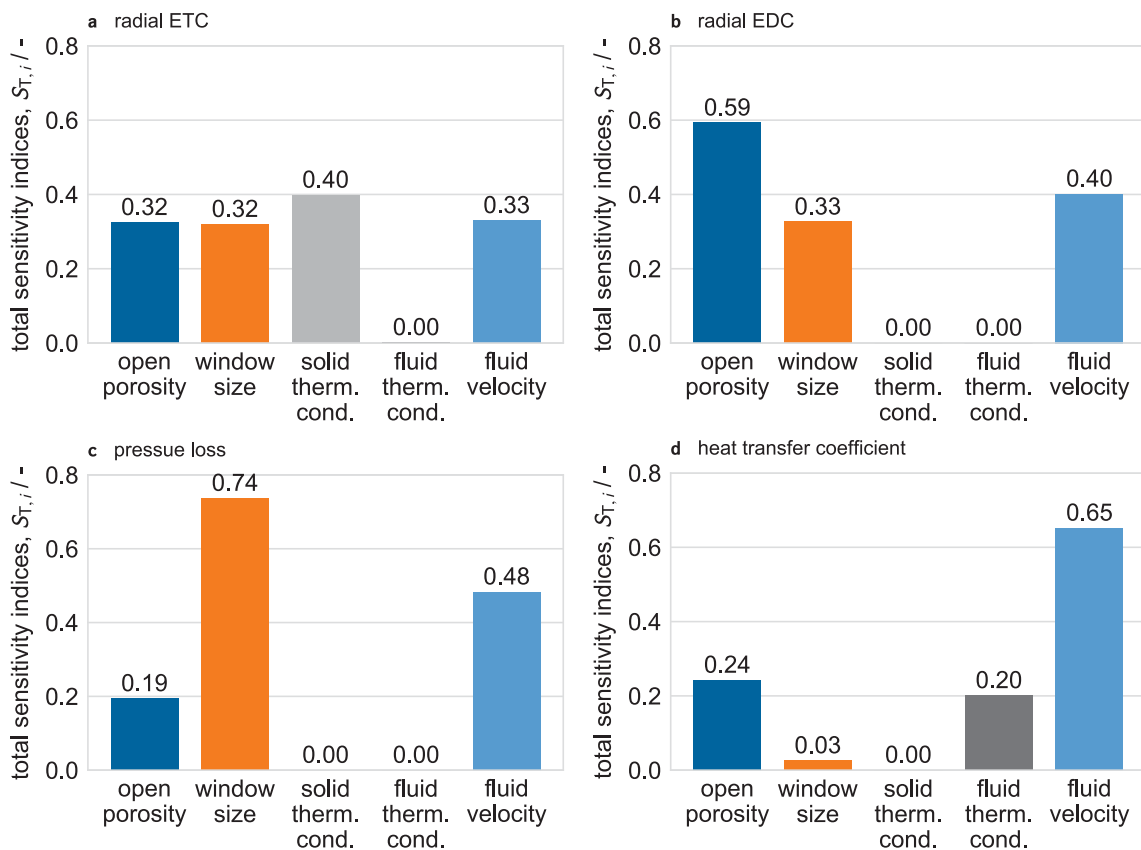


**FIG. 2.15.** Total sensitivity indices for the radial ETC (a), the radial EDC (b), the pressure loss (c), and the heat transfer coefficient (d) in and along solid sponges. The fluid used for the calculations was a 4:1  $H_2/CO_2$  mixture at 10 bar and 300 °C. The radial ETC and EDC were calculated with the model of Fishedick et al. [70], the pressure loss was calculated with the model of Inayat et al. [126], and the heat transfer coefficient was calculated with the model of Dietrich [46]. The base sample size was 10 000. The parameter ranges are given in Tab. 2.5.

conductivity, however, does not have any influence on the effective radial ETC under the considered conditions.

For the radial EDC (see Fig. 2.15 b), the most sensitive parameter is the open porosity because it not only determines the fraction of void space that is available for diffusion, but also the intrinsic fluid velocity that governs hydrodynamic dispersion. In addition, the window size has a significant effect on the mixing length for dispersion and thus influences the radial EDC. Again, the sum of the total sensitivity indices exceeds one (1.32) indicating second-order interactions between the parameters. In general, however, radial mass transport in fixed-bed reactors is of minor relevance for the temperature and conversion profiles as demonstrated by Gräf et al. [95]. They artificially increased the radial EDC by factors of 2 or 5 in their 2-d homogeneous reactor model for catalytic sponges and did not observe changes of the hot-spot temperature, the conversion, or the selectivity.

The pressure loss (here per unit length) is most sensitive to changes of the window diameter, followed by variations of the fluid velocity, and of the open porosity (see Fig. 2.15 c).

Finally, the heat transfer coefficient is most sensitive to changes in the fluid thermal conductivity, the open porosity, and the fluid velocity (see Fig. 2.15 d). Thus, heat transfer in solid sponges can only be controlled to a certain extent by adjustments of sponge

**TAB. 2.5.** Summary of variable and fixed parameters used in the global sensitivity analysis of the transport properties in solid ceramic sponges. The ranges represent typical values of ceramic solid sponges, and operation conditions encountered in heterogeneous catalysis. Except for the fluid thermal conductivity, the fluid properties were calculated for a 4:1 H<sub>2</sub>/CO<sub>2</sub> mixture at 300 °C and 10 bar

Parameter	Unit	Lower bound	Upper bound
<b>(a) Variable parameters</b>			
open porosity	-	0.7	0.95
window diameter	mm	0.2	3
solid thermal conductivity	W m <sup>-1</sup> K <sup>-1</sup>	3	50
fluid thermal conductivity	W m <sup>-1</sup> K <sup>-1</sup>	0.05	0.25
fluid velocity	m s <sup>-1</sup>	0	1
<b>(b) Fixed parameters</b>		<b>Value</b>	
temperature	°C	300	
pressure	bar	10	
fluid density	kg m <sup>-3</sup>	2.19	
fluid viscosity	μPa s	23.7	
fluid specific heat capacity	J kg <sup>-1</sup> K <sup>-1</sup>	3133	

morphology. Nevertheless, it has to be considered that only few studies about heat and mass transfer in solid sponges are available, and that the accuracy of the models is only ±40%. In addition, because of the high sensitivity of the heat transfer coefficient on the fluid velocity, it becomes clear that reliable flow models should be applied when creating correlations for heat and mass transfer coefficients.

Although certain parameters could be identified to be more relevant for adjusting heat and mass transport, pressure loss, and heat and mass transfer, the overall result shows diverse dependencies of the radial ETC, the radial EDC, the pressure loss, and the heat transfer coefficient on the sponge and fluid parameters. Thus, tradeoffs clearly have to be considered in the design of catalytic sponges, and different applications certainly will require different sponge designs.

### 2.3.8 Detailed simulations of fluid flow, heat, and mass transport in solid sponges

Alongside experimental investigations, numerous studies made use of Computational Fluid Dynamics (CFD) to get insight into pressure loss, heat and mass transfer, and heat and mass transport in solid sponges. Therefore, 3-d models of real sponges were created with volume imaging techniques (μCT and MRI, see Section 2.3.2, pp. 19 ff.) to create the necessary computational domains and grids [18–20, 45, 178, 185, 211, 230–232, 312]. In general, the simulations confirmed the experimentally obtained dependencies of the pressure loss [45, 230, 232] and effective thermal conductivity [19, 230, 312] on the window diameter and the porosity. Although, CFD in principle allow insights into local flow patterns (see Fig. 2.16) and their influence on heat and mass transport and transfer, detailed simulations of real structures require high performance computing (HPC) resources and

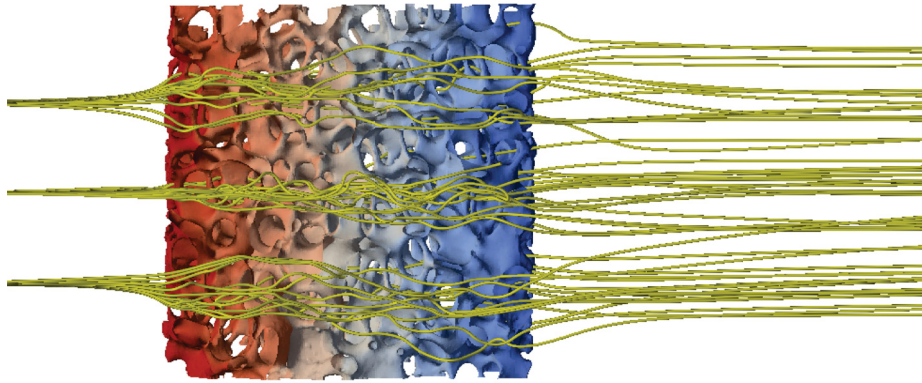


**FIG. 2.16.** Example of a detailed flow simulation in solid sponges using Computational Fluid Dynamics (CFD). The yellow streamlines visualize the tortuous flow in a 20 ppi mullite sponge ( $\varnothing 25 \text{ mm} \times 25 \text{ mm}$ ) for a  $5 \text{ NL min}^{-1}$  flow of air at  $20^\circ \text{C}$  and 1 bar (flow direction left to right). The color of the sponge indicates the pressure along the sponge (red: high pressure; blue: low pressure). For details about the simulation and the analysis of the flow patterns see Appendix D, pp. 149 ff.

expert knowledge. Consequently, the dimensions of monolithic samples are restricted to a few centimeters by the available memory and computer power (see Ranut et al. [230]).

To overcome this problem, researchers used idealized geometries such as tetracaidecahedral or Weaire-Phelan unit cells that can readily be created using computer aided design (CAD) [11, 25, 105, 110, 111, 217, 300, 309]. Horneber et al. [110], however, demonstrated that the use of single unit cells is not sufficient to accurately deduce transport parameters from simulations because in- and outflow effects might have a significant influence. Thus, they proposed to create representative packings of unit cells to describe irregular solid sponges. Because of the regular structure of the packings, however, the pressure loss is up to 20 % lower than the one obtained from simulations with real solid sponges [105, 309]. Recently, Lucci et al. [178] compared the pressure loss and the mass transfer obtained from simulations in real sponges and idealized unit cells. They confirmed lower pressure losses and increased heat and mass transfer in idealized packings than in real sponges. Thus, the deduction of transport parameters from simulations with idealized packings results in too optimistic conclusions regarding pressure loss and heat and mass transfer in real solid sponges.

Of particular interest for solid sponges are the simulation studies of Bianchi et al. [18] and Razza et al. [231] who used CFD to investigate the influence of a possible micrometer-sized gap between the sponge and the tube wall. Based on their results, Bianchi et al. [18] developed an empirical correlation to predict the influence of the gap on the wall heat transfer coefficient and concluded that a tight coupling of the sponge and the tube wall is crucial to exploit the full potential of solid sponges regarding improved heat transport. Later, Razza et al. [231] confirmed the findings of Bianchi et al. [18]. By artificially changing the relative fraction of struts that are in ideal (isothermal) contact with the tube wall, they found that the temperature distribution does not change significantly if more than 20 % of the sponges are in ideal contact with the wall. Thus, for practical applications it is sufficient if only 20 % of the struts are tightly connected to the wall, e. g., by wrapping the sponges with a thermally well conducting foil (see Mülheims et al. [193]).

Another noteworthy study is the work of Meinicke et al. [185] who used CFD in real sponges to distinguish between the fluid and solid temperature, which poses major challenges in experimental setups (see Section 2.3.4). Their determined heat transfer coefficients match well to the experimentally measured values of Dietrich [46]. Thus, detailed flow and conjugate heat transfer simulations are a promising tool to investigate heat and mass transfer phenomena in monolithic sponges, especially close to phase boundaries where experimental methods suffer from insufficient spatial resolution.

### 2.3.9 Solid sponges as catalyst supports

First reviews about early applications of solid sponges as catalyst support were presented by Twigg and Richardson [282] and Carty and Lednor [34] in the 1990s, and later by Reitzmann et al. [234]. The authors concluded that, because of their high porosity, excellent heat transport properties, and thin catalyst coatings, sponges would have the potential to improve catalytic processes that require high throughputs, are operated at high temperature or low pressure, or that suffer from poor diffusional mass transport in and around the catalyst. In particular, they state the oxidation of ammonia, catalytic combustion of hydrocarbons, and steam reforming of methane as promising applications for solid sponges as monolithic catalyst support. Since the early 2000s, researchers applied either ceramic or metallic solid sponges as monolithic catalyst supports to a much wider spectrum of catalytic processes such as dry reforming of methane [215, 235, 301], conversion of methanol to olefins [212], dehydrogenation of ethane to ethylene [55, 200], production of phthalic anhydride [192, 193, 252], oxidation of CO [213] and volatile organic compounds [246], oxidative coupling of methane [174], autothermal reforming of methane [36], Fischer-Tropsch synthesis [162, 176, 209], hydrogenation of benzene [95, 96] and other hydrogenation reactions [164], steam reforming of biogas [239], water-gas shift [206], and methanation of CO [169] and CO<sub>2</sub> [72, 73]. Concurrently, the authors report improved catalytic activity and efficiency [235, 252], improved selectivity [252], a better tradeoff between mass transfer and pressure loss [55, 213], and, most frequently, smoother temperature profiles and lower hot-spot temperatures [36, 96, 162, 169, 174, 192, 206], when using solid sponges compared to packed beds of pellets. The available studies on solid sponges as catalyst support, however, are limited to the lab scale and thus to low flow rates.

#### Experimental studies on catalytic sponges

Among the *experimental studies*, remarkable contributions were presented by Mülheims et al. [193], Mülheims and Kraushaar-Czarnetzki [192], Gräf et al. [95, 96], and Frey et al. [73]. Mülheims et al. [193] investigated the influence of the thermal contact between monolithic sponges and the reactor wall—a major challenge for the implementation of monolithic catalyst supports in industry—on the temperature distribution in solid sponges during production of phthalic anhydride. In total, they compared three cases: first, an approximately 1 mm thick gap of gas between the sponges and the reactor wall, second, sponges wrapped in a glass fiber mat, and third, sponges wrapped in a carbon foil. They found that the outlet temperature was approximately 3 K–7 K lower for sponges wrapped in the thermally well-conducting carbon foil compared to sponges wrapped with the glass fiber mat or sponges not wrapped at all. They attributed the lower outlet temperatures for

sponges wrapped with the carbon foil to the improved thermal contact and thus improved heat transport between the solid sponges and the reactor wall. Since then, wrapping the sponges in a foil with high thermal conductivity has become a standard procedure for the application of solid sponges as catalyst support. In addition, they estimated the fraction of the total flow rate that passes through the gap between the sponges and the reactor wall using a simple flow model. Although the fraction passing through the gap is almost negligible for sponges with a low pore density (10 ppi) or large window diameters, up to 25 % of the total flow rate might pass through the gap for a 30 ppi sponge at  $0.6 \text{ NL min}^{-1}$ , which led to a 30 % relative reduction of the conversion in their experiments. The amount of bypass flows will probably increase at higher flow rates and even smaller window diameters. Consequently, creating a tight contact between solid sponges and the reactor wall is not only necessary regarding effective heat removal, but also to prevent significant bypass flows.

In a followup study, Mülheims and Kraushaar-Czarnetzki [192] measured axial temperature and conversion profiles in packed beds of pellets (egg-shell, steatite) and solid sponges (mullite, SSiC) during production of phthalic anhydride using a multisampling reactor with 7 sampling ports and 15 radially mounted thermocouples, distributed along the reactor axis. With a 1.5 m long catalyst bed ( $\varnothing 20.5 \text{ mm}$ ), the reactor is the largest one used for the investigation of solid sponges as monolithic catalyst supports so far, and is thus closest to pilot and production scale. For a constant phthalic anhydride space-time-yield (STY) of  $25 \text{ kg m}^{-3} \text{ h}^{-1}$  the hot-spot temperature could be reduced from  $427 \text{ }^\circ\text{C}$  in case of the pellets to  $416 \text{ }^\circ\text{C}$  for the mullite sponges and to even  $388 \text{ }^\circ\text{C}$  in case of the SSiC sponges. Although the results clearly indicate smoother temperature profiles and lower hot-spot temperatures in the case of sponges, the comparison is incomplete because of the different solid thermal conductivities considered (steatite pellets:  $3 \text{ W m}^{-1} \text{ K}^{-1}$ ; mullite sponges  $4.4 \text{ W m}^{-1} \text{ K}^{-1}$ ; SSiC sponges  $120 \text{ W m}^{-1} \text{ K}^{-1}$  [192]). In addition, as mentioned by the authors themselves, the wall temperature of the reactor was probably not uniform because of the electrical heating system that does not allow to actively remove heat from the reactor tube. Thus, heat transport limitations within the surroundings of the reactor tube might have influenced the resulting axial temperature profiles within the sponges, and thus prevented a complete comparison of the temperature distribution in the different catalyst supports.

Based on the conclusions of Mülheims and Kraushaar-Czarnetzki [192], Gräf et al. [96] build a dedicated jacketed lab-scale reactor setup (catalyst bed:  $\varnothing 19.2 \text{ mm} \times 150 \text{ mm}$ ) with 15 radially moveable thermocouples and an oil bath to actively cool the reactor, and thus remove heat transport limitations in the surroundings of the reactor tube. In total, the temperature within the catalyst bed could be measured at more than 50 locations because of the radially moveable thermocouples. Due to the upper temperature limit of thermal oils (approx.  $300 \text{ }^\circ\text{C}$ ), they chose the hydrogenation of benzene as model reaction, which can be operated around  $200 \text{ }^\circ\text{C}$ . They found, that in comparison to 6 mm spherical alumina pellets, the maximal temperature in an alumina sponge with total porosity of 0.81 was only 5 K–10 K lower at equivalent operating conditions. The differences between pellets and sponges were hence less impressive than expected from previous studies. Nevertheless, mass transport limitations in the 6 mm pellets certainly limited the reaction and thus the release of heat.

Still, the authors confirmed a strong dependency of the hot-spot temperature in solid sponges on the solid thermal conductivity and the total porosity, and thus concluded that sponges could probably outperform packed beds of pellets if a material with high thermal conductivity is chosen and the total porosity is designed to balance heat transport and pressure loss.

In a followup study, Gräf et al. [95] used a 2-d homogeneous reactor model to obtain insight into heat and mass transport in solid sponges during hydrogenation of benzene. They fitted their simulated temperature profiles to measured ones to determine the axial and radial ETC, and thus to calibrate their model. With the calibrated model, they confirmed the potential of materials with high thermal conductivity (SSiC, Al) to improve heat transport in solid sponges and thus decrease hot-spot temperatures by about 30 K for the investigated lab-scale experiments.

In addition, Gräf et al. [96] demonstrated the difficulties of accurately measuring temperatures in catalytic sponges with radially mounted thermocouples. The thermocouples will overdetermine the temperature if they are inserted beyond the centerline of the reactor because of thermal conduction in the sheath of the thermocouples from the centerline (hottest point) to the tip of the thermocouple. Accordingly, the thermocouples will underdetermine the temperature if they measure the temperature between the centerline and the cooled reactor wall, because of thermal conduction in the sheath from the tip of the thermocouple to the cooled wall. Thus, Gräf et al. [96] proposed to average temperatures at equivalent radial positions that are measured beyond the centerline and in front of the centerline. In addition, the thermocouples should have a small diameter (e. g. 0.5 mm) to decrease thermal conduction in the sheath, and to increase heat transfer from the gas phase to the thermocouple itself. Nevertheless, thin thermocouples bend and break easily and hence are difficult to position accurately. Consequently, a compromise between accuracy and robustness has to be made when designing reactor setups to investigate temperature distributions in catalyst packings.

Recently, Frey et al. [73] used an infrared (IR) camera to measure the surface temperature of  $\text{Al}_2\text{O}_3$ , SSiC, and Al sponge plates ( $50\text{ mm} \times 50\text{ mm} \times 5\text{ mm}$ ) during methanation of  $\text{CO}_2$  at  $220^\circ\text{C}$ . The authors evaluated the different sponges by the cumulated temperature increase normalized to the amount of heat generated by the reaction. They found that the SSiC sample ( $0.11\text{ K W}^{-1}$ ) showed a lower temperature increase than  $\text{Al}_2\text{O}_3$  ( $2.3\text{ K W}^{-1}$ ) and Al ( $1.7\text{ K W}^{-1}$ ). While the difference between SSiC and  $\text{Al}_2\text{O}_3$  is consistent with the different solid thermal conductivities of the materials, the poor performance of Al was attributed to the unfavorable influence of the ceria-zirconia washcoat and the preceding heat treatment on the solid thermal conductivity of the Al sponge. Although the authors concluded that further studies are needed to improve the experimental technique, it has the potential to solve the issues related to the temperature measurement with conventional thermocouples (see above and Gräf et al. [96]). In addition, it explicitly allows the measurement of the solid temperature which is necessary for the determination of heat transfer coefficients in solid sponges. If the technique is combined with optical fibers with low thermal conductivity, it will not only be able to measure the solid temperature at the outer surface of the sponge, but also inside catalytic sponges.

## Simulation-based studies on catalytic sponges

In contrast to the numerous experimental studies, only few *simulation-based studies* on catalytic sponges are available. Reitzmann et al. [233] conducted some of the first numerical simulations of temperature and concentration distributions in solid sponges during the production of phthalic anhydride using a 2-d pseudo-homogeneous reactor model. Their results indicate that the STY of phthalic anhydride could be doubled from  $247 \text{ kg m}^{-3} \text{ h}^{-1}$  (egg-shell pellets) to  $545 \text{ kg m}^{-3} \text{ h}^{-1}$  (sponges) by exploiting the effective heat transport properties and the high porosity and thus low pressure losses of solid sponges. Nevertheless, due to the lack of validated heat and mass transport models for solid sponges at that time, the simulations were in part based on heat and mass transport models that were originally developed for packed beds of pellets. Consequently, the presented simulations for the sponges did probably not capture heat and mass transport in solid sponges accurately.

Another simulation study on solid sponges as catalyst support was presented by Philippe et al. [223], who simulated the performance of solid sponges and packed beds of pellets for Fischer-Tropsch synthesis using a 2-d pseudo-homogeneous reactor model. In order to estimate the radial ETC of the sponges, they used the model of Singh and Kasana [262] that was, however, developed for Al sponges with total porosities above 0.9. For the radial ETC of the packed bed of pellets, they used the well established models of Tsotsas [280] and Winterberg et al. [305]. The authors concluded that the solid thermal conductivity is the most important parameter to influence the temperature distribution in solid sponges and thus control the product distribution in the Fischer-Tropsch process at low gas velocities. At high gas velocities around  $0.5 \text{ m s}^{-1}$ , which are typical in industrial reactors, the type and structure of the support however would be almost negligible because of the high amount of radial dispersion. In addition they concluded that the smoother temperature profiles in solid sponges compared to the ones in packed beds of pellets are probably not only caused by the improved heat transport properties of the sponges, but also by the dilution of the catalyst due to the high void fraction of the sponges. Consequently, a compromise between a high ETC and a high catalyst density would have to be considered when tuning solid sponges for catalytic applications. A detailed analysis of the tradeoff, however, is not available yet.

## Unconventional applications of solid sponges in catalysis

Alongside the application of solid sponges as monolithic catalyst support, Visconti et al. [294] and Kolaczkowski et al. [150] presented unconventional applications of solid sponges for catalytic applications. Visconti et al. [294] proposed *packed solid sponges* in which the voids of the (uncoated) solid sponge are filled with small spherical catalyst pellets to increase the bulk catalyst density. First preliminary results indicate that the excellent heat transport properties of solid sponges can be maintained to a large extent. The pressure loss, however, is obviously in the same order of magnitude as the pressure loss of packed beds of pellets. Nevertheless, the authors conclude that packed sponges would be an interesting option if compact reactors and effective heat removal is required. Anyway, more research on packed sponges is necessary to obtain a complete picture about their heat and mass transport properties during catalytic applications.

Instead of using pellets or extrudates, Kolaczowski et al. [150] used cubic metal sponges (10 mm edge length, FeCrAlloy®) to create randomly packed beds. The random sponge packings promise high catalyst efficiencies and low pressure drops because of thin catalyst coatings and high porosities of the individual sponge bodies. In contrast to monolithic applications, however, heat transport within the packed bed can only occur via thermal conduction through point contact between the individual sponge bodies and through hydrodynamic dispersion. The latter, however, is less pronounced in random sponge packings than in packed beds of pellets because of the high porosity of the sponge bodies. Consequently, radial heat transport might even be worse than in packed bed of pellets, and the success of packed beds of sponges is questionable for highly exo- or endothermic processes. Again, more research is required to make a fair judgement.

### Other monolithic catalyst support

Besides solid sponges, other monolithic structures such as ceramic and metallic honeycombs [8, 55, 79, 189, 213, 247, 254, 278] and cross-flow structures [138, 251, 292, 293] have been investigated as alternative catalyst supports. In contrast to the irregular morphology of solid sponges, honeycombs feature a well defined regular morphology that consists of parallel straight channels. Thus, the pressure loss along honeycombs is even lower than the one along solid sponges. Nevertheless, radial mixing and heat and mass transfer in honeycombs is typically less pronounced because of laminar flow in the parallel channels. In addition, unless thick walls between the channels are used, heat transport in honeycombs is usually worse than in solid sponges.

Alike honeycombs, cross-flow structures consist of angled parallel channels that direct the fluid flow to the reactor wall to improve radial heat transport. Thus, they can be interpreted as angled honeycombs. Because of the zig-zag flow pattern, the pressure loss along cross-flow structures is slightly higher than that along honeycombs, however, convective heat transport is improved significantly. Anyways, only few studies on cross-flow structures are available.

**TAB. 2.6.** Qualitative comparison of pellet beds, solid sponges, and honeycombs regarding their potential as catalyst supports; adapted and extended from [94].

Feature	Pellet beds	Solid sponges	Honeycombs
porosity	0.35–0.45	0.7–0.95	0.7–0.8
radial dispersion	high	moderate	no <sup>a</sup>
bulk catalyst density	high	moderate–low	low
effectiveness factors	moderate–low	high	high
pressure drop	high	moderate–low	low
heat and mass transfer <sup>b</sup>	high–moderate	high–moderate	low
radial heat transport <sup>c</sup>	high–moderate <sup>d</sup>	high–moderate <sup>e</sup>	high–low <sup>e</sup>
technological maturity	commercial (TRL <sup>f</sup> 9)	research & development (TRL <sup>f</sup> 2–4)	research & development <sup>g</sup> (TRL <sup>f</sup> 2–4), commercial <sup>h</sup> (TRL <sup>f</sup> 9)

<sup>a</sup> can be incorporated by special perforated metal structures (see [157])    <sup>b</sup> transfer between fluid and solid phase    <sup>c</sup> includes conduction, dispersion, and radiation    <sup>d</sup> strongly depends on fluid velocity    <sup>e</sup> strongly depends on solid material (ceramic vs. metal)    <sup>f</sup> Technology Readiness Level (see for example [64, 131])    <sup>g</sup> production of chemicals    <sup>h</sup> exhaust gas treatment

A qualitative comparison between pellet beds, solid sponges, and honeycombs regarding their application as catalyst support is shown in Tab. 2.6. Accordingly, solid sponges can be classified in between randomly packed beds of pellets and honeycombs. They combine the radial mixing of packed beds of pellets with the high effectiveness factors and high porosities, and thus low pressure losses, of honeycombs, and therefore probably provide the best compromise between both extremes, at least for certain applications. Nevertheless, solid sponges and honeycombs suffer from a low bulk catalyst densities. Consequently, it is crucial to further explore the tradeoffs between high bulk catalyst densities, high ETC, high heat and mass transfer, and low pressure losses, that have to be made when tailoring the porosity and window diameters of solid sponges.

### 2.3.10 Additive manufacturing of monolithic catalyst supports – a recent trend

Driven by the promising performance of monolithic sponge catalysts in lab-scale chemical reactors, researchers and engineers recently started to apply *additive manufacturing techniques* such as 3-d printing [9, 165, 317], 3-d fiber deposition (3DFD) [39, 40, 224], selective laser sintering (SLS) [61, 116–118, 224], and selective electron beam melting (SEBM) [21, 107, 127, 148, 149, 221] to create novel regular catalyst supports. Because of their regular periodic morphology, Schwieger, Freund, and their coworkers [21, 127, 148, 149, 165, 221] coined the term *periodic open cellular structures* (POCS) for the new type of monolithic catalyst supports.

POCS (see Fig. 2.17) consist of regularly arranged unit cells, such as the well-known tetrakaidecahedral or Kelvin unit cells [127, 165], cubic unit cells [40, 148], diamond unit cells [165], or even combinations thereof [165]. Depending on the manufacturing technique, POCS can be made out of polymers, e. g., acrylonitrile butadiene styrene (ABS [165]), metals (stainless steel [40], Ti-6Al-4V [127, 148, 221]), or zeolithes (ZSM-5 [39]). Up to today,

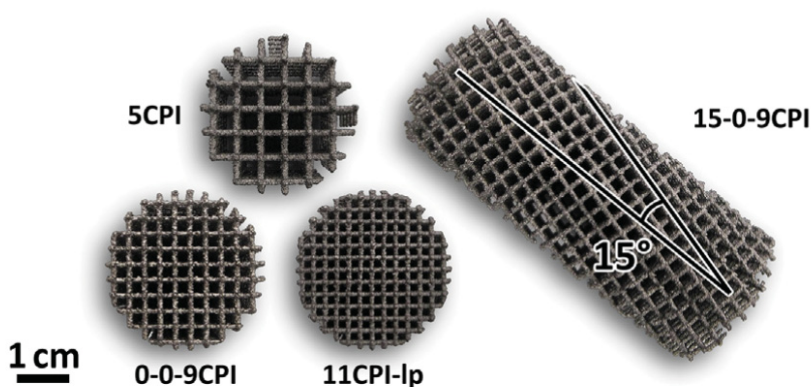


**FIG. 2.17.** Examples of periodic open cellular structures (POCS) with ideal cubic unit cell geometry and 5 cpi, 9 cpi and 11 cpi (cells per inch) made out of Ti-6Al-4V via SEBM (see [148]). Reprinted from Chemical Engineering Journal, 242, M. Klumpp, A. Inayat, J. Schwerdtfeger, C. Körner, R.F. Singer, H. Freund, W. Schwieger, “Periodic open cellular structures with ideal cubic cell geometry: Effect of porosity and cell orientation on pressure drop behavior”, 364–378, Copyright (2014), with permission from Elsevier.

POCS with outer dimensions in the centimeter-range have been successfully produced and applied, e. g.,  $\varnothing 10 \text{ cm} \times 10 \text{ cm}$  [165].

Like honeycombs, POCS feature a well-defined geometry but still allow for radial mixing through the interconnected cells as in solid sponges. Consequently, they can be classified in between solid sponges and honeycombs (see Tab. 2.6). While the regular geometry guarantees low pressure losses as in honeycombs, the dispersive flow pattern increases heat and mass transfer between the solid to the fluid phase like in solid sponges. In addition, the high effective thermal conductivity of monolithic solid sponges is preserved by the continuous solid phase.

Remarkable studies on the use of additive manufacturing for catalytic applications were presented by Klumpp et al. [148], Lämmermann et al. [165], and Peters et al. [221]. Klumpp et al. [148] produced metallic POCS with cubic unit cells using SEBM to investigate the pressure loss along these structures. Moreover, they conducted a thorough geometric characterization of the produced POCS using  $\mu\text{CT}$  (see Section 2.3.2, pp. 19 ff.). Compared to the original computer aided design (CAD) of the POCS, the measured values of the porosity, the window and strut diameters, and the specific surface area deviated by less than 13 %. The deviations were probably caused by shrinkage and sintering during the SEBM process. The results demonstrate that additive manufacturing techniques are already able to produce POCS with reasonable accuracy, that will likely be improved as the techniques mature in the near future.

Lämmermann et al. [165] produced POCS made out of ABS using a 3-d printing technique called fused deposition modeling (FDM). They investigated the radial distribution of liquids in Kelvin- and diamond-cell-based POCS, and found that Kelvin-cell-based POCS tend to direct the initially uniformly distributed liquid to the outer wall, while diamond-cell-based POCS direct the liquid to the center of the cylindrical structures. Consequently, an alternating stacking of Kelvin- and diamond-cell-based POCS would lead to a more uniform radial distribution of the liquid along the height of a column. In addition, they fully exploited the freedom of additive manufacturing techniques regarding design and developed a new unit cell that combines the Kelvin unit cell and the diamond unit cell. Indeed, POCS based on the new unit cell also lead to a more uniform distribution of the liquid. The results clearly illustrate, first, the potential of additive manufacturing techniques to tailor monolithic structures towards a specific goal or application, and second, the potential for process intensification due to the design *on a local scale*.

Furthermore, Lämmermann et al. [165] directly printed a solid wall around their POCS to avoid liquid bypass streams. For their Kelvin-cell-based POCS, they obtained a more uniform radial liquid distribution in the structure with the added wall than in the Kelvin-cell-based structure without the added wall. Peters et al. [221] also added a wall around their Ti-alloy POCS manufactured by SEBM to produce a full reactor tube with additive manufacturing. They demonstrated that the manufactured reactor tube can be mechanically post-processed after the SEBM process by conventional techniques, e. g., to finish the outer surface of the reactor tube and to add threads and other features to insert sensors or draw samples. Adding a solid wall directly to the catalyst structures could solve the problem of creating a good thermal contact between the monolithic catalyst and the reactor tube

(see [193]). Nevertheless, it has to be checked whether the added walls are sufficiently impermeable for the reactants and products, and whether they provide enough stability to be operated at moderate and high pressures.

Recently, Zhou and Liu [317] reviewed additive manufacturing techniques and their application to produce monolithic catalyst supports. In addition to the above mentioned advantages, they concluded that existing additive manufacturing techniques still require an improved control of the resulting micro- and mesostructure, a more diverse feedstock of materials, and advanced catalyst design to exploit their full potential. Moreover, the outer dimensions of the final samples have probably to be increased, and affordable production at medium to large scales has to be demonstrated. Nevertheless, BASF [13], the world's largest chemical company, just announced its start of a new group company especially committed to 3-d printing, which will certainly boost additive manufacturing techniques in the chemical industry.

Consequently, additive manufacturing techniques have the potential to gain almost full control over the morphology of monolithic catalyst supports and remove the drawbacks of the irregular morphology of solid sponges, such as the requirement of intensive geometric characterization and relatively large uncertainties in the modeling of effective transport parameters. Nevertheless, more research on additive manufacturing techniques in general, and on tailoring monolithic catalyst supports in particular is necessary to successfully develop next-generation catalyst supports based on POCS.

### 2.3.11 Summary and concluding remarks

The above review of the characterization, heat and mass transport, pressure loss, heat and mass transfer, and of applications of solid sponges of catalyst support shows that intensive research on solid sponges has been conducted in the last 20 years. Today, solid sponges can be mass produced and the techniques for characterization have been developed and are, except for volume imaging techniques, available in most laboratories. In addition, heat transport and pressure loss in solid sponges can be calculated to a certain accuracy using pseudo-homogeneous models. Furthermore, solid sponges have been successfully applied as catalyst support in lab- and bench-scale setups, and first comparisons against conventional packed beds of pellets show promising results regarding lower hot-spot temperatures and comparable space-time yields and selectivities.

Nevertheless, models to calculate mass transport in solid sponges are still scarce and lack experimental validation. Moreover, little is known about heat transfer in solid sponges although it might lead to severe limitations at low fluid velocities, which are usually applied in lab- and bench-scale setups. Additionally, a thorough comparison of catalytic sponges and packed beds of pellets at the production scale is still missing to evaluate whether solid sponges can indeed outperform packed beds of pellets in production-scale chemical reactors.



## 3.1 Morphological characterization of the investigated solid sponges

The solid sponges investigated experimentally in this work were commercially manufactured by Hofman Ceramics GmbH (Breitscheid, Germany) using the well-established Schwarzwald replica process [260]. The cylindrical samples ( $\varnothing 25\text{ mm} \times 25\text{ mm}$ ) consist of mullite ( $\text{Al}_2\text{O}_3\text{-SiO}_2$ , approx. 85 wt%  $\text{Al}_2\text{O}_3$ ) and were sintered at  $1300\text{ }^\circ\text{C}$ . In total, four different sponge types with different pore densities ranging from 10 ppi–40 ppi were available (see Fig. 3.1 a). Although the pore density does not describe the real window and cell diameters accurately, it is used in this work as a label to identify the different solid sponges.

The diameter, height, and mass of the custom-sized cylindrical samples were each measured three times for 12 randomly picked sponges of each pore density using a standard caliper and a lab balance, respectively. The open porosity, window size distribution (area-equivalent circle) and specific surface area of one sample of each pore density were measured using X-ray absorption micro computer tomography ( $\mu\text{CT}$ , see Section 2.3.2, pp. 19 ff.) with an isotropic resolution of  $35\text{ }\mu\text{m}$ . In addition, three replicate measurements were performed for the 30 ppi sponge using different samples. For the 10 ppi sponge, the strut diameter was also determined from the  $\mu\text{CT}$  data. The  $\mu\text{CT}$  measurements and the

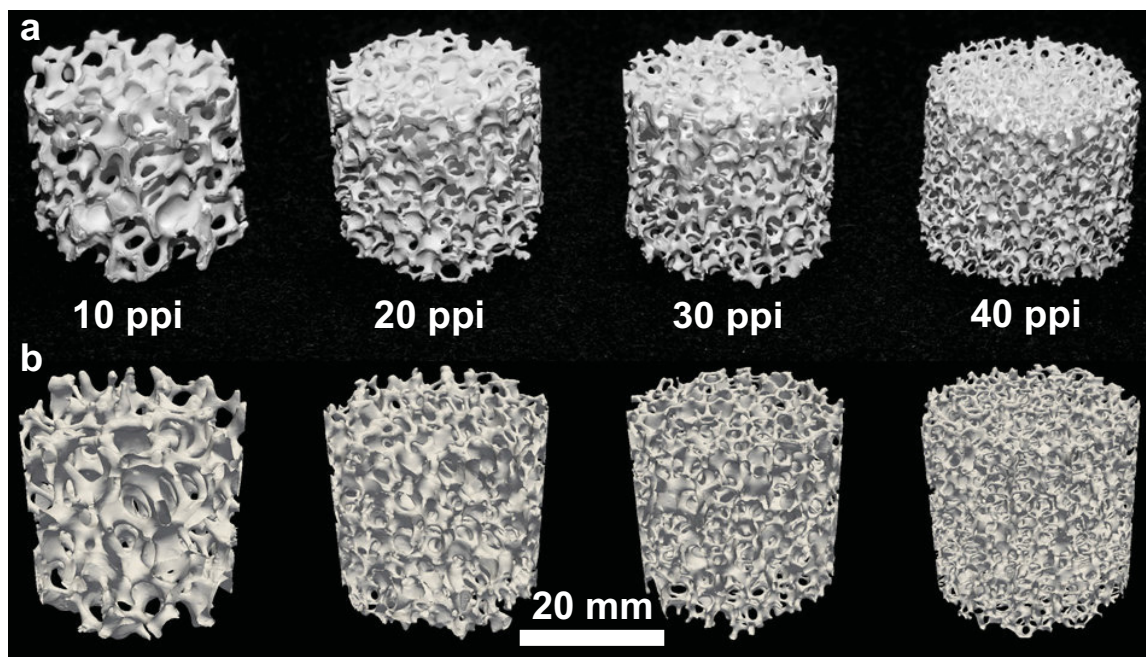


**FIG. 3.1.** Investigated mullite sponges ( $\varnothing 25\text{ mm} \times 25\text{ mm}$ ) with decreasing window diameter from left to right (a), and the corresponding 3-d models obtained from  $\mu\text{CT}$  (b).

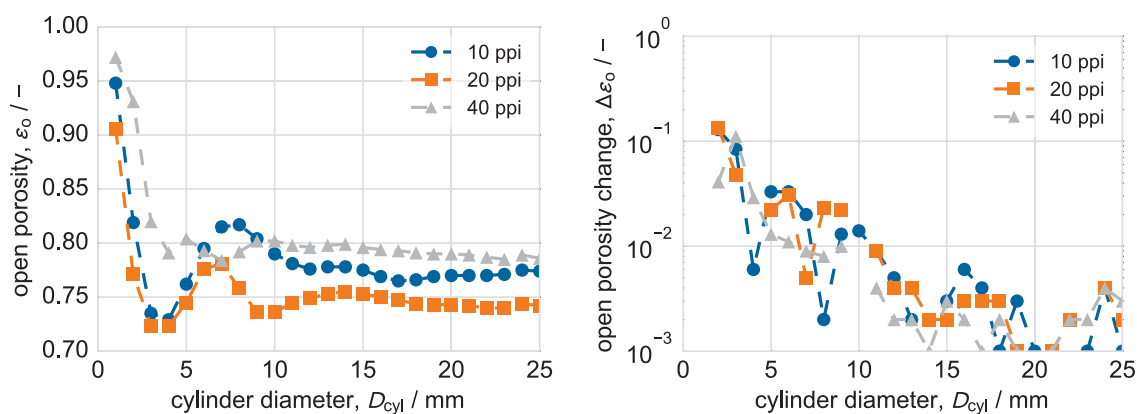


**FIG. 3.2.** Absolute (a) and relative (b) change of the average open porosity with increasing diameter of a cylindrical volume element placed in the center of the 3-d  $\mu$ CT-model ( $H_{cyl}=D_{cyl}$ ). The diameters of the representative volume element (RVE,  $\Delta\varepsilon_0 \leq 10^{-2}$ ) are 11 mm, 10 mm, and 7 mm for the 10 ppi, 20 ppi, and 40 ppi samples.

evaluation of the data was performed in cooperation with the Chair of Magnetofluidynamics, Measurement, and Automation Technology (Prof. Odenbach) at the Technische Universität Dresden, Germany.

For verification of the  $\mu$ CT analysis, the total and open porosity were determined from gravimetric techniques (see Section 2.3.2, pp. 19 ff.) and calculated using Eqns. (2.9) and (2.10). Additionally, the average window diameter (area-equivalent circle) was estimated from microscopic images using at least 19 windows that were parallel to the observation plane.

### Results of the morphological characterization of the solid sponges

Using the 3-d models obtained from  $\mu$ CT, the size of the representative volume element (RVE) of each pore density can be determined. Therefore, cylindrical volumes ( $H_{cyl}=D_{cyl}$ ) with increasing diameter were selected from the center of the 3-d  $\mu$ CT-models, and the open porosity was averaged over the corresponding volume (see Fig. 3.2 a). After initial oscillations for small element diameters, the average open porosity of the cylindrical element volumes for 10 ppi, 20 ppi and 40 ppi converges to 0.77, 0.75, and 0.79 with increasing diameter. The diameters of the cylindrical RVE for the 10 ppi, 20 ppi, and 40 ppi samples ( $\Delta\varepsilon_0 \leq 10^{-2}$ ) are 11 mm, 10 mm, and 7 mm, respectively (see Fig. 3.2 b). Consequently, the 25 mm sponge samples are representative for the available pore densities. The open porosities ranging from 0.75–0.79 lie in the lower range of open porosities reported for ceramic solid sponges (see Fig. 2.5 a, p. 20).

The distributions of the window size (area-equivalent circle) obtained from the  $\mu$ CT analysis, and the corresponding fits (normal distribution) are shown in Fig. 3.3. With increasing pore count, the average window diameter decreases from 3.3 mm for the 10 ppi samples to 1.43 mm in case of the 40 ppi samples. Nevertheless, the samples with a pore density of 20 ppi and 30 ppi exhibit similar window size distributions. In general, the relative standard deviation of the window sizes is consistently between 24%–27% for all the investigated pore densities. Thus as a rule of thumb, a 25% variation of the geometrical properties of solid sponges manufactured by the replica method can be assumed, at least

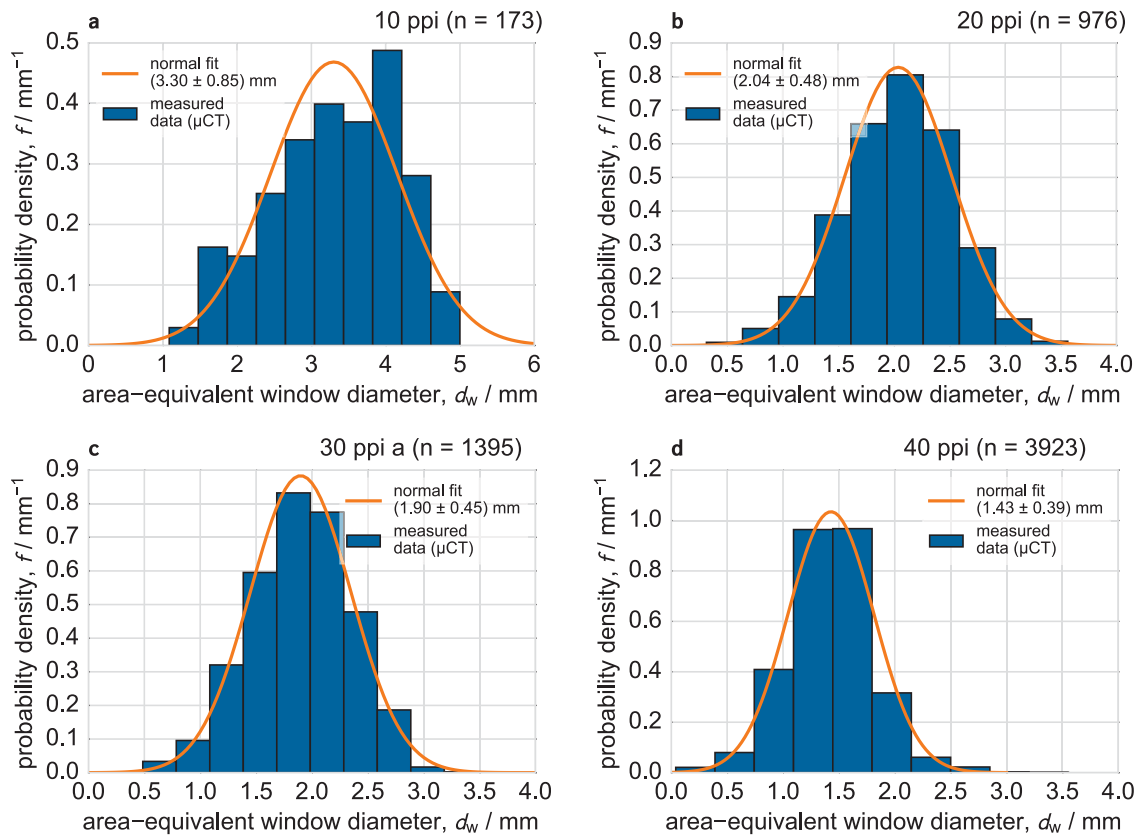


**FIG. 3.3.** Measured window size distributions from the  $\mu$ CT data and fitted normal distributions for the 10 ppi (a), 20 ppi (b), 30 ppi (c), and 40 ppi (d) sponges.

for this batch. In addition, the window size distribution of the 10 ppi samples does not resemble a symmetrical bell curve for a sample size of 173 windows. Thus, with the given variations induced by the manufacturing process, a high number of windows has to be considered to accurately determine the average window diameter.

Although the window diameter varies up to approximately 25% within the sponges, the variations among different samples of a certain pore density (here 30 ppi) were remarkably small (see Fig. 3.4 a). For the three randomly selected samples, the deviations of the average window diameter was only around 1%. Furthermore, the standard deviations agree within less than 1%. A relative accuracy of 10% of the  $\mu$ CT results because of discretization errors, however, has to be considered in this comparison. Nevertheless, the good match of determined average window diameters among different samples with the same pore density indicates that ceramic solid sponges can be mass produced with constant quality.

Finally, the measured specific surface area was compared to the values obtained with the Kelvin-unit-cell model of Inayat et al. [124] (see Section 2.3.3, pp. 24 ff.) for different strut shapes (see Fig. 3.4 b, p. 60). Although, the investigated sponges exhibited a circular strut cross section (see Fig. 2.4, p. 20), the measured values of the specific surface area matched better to the model predictions for a triangular strut cross section. A possible reason might be errors in the calculation of the specific surface area from the  $\mu$ CT data because of voxelization. Assuming a 2-d square pixel of side length  $a$ , the diagonal is  $\sqrt{2}a$ . Hence, the ratio of the length of the diagonal and the outer perimeter around the half pixel

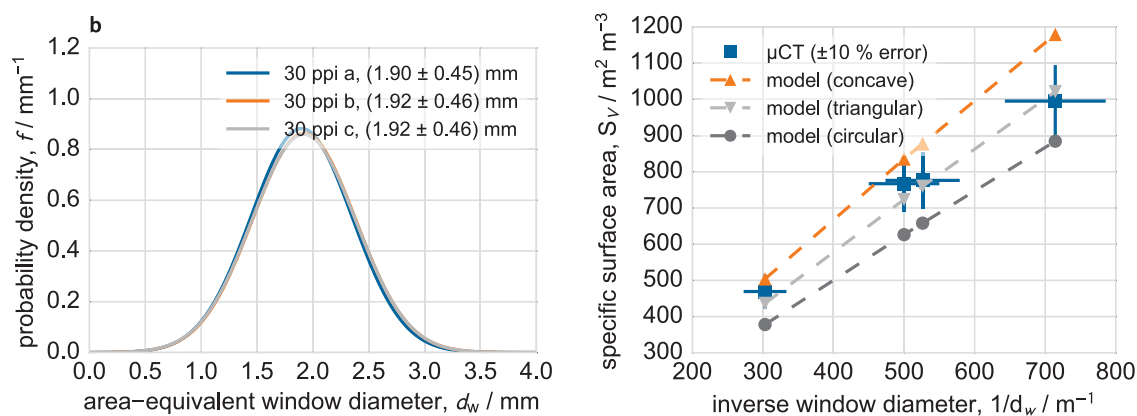


**FIG. 3.4.** Comparison of the determined window size distributions of three randomly chosen 30 ppi sponges (a), and comparison of measured and calculated specific surface areas of the investigated sponges using the Kelvin-unit-cell model of Inayat et al. [125] for different strut shapes (see Section 2.3.2, pp. 23 ff.). The error of the  $\mu\text{CT}$ -measurements is estimated to be 10 %.

(2a) is  $\sqrt{2}/2 \approx 0.71$ . Multiplication of the measured values of the specific surface area by 0.71 yields  $370 \text{ m}^2 \text{ m}^{-3}$ ,  $605 \text{ m}^2 \text{ m}^{-3}$ ,  $613 \text{ m}^2 \text{ m}^{-3}$  and  $785 \text{ m}^2 \text{ m}^{-3}$  for the 10 ppi, 20 ppi, 30 ppi and 40 ppi samples, which matches well with the model predictions (see Tab. 3.1). Nevertheless, the Kelvin-unit-cell model is also only accurate within  $\pm 10\%$ .

All results from the morphological characterization of the solid sponges are summarized in Tab. 3.1. In comparison, the open porosities determined from the  $\mu\text{CT}$  characterization and the gravimetric analysis match remarkably well. Contrarily, the average window diameters measured with light microscopy are consistently smaller than the ones obtained from  $\mu\text{CT}$ , probably because only a few windows were accessible to incident light microscopy. In addition, alignment errors of the measured windows and the observation plane always lead to an underestimation of the window diameter. Finally, the strut diameter obtained from the  $\mu\text{CT}$  data for the 10 ppi samples matches reasonably well with the model predictions

**TAB. 3.1.** Morphological properties of the investigated sponges obtained with different techniques (see footnotes). Values in parentheses are given for comparison and were not used in the simulations of this work.

Sample	Mass g	Porosity total <sup>a</sup> /open <sup>b</sup> -	Window diameter <sup>b</sup> mm	Strut diameter <sup>c</sup> mm	Surface area <sup>b</sup> $\text{m}^2 \text{ m}^{-3}$
10 ppi	$5.6 \pm 0.1$	$0.86 / 0.77$ / $(0.79)^a$	$3.30 \pm 0.98$ $(2.73 \pm 0.66)^d$	1.83 $(1.4 \pm 0.5)^b$	521 $(378)^c$
20 ppi	$6.1 \pm 0.0$	$0.85 / 0.75$ / $(0.75)^a$	$2.04 \pm 0.48$ $(1.35 \pm 0.25)^d$	1.22	852 $(614)^c$
30 ppi	$5.8 \pm 0.0$	$0.85 / 0.76$ / $(0.77)^a$	$1.92 \pm 0.46$ $(1.53 \pm 0.22)^d$	1.11	863 $(651)^c$
40 ppi	$5.3 \pm 0.1$	$0.86 / 0.79$ / $(0.80)^a$	$1.43 \pm 0.39$ $(1.01 \pm 0.22)^d$	0.73	1106 $(866)^c$

<sup>a</sup> gravimetric analysis (see Section 2.3.2, pp. 19 ff.)    <sup>b</sup>  $\mu\text{CT}$  (approx. 10 % relative error)

<sup>c</sup> tetrakaidehedral unit cell model (see [125])    <sup>d</sup> incident light microscopy

of the Kelvin-unit-cell model considering the large variations of the struts within a single sample.

## 3.2 Synthesis, application, and characterization of the catalytic coating

### 3.2.1 Catalyst synthesis and coating procedure

In order to use the solid sponges as catalysts, they were coated with a thin 5 wt% Ni/Al<sub>2</sub>O<sub>3</sub> mesoporous catalyst layer (see Fig. 3.5). Therefore, 5.5 g nickel(II) nitrate hexahydrate (Ni(NO<sub>3</sub>)<sub>2</sub> · 6H<sub>2</sub>O, VWR Prolabo®) were dissolved in 16 mL distilled water, and mixed with 50 g of an aqueous suspension containing 40 wt%  $\gamma$ -Al<sub>2</sub>O<sub>3</sub> (BASF Catalysts Germany GmbH, Nienburg/Weser, Germany). Subsequently, five samples of the 10 ppi, 20 ppi, and 40 ppi sponges were completely dipped into the suspension one by one, drawn out, and residue of the suspension was removed with pressurised air in order to avoid blocked windows. Afterwards, the coated sponges were dried in air at 120 °C for 30 min (heating rate 3 K min<sup>-1</sup> from room temperature) and calcined at 600 °C for 3 h (heating rate 1.6 K min<sup>-1</sup>). After calcination, the coated sponges cooled down to room temperature within the oven.

A fraction of the the remaining catalyst suspension was poured into a crucible to form a thin layer that was dried and calcined together with the coated sponges. Afterwards, the catalyst layer in the crucible was crushed to obtain a powder with identical micro- and mesostructure as the catalyst layer on the sponges for subsequent characterization (see Section 3.2.2, pp. 61 ff.) and determination of the kinetic parameters for CO<sub>2</sub>-methanation (see Section 3.3, pp. 64 ff.).

### 3.2.2 Characterization of the catalyst and the catalytic layer

In addition to the thickness of the catalyst layer, the meso-structure of the catalyst significantly influences mass transport and thus the effectiveness factors during operation.

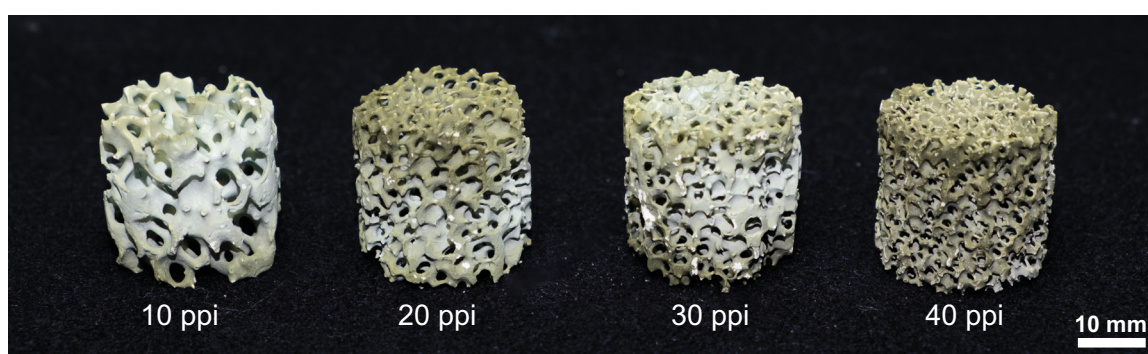


**FIG. 3.5.** Catalytic sponges with decreasing window size from left to right after application of the catalytic coating, drying, and calcination. The greenish color indicates the presence of nickel oxide that was reduced to metallic nickel during the initial reduction procedure. Some windows were already blocked during the manufacturing of the sponges.

**TAB. 3.2.** Properties of the mesoporous catalyst powder obtained with different techniques. For comparison, reference values from other studies on Ni-based methanation catalyst are listed as well.

Technique, Reference	Apparent density $\text{g cm}^{-3}$	Open porosity $\text{cm}^3 \text{cm}^{-3}$	Pore diameter nm	Specific surface area $\text{m}^2 \text{g}^{-1}$
N <sub>2</sub> -adsorption	-	-	13.8	163
Hg-intrusion	3.22	0.71	10.8	147
He-pycnometry	3.18	-	-	-
	3.21	-	-	-
Xu and Froment [308] <sup>a</sup>	-	0.53	16	145
Zhang et al. [315] <sup>b</sup>	3.12	-	-	131
Koschany et al. [154]	2.3	-	-	235
Martinez Molina et al. [182] <sup>c</sup>	-	-	7	184

<sup>a</sup> commercial steam-reforming catalyst    <sup>b</sup> commercial methanation catalyst

<sup>c</sup> commercial methanation catalyst (NiSAT® 310 RS by Clariant)

Hence, the porosity and the average pore diameter have to be determined experimentally to accurately simulate mass transport within the mesoporous catalyst layer.

### Characterization of the catalyst

For the characterization of the catalyst, nitrogen-adsorption (N<sub>2</sub>-adsorption), mercury-intrusion (Hg-intrusion), and helium-pycnometry (He-adsorption) were applied to individual samples of the catalyst powder that has been specifically produced for characterization. The results for the apparent density, the open porosity, the average pore diameter, and the specific surface area of the catalyst are summarized in Tab. 3.2. For comparison, reference values of Ni-based methanation catalysts from other studies are listed in Tab. 3.2 as well. The results of the measured properties are not only consistent among the different techniques, but also correspond reasonably well to the reported values for academic and commercial methanation catalysts.

### Characterization of the catalytic layer

The catalyst layer on the sponges was analyzed using scanning electron microscopy (SEM) and energy-dispersive X-ray spectroscopy (EDX). Therefore, individual struts of the fifth coated sample of the different pore densities were broken off and placed on sample holders. The EDX measurements confirmed the presence of nickel on the surface of the catalyst layer. In addition, the thickness of the layer was measured at least 70 times at different struts and different locations to obtain the distribution of the layer thickness (see Fig. 3.6). The measured distributions were then used to fit a normal distribution to quantify the average catalyst layer thickness and its standard deviation (Fig. 3.6 b). Furthermore, the applied coat mass was measured by weighting the individual samples before the coating and after the calcination procedure. The weight difference is the mass of the applied coating. The results of the SEM analysis and the applied coat masses are summarized in Tab. 3.3.

The SEM analysis suggests that the average thickness of the layer on the different sponges with different pore density is consistently between 55  $\mu\text{m}$ –64  $\mu\text{m}$  with standard deviations from 16  $\mu\text{m}$ –22  $\mu\text{m}$  which indicate broad distributions of the layer thickness (see Tab. 3.3). The broad character of the distribution is also visible in Fig. 3.6 b. Further,

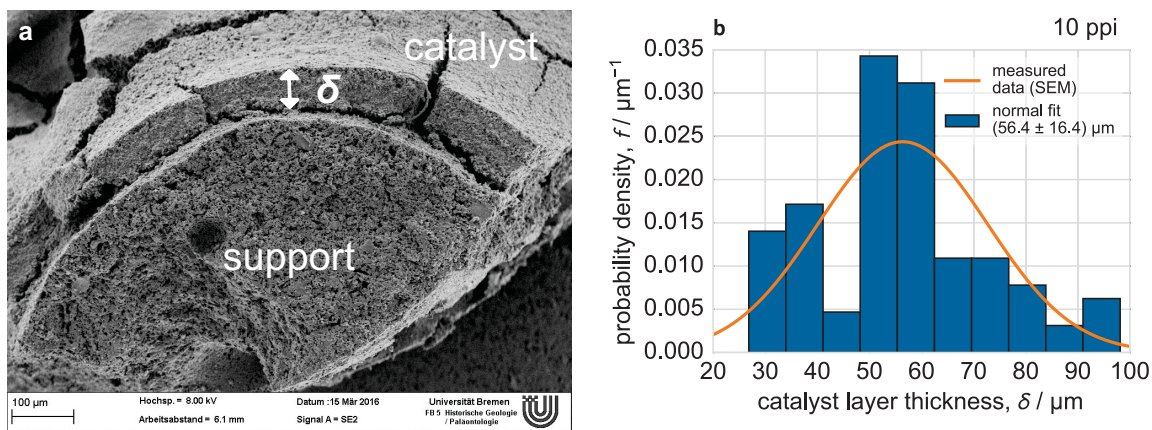


**FIG. 3.6.** SEM image of the catalyst layer on a strut of a 10 ppi sponge (a), and measured and fitted distribution of the layer thickness (b).

the measured distribution merely resembles the shape of a bell curve indicating that more measurements would have been necessary to determine the distribution of the layer thickness more accurately.

In contrast to the layer thickness, the applied coat mass increases with the specific surface area of the sponges (see Tab. 3.3). The increase in coat mass from the 20 ppi samples to the 40 ppi samples, however, is only small. A possible explanation for the small increase might be higher gas velocities during blow out of the residue in the 40 ppi sponges because of smaller windows. This is consistent with the slightly smaller layer thickness on the 40 ppi samples.

Furthermore, the knowledge of the specific surface areas of the sponges  $S_V$  (see Tab. 3.1), of the apparent catalyst density  $\rho_{\text{cat}}^{(\text{app})}$  and catalyst porosity  $\varepsilon_{\text{cat}}$  (see Tab. 3.2), and of the applied coat mass  $m_{\text{coat}}$  (see Tab. 3.3) allows the estimation of the catalyst layer thickness  $\delta_{\text{coat}}$  [84]:

$$\delta = \frac{m_{\text{coat}}}{S_V V_{\text{bulk}} (1 - \varepsilon_{\text{cat}}) \rho_{\text{cat}}^{(\text{app})}}. \quad (3.1)$$

A comparison between the measured and calculated layer thicknesses is shown in Fig. 3.7. Taking into consideration the measurement uncertainties, and assuming a  $\pm 10\%$  relative error of the window diameters obtained from  $\mu\text{CT}$ , Eq. 3.1 estimates the layer thickness reasonably well, except for the 10 ppi sponges. Here, the suspension might have been

**TAB. 3.3.** Summary of catalyst layer thickness, applied coat mass, and bulk catalyst density for the different investigated sponges.

Sponge	Number of measurements thickness / mass	Layer thickness <sup>a</sup> $\mu\text{m}$	Applied coat mass <sup>b</sup> mg	Bulk catalyst density <sup>c</sup> $\text{kg m}^{-3}$
10 ppi	90 / 4	$56 \pm 16$	$434 \pm 40$	35
20 ppi	70 / 4	$64 \pm 20$	$610 \pm 54$	50
40 ppi	73 / 4	$55 \pm 22$	$642 \pm 52$	52

<sup>a</sup> from Scanning Electron Microscopy (SEM)    <sup>b</sup> mass difference between coated and uncoated sponges after calcination    <sup>c</sup> coat mass per cylindrical sample volume

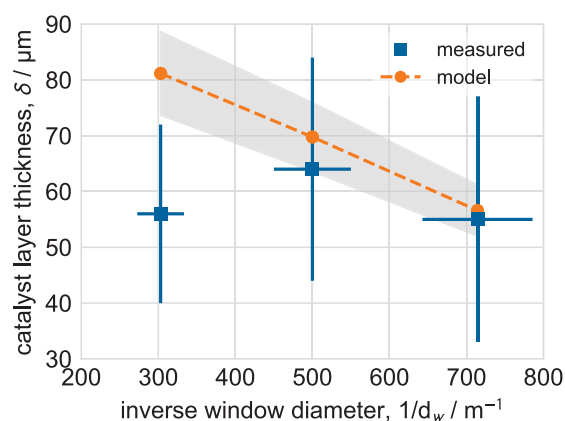


**FIG. 3.7.** Comparison of measured and modeled layer thickness (Eq. (3.1)) using the measured specific surface area, applied coat mass, apparent catalyst density, and catalyst porosity. The indicated errorbars for the layer thickness are the standard deviation of the measurements. The errorbars for the average inverse window size are estimated to be 10% (see  $\mu\text{CT}$  data). The grey region indicates the model prediction taking into account the standard deviation of the applied coat mass.

accumulated at the nodes of the sponge cells which subsequently led to thick layers that were not taken into account in the SEM analysis because only the struts were investigated. Thus, the model uses a too high coat mass and overpredicts the layer thickness. The match between the measured and calculated values, however, improves if the standard deviation of the applied coat mass is taken into account in the evaluation of Eq. (3.1) (see grey region in Fig. 3.7).

In conclusion, the characterization of the catalyst layer not only provides the required parameters for the calculation of concentration profiles in mesoporous catalysts, for example the average pore diameter and the layer thickness, but also indicates possible improvements of the coating procedure. In particular, the removal of the residue with pressurized air probably leads to non-uniform layer thicknesses because of the non-uniform flow distribution within the sponges. The application of centrifugation or agitator plates might lead to more uniform and thus more predictable catalyst layers.

### 3.3 Determination of kinetic parameters

The knowledge of the intrinsic kinetic of the synthesized catalyst is important for later simulations of temperature and concentration profiles in the catalytic sponges. In addition, it allows to compare the synthesized catalyst with methanation catalysts discussed in other studies. Therefore, isothermal kinetic experiments were conducted.

#### 3.3.1 Reactor setup, experimental procedure, and data evaluation

##### Reactor setup

For the isothermal experiments, 20 mg of the ground catalyst powder with a particle diameter of 150  $\mu\text{m}$ –250  $\mu\text{m}$  were mixed with 200 mg inert  $\text{Al}_2\text{O}_3$  particles of the same size and filled into an u-shaped fused quartz glass reactor with an inner diameter of 4 mm (see Fig. 3.8). Two quartz wool plugs in front of and behind the catalyst bed provided regularized

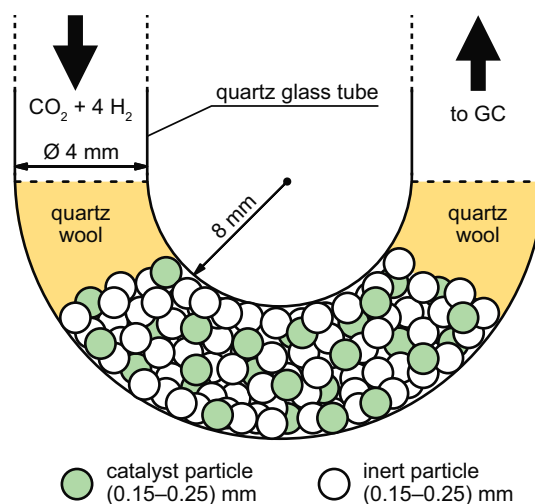


**FIG. 3.8.** Illustration of the used reactor tube to determine the intrinsic kinetic parameters of the synthesized catalyst. The catalyst particles (green, 20 mg) were mixed with 200 mg inert  $\text{Al}_2\text{O}_3$  particles (white) to prevent local hot-spots. The two quartz wool plugs at the in- and outlet provide regularized flow and prevent blowout of the catalyst particles. The quartz glass reactor tube was placed in the isothermal zone of a laboratory oven (not shown here). The product gas composition was analyzed downstream with a GC.

flow and prevented blow out of the catalyst particles at high flow rates. The reactor itself was placed within the isothermal zone of a laboratory oven; a digital thermometer was placed at the reactor outlet to manually monitor the temperature. A pressure indicator at the reactor inlet allowed to monitor the pressure in the reactor, which was set to 1.05 bar using a needle valve at the reactor outlet. The reactants were fed to the reactor with three mass flow controllers (MFC; Bronkhorst EL-FLOW®). Water, that was formed during the reaction, was condensed downstream and collected in a small tank. The product gas composition was then analyzed with a gas chromatograph (GC, compactGC by Axel Semrau, Sprockhövel, Germany) equipped with Restek's (Bellefonte, PA, USA) Molsieve 5A (15 m × 0.32 mm i.d.) and Q-BOND (30 m × 0.32 mm i.d.) columns and two thermal conductivity detectors (TCD). A detailed summary of the applied GC-method is given in Tab. C.2, p. 146. The retention times and response factors determined during the calibration of the GC are listed in Tab. C.3, p. 146, in Appendix C.

### Experimental procedure

Prior to the catalytic experiments, the catalyst was reduced *in situ* at 500 °C for 12 h in a pure  $\text{H}_2$ -flow of  $0.68 \text{ NL g}_{\text{cat}}^{-1} \text{ min}^{-1}$ . Therefore, the temperature was increased from ambient conditions to 200 °C at  $10 \text{ K min}^{-1}$  and held for 5 min. Then, it was further increased to the activation temperature at  $1 \text{ K min}^{-1}$ . After reduction, the catalyst cooled down to 200 °C in  $\text{H}_2$ -flow before measurements were started.

For the kinetic measurements, the temperature and flow rate were varied from 300 °C to 500 °C in steps of 50 °C and from  $0.68 \text{ NL g}_{\text{cat}}^{-1} \text{ min}^{-1}$  to  $2.71 \text{ NL g}_{\text{cat}}^{-1} \text{ min}^{-1}$  in steps of  $0.69 \text{ NL g}_{\text{cat}}^{-1} \text{ min}^{-1}$ , respectively. The feed composition remained constant at a 4:1  $\text{H}_2/\text{CO}_2$ -mixture in 9 vol% Ar, which corresponds to the stoichiometric feed ratio for methanation of carbon dioxide (see Eq. (2.2)). Initially, Ar was intended to be used as internal standard,

**TAB. 3.4.** Experimental parameters and operating conditions of selected studies providing kinetic models for methanation of CO and/or CO<sub>2</sub> over Ni-based catalysts. All studies use a Langmuir-Hinshelwood approach and consider reverse reactions.

Study (catalyst)	Particle size μm	Pressure bar	Temperature °C	Reactor diameter mm	Specific flow rate NL g <sub>cat</sub> <sup>-1</sup> min <sup>-1</sup>
Xu and Froment [308] (15.2 wt% Ni/MgAl <sub>2</sub> O <sub>4</sub> )	180–250	3–10	300–400	10.7	-
Zhang et al. [315] (50 wt% Ni/Al <sub>2</sub> O <sub>3</sub> )	140	1–5	250–360	1.4	0.7–8
Koschany et al. [154] (18.7 wt%Ni/Al <sub>2</sub> O <sub>3</sub> )	150–200	1–15	180–340	4	0.6–3
this work (5 wt% Ni/Al <sub>2</sub> O <sub>3</sub> )	150–250	1	300–500	4	0.68–2.71

however, using an external standard calibration lead to more consistent measurements. After each change of the temperature or flow rate, the system was given 15 min to stabilize before five repetitive measurements of the product gas composition were recorded. Finally, the first experiment after reduction was repeated to ensure that no significant deactivation took place during the experiments.

In comparison, the chosen reactor and particle diameters, and the operating conditions correspond well to other studies that investigated the kinetics of CO<sub>2</sub>-methanation over Ni-based catalysts (see Tab. 3.4). Consequently, the influence of interfacial mass transfer and internal mass transport limitations were likely to be negligible for the experiments in this work.

### Data evaluation

During the experiments, no C<sub>2</sub>H<sub>x</sub>-species were detected, which is characteristic for Ni-based methanation catalysts. In addition, it was concluded from thermodynamic calculations (see Section 2.2.2, pp. 10 ff.) that the formation of solid carbon is negligible at a H<sub>2</sub>/CO<sub>2</sub>-ratio of 4. Consequently, the CO<sub>2</sub>-conversion and the CH<sub>4</sub>-yield were calculated using a carbon balance (see Ducamp et al. [56]):

$$X_{\text{CO}_2}^{(\text{exp})} = 1 - \frac{y_{\text{CO}_2}^{(\text{exp})}}{y_{\text{CO}_2}^{(\text{exp})} + y_{\text{CO}}^{(\text{exp})} + y_{\text{CH}_4}^{(\text{exp})}}, \quad (3.2a)$$

$$Y_{\text{CH}_4}^{(\text{exp})} = \frac{y_{\text{CH}_4}^{(\text{exp})}}{y_{\text{CO}_2}^{(\text{exp})} + y_{\text{CO}}^{(\text{exp})} + y_{\text{CH}_4}^{(\text{exp})}}, \quad (3.2b)$$

$$S_{\text{CH}_4}^{(\text{exp})} = \frac{Y_{\text{CH}_4}^{(\text{exp})}}{X_{\text{CO}_2}^{(\text{exp})}}, \quad (3.2c)$$

with  $y_i^{(\text{exp})}$  being the molar fraction of species  $i$  in the product gas obtained from the GC analysis.

### 3.3.2 Determination of the pre-exponential factors and activation energies

#### Description of the numerical procedure

For the determination of the pre-exponential factors and activations energies, the Langmuir-Hinshelwood-Hougen-Watson rate equations of Xu and Froment [308] have been adopted (see Section 2.2.3, pp. 13 ff.). The adsorption parameters were not determined in this work; instead the original values of Xu and Froment [308] were used in all calculations. As the reactor for the isothermal experiments was operated in integral mode, i. e., the species concentrations vary along the catalyst bed, the design equations for an 1-d isothermal plug-flow reactor, Eqns. (3.3d), were integrated numerically for all combinations of the applied temperatures and flow rates. The feed gas composition was used as initial condition, Eq. (3.3e). Afterwards, the CO<sub>2</sub>-conversion and CH<sub>4</sub>-yield,  $X_{\text{CO}_2}^{(\text{mod})}$  and  $Y_{\text{CH}_4}^{(\text{mod})}$ , were calculated according Eqns. (3.3b) and (3.3c). Finally, the sum of the weighted residual sum of squares (RSS) of the CO<sub>2</sub>-conversion and the CH<sub>4</sub>-yield was minimized for all combinations of the applied temperatures and flow rates, Eq. (3.3a), forcing the activation energies  $E_{a,j}$  to be positive, Eq. (3.3f). Mathematically, the minimization problem is written as:

$$\text{minimize}_{\theta_{k,j}, \theta_{E,j}} \sum_{l=1}^n \left[ \left( \frac{X_{\text{CO}_2,l}^{(\text{mod})} - X_{\text{CO}_2,l}^{(\text{exp})}}{\sigma_{X,l}^{(\text{exp})}} \right)^2 + \left( \frac{Y_{\text{CH}_4,l}^{(\text{mod})} - Y_{\text{CH}_4,l}^{(\text{exp})}}{\sigma_{Y,l}^{(\text{exp})}} \right)^2 \right] \quad (3.3a)$$

$$\text{subject to} \quad X_{\text{CO}_2,l}^{(\text{mod})} = 1 - \frac{\omega_{\text{CO}_2,l}}{\omega_{\text{CO}_2,0}}, \quad \text{CO}_2\text{-conversion,} \quad (3.3b)$$

$$Y_{\text{CH}_4,l}^{(\text{mod})} = \frac{M_{\text{CO}_2}}{M_{\text{CH}_4}} \frac{\omega_{\text{CH}_4,l} - \omega_{\text{CH}_4,0,l}}{\omega_{\text{CO}_2,0,l}}, \quad \text{CH}_4\text{-yield,} \quad (3.3c)$$

$$\frac{\partial \omega_{i,l}}{\partial (m_{\text{cat}} / \dot{V}_l)} = \frac{M_i}{\rho_f} \sum_{j=1}^{n_R} \nu_{ij} r_j^{(m)}, \quad i = 1, \dots, n_s, \quad \text{PFR equation,} \quad (3.3d)$$

$$\omega_{i,l}(m_{\text{cat}} / \dot{V}_l = 0) = \omega_{i,0}, \quad \text{PFR initial cond.,} \quad (3.3e)$$

$$\theta_{E,j} > 0, \quad \text{positive } E_{a,j}. \quad (3.3f)$$

Here, the index  $l$  runs over all combinations of the applied temperatures and flow rates, and  $\sigma_{X,l}^{(\text{exp})}$  and  $\sigma_{Y,l}^{(\text{exp})}$  are the corresponding standard deviations of the five replicate GC measurements. In addition, the scaled decision variables

$$\theta_{k,j} = \ln \left( k_{m,j}^{(\text{ref})} \right) \quad \text{and} \quad (3.4a)$$

$$\theta_{E,j} = \frac{E_{a,j}}{R_u T_{\text{ref}}} \quad (3.4b)$$

were used in the minimization problem (3.3) to increase numerical stability and thus improve convergence (see [153, 154, 308]). The reference temperature  $T_{\text{ref}}$  was arbitrarily chosen to be 673.15 K, the midpoint of the investigated temperature range. The pre-exponential factors at reference conditions,  $k_j^{(\text{ref})}$ , and the activations energies  $E_{a,j}$  were readily calcu-

**TAB. 3.5.** Kinetic parameters for the rate equations of Xu and Froment [308], Eqns. (2.4), determined for the 5 wt% Ni/Al<sub>2</sub>O<sub>3</sub> catalyst synthesized in this work. For comparison, the original parameters reported by Xu and Froment [308] are also given. All parameters are given in SI units.

Parameter	Unit	Numeric value	
		this work	Xu and Froment [308]
$k_{m,1}^{(\text{inf})}$	$\text{mol Pa}^{0.5} \text{ kg}^{-1} \text{ s}^{-1}$	$6.514 \cdot 10^{15} \pm 0.291 \cdot 10^{15}$	$4.547 \cdot 10^{17}$
$k_{m,2}^{(\text{inf})}$	$\text{mol Pa}^{0.5} \text{ kg}^{-1} \text{ s}^{-1}$	$9.158 \cdot 10^{18} \pm 0.133 \cdot 10^{18}$	$1.098 \cdot 10^{17}$
$k_{m,3}^{(\text{inf})}$	$\text{mol Pa}^{-1} \text{ kg}^{-1} \text{ s}^{-1}$	$5.600 \cdot 10^{-1} \pm 0.087 \cdot 10^{-1}$	6.652
$E_{a,1}$	$\text{kJ mol}^{-1}$	$224.7 \pm 0.2$	240.1
$E_{a,2}$	$\text{kJ mol}^{-1}$	$263.1 \pm 0.1$	243.9
$E_{a,3}$	$\text{kJ mol}^{-1}$	$56.6 \pm 0.1$	67.13
$K_{\text{CO}}^{\text{a}}$	$\text{Pa}^{-1}$	-	$8.23 \cdot 10^{-10}$
$K_{\text{H}_2}^{\text{a}}$	$\text{Pa}^{-1}$	-	$6.12 \cdot 10^{-14}$
$K_{\text{CH}_4}^{\text{a}}$	$\text{Pa}^{-1}$	-	$6.65 \cdot 10^{-9}$
$K_{\text{H}_2\text{O}}^{\text{a}}$	-	-	$1.77 \cdot 10^5$
$\Delta H_{\text{CO}}^{\text{a}}$	$\text{kJ mol}^{-1}$	-	-70.65
$\Delta H_{\text{H}_2}^{\text{a}}$	$\text{kJ mol}^{-1}$	-	-82.90
$\Delta H_{\text{CH}_4}^{\text{a}}$	$\text{kJ mol}^{-1}$	-	-38.28
$\Delta H_{\text{H}_2\text{O}}^{\text{a}}$	$\text{kJ mol}^{-1}$	-	88.68

<sup>a</sup> the adsorption parameters were not determined in this work; the original values of Xu and Froment [308] were used instead

lated from Eqns. (3.4a) and (3.4b). The reaction rate coefficients  $k_j$  are then calculated using Arrhenius' equation:

$$k_{m,j} = k_{m,j}^{(\text{ref})} \exp \left\{ -\frac{E_{a,j}}{R_u} \left( \frac{1}{T} - \frac{1}{T_{\text{ref}}} \right) \right\}. \quad (3.5)$$

Ultimately, the pre-exponential factors at infinite temperature  $k_j^{(\text{inf})}$  are obtained from

$$k_{m,j}^{(\text{inf})} = k_{m,j}^{(\text{ref})} \exp \left\{ \frac{E_{a,j}}{R_u T_{\text{ref}}} \right\}. \quad (3.6)$$

The minimization problem (3.3) was implemented in Python [289, version 2.7] and solved using PyGMO's [23] implementation of Differential Evolution (a powerful genetic algorithm for global optimization, see [41, 60, 226]) with a population of 50 individuals evolved over 200 generations. Afterwards, the obtained solution was smoothed using a local least-squares solver [27] to guarantee optimality of the final solution. Three replicate runs with different initial populations converged to the same solution, indicating that the global solution to Eq. (3.3) was found.

### Results and discussion of the determined kinetic parameters

The pre-exponential factors and activation energies obtained from the minimization of the weighted RSS between the experimental and modeled CO<sub>2</sub>-conversions and CH<sub>4</sub>-yields, and the original parameters of Xu and Froment [308] are listed in Tab. 3.5. Compared to the original values of Xu and Froment [308], the determined activation energies agree reasonably well. Moreover, the low standard deviations obtained from the least-squares fitting indicate that all six parameters could be estimated accurately from the experimental data. The total RSS per combination of temperature and flow rate (20 in total) is  $6.48 \cdot 10^{-4}$ ,

demonstrating a good match between the model and the experimental data. In addition to the rate equations of Xu and Froment [308], the rate equations of Zhang et al. [315] with the adaption for reverse reactions by Rönsch et al. [237] were applied to describe the experimental data. Nevertheless, the overall match between the experimental and modeled CO<sub>2</sub>-conversions and CH<sub>4</sub>-yields was not as good as the one of the rate equations of Xu and Froment [308]. Also, a small amount of carbon monoxide (0.1 vol%) had to be added artificially in case of the rate equations of Zhang et al. [315] to ensure convergence because the kinetic model solely considers the reactions for CO-methanation and reverse water-gas shift.

Because Xu and Froment [308] originally developed their kinetic model for steam reforming of methane, which is the reverse reaction of methanation, the activation energies given in Tab. 3.5 are valid for the reverse reactions of methanation. By using van't Hoff's and Arrhenius' equation, the activation energies of the forward reaction, i. e., for the methanation of carbon dioxide, can be estimated from the sum of the reverse activation energy and the reaction enthalpy:

$$E_{a,f} = E_{a,r} + \Delta_R H = 263.1 \text{ kJ mol}^{-1} + (-165 \text{ kJ mol}^{-1}) = 98.1 \text{ kJ mol}^{-1}. \quad (3.7)$$

The resulting activation energy of 98.1 kJ mol<sup>-1</sup> is in reasonable agreement with the values determined by Koschany et al. [154] (77.5 kJ mol<sup>-1</sup>) and Martinez Molina et al. [182] (83.9 kJ mol<sup>-1</sup>) for the methanation of carbon dioxide over nickel catalysts.

Figure 3.9 shows a comparison of the experimentally measured and modeled CO<sub>2</sub>-conversions and CH<sub>4</sub>-yields for all considered temperatures and flow rates (residence times). The modeled CO<sub>2</sub>-conversions and CH<sub>4</sub>-yields agree well with the measured ones up to 450 °C (see Figs. 3.9 a and b). For 500 °C, the model slightly overpredicts the CO<sub>2</sub>-conversions and CH<sub>4</sub>-yields. A possible explanation were mass transport limitations within the mesoporous catalyst. Solving the heat and mass transport equations numerically (see the description of the catalyst-scale model in Section 4.4, pp. 83 ff.) for a spherical catalyst particle of 200 μm diameter at 500 °C, 1 bar, and a H<sub>2</sub>/CO<sub>2</sub> of 4 in 9 vol% Ar, yields an effectiveness factor  $\eta$  for the CO<sub>2</sub>-methanation reaction of 0.75. Thus, mass transport was very likely limiting the conversion of CO<sub>2</sub> at 500 °C, leading to a lower CO<sub>2</sub>-conversion than predicted. The temperature difference between the gas phase and the solid catalyst particle, however, did not exceed 0.1 K based on the simulations, even at the lowest applied flow rate of 14 NmL min<sup>-1</sup>. Consequently, heat transfer limitations did probably not influence the reaction rates in the kinetic experiments. Repeating the calculation at 450 °C gives an effectiveness factor  $\eta$  for the CO<sub>2</sub>-methanation reaction of 0.89. Hence, mass transport limitations did not significantly affect the kinetic experiments up to 450 °C in this work.

As mentioned above, the first measurement after the reduction procedure was repeated after all experiments had been completed to monitor if the catalyst changed during the experiments. For a specific flow rate of 1.36 NL g<sub>cat</sub><sup>-1</sup> min<sup>-1</sup> and a temperature of 350 °C, the CO<sub>2</sub>-conversion and CH<sub>4</sub>-yield in the first experiment were 5.2 % and 3.3 %, respectively. After all experimental runs, a CO<sub>2</sub>-conversion of 5.7 % and a CH<sub>4</sub>-yield of 4.1 % were

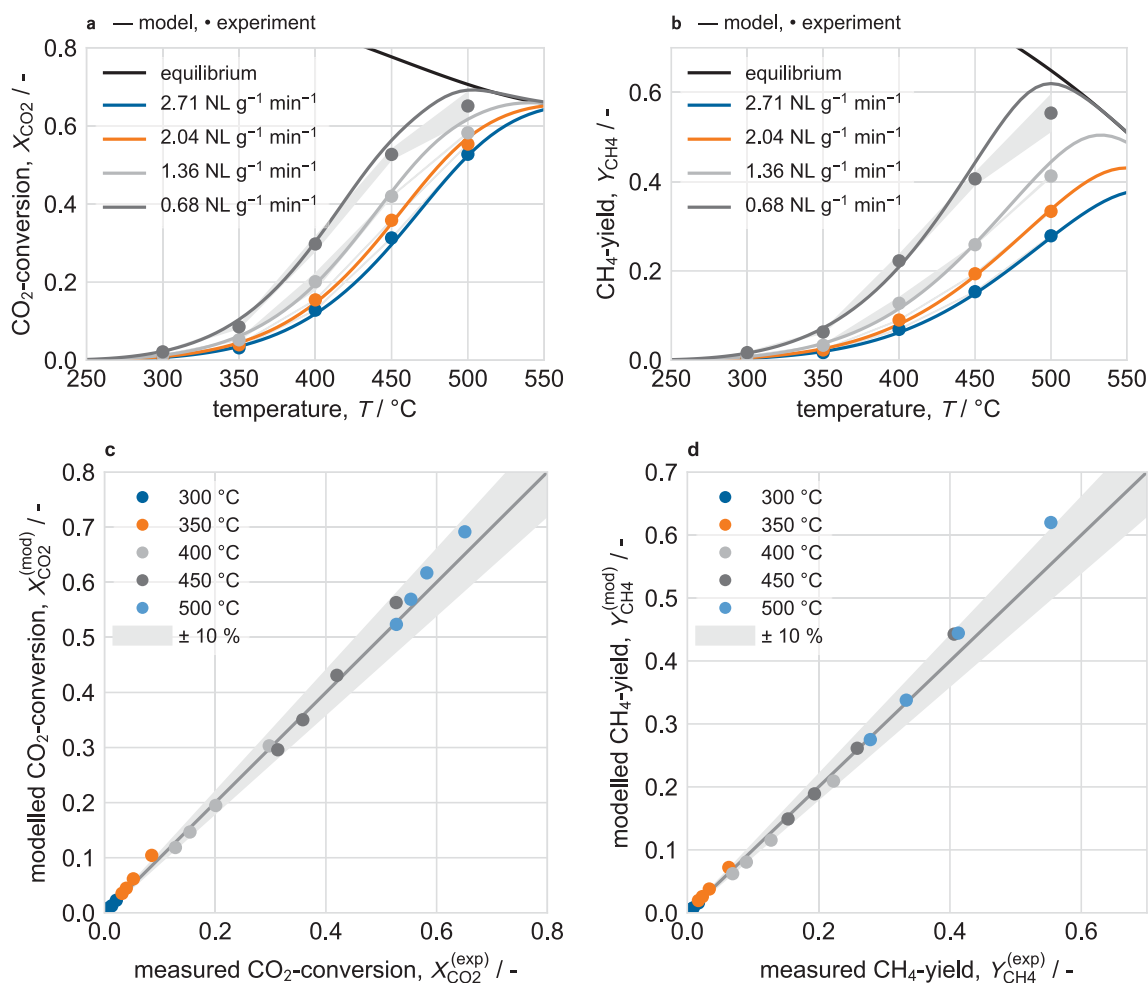


**FIG. 3.9.** Comparison of the measured and calculated CO<sub>2</sub>-conversion (a) and CH<sub>4</sub>-yield (b) over temperature, and comparison (parity plots) of the measured and calculated CO<sub>2</sub>-conversion (c) and CH<sub>4</sub>-yield (d). All calculations were performed with the adjusted pre-exponential factors and activation energies (see Tab. 3.5). The gray bands in (a) and (b) indicate the standard deviation among five replicate measurements. Experimental conditions: 1.05 bar, H<sub>2</sub>/CO<sub>2</sub>=4.

obtained. The deviations are within the accuracy of the GC analysis. Thus, catalyst deactivation during the measurements did not influence the reaction rates.

The comparison of the measured and modeled CO<sub>2</sub>-conversions and CH<sub>4</sub>-yields in form of parity plots (see Figs. 3.9 c and d) shows that CO<sub>2</sub>-conversion and CH<sub>4</sub>-yield can actually be calculated within ±10% accuracy with the determined kinetic parameters. Consequently, the determined kinetic model allows to calculate the reaction rates and the heat released by the chemical reactions with good accuracy and can thus be used for the simulation of concentration and temperature profiles in solid sponges during CO<sub>2</sub>-methanation.

### Comparison of the synthesized catalyst with other Ni-based methanation catalysts

In comparison with other Ni-based methanation catalysts, the 5 wt% Ni/Al<sub>2</sub>O<sub>3</sub> catalyst synthesized in this work shows a low activity for CO<sub>2</sub>-methanation (see Fig. 3.10). While the commercial methanation catalysts studied by Zhang et al. [315] and Martinez Molina et al. [182], and the co-precipitated catalyst synthesized by Koschany et al. [154], become active between 250 °C–300 °C, the catalyst investigated by Xu and Froment [308] and the

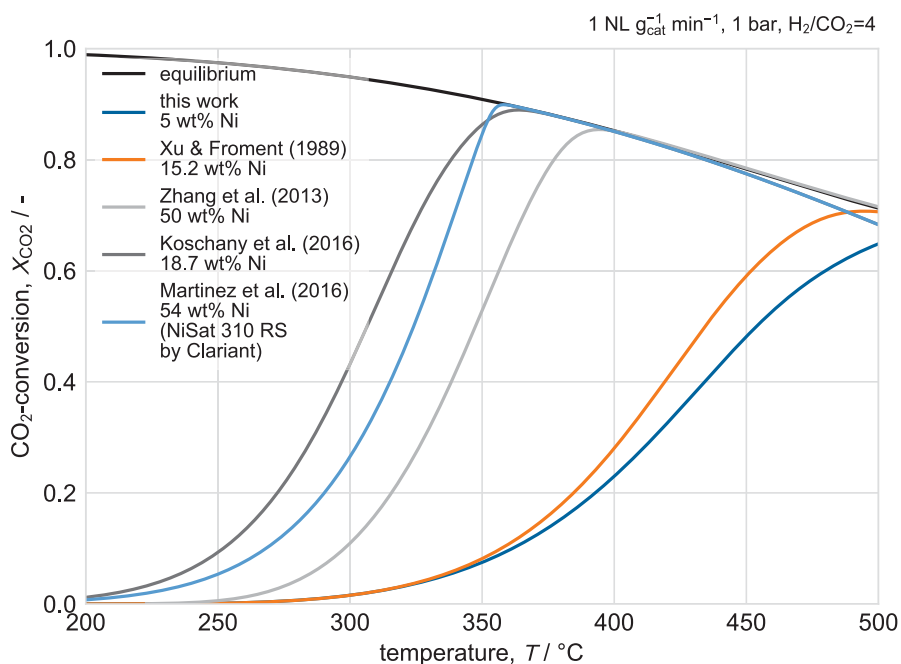


**FIG. 3.10.** Comparison of the CO<sub>2</sub>-conversion of various Ni-based methanation catalysts under ideal conditions (no limitations considered) for a specific flow rate of 1 NL g<sub>cat</sub><sup>-1</sup> min<sup>-1</sup>, a pressure of 1 bar, and a H<sub>2</sub>/CO<sub>2</sub>-ratio of 4. Some of the kinetic models were not validated at high temperatures and were thus extrapolated for this comparison.

one synthesized in this work become active only at 350 °C and above. Nevertheless, the low nickel content of the synthesized catalyst has to be considered. Typically, the nickel content of state-of-the-art methanation catalysts is 3–10 times higher than the one used in this work, where the nickel content was intentionally reduced to 5 wt% to compensate the missing active cooling of the polytropic (non-isothermal, non-adiabatic) lab-scale reactor (see Section 3.4.1). Still, the synthesized catalyst is able to compete with the 15 wt% Ni/MgAl<sub>2</sub>O<sub>4</sub> catalyst studied by Xu and Froment [308], however, almost 30 years ago. In addition, it is interesting to observe that the co-precipitated catalyst of Koschany et al. [154] exhibits a better activity than the two commercial catalysts considered in the comparison, although the nickel content is approximately 60 % lower.

## 3.4 Polytropic CO<sub>2</sub>-methanation experiments

### 3.4.1 Reactor setup

In order to investigate heat transport in catalytic sponges during CO<sub>2</sub>-methanation, and to obtain experimental data for the validation of reactor models, a lab-scale fixed-bed reactor (FBR) has been set up. The setup consists of three main sections: a gas mixing and pre-heating section to prepare the feed, the FBR holding a 100 mm long catalyst bed with a diameter of 25 mm, and a downstream post-processing section to condense water and analyze the dry product gas with a GC. The tube diameter of 25 mm is industrially relevant for exothermic reactions. Photos of the setup and the reactor are shown in Appendix C, pp. 145 ff. Figure 3.11 shows a process flow diagram of the setup.

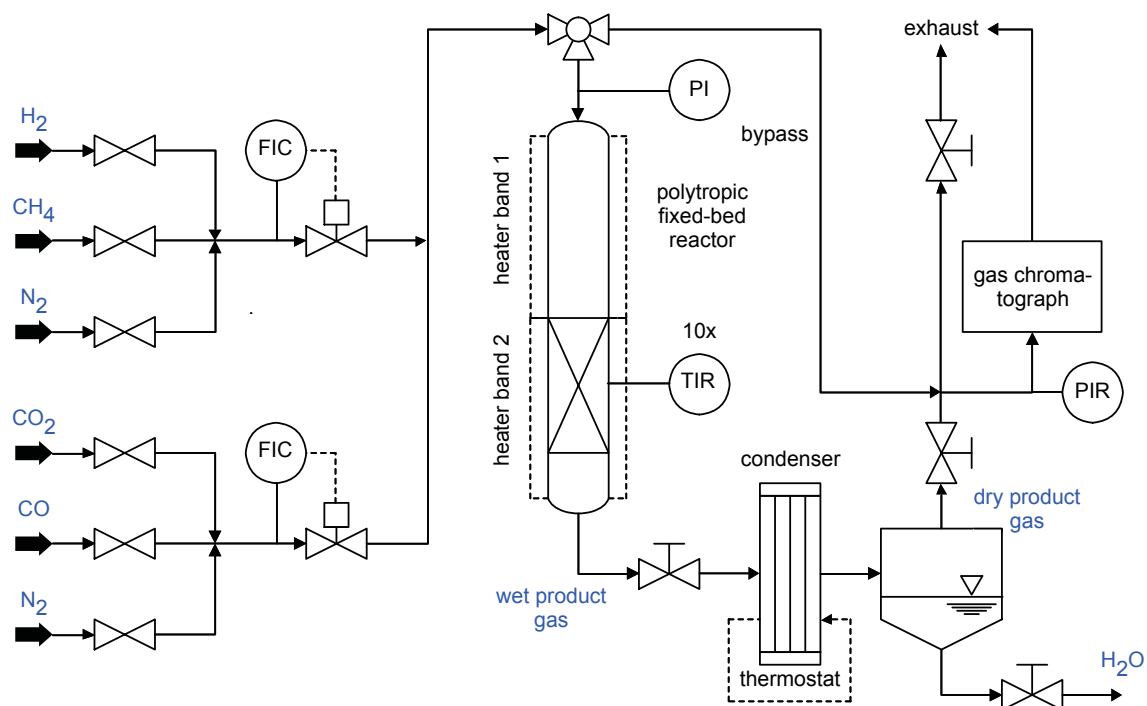


**FIG. 3.11.** Process flow diagram of the polytropic lab-scale fixed-bed reactor setup. The gases are fed to the reactor by two mass flow controllers. After passing the pre-heating section (heater band 1), the reactants flowed through the catalyst bed (heat band 2). An array of 10 thermocouples allowed to measure axial temperature profiles within the catalyst bed during operation. Downstream, water is condensed and the dry product gas is analyzed with a GC.

In the upstream section, two mass flow controllers (EL-FLOW® by Bronkhorst, Ruurlo, The Netherlands) allowed to feed various process gases ( $\text{H}_2$  5.0,  $\text{CH}_4$  3.5,  $\text{CO}_2$  3.0,  $\text{CO}$  3.7,  $\text{N}_2$  5.0 by Linde, Pullach, Germany) and binary mixtures thereof to the reactor. The feed was heated up to  $250\text{ }^\circ\text{C}$ – $400\text{ }^\circ\text{C}$  in the preheating section (32 mm i.d.  $\times$  500 mm) by a flexible heater sleeve (Horst GmbH, Lorsch, Germany). Then, the reactants passed the catalytic bed in the main reactor section which was heated by a second heater sleeve. Downstream, the product gas was cooled down and water was removed in a condenser operated at  $0\text{ }^\circ\text{C}$  and 1.3 bar with a 30 wt% ethylene-glycol-water mixture (freezing temperature  $-12\text{ }^\circ\text{C}$ , boiling temperature  $105\text{ }^\circ\text{C}$ ). The condensed water was collected in a separation tank; the dry product gas left the tank at the top. Before it proceeded to the exhaust, the composition of the product gas was analyzed by a GC (Hewlett Packard 6890) equipped with a Supleco PLOT 1010 column (530  $\mu\text{m}$  i.d.  $\times$  30 m) and a TCD. The detailed configuration of the GC is listed in Tab. C.2 in Appendix C (p. 146). Prior to the experiments the GC was calibrated using an external standard scheme (binary mixtures with  $\text{N}_2$ ). The retention times and the obtained response factors are summarized in Tab. C.3 Appendix C (p. 146). In addition, a typical chromatogram recorded during  $\text{CO}_2$ -methanation is shown in Fig. C.2 in Appendix C (p. 146). Regular benchmarks with a 1:1  $\text{CO}_2/\text{CH}_4$ -mixture were conducted to monitor temporal changes of the column and the TCD, and thus ensured a consistent analysis of the product gas composition throughout the experiments.

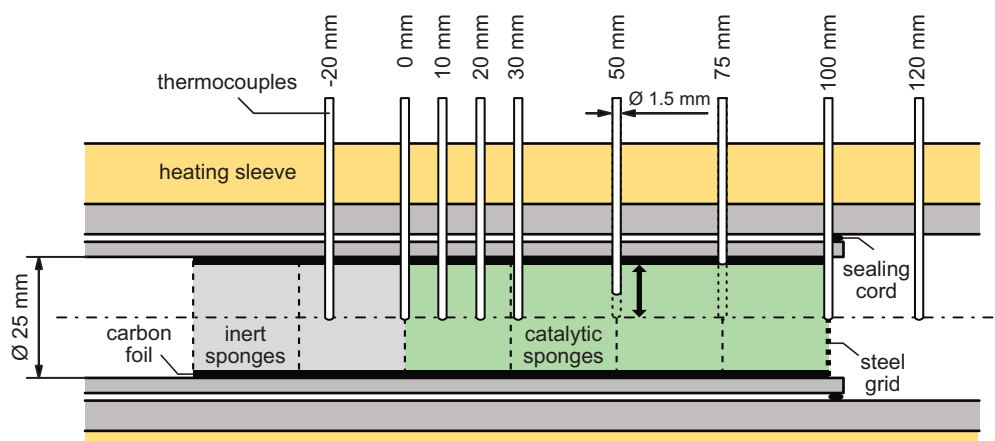


**FIG. 3.12.** Detailed illustration of the polytropic lab-scale reactor and the arrangement of the thermocouples to measure axial temperature profiles in catalytic sponges. A second set of thermocouples was available to measure the temperature at the outer perimeter of the sponges in close vicinity to the tube wall. The carbon foil not only prevented bypass streams, but also created a good thermal contact between the sponges and the tube wall. In front of the catalyst bed, two uncoated sponges were placed to ensure fully developed flow in the catalyst bed.

The main reactor section holding the catalyst is illustrated in detail in Fig. 3.12. Four coated sponges of the same pore density were wrapped in carbon foil (Kerafoil 90/10, 200  $\mu\text{m}$  thick by Keramische Folien GmbH, Eschenbach, Germany) to create a good thermal contact between the sponges and the reactor wall, and to avoid bypass flows (see [95, 192, 193]). Subsequently, the sponges were inserted into the reactor tube one by one. The carbon foil slid smoothly in the reactor tube and thus helped to insert the sponges. According to the supplier, the carbon foil is chemically stable up to 500  $^{\circ}\text{C}$ , which was confirmed by experiments without a catalyst (see Tab. C.1, p. 145 in Appendix C). Two uncoated sponges of the same pore density, placed in front of the coated sponges and also wrapped in carbon foil, ensured fully developed flow at the beginning of the catalyst bed. Afterwards, small, 12.5 mm long channels were drilled into the sponges to insert the thermocouples. In total, two sets of thermocouples (Type K,  $\varnothing 1.5$  mm, B+B Sensors, Donaueschingen, Germany) were used to measure either the core temperature or the wall temperature. Thus, every experiment had to be repeated at least two times to obtain a complete set of temperature profiles. For calibration, the thermocouples were tightly put into a stainless steel tube together with a digital thermometer (GTH 1200 by GHM Messtechnik GmbH, Greisinger, Germany). The tube was heated to specific temperatures with on of the heater sleeves. Once the reference temperature remained stable for 30 min, the temperatures by the thermocouples were recorded and averaged over 15 min. Afterwards, linear regression was used to obtain the calibration curves of each thermocouple. The determined coefficients are listed in Tab. C.4 in Appendix C, p. 147. All non-catalytic materials within the reactor, i. e., the carbon foil, the uncoated sponges, and the empty reactor tube itself were tested under methanation conditions up to 500  $^{\circ}\text{C}$  to exclude possible influences on the conversion of carbon dioxide. For all materials, no significant methane formation was observed (see Tab. C.1, p. 145 in Appendix C).

Because of the electric heating, no active cooling of the reactor was possible, and thus heat transport limitations in the surroundings of the catalyst bed might have influenced the axial temperature profiles in the catalyst bed. Hence, the measurement of the wall temperature was crucial for later comparison with simulations. Typically, jacketed FBRs with liquid cooling media are applied to ensure a uniform wall temperature. Because of the high temperature levels of the methanation process (300 °C–500 °C), however, only molten salt baths, which are elaborate to operate, would have been applicable. In addition, Gräf et al. [95] also measured a slight increase of the wall temperature by 10 K–20 K in their oil-cooled FBR for benzene hydrogenation at 170 °C.

After insertion of the thermocouples, the reactor was assembled and the heater sleeves mounted. Finally, the reactor was heated up to 300 °C–400 °C and a pressure test with nitrogen (5 bar) was conducted.

### 3.4.2 Experimental procedure and data evaluation

Prior to the catalytic experiments, the catalyst was activated *in situ* in a 1:1 H<sub>2</sub>/N<sub>2</sub>-mixture (1 NL min<sup>-1</sup> each) at 4 bar. Therefore, the reactor was heated up from ambient conditions to 430 °C, measured in the middle of the catalyst bed, within 2 h. The temperature was held constant for another 2 h. The reduction procedure was only performed once for a fresh catalyst. To run experiments with an already reduced catalyst, the reactor was heated up to the desired inlet temperature at 3 K min<sup>-1</sup>–5 K min<sup>-1</sup> using a 1:1 H<sub>2</sub>/N<sub>2</sub>-mixture (1 NL min<sup>-1</sup> each). Subsequently, the heater sleeve temperature was adjusted until the desired temperature at the inlet of the catalyst bed was reached. Next, the feed was switched to an undiluted 4:1 H<sub>2</sub>/CO<sub>2</sub>-mixture to start the reaction. Depending on the flow rate and inlet temperature, the process reached steady state after 30 min–60 min. Once temperatures remained stable, they were recorded with a sampling rate of 1 Hz. In the meantime, at least three replicate GC measurements were conducted to analyze the dry product gas composition. CO<sub>2</sub>-conversion and CH<sub>4</sub>-yield were calculated according Eqns. (3.2) using the average composition of the three GC measurements. To obtain the axial temperatures profiles, the recorded temperatures during the steady period of operation

**TAB. 3.6.** Summary of setup size and operating conditions for the polytropic and kinetic experiments.

Quantity	Unit	Polytropic experiments	Kinetic experiments
inner tube diameter	mm	25	4
bed length	mm	100	30
catalyst mass	g	1.74–2.57	0.02
bulk catalyst density	kg m <sup>-3</sup>	35.2–52.3	51.3
feed temperature	°C	300–400	300–450
bed temperature	°C	≤650	300–450
pressure	bar	4	1
flow rate	NmL min <sup>-1</sup>	3750–7500	14–55
H <sub>2</sub> /CO <sub>2</sub> ratio	-	4	4
specific flow rate	NL g <sub>cat</sub> <sup>-1</sup> min <sup>-1</sup>	1.46–4.32	0.69–2.75
WHSV	NL g <sub>cat</sub> <sup>-1</sup> h <sup>-1</sup>	87–259	41–165

were averaged over time for each thermocouple, and plotted along the fixed positions of the thermocouples in the catalyst bed. Finally, the feed temperature or flow rate was varied and the measurement procedure was repeated for the new set of operating conditions.

To shut down the reactor, the heater sleeves were turned off and the reactor was purged with pure nitrogen ( $2 \text{ NL min}^{-1}$ ) for 30 min to remove all product gases, and thus prevent formation of toxic  $\text{Ni(CO)}_4$  from CO and dispersed Ni below  $180^\circ\text{C}$ . Finally, the valve at the reactor outlet was closed and the reactor was pressurized up to 5 bar with nitrogen. Once the desired pressure was reached, the valve at the inlet of the reactor was closed to contain the catalyst bed in an inert atmosphere for the next operation period (usually the following day). For comparison, a summary of the operating conditions for the polytropic and the kinetic catalysis experiments is given in Tab. 3.6.



## 4.1 Introduction to reactor models

Reactor models allow the simulation of concentration and temperature distributions in catalytic reactors from which conversion, space-time yield, and required heating or cooling loads can be calculated. Once a reactor model has been validated against experimental data, it can readily be solved many times and thus allows to assess different reactor dimensions, operating conditions, catalysts, and supports at the fraction of the costs and time of experimental investigations. Consequently, reactor models are used in industry to guide experiments and operation, for optimization, and to scale up reactors from the lab, over the pilot, to the production scale. In research, reactor models are frequently used to investigate the sensitivity of parameters and to explore the influence of certain phenomena, e. g., the flow pattern, on the performance of reactors.

In this work, a fixed-bed reactor model has been implemented to compare catalytic sponges to conventional packed pellet beds at production scale, deduce design guidelines for catalytic sponges, and give an outlook on the potential of tailored catalytic sponges with radial porosity gradients.

## 4.2 General description of the implemented reactor model

The fixed-bed reactor model in this work was specifically developed for catalytic sponges. The governing equations, however, can also be used to simulate catalytic packed beds of pellets if the corresponding models for the velocity distribution and the effective transport coefficients are applied. The implemented reactor model adopts a pseudo-homogeneous approach to describe heat and mass transport, and chemical reactions in the catalyst bed (see Fig. 4.1). Concentration and temperature variations in the circumferential direction are disregarded so that the 3-d geometry can be reduced to a 2-d plane with axial and radial dimensions  $L_t$  and  $R_t$ , and axial and radial coordinates  $z$  and  $r$ . Moreover, radial fluid flow was neglected, which is justified for the slender reactor tubes ( $L_t \gg D_t$ ) that are applied in heterogeneous catalysis. In addition to heat and mass transport at the reactor scale, the model explicitly takes into account heat and mass transport in the diffusional film around the catalyst, and within the mesoporous catalyst itself. The catalyst-scale model is solved at every point of the computational grid of the reactor-scale model. Both models are coupled via the boundary conditions at the catalyst surface that act as scale bridge between the reactor scale (mm–m) and the catalyst scale (nm– $\mu$ m). Although the model distinguishes between the fluid and solid concentrations and temperatures in the catalyst model (local scale), it is rather classified as pseudo-homogeneous model because it does not distinguish fluid from solid concentrations and temperatures at the reactor scale. For catalytic sponges in polytropic applications, pseudo-heterogeneous reactor models have not been applied

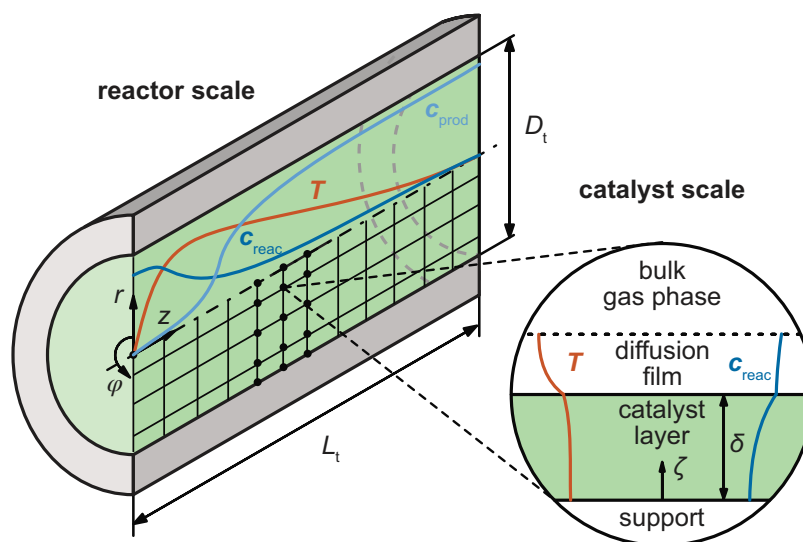


**FIG. 4.1.** Illustration of the 2-d pseudo-homogeneous multi-scale fixed-bed reactor model. At the reactor scale, the catalyst bed is assumed axisymmetric. The concentration and temperature fields are thus modeled in a 2-d plane with dimensions  $R_t$  and  $L_t$ , and radial and axial coordinates  $r$  and  $z$ , respectively. The catalyst-scale model is solved at every point of the computational grid of the reactor-scale model, to calculate the influence of heat and mass transfer limitations, and the influence of mass transport limitations within the mesoporous catalyst. The reactor- and catalyst-scale model are linked by the boundary condition (scale bridge) at the surface of the catalyst ( $\zeta = \delta$ ).

yet because of the mathematical and numerical efforts associated with their solution, and the lack of reliable models for the heat and mass transfer coefficients.

In the case of packed beds of pellets, 2-d pseudo-homogeneous reactor models have become standard in industry and research in the past (see [75, Chapter 11] and for instance [28, 305]). The combination of the reactor and the catalyst scale has also been adopted for packed beds by, among others, Adams and Barton [2], Ghose and Adams [83], and Petera et al. [220]. For catalytic sponges, 2-d pseudo-homogeneous models were recently applied by Gräf et al. [95], Philippe et al. [223], and Reitzmann et al. [233], however, multi-scale models that explicitly take into consideration heat and mass transfer between the solid and the fluid phase and heat and mass transport in the mesoporous catalyst layer have not been reported yet. Consequently, the reactor-scale and the catalyst-scale model are described in detail in the following sections.

## 4.3 Description of the reactor-scale model

### 4.3.1 Heat, mass, and momentum balances

The heart of the reactor-scale model are the mass and energy balances for the cylindrical catalyst bed, Eqns. (4.1) and (4.2), that consider accumulation, axial convection and dispersion, radial dispersion, and chemical reactions:

$$\underbrace{\varepsilon_o \rho_f \frac{\partial \omega_i}{\partial t}}_{\text{accumulation}} = - \underbrace{\rho_f v_{\text{sup}} \frac{\partial \omega_i}{\partial z}}_{\text{axial convection}} - \underbrace{\frac{\partial j_{\text{ax},i}}{\partial z}}_{\text{axial dispersion}} - \underbrace{\frac{\partial j_{\text{rad},i}}{\partial r} - \frac{1}{r} j_{\text{rad},i}}_{\text{radial dispersion}} + \underbrace{\rho_{\text{cat}}^{(\text{bulk})} M_i \sum_{j=1}^{n_R} v_{ij} \eta_j r_j^{(m)}}_{\text{chemical reactions}}, \quad (4.1)$$

$$\underbrace{[\rho c_p]_{\text{eff}} \frac{\partial T}{\partial t}}_{\text{accumulation}} = - \underbrace{\rho_f c_{p,f} v_{\text{sup}} \frac{\partial T}{\partial z}}_{\text{axial convection}} - \underbrace{\frac{\partial q_{\text{ax}}}{\partial z}}_{\text{axial dispersion}} - \underbrace{\frac{\partial q_{\text{rad}}}{\partial r} - \frac{1}{r} q_{\text{rad}}}_{\text{radial dispersion}} + \underbrace{\rho_{\text{cat}}^{(\text{bulk})} \sum_{j=1}^{n_R} (-\Delta_R H_j) \eta_j r_j^{(m)}}_{\text{reaction heat}}. \quad (4.2)$$

Herein,  $v_{\text{sup}}$  is the superficial velocity and  $j_{\text{ax},i}$  and  $j_{\text{rad},i}$ , and  $q_{\text{ax}}$  and  $q_{\text{rad}}$ , are the mass and heat fluxes in the axial and radial direction, respectively. The bulk catalyst density  $\rho_{\text{cat}}^{(\text{bulk})}$  is defined as the amount of catalytic material per reactor volume. The heat capacity of the effective medium,  $(\rho c_p)_{\text{eff}}$  is approximated by the weighted average (volumetric fraction) of the fluid and solid heat capacities:

$$(\rho c_p)_{\text{eff}} = (\varepsilon_t \rho_f c_{p,f} + (1 - \varepsilon_t) \rho_s c_{p,s}). \quad (4.3)$$

The axial and radial mass and heat fluxes are modeled in analogy to Fick's and Fourier's law with effective diffusion coefficients and effective thermal conductivities, which were thoroughly reviewed in Chapter 2, pp. 7 ff.:

$$j_{\text{ax},i} = -\rho_f D_{\text{ax},i}^{(\text{eff})} \frac{\partial \omega_i}{\partial z}, \quad (4.4a)$$

$$j_{\text{rad},i} = -\rho_f D_{\text{rad},i}^{(\text{eff})} \frac{\partial \omega_i}{\partial r}, \quad (4.4b)$$

$$q_{\text{ax}} = -\lambda_{\text{ax}}^{(\text{eff})} \frac{\partial T}{\partial z}, \quad (4.4c)$$

$$q_{\text{rad}} = -\lambda_{\text{rad}}^{(\text{eff})} \frac{\partial T}{\partial r}. \quad (4.4d)$$

In order to calculate the pressure loss along the catalyst bed, the reactor-scale model includes a pseudo-steady-state momentum balance in form of the Darcy-Forchheimer equation:

$$\frac{\partial p}{\partial z} = -\frac{\mu_f^{(\text{av})}}{K} v_{\text{sup}}^{(\text{av})} - \frac{\rho_f^{(\text{av})}}{c_F} v_{\text{sup}}^{(\text{av})2}. \quad (4.5)$$

Its use in transient reactor models is common because the full transient momentum balance is very stiff and thus difficult to solve. As the pressure drop caused by the solid catalyst is usually dominant, the pseudo-steady-state momentum balance provides a good description of the pressure distribution in fixed-bed reactors (see [2, 83]). The calculation of the fluid velocity and its distribution from mass continuity is discussed in the next section.

Finally, the reactor-scale model is completed by an equation of state (EOS), here for a perfect gas, to link the fluid density to pressure, temperature, and gas phase composition:

$$\rho_f = \frac{p M_f}{R_u T}. \quad (4.6)$$

For high pressure applications or highly non-ideal species, the use of real gas EOS should be considered to obtain accurate predictions.

The remaining fluid properties such as the viscosity  $\mu_f$  and the specific heat capacity  $c_{p,f}$  are calculated in dependency of the local temperature and gas phase composition using established correlations by Kleiber and Joh [146] and mixture rules [22] (see Appendix F, pp. 157 ff.).

### 4.3.2 Flow models

As described in Section 2.3.7, pp. 44 ff., the fluid velocity has a significant influence on the effective transport parameters of catalytic sponges. So far, two different approaches were applied to calculate the superficial fluid velocity and its distribution in solid sponges.

#### Plug flow

Most frequently, plug flow with a uniform radial velocity distribution is assumed for catalytic sponges in monolithic applications because of the constant porosity along the radius [5, 19, 48, 59, 70, 223, 296]. For a constant cross-sectional area, the total mass flux or gas load  $G$  remains constant within the catalyst bed because of mass conservation:

$$G = \rho_f v_{\text{sup}} = \text{const.} \quad (4.7)$$

Thus, the superficial velocity  $v_{\text{sup}}$  can easily be obtained from the gas load, which is defined by the operating conditions, and the fluid density.

#### Radial velocity distribution

In analogy to the complex velocity distribution in packed beds of pellets, which exhibits a maximum in the near-wall region as a result of the increasing bed porosity and then decreases to zero at the wall because of wall friction, Gräf et al. [95] and Reitzmann et al. [233] assumed a radial velocity distribution for catalytic sponges. They used the extended Brinkmann equation to calculate the decrease of the superficial velocity near the reactor wall:

$$\frac{\partial p}{\partial z} = -\frac{\mu_f}{K} v_{\text{sup}}(r) - \frac{\rho_f}{c_F} v_{\text{sup}}^2(r) + \mu^{(\text{eff})} \left( \frac{\partial^2 v_{\text{sup}}(r)}{\partial r^2} + \frac{1}{r} \frac{\partial v_{\text{sup}}(r)}{\partial r} \right). \quad (4.8)$$

Herein,  $\mu^{(\text{eff})}$  is the effective viscosity that accounts for the increased momentum transport in the catalyst bed. Because of the lack of models for the effective viscosity of solid sponges, Gräf et al. [95] and Reitzmann et al. [233] used the model of Giese et al. [87] that was originally developed for packed beds of spherical pellets:

$$\mu_{\text{eff}} = 2\mu_f \exp(2 \cdot 10^{-3} Re_h). \quad (4.9)$$

For catalytic sponges, Gräf et al. [95] used  $Re_h = \rho_f v_{\text{sup}}^{(\text{av})} d_h / \mu_f$  with the hydraulic diameter  $d_h$  as characteristic length.

The solution of the extended Brinkman equation, Eq. (4.8), however, is only possible for constant temperature, which cannot be assumed for most catalytic applications. Consequently, Gräf et al. [95] proposed the following procedure to calculate the velocity distribution in catalytic sponges. First, the Darcy-Forchheimer equation, Eq. (4.5), is integrated

using the inlet conditions to estimate the pressure at the reactor outlet. Second, the extended Brinkmann equation, Eq. (4.8), is solved numerically, again using the inlet conditions, subject to

$$\left. \frac{\partial p}{\partial z} \right|_{z=0} = \frac{p_{\text{out}}^2 - p_{\text{in}}^2}{2p_{\text{in}}L}, \quad (4.10a)$$

$$\left. \frac{\partial v_{\text{sup}}}{\partial r} \right|_{r=0} = 0 \quad (4.10b)$$

$$v_{\text{sup}}(r = R) = 0. \quad (4.10c)$$

A detailed derivation of the pressure gradient at the inlet is given by Brandstädter and Kraushaar-Czarnetzki [28].

Afterwards, the average superficial velocity is calculated from the obtained velocity distribution:

$$v_{\text{sup}}^{(\text{av})} = \frac{8}{D_{\text{t}}^2} \int_0^{R_{\text{t}}} v_{\text{sup}}(r) r dr'. \quad (4.11)$$

Finally, a velocity damping factor  $D_{\text{v}}$  is defined as the ratio of the local superficial velocity and the average velocity:

$$D_{\text{v}}(r) = \frac{v_{\text{sup}}(r)}{v_{\text{sup}}^{(\text{av})}}. \quad (4.12)$$

The velocity damping factor is thus zero at the wall, and approximately one in the center of the catalyst bed. During the solution of the reactor model, the superficial velocity can then be calculated by

$$v_{\text{sup}}(r) = \frac{G}{\rho_{\text{f}}} D_{\text{v}}(r). \quad (4.13)$$

By using the velocity damping factor, the absolute magnitude of the superficial velocity is calculated from mass conservation taking into account the local pressure, temperature, and composition within the catalyst bed (see perfect gas equation, Eq. (4.6)), while the shape of the superficial velocity distribution is given by the velocity damping factor  $D_{\text{v}}$ . Thus, the influence of the radial velocity distribution can be incorporated into the reactor model. The pressure loss along the catalyst bed is still calculated using average superficial velocity (see Eq. (4.5)). Nevertheless, neither the influence of the radial velocity distribution on heat and mass transport in solid sponges, nor the radial velocity distribution in solid sponges itself has been investigated yet.

### 4.3.3 Initial and boundary conditions

The applied initial and boundary conditions to solve Eqns. (4.1) to (4.5) are listed in Tab. 4.1. Special attention is required in case of the boundary conditions at the reactor outlet, and in case of the set temperature at the reactor wall. For the Neumann boundary conditions at the reactor outlet, the physical domain of the catalyst bed is enlarged in the axial direction by an outflow region of length  $L_{\text{out}}$ , in which the bulk catalyst density was set to zero. This corresponds to the application of uncoated sponges in the outflow region. The consideration of the outflow region is necessary to reduce the influence of the no-flux boundary conditions at the outlet on the temperature and concentration distribution in the

**TAB. 4.1.** Summary of initial and boundary conditions applied for the solution of the reactor-scale model.

Location		Mass balances Eqns. (4.1)	Energy balance Eq. (4.2)	Momentum balance Eq. (4.5)
initial values	$t = 0$	$\omega_i(0, z, r) = \omega_i^{(\text{in})}$	$T(0, z, r) = T_{\text{in}}$	-
reactor inlet	$z = 0$	$\omega_i(t, 0, r) = \omega_i^{(\text{in})}$	$T(t, 0, r) = T_{\text{in}}$	$p(t, 0, r) = p_{\text{in}}$
reactor outlet	$z = L_{\text{tot}}$	$j_{\text{ax},i}(t, L_{\text{tot}}, r) = 0$	$q_{\text{ax}}(t, L_{\text{tot}}, r) = 0$	-
reactor axis	$r = 0$	$j_{\text{rad},i}(t, z, 0) = 0$	$q_{\text{rad}}(t, z, 0) = 0$	-
reactor wall	$r = R_t$	$j_{\text{rad},i}(t, z, R_t) = 0$	$T(t, z, R_t) = T_{\text{wall}}(t, z)$	-

catalyst bed. The length of the outflow region should be chosen based on the fluid velocity. For the simulations in this work, however, an outflow length of 20 % of the total length of the catalyst bed was sufficient to remove the influence of the outlet boundary conditions on the temperature and concentration distribution in the catalyst bed.

At the reactor wall, a Dirichlet boundary condition was chosen for the energy balance because an ideal contact between the struts of the catalytic sponges and the reactor wall was assumed. Experimentally this can be achieved by wrapping the sponges in a highly thermally conductive foil, e. g., carbon (see Mülheims et al. [193]). As mentioned in Section 2.3.8 (pp. 46 ff.), an ideal thermal contact can be assumed if more than 20 % of the struts are in good with the reactor wall (see Razza et al. [231]).

#### 4.3.4 Numerical approach and solution procedure

The reactor-scale model equations were solved using a numerical method of lines [249, 291]. Therefore, the spatial derivatives in the axial and the radial direction were discretized on a grid of Gauss-Lobatto-Chebyshev nodes using a pseudo-spectral method [71]. The convective terms in Eqns. (4.1) and (4.2), however, were discretized using a standard upwind procedure to ensure numerical stability (see for example Ferziger and Peric [68]). For the time-integration, the well-established CVODE solver from the SUNDIALS suite [109] was used. During each integration step, the fluid properties, the effective transport parameters, the heat and mass transfer coefficients, and the effectiveness factors were updated at every point of the computational grid using the local pressure, temperature, and composition of the fluid mixture.

Again, all models were implemented in Python [289, version 2.7, [www.python.org](http://www.python.org)] to allow easy access to the code for non-professional programmers, and flexibility regarding different reactions and catalyst supports. Performance-critical parts of the code, such as the evaluation of the kinetic rate equations and the fluid mixture models, were translated to C to reduce computation time (speedup of 1.5–8.5 depending on the function).

#### 4.3.5 Simplified steady-state reactor model without axial dispersion

In addition to the full transient reactor-scale model described in Section 4.3.1, a simplified model that disregards axial dispersive transport of heat and mass as well as transient changes was implemented. Such models are typically used for packed beds of pellets

(see for example Schlereth and Hinrichsen [255]) because of the discontinuous solid phase and the dominance of convective transport in the axial direction. Reitzmann et al. [233] used the same model for catalytic sponges, however, did not take the catalyst scale into consideration. The simplified mass, heat, and momentum balances for the simplified model are:

$$\underbrace{\rho_f v_{\text{sup}} \frac{\partial \omega_i}{\partial z}}_{\text{axial convection}} = - \underbrace{\frac{\partial j_{\text{rad},i}}{\partial r} - \frac{1}{r} j_{\text{rad},i}}_{\text{radial dispersion}} + \underbrace{\rho_{\text{cat}}^{(\text{bulk})} M_i \sum_{j=1}^{n_R} v_{ij} \eta_j r_j^{(m)}}_{\text{chemical reactions}} \quad (4.14)$$

$$\underbrace{\rho_f c_{p,f} v_{\text{sup}} \frac{\partial T}{\partial z}}_{\text{axial convection}} = - \underbrace{\frac{\partial q_{\text{rad}}}{\partial r} - \frac{1}{r} q_{\text{rad}}}_{\text{radial dispersion}} + \underbrace{\rho_{\text{cat}}^{(\text{bulk})} \sum_{j=1}^{n_R} (-\Delta_R H_j) \eta_j r_j^{(m)}}_{\text{reaction heat}} \quad (4.15)$$

$$\frac{\partial p}{\partial z} = - \frac{\mu_f^{(\text{av})}}{K} v_{\text{sup}}^{(\text{av})} - \frac{\rho_f^{(\text{av})}}{c_F} v_{\text{sup}}^{(\text{av})^2}. \quad (4.16)$$

From a numerical point of view, the main advantage of the simplified model is that the outlet boundary equations can be omitted. Consequently, the partial differential equations (4.14) to (4.16) can be integrated numerically along the reactor coordinate  $z$  instead of along time  $t$ . Thus, only the derivatives in the radial direction have to be discretized, which reduces the computational costs for integration massively. Accordingly, for the simulations in this work, the computational time for a single simulation dropped approximately by a factor of 60–100 on a standard workstation (Intel®Core™ i5-2400, 3.1 GHz, 32 GB RAM) from several hours for the full transient model to several minutes for the simplified model. All other boundary conditions are identical to the full transient model (see Tab. 4.1); the initial conditions are not required in the simplified model.

## 4.4 Description of the catalyst-scale model

### 4.4.1 Heat, mass, and momentum balances

The catalyst-scale model describes the combined reaction-diffusion processes within the mesoporous catalyst (see Fig. 4.1) and thus allows to calculate the effectiveness factors  $\eta_j$ , which are required in the reactor scale model. Additionally, interfacial transfer of mass and heat from the bulk gas phase through the diffusion film to the catalyst surface is considered in the boundary conditions of the model (see Section 4.4.3). Thorough studies on reaction-diffusion problems were presented, among others, by Lim and Dennis [172], Solsvik and Jakobsen [264, 265], and Solsvik et al. [266].

Similar to the reactor-scale model, the catalyst-scale model describes the mesoporous catalyst as a pseudo-homogeneous medium with effective transport properties. Consequently, it is sufficient to consider only the coordinate perpendicular to the catalyst surface, which

simplifies the model to 1-d. Thus, the mass, heat, and momentum balance at the catalyst scale read

$$\underbrace{\frac{dj_i}{d\zeta} + \frac{g}{\zeta}j_i}_{\text{transport}} = \underbrace{\rho_{\text{cat}}^{(\text{cat})} M_i \sum_{j=1}^{n_R} \nu_{ij} r_j^{(m)}}_{\text{chemical reactions}}, \quad (4.17)$$

$$\underbrace{\frac{dq}{d\zeta} + \frac{g}{\zeta}q}_{\text{transport}} = \underbrace{\rho_{\text{cat}}^{(\text{cat})} \sum_{j=1}^{n_R} (-\Delta_R H_j) r_j^{(m)}}_{\text{reaction heat}}, \quad (4.18)$$

$$\frac{\varepsilon_{\text{cat}}}{\tau_{\text{cat}}^2} \frac{dp}{d\zeta} = -A_A \sum_{i=1}^{n_s} M_i^{-1/2} j_i. \quad (4.19)$$

Herein, the factor  $g$  takes into account the shape of the catalyst (flat coating:  $g = 0$ ; cylindrical pellet:  $g = 1$ ; spherical pellet:  $g = 2$ ), and  $\varepsilon_{\text{cat}}$  and  $\tau_{\text{cat}}$  are the open porosity and tortuosity of the catalyst. The calculation of the mass and heat fluxes,  $j_i$  and  $q$ , and the definition of the coefficient  $A_A$  in the momentum equation (4.19), are given in the next section.

#### 4.4.2 Flux models

The diffusive mass fluxes  $j_i$  in the catalyst-scale model are calculated with the *cylindrical pore interpolation model* (CPIM) developed by Young and Todd [311]. The CPIM allows to model simultaneous molecular multicomponent diffusion, viscous flow, and Knudsen diffusion in capillaries and porous media over the whole range of Knudsen numbers. Thus, it is well suited to simulate mass transport in mesoporous catalysts. The heat flux is modeled as usual using Fourier's law. In mathematical form, the flux relations are

$$\frac{\varepsilon_{\text{cat}}}{\tau_{\text{cat}}^2} \frac{d\rho_i}{d\zeta} = \sum_{k=1}^{n_s} \left( \frac{\omega_{ij} j_k}{D_{ki}^{(\text{eff})}} - \frac{\omega_{kj} j_i}{D_{ik}^{(\text{eff})}} \right), \quad (4.20a)$$

$$q = -\lambda_{\text{coat}} \frac{dT}{d\zeta}, \quad (4.20b)$$

with the effective binary diffusion coefficients  $D_{ik}^{(\text{eff})}$  of species  $i$  in species  $k$ . The quantities,  $\varepsilon_{\text{cat}}$  and  $\tau_{\text{cat}}$  are the open porosity and the tortuosity of the mesoporous catalyst. The binary effective diffusion coefficients and the coefficient  $A_A$  in the momentum equation (4.19) are calculated by the following interpolation relations between the continuum regime (index c) and the Knudsen regime (index Kn):

$$\frac{1}{D_{ij}^{(\text{eff})}} = \frac{1}{D_{ij}} + \frac{1}{D_i^{(\text{Kn})}}, \quad (4.21a)$$

$$\frac{1}{A_A} = \frac{1}{A_c} + \frac{1}{A_{\text{Kn}}}, \quad (4.21b)$$

**TAB. 4.2.** Summary of the boundary conditions applied for the solution of the catalyst-scale model in case of infinite transfer rates (a), and finite transfer rates (b). The boundary conditions at the catalyst surface act as scale bridge and connect the catalyst-scale model with the reactor-scale model.

Location	Mass balances Eqns. (4.17)	Energy balance Eq. (4.18)	Pressure balance Eq. (4.19)
(a) neglecting transfer limitations—infinite transfer rates			
catalyst center	$\zeta = 0$	$j_i(0) = 0$	$q(0) = 0$
catalyst surface	$\zeta = \delta$	$\omega_i(\delta) = \omega_i^{(\text{bulk})}$	$T(\delta) = T_{\text{bulk}}$
(b) considering transfer limitations—finite transfer rates			
catalyst center	$\zeta = 0$	$j_i(0) = 0$	$q(0) = 0$
catalyst surface	$\zeta = \delta$	$\omega_i(\delta) = \omega_i^{(\text{bulk})} + \frac{j_i(\delta)}{\rho_f \beta_i}$	$T(\delta) = T_{\text{bulk}} + \frac{q(\delta)}{\alpha}$

with

$$D_i^{(\text{Kn})} = \frac{d_p}{3} \left( \frac{8R_u T}{\pi M_i} \right)^{1/2}, \quad (4.22a)$$

$$A_c = \frac{32\mu_f}{\rho_f d_p^2 \sum_{i=1}^{n_s} \omega_i M_i^{-1/2}}, \quad (4.22b)$$

$$A_{\text{Kn}} = \frac{3}{2d_p} \left( \frac{\pi R_u T}{2} \right)^{1/2}. \quad (4.22c)$$

Here,  $d_p$  denotes the average diameter of the pores in the catalyst. The CPIM was first applied to reaction-diffusion problems by Lim and Dennis [172]. In comparison to the frequently used, but often criticized dusty gas model (DGM, see Kerkhof [139]), the CPIM provided similar values regarding the simulated mass fluxes and effectiveness factors.

#### 4.4.3 Boundary conditions and solution of the catalyst-scale model

For the catalyst-scale model, two sets of boundary conditions are considered. First, if interfacial heat and mass transfer limitations are disregarded, i. e., the heat and mass transfer rates are theoretically infinite (see Tab. 4.2 a), the mass fractions and temperature at the catalyst surface are set to equal the mass fractions and temperature of the bulk gas phase. If, however, heat and mass transfer limitations need to be considered, the mass and heat fluxes at the catalyst surface are set equal to the heat and mass fluxes through the diffusional film above the catalyst surface:

$$j_i(\delta) = \rho_f \beta_i \left[ \omega_i(\delta) - \omega_i^{(\text{bulk})} \right], \quad (4.23a)$$

$$q(\delta) = \alpha [T(\delta) - T_{\text{bulk}}]. \quad (4.23b)$$

In Tab. 4.2 b, the Robin boundary conditions at the surface, Eqns. (4.23a) and (4.23b), were rewritten to provide one boundary condition for each variable ( $\omega_i$ ,  $j_i$ ,  $T$ , and  $q$ ) and thus ensure a well-posed system of equations. For the limiting case of fast mass and heat transfer,  $\beta_i \rightarrow \infty$  and  $\alpha \rightarrow \infty$ , the boundary conditions in Tab. 4.2 b are equivalent to the

ones in Tab. 4.2 a. Nevertheless, in cases in which mass and heat transfer limitations can be disregarded anyway, the use of the Dirichlet boundary conditions in Tab. 4.2 a allows a slightly faster and more stable solution of the reaction-diffusion problem.

### Numerical solution of the catalyst-scale model

The catalyst model was solved during each integration step and at every grid point of the reactor-scale model using a well-established 4th-order collocation method [143] with automatic grid refinement and a damped Newton-Raphson method to solve the system of non-linear equations.

#### 4.4.4 Calculation of the effectiveness factor

The effectiveness factors  $\eta_j$ , required in the reactor-scale models, were calculated as the ratio of the average reaction rate in the mesoporous catalyst and the reaction rate at bulk conditions:

$$\eta_j = \frac{r_{m,j}^{(av)}}{r_{m,j}^{(bulk)}} = \frac{1}{r_{m,j}^{(bulk)}} \frac{g+1}{\delta^{g+1}} \int_0^\delta r_{m,j}(\zeta) \zeta^g d\zeta. \quad (4.24)$$

Again, the factor  $g$  takes into account the shape of the catalyst (thin coating:  $g = 0$ ; cylindrical pellet:  $g = 1$ ; spherical pellet:  $g = 2$ ).

If heat transfer limitations are absent, the effectiveness factors take values between zero and unity because of mass transfer limitations between the fluid and solid phase, and, more relevant, mass transport limitations in the mesoporous catalyst. If heat transfer limitations are dominant, however, the effectiveness factors might be larger unity for exothermic reactions because the catalyst heats up. The increased temperature accelerates the chemical reactions and thus over-compensates mass transport limitations in the catalyst leading to higher reaction rates in the catalyst than in the bulk gas phase.

#### 4.4.5 Simplified models to approximate the effectiveness factor

Another approach to calculate the effectiveness factors  $\eta_j$  in the reactor-scale models, at least for single reactions, are analytical approximations such as the frequently used first-order approximation and Bischoff's [24] underestimated general-reaction-rate approximation.

##### First-order approximation

The first-order approximation is the simplest model to calculate effectiveness factors, and it is thus found in many chemical engineering textbooks (see for example Jess and Wasserscheid [135, Sect. 4.5.4, p. 250]). Based on the analytical solution of the reaction-diffusion problem for a first-order, irreversible power-law reaction rate model, the effectiveness factor is approximated by

$$\eta_j = \frac{\tanh(\phi_j)}{\phi_j}, \quad (4.25)$$

with the Thiele modulus

$$\phi_j = \frac{V_{cat}}{A_{cat,ext}} \sqrt{\frac{k_{m,j} \rho_{cat}^{(env)}}{D_i^{(eff)}}}. \quad (4.26)$$

Herein,  $k_{m,j}$  is the mass-based reaction rate coefficient, and  $D_i^{(\text{eff})} = \varepsilon_{\text{cat}}/\tau_{\text{cat}}^2 D_{\text{mol},i}$  is the effective diffusion coefficient of a key species  $i$  in the catalyst;  $D_{\text{mol},i}$  is the molar diffusion coefficient of the key species  $i$  (see Appendix F, pp. 157 ff.). The first-order approximation is simple and easy to apply, however, it fails to accurately estimate the effectiveness factors of many real-world applications because of its reduction to first-order, irreversible reactions.

### Bischoff's general-reaction-rate approximation

A more practical approximation is Bischoff's [24] general-reaction-rate approximation. He solved the reaction-diffusion problem for general forms of the reaction rate, including power-law and Langmuir-Hinshelwood models, under the following assumptions: first, only one key species encounters mass transport limitations in the mesoporous catalyst; second, the concentration of the key species in the center of the catalyst is exactly zero, corresponding to moderate mass transport limitations. Recently, a modern derivation of Bischoff's approximation was presented by Kaiser et al. [137]. Accordingly, the generalized Thiele modulus is defined as

$$\phi_j = \frac{V_{\text{cat}}}{A_{\text{cat,ext}}} \frac{\rho_{\text{cat}}^{(\text{env})} r_{m,j}(p_i^{(\text{bulk})})}{\sqrt{2D_i^{(\text{eff})}}} \left[ \int_0^{p_i^{(\text{bulk})}} \rho_{\text{cat}}^{(\text{env})} r_{m,j}(p_i) dp_i' \right]^{-1/2}. \quad (4.27)$$

Herein,  $p_i$  is the partial pressure (concentration) of the key species  $i$ . The antiderivative of the integral in Eq. (4.27) can readily be determined using modern computer algebra systems (CAS, e. g., Wolfram Mathematica [306]), and hard-coded in computer programs for fast evaluation. The effectiveness factor is then calculated from the asymptotic solution of Eq. (4.25) for  $\phi_j \rightarrow \infty$  (see [24, 137]):

$$\eta_j = 1/\phi_j. \quad (4.28)$$

Because of the applied assumptions, however, the approximation fails in cases in which the concentration of the key species does not decrease to zero in the center of the catalyst (only slight mass transport limitations for  $\phi_j \rightarrow 0$ ), or in which other than the key species encounter significant mass transport limitations in the mesoporous catalyst.

### Comparison of the full catalyst-scale model and general-rate-approximation

Figure 4.2 a shows a comparison of the effectiveness factor calculated with the full catalyst-scale model and the general-rate-approximation of Bischoff [24] for CO<sub>2</sub>-methanation in a spherical catalyst pellet ( $\varnothing 3$  mm) at 10 bar and H<sub>2</sub>/CO<sub>2</sub>=4 over different temperatures. For the calculations, the kinetic model of Koschany et al. [154] and the average catalyst properties summarized in Tab. 3.2, p. 62, were used; mass and heat transfer limitations were disregarded. The gaps for the full model are due to a singularity in the kinetic model of Koschany et al. [154] at  $p_{\text{CO}_2} = 0$  that causes a failure of the numerical Newton-Raphson solver. Vanishing carbon dioxide concentrations occur frequently if internal mass transport limitations within the mesoporous catalyst are dominant, e. g., for conventional pellets and high temperatures.

For the considered configuration, the general-rate approximation of Bischoff [24] reproduces the effectiveness factor calculated with the full catalyst-scale model within 10 %

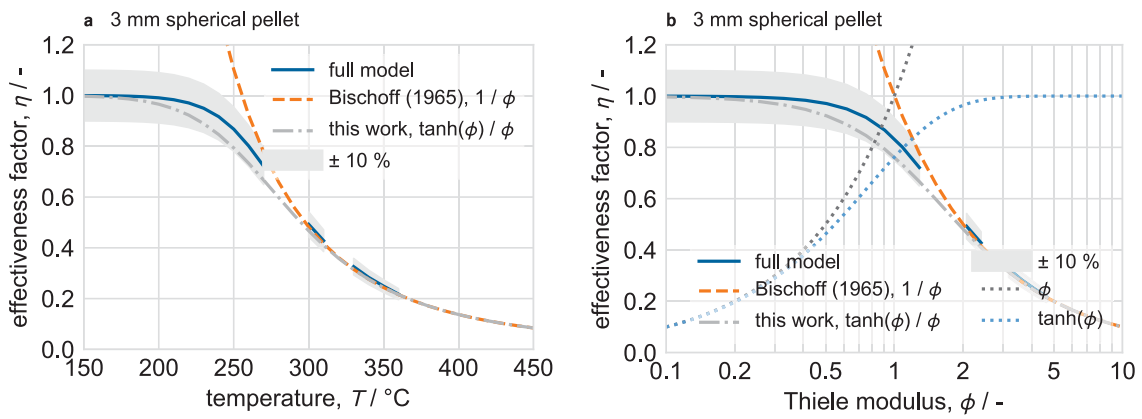


**FIG. 4.2.** Effectiveness factor over temperature (a) and Thiele modulus (b) calculated with the full model, the general-rate-approximation of Bischoff [24], and the cured approximation presented in this work for CO<sub>2</sub>-methanation in a spherical catalyst pellet ( $\varnothing$ 3 mm) at 10 bar and H<sub>2</sub>/CO<sub>2</sub>=4. For the calculations, the kinetic model of Koschany et al. [154] and the average catalyst properties summarized in Tab. 3.2, p. 62, were used. In addition, mass and heat transfer limitations were disregarded.

relative accuracy for temperatures above 275 °C. At lower temperatures the general-rate approximation significantly overestimates the effectiveness factor, which would lead to an overestimated heat release in the reactor-scale model. If the expression for the effectiveness factor of the first-order approximation, Eq. (4.25), is used with the definition of the general Thiele modulus, Eq. (4.27), however, the cured approximation agrees within 10 % over the whole temperature range. The reason for the good match between the cured approximation and the full catalyst-scale model is seen in Fig. 4.2 b, which shows the calculated effectiveness factor over the generalized Thiele modulus. For Thiele moduli up to approximately 0.5,  $\tanh(\phi)$  behaves like  $\phi$  (see dotted lines in Fig. 4.2 b). Thus, the cured solution,  $\tanh(\phi)/\phi$ , gives an effectiveness factor of approximately 1 for low Thiele moduli. For Thiele moduli above 2,  $\tanh(\phi)$  is 1. As a consequence, the cured approximation,  $\tanh(\phi)/\phi$ , converges with the approximation of Bischoff, which uses  $\eta = 1/\phi$ . Consequently,  $\tanh(\phi)$  smoothly switches between the regime of negligible transport limitations ( $\phi \leq 0.5$ ) and the one of significant transport limitations ( $\phi \geq 2$ ), and thus allows an accurate estimation of the effectiveness factor over the whole range of Thiele moduli, at least for the considered case.

Even if the assumptions made during the derivation of Bischoff's general-reaction-rate approximation are not justified, the cured approximation will still give good estimations for low to moderate Thiele moduli because of the mathematical nature of the tanh-function. This is particularly useful for thin catalyst coats on solid sponges, honeycombs, and POCS. Figure 4.3 shows the comparison between the full catalyst-scale model, Bischoff's general-reaction-rate approximation, and the cured approximation regarding the effectiveness factor for a 100  $\mu$ m thick catalyst coat. The conditions are the same as for the spherical catalyst pellet discussed above. Because of the thin coating, mass transport in the mesoporous catalyst only limits the reaction for temperatures above 350 °C. While the cured approximation provides a good estimation of the effectiveness factor within 10 % over the

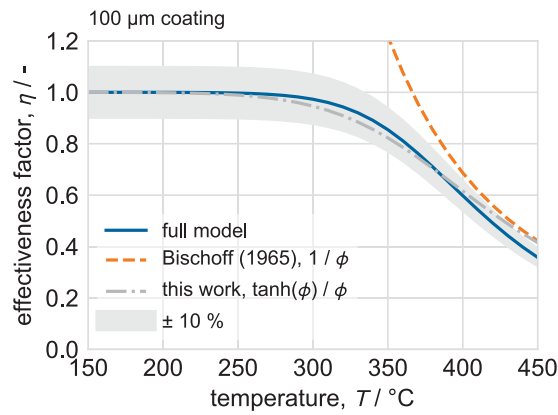


**FIG. 4.3.** Effectiveness factor over temperature calculated with the full model, the general-rate-approximation of Bischoff [24], and the cured approximation presented in this work for CO<sub>2</sub>-methanation in a 100 μm thick catalyst coating at 10 bar and H<sub>2</sub>/CO<sub>2</sub>=4. For the calculations, the kinetic model of Koschany et al. [154] and the average catalyst properties summarized in Tab. 3.2 (see Section 3.2.2) were used; mass and heat transfer limitations were disregarded.

whole temperature range, the original general-rate-approximation merely reaches the same accuracy for temperatures above 400 °C.

Consequently, for solid sponges and single reactions, the cured approximation allows to accurately calculate the effectiveness factors of the thin catalyst coating at a fraction of the cost of the full catalyst-scale model. In case of the coating, speedups of up to 500 were achieved with the current implementation of the cured solution.



## 5.1 Validation of the implemented reactor model

The validation of the implemented reactor model against experimental data is crucial to assess the predictive quality of the model. Therefore, the reactor model was used to simulate the conducted polytropic fixed-bed reactor experiments (see Section 3.4, pp. 71 ff.). The resulting temperature profiles were then compared to the measured temperature profiles for CO<sub>2</sub>-methanation. Furthermore, the calculated carbon-dioxide conversions and methane yields were compared to the corresponding values obtained from the downstream GC analysis in the experiments. It should be noted that, in contrast to the study of Gräf et al. [95], no model parameter was adjusted during the solution of the reactor model to fit the calculated temperature profiles to the measured ones.

If not stated otherwise, the models of Fishedick et al. [70], Dietrich et al. [48], and Dietrich [46] were used in the simulations to calculate the radial and axial effective thermal conductivities, and the heat and mass transfer coefficients. The solid thermal conductivity was set to  $3 \text{ W m}^{-1} \text{ K}^{-1}$  (mullite, see Tab. 2.3, p 29) for all temperatures because of its low dependency of the temperature. Based on a grid study (see Tab. A.1, p. 138, in Appendix A), 15 axial and 7 radial nodes were used to discretize the governing equations of the reactor-scale model for all simulations. Accordingly, 7 radial nodes were chosen in case of the simplified reactor model. For comparison, Bremer et al. [29] applied a Finite-Volume method to simulate methanation reactors and obtained a convergent solution for 16 axial and 5 radial cells, which is consistent with the results acquired in this study. Depending on the operating conditions, the resulting computational times varied between 2 h–5 h for the full transient reactor model, and between 2 min–5 min for the simplified reactor model on a standard workstation (Intel® Core™ i5-2400, 3.1 GHz, 32 GB RAM). For the full transient reactor model, a simulation time of 60 min was chosen to ensure steady state for all considered operating conditions. The velocity profile was assumed uniform in all validation simulations. An analysis of the influence of the radial velocity profile on the temperature and concentration fields is given in Section 5.1.2.

### 5.1.1 Stability of the catalyst during polytropic operation and reproducibility of the lab-scale fixed-bed reactor experiments

A necessary prerequisite for the validation of the reactor model, is the stability of the catalyst for the time of the measurements and the reproducibility of the polytropic CO<sub>2</sub>-methanation experiments. As described above, all experiments for sponges of a certain pore density, e. g., 10 ppi, were conducted with the same catalyst. In addition, at least two experimental runs had to be conducted to measure the axial *and* the wall temperature and thus to obtain a complete set of temperature profiles. In order to assess the stability of the catalyst, the first set of operation conditions for each catalyst was repeated two times, once in between and once at the end of all experiments with the same catalyst. In between

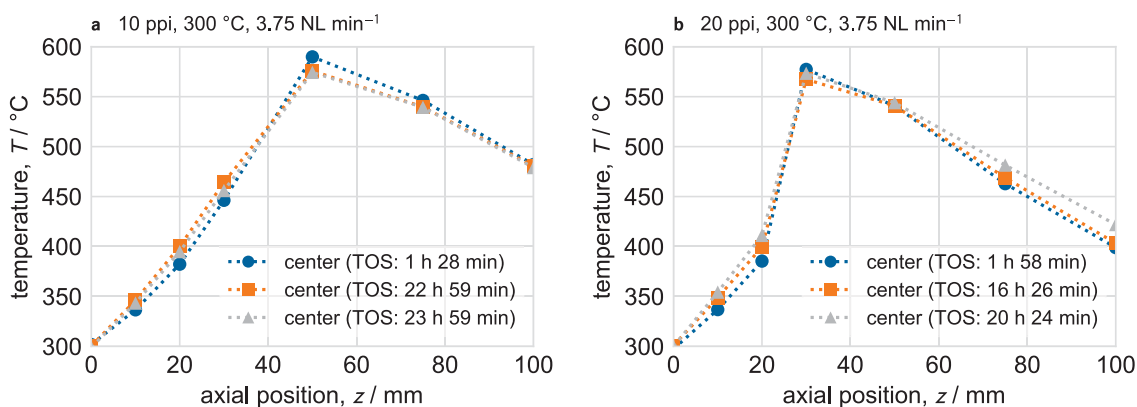


**FIG. 5.1.** Comparison of measured axial temperature profiles for the 10 ppi (a) and 20 ppi (b) sponges after different times on stream (TOS) during discontinuous operation of the same catalyst. The feed was a 4:1  $\text{H}_2/\text{CO}_2$ -mixture at  $300\text{ }^\circ\text{C}$  and 4 bar; the flow rate was  $3.75\text{ NL min}^{-1}$ .

the replicate measurements, the catalyst was tested under different operating conditions. Figure 5.1 shows the axial temperature profiles of the 10 ppi (a) and 20 ppi (b) catalytic sponges measured after different time on stream (TOS) during discontinuous operation (multiple periods of continuous operation ranging from 1.5 h–7 h; in between the operation periods the reactor was shut down and the catalyst was contained in an inert nitrogen atmosphere, see Section 3.4, pp. 71 ff.) at feed conditions of  $300\text{ }^\circ\text{C}$ , 4 bar,  $\text{H}_2/\text{CO}_2 = 4$ , and  $3.75\text{ NL min}^{-1}$ .

For both sponge types, the measured axial temperature profiles are almost identical after approximately 24 h and 20.5 h of operation, respectively, even at temperature peaks up to  $600\text{ }^\circ\text{C}$ . The corresponding conversions of 0.77 (10 ppi, for all three experiments) and 0.77–0.79 (20 ppi) remained also stable over the whole operation period. Similar results were obtained for the 40 ppi catalytic sponges. Consequently, the catalyst did not deactivate notably during the time of the experiments. In addition, the results demonstrate that the polytropic methanation experiments were reproducible regarding flow rate and inlet temperature.

### 5.1.2 Comparison of simulated and measured axial temperature profiles during $\text{CO}_2$ -methanation

Figures 5.2 a–f show the comparison of the measured and simulated axial temperature profiles for the 10 ppi, 20 ppi and 40 ppi sponges at an inlet temperature of  $300\text{ }^\circ\text{C}$  and flow rates of  $3.75\text{ NL min}^{-1}$  and  $7.5\text{ NL min}^{-1}$ . In addition to the results of the full reactor model, the temperature profile calculated with the simplified model that disregards axial dispersion are shown. The wall temperature profiles were used as boundary condition in the simulations (see Tab. 4.1, p. 82). In all cases, the measured wall temperature was not uniform because of heat transport limitations in the surroundings of the catalyst bed that were caused by the lack of active cooling. Thus, the wall temperature was higher in the first 20 mm of the catalyst bed than the center temperature because of thermal conduction in the reactor tube.

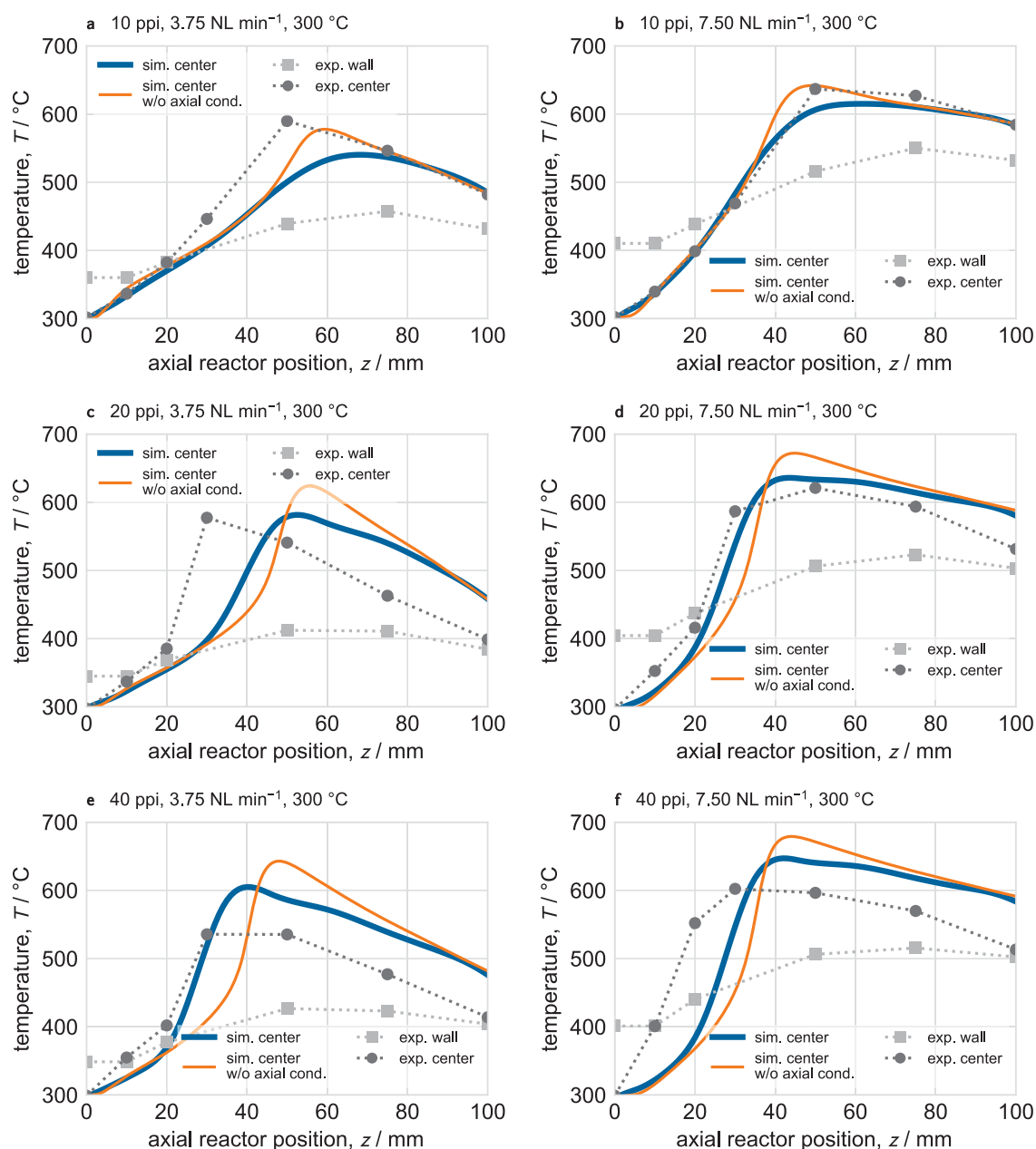


**FIG. 5.2.** Comparison of the measured and simulated axial steady-state temperature profiles in 10 ppi (a and b), 20 ppi (c and d), and 40 ppi (e and f) catalytic sponges during CO<sub>2</sub>-methanation over a 5 wt% Ni/Al<sub>2</sub>O<sub>3</sub> catalyst. The dimensions of the catalyst bed were  $\varnothing 25 \text{ mm} \times 100 \text{ mm}$ ; the feed was a 4:1 H<sub>2</sub>/CO<sub>2</sub>-mixture at 300 °C and 4 bar; the flow rates were 3.75 NL min<sup>-1</sup> (a, c, e) and 7.5 NL min<sup>-1</sup> (b, d, f). For the simulations, the models of Fishedick et al. [70], Dietrich et al. [48], and Dietrich [46] were used to calculate the radial and the axial ETC, and the heat and mass transfer coefficients, respectively.

In case of the 10 ppi and 20 ppi sponges at 300 °C and 3.75 NL min<sup>-1</sup> (see Fig. 5.2 a and c), the onset of the reaction at around 20 mm is underestimated by the reactor model. Nevertheless, the shape of the measured and simulated temperature profiles matches well in case of the full reactor model. If the flow rate is doubled (see Fig. 5.2 b and d), the simulated temperature profiles of both, the full and the simplified reactor model, agree almost perfectly with the measured temperature profiles for the 10 ppi and 20 ppi sponges

at 300 °C inlet temperature. The small difference between the full and the simplified reactor model, which disregards axial dispersion of heat and mass, at the higher flow rates is due to the dominance of convective heat and mass transport in the axial direction. Thus, axial dispersion of heat and mass does not have a considerable influence. In contrast to the lower flow rate (3.75 NL min<sup>-1</sup>), the good match of the simulated and measured temperature profiles at the higher flow rate is probably explained by the more accurate measurement of the inlet and the wall temperature profile, which were used as boundary conditions for the simulations. Because of the metallic sheath of the thermocouples, not only heat transfer from the fluid to the thermocouple sheath, but also thermal conduction within the metal sheath of the thermocouples influenced the temperature measurement. A simulation study of the temperature distribution within the used thermocouples (see Appendix A.3, pp. 139 ff.) revealed that the temperature measurement in the given setup and at the given conditions is only accurate within 5 K–30 K depending on the fluid velocity and the temperature difference between the wall and the center of the catalyst bed. At high flow rates, heat transfer from the fluid to the sheath of the thermocouples is dominant compared to the thermal conduction within the thermocouple case. Consequently, the temperatures are measured more accurately at high flow rates. The influence of the measured wall temperature is discussed in more detail further below.

For the 40 ppi sponges at 3.75 NL min<sup>-1</sup> and 300 °C (see Fig. 5.2 e), the onset of the reaction in the first 30 mm of the catalyst bed is predicted well by the full reactor model. In the experimental data, the hot spot probably lies between 30 mm–50 mm and was not captured because of the spatial resolution of the thermocouples in that region. After the hot spot, the simulated temperatures are significantly higher than the measured temperatures. Again, a possible explanation for the discrepancies is the accuracy of the temperature measurement with the thermocouples. In addition, the full reactor model, which takes into account axial dispersion, assumes a continuous catalyst bed. In the experiment, however, four sponges were stacked to obtain the full catalyst bed. Consequently, the full reactor model overestimates the influence of axial heat conduction which is certainly limited at the boundaries of the individual sponge segments in the experiment. Furthermore, the comparison between the measured and simulated temperature profiles indicates the relevance of axial conduction *against* the flow direction. In case of the full reactor model, which includes thermal conduction in the axial direction, the temperatures at 20 mm is increased by a conductive heat flux against the flow direction. Hence, the position of the temperature peak is captured well. In contrast, heat transport against the flow direction is not possible in case of the simplified reactor model, and the position of the hot spot is thus overestimated.

At the high flow rate (7.5 NL min<sup>-1</sup>), the match of the simulated and measured temperature profiles for the 40 ppi sponges and 300 °C (see Fig. 5.2 f) is not as good as for the 10 ppi and 20 ppi sponges. Compared to the 20 ppi sponges, the measured temperature, however, increased rapidly in the first 20 mm although both sponges exhibit a similar bulk catalyst density. A possible reason might be the insufficient thermal coupling of the first sponge to the reactor wall. Based on the available information, however, no clear explanation for the discrepancy could be found.

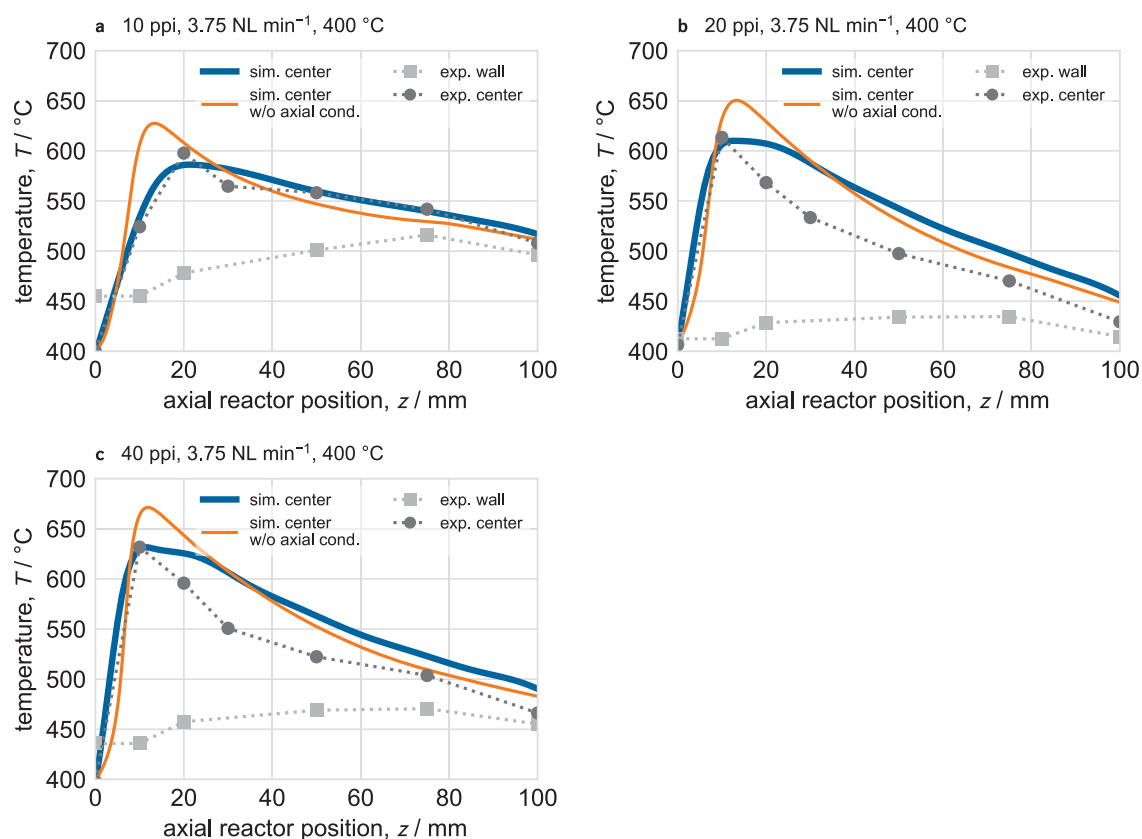


**FIG. 5.3.** Comparison of the measured and simulated axial steady-state temperature profiles in 10 ppi (a), 20 ppi (b), and 40 ppi (c) catalytic sponges during CO<sub>2</sub>-methanation over a 5 wt% Ni/Al<sub>2</sub>O<sub>3</sub> catalyst. The dimensions of the catalyst bed were  $\varnothing 25 \text{ mm} \times 100 \text{ mm}$ ; the feed was a 4:1 H<sub>2</sub>/CO<sub>2</sub>-mixture at 400 °C and 4 bar; the flow rate was 3.75 NL min<sup>-1</sup>. For the simulations, the models of Fishedick et al. [70], Dietrich et al. [48], and Dietrich [46] were used to calculate the radial and the axial ETC, and the heat and mass transfer coefficients, respectively.

At inlet temperatures of 400 °C and a flow rate of 3.75 NL min<sup>-1</sup> (see Fig. 5.3), the models match the experimental data reasonably well for all sponges. Because of the higher activity of the catalyst at high temperatures, the hot spot shifted to the first 10 mm–20 mm of the catalyst bed. As a result of the high reaction rates, the heat released by the chemical reaction controls the shape of the axial temperature profile, which is well captured by the full and the simplified reactor model for all investigated sponges. After the hot spot, the measured temperature is significantly lower than the simulated temperature for the 20 ppi and 40 ppi sponges (see Fig. 5.3 b and c). Again, the accuracy of the temperature measurement with the thermocouples might lead to the consistent discrepancy of the center temperature after the hot spot, especially at this low flow rate. If the temperature increases, as in the beginning of the catalyst bed, also the fluid velocity increases which leads to more effective heat transfer between the fluid and the thermocouples and thus to a better accuracy of the temperature measurement. At higher flow rates, an inlet temperature of 400 °C could not be maintained with the used heater sleeves in the experiments.

In case of the 10 ppi sponge, the measured and simulated temperatures also match well after the hot spot (see Fig. 5.3 a). This might indicate that the heat transfer between the fluid and the thermocouples was better in the large cells of the 10 ppi sponge, than in the small

**TAB. 5.1.** Comparison of the measured and simulated carbon-dioxide conversions,  $X_{\text{CO}_2}$ , and methane yields,  $Y_{\text{CH}_4}$ , calculated with the full reactor model and with the simplified reactor model that disregards axial dispersive heat and mass transport. The values should be compared column-wise in stacks of three for each feed condition.

Feed conditions	Method	10 ppi		20 ppi		40 ppi	
		$X_{\text{CO}_2}$	$Y_{\text{CH}_4}$	$X_{\text{CO}_2}$	$Y_{\text{CH}_4}$	$X_{\text{CO}_2}$	$Y_{\text{CH}_4}$
300 °C, 3.75 NL min <sup>-1</sup>	experiment	0.77	0.71	0.77	0.75	0.76	0.74
	full model	0.65	0.57	0.68	0.62	0.75	0.71
	simpl. model	0.70	0.63	0.71	0.66	0.76	0.73
300 °C, 7.50 NL min <sup>-1</sup>	experiment	0.73	0.53	0.73	0.62	0.73	0.65
	full model	0.72	0.59	0.74	0.64	0.74	0.64
	simpl. model	0.73	0.61	0.74	0.64	0.74	0.64
400 °C, 3.75 NL min <sup>-1</sup>	experiment	0.78	0.72	0.82	0.80	0.79	0.76
	full model	0.78	0.74	0.79	0.77	0.81	0.79
	simpl. model	0.79	0.77	0.81	0.80	0.83	0.81

cells of the 20 ppi and 40 ppi sponges. Here, the sponges might have caused unfavorable flow patterns around the thermocouples that caused inefficient heat transfer between the fluid and the thermocouples.

Again, the simplified reactor model consistently predicts higher hot spot temperatures because axial dispersion of heat, which broadens the temperature peak, is disregarded. Other than that, the temperature profiles calculated with the simplified model also match reasonably well with the experimental data.

In addition to the axial center temperature profiles, the measured and calculated carbon dioxide conversions and methane yields were compared (see Tab. 5.1). Except for the cases in which the temperature profiles do not match, i. e., for the 10 ppi and 20 ppi sponges at 300 °C at 3.75 NL min<sup>-1</sup>, the measured and simulated conversions and yields agree well considering a 10 % relative error of the experimental measurement because of the use of the simple carbon balance (see Ducamp et al. [56]).

In conclusion, the presented experimental and numerical results demonstrate the many difficulties, such as heat transport limitations in the surrounding of the catalyst bed and the accuracy of the temperature measurement with thermocouples, that have to be dealt with when validating reactor models for heterogeneous catalyst in gas-phase reactions. Nevertheless, a very good comparison could be obtained for cases in which the boundary conditions such as the inlet and wall temperature are well characterized. Again, it should be noted that no parameter was adjusted in the reactor models to fit the simulated temperature profiles to the measured ones. Thus, although the experimental data is not accurate enough to explore the bounds of the reactor models, it can be concluded that both implemented reactor models provide realistic temperature distributions and yields for the methanation of carbon dioxide within catalytic sponges.

### **Influence of the measured wall temperature on the simulated temperature profiles**

As described above and in Appendix A.3, pp. 139 ff., the measurement of the temperature with the used thermocouples was subject to systematic errors. Especially at low flow rates heat transfer from the fluid to the sheath of the thermocouples and thermal conduction

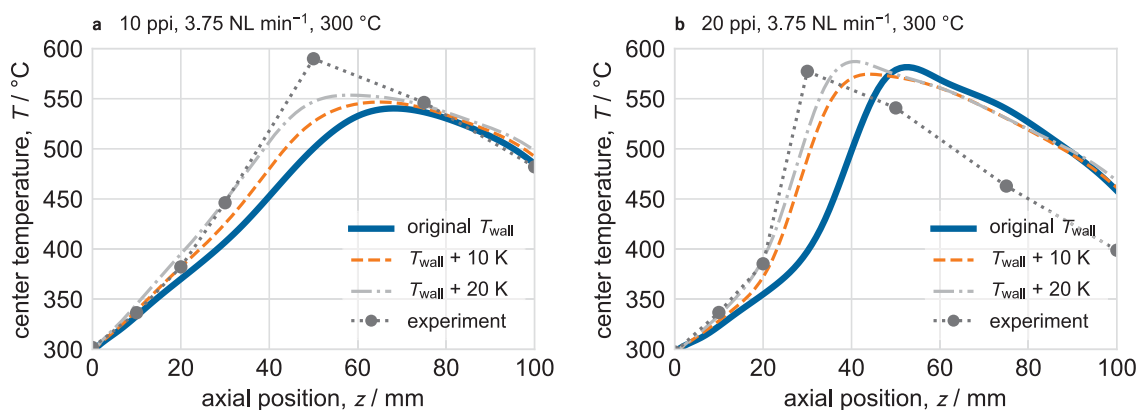


**FIG. 5.4.** Influence of the wall temperature on the axial center temperature profile for the 10 ppi (a) and 20 ppi (b) catalytic sponges and a 4:1  $\text{H}_2/\text{CO}_2$ -mixture at  $300^\circ\text{C}$  and 4 bar as feed. For the simulations, the measured wall temperatures were artificially increased by 10 K and 20 K, respectively.

within the thermocouples limited the accuracy of the measurement. Thus, the measured wall temperatures, which serve as boundary condition in the model, could have been actually higher in the experiments. Therefore, the simulations for the 10 ppi and 20 ppi at an inlet temperature of  $300^\circ\text{C}$  and a flow rate of  $3.75 \text{ NL min}^{-1}$  were repeated with artificially increased wall temperatures by 10 K and 20 K.

In both cases, the increase of the wall temperature by 20 K leads to a better comparison of the measured and simulated temperature profiles (see Fig. 5.4). Especially in the case of the 20 ppi catalytic sponges, an increase of the wall temperature by 20 K provides a much better prediction of the onset of the reaction and the development of the hot spot. Thus, the results indicate that the wall temperature has a significant influence on the simulated temperature profile, particularly in regimes of high parametric sensitivity as in the case of the 20 ppi sponges. Thus, accurate temperature measurements are necessary for the validation of reactor models.

### **Influence interfacial heat and mass transfer, and internal heat and mass transport limitations**

The influence of interfacial heat and mass transfer limitations between the fluid and solid phase, and the one of internal heat and mass transport limitations within the catalyst layer were additionally investigated for the 20 ppi catalytic sponges. At an inlet temperature of  $300^\circ\text{C}$  and a flow rate of  $3.75 \text{ NL min}^{-1}$ , the full model provides the best match with the experimental data, at least in terms of the hot-spot temperature, because heat transfer between the fluid and solid phase was relevant (see Fig. 5.5 a). If interfacial heat transfer is disregarded, the model failed to correctly calculate the hot-spot temperature by about 75 K. Almost the same result is obtained if neither interfacial transfer nor internal transport limitations are considered in the model, indicating that internal mass transport in the catalyst coat was not limiting the reaction at the given temperatures.

For a flow rate of  $7.5 \text{ NL min}^{-1}$  and an inlet temperature of  $300^\circ\text{C}$ , all three model variants matched well with the measured axial temperature profile because external heat and mass transfer was improved as a result of the higher flow rate (see Fig. 5.5 b). While the

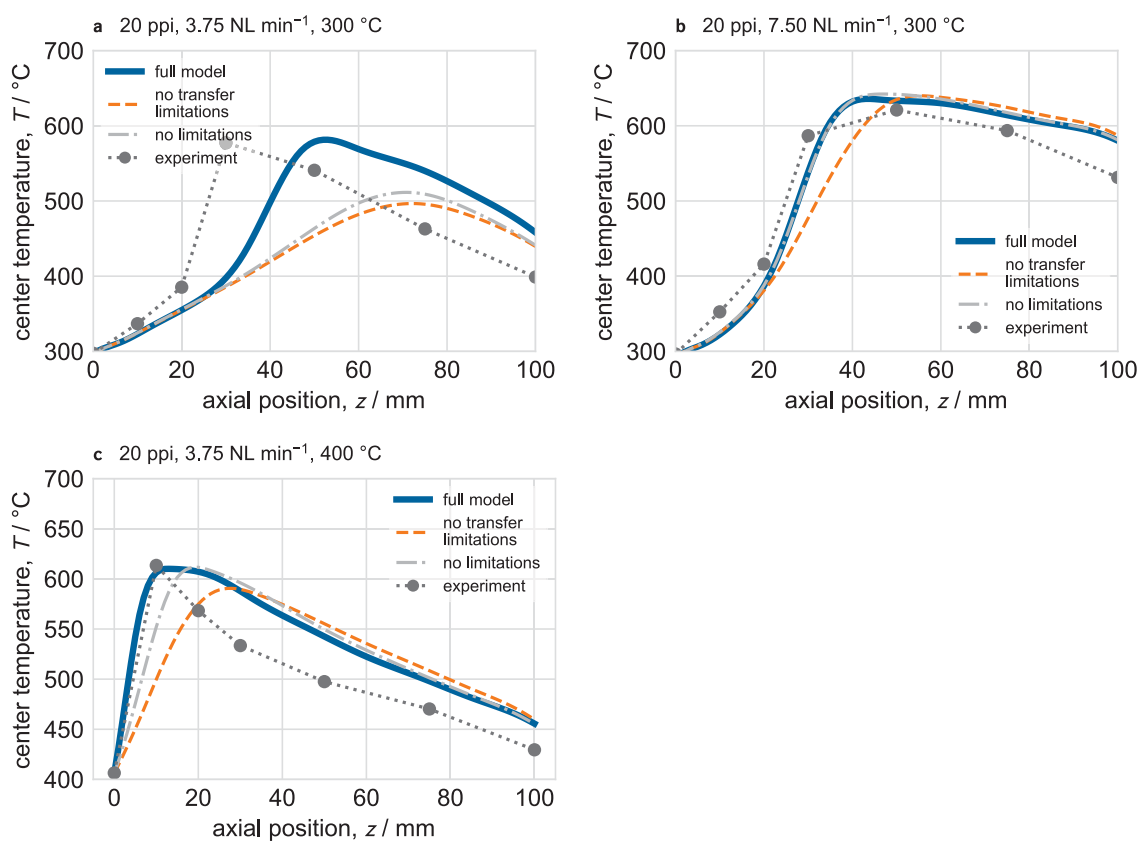


**FIG. 5.5.** Comparison of measured and simulated axial center temperature profiles in 20 ppi sponges for (a) 300 °C, 3.75 NL min<sup>-1</sup>, (b) 300 °C, 7.5 NL min<sup>-1</sup>, and (c) 400 °C, 3.75 NL min<sup>-1</sup> at the beginning of the catalyst bed. The simulations show the influence of interfacial heat and mass transfer, and mass transport within the catalyst, on the predictive quality of the reactor-scale model. The feed was a 4:1 H<sub>2</sub>/CO<sub>2</sub>-mixture at 4 bar. The models of Fishedick et al. [70], Dietrich et al. [48], and Dietrich [46] were used to calculate the radial and the axial ETC, and the heat and mass transfer coefficients, respectively.

full model and the variant that completely disregards interfacial and internal limitations almost yielded the same temperature profile, the variant that only considered internal transport limitations slightly underestimated the measured temperature profile in regions of high temperatures. Consequently, internal mass transport was in this case compensated by external heat transfer limitations that led to an increase of the catalyst temperature, and thus increased the productivity of the catalyst. The same effect is observed for an inlet temperature of 400 °C and a flow rate of 3.75 NL min<sup>-1</sup> (see Fig. 5.5 c). Nevertheless, the difference between the full model and the model variant that completely neglects interfacial and internal transport limitations is larger than for an inlet temperature of 300 °C because the effects of internal mass transport limitations were only partially compensated by an increase of the catalyst temperature as a result of heat transfer limitations.

The results clearly illustrate the complex interplay of interfacial heat and mass transfer limitations and internal heat and mass transport limitations. Therefore, the influence of interfacial transfer limitations should always be checked when comparing simulations to data from lab-scale experiments, either by solving a dedicated catalyst-scale model or by using well-established approximations (Weisz-Prater criteria, see for instance [135]). If

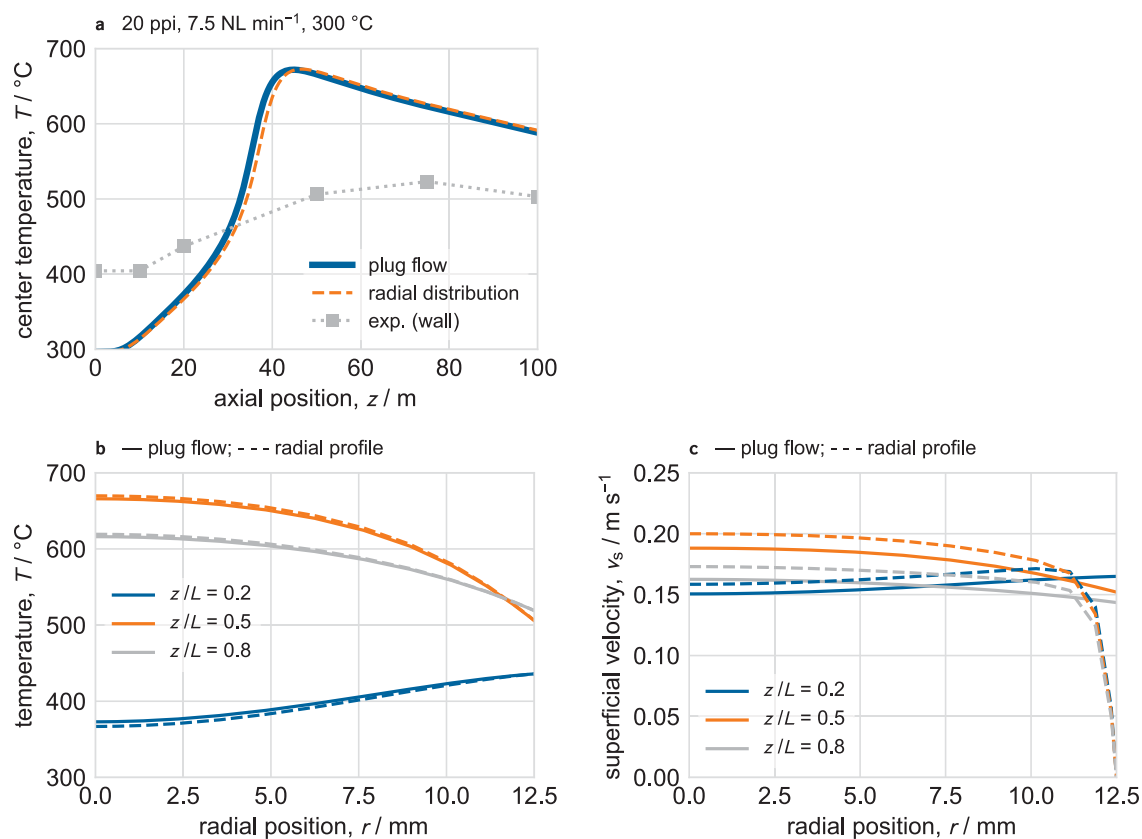


**FIG. 5.6.** Influence of the of the radial velocity profile on the axial center temperature profile (a) and the radial temperature profiles (b) for the 20 ppi catalytic sponges at 300 °C and 7.5 NL min<sup>-1</sup>. The calculated radial velocity profiles are shown in c.

interfacial transfer limitations are disregarded completely, one can still obtain good matches between simulations and experiments, however, one would also draw wrong conclusions from the results.

### Influence of the radial velocity profile on the temperature distribution

In addition to the influence of interfacial heat and mass transfer and internal heat and mass transport limitations on the simulated axial temperature profiles, the influence of the radial velocity distribution was investigated. Therefore, the flow models described in Section 4.3.2, pp. 80 ff., were used in the simplified reactor model. Based on the 3-d  $\mu\text{CT}$  models and detailed CFD simulations (see Appendix D, pp. 149 ff.), it was shown in this work that the solution of the extended Brinkmann equation and the utilization of the velocity damping factor introduced by Gräf et al. [95] can successfully describe the radial velocity profile in solid sponges, although it uses an effective viscosity model that was originally developed for packed beds of pellets.

Figure 5.6 shows the comparison of the axial center temperature profile for the 20 ppi catalytic sponges at 300 °C and 7.5 NL min<sup>-1</sup>, calculated with the plug flow model and the radial superficial velocity profile estimated from the extended Brinkman equation. In order to resolve the small hydrodynamic boundary layer at the wall, 15 instead of 7 radial nodes were applied in the simulations. Also, the simplified reactor model was used. Although the superficial velocities differ remarkably in the vicinity of the reactor wall (see Fig. 5.6 c), the

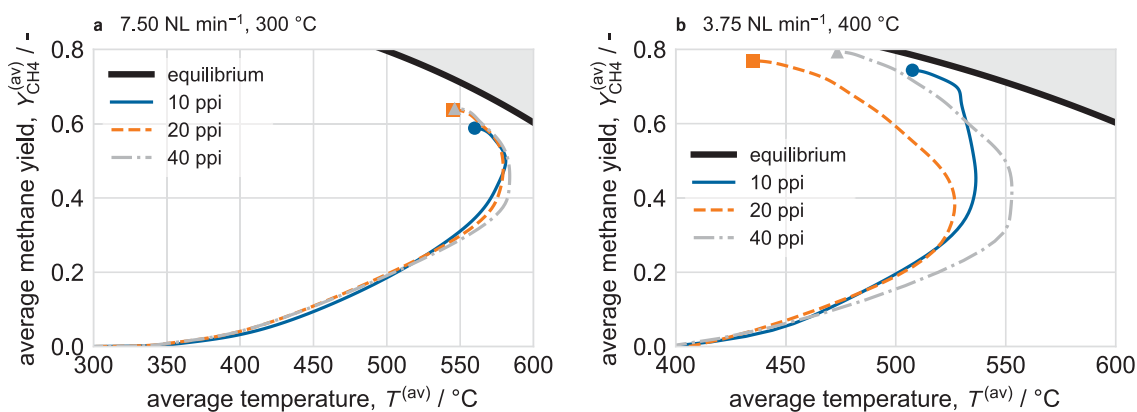


**FIG. 5.7.** Comparison of the 10 ppi, 20 ppi and 40 ppi catalytic sponges in the yield-temperature plane for feed conditions of (a) 300 °C and 7.5 NL min<sup>-1</sup>, and (b) 400 °C and 3.75 NL min<sup>-1</sup>. The pressure was 4 bar and H<sub>2</sub>/CO<sub>2</sub> = 4. The radially averaged yield-temperature profiles were extracted from the solution of the full reactor-scale model.

resulting axial center temperature profiles are almost identical (see Fig. 5.6 c). The methane yields are also equal regardless which flow model was applied. In addition, the radial temperature profiles at different axial positions are almost identical, even close to the wall. Consequently, for the investigated sponges, the shape of the superficial velocity profile is not relevant because of the uniform radial porosity, and the dominance of thermal conduction regarding radial heat transport. Nevertheless, at higher flow rates, the low superficial velocities near the wall could have an influence on heat transport if the contributions of thermal conduction and hydrodynamic dispersion are in the same order of magnitude.

#### Assessment of the performance of the investigated sponges during CO<sub>2</sub>-methanation

Finally, the performance of the investigated sponges as catalyst support for the methanation of carbon dioxide was compared. Figure 5.7 a and b show the simulated, radially averaged methane yields  $Y_{\text{CH}_4}^{(\text{av})}$  over the radially averaged temperature  $T^{(\text{av})}$  at 300 °C and 7.5 NL min<sup>-1</sup>, and at 400 °C and 3.75 NL min<sup>-1</sup>. The profiles were calculated with the full reactor-scale model including axial dispersion of heat and mass. The radially averaged values were chosen because they also take the radial distribution of the yield and the temperature into account.

At 300 °C and a flow rate of 7.5 NL min<sup>-1</sup> no significant difference between the 10 ppi, 20 ppi and 40 ppi sponges is observable regarding the yield and hot-spot temperature. The final yield is slightly higher for the 20 ppi and 40 ppi sponges because of the higher bulk catalyst density. At 400 °C and a flow rate of 3.75 NL min<sup>-1</sup>, however, the 20 ppi sponges show the best performance. Similar to the 40 ppi sponges, they reach a methane yield of approximately 0.8, but exhibit a 25 K lower hot-spot temperature which indicates better heat transport in the 20 ppi sponges, probably as a result of the slightly lower porosity. The 10 ppi sponges lie in the middle of the 20 ppi and 40 ppi sponges regarding the hot-spot temperature but reach a slightly lower methane yield. Consequently, based on the conducted experiments, sponges should exhibit a high catalyst load, and thus a large specific surface area, to reach high methane yields, and a rather low porosity to control the hot-spot temperature for exothermic gas-phase reactions.

### 5.1.3 Model validation against operando Magnetic Resonance Spectroscopy Imaging measurements

In addition to the comparison against conventionally obtained temperature profiles and downstream integral conversion measurements, the implemented reactor-scale model was compared to *operando* Magnetic Resonance Spectroscopy Imaging (MRSI) measurements during the hydrogenation of ethylene to ethane over a 1 wt% Pt/Al<sub>2</sub>O<sub>3</sub> catalyst supported on the 10 ppi sponges investigated in this work (see Ulpts et al. [285]). MRSI allows to measure the local distribution of MRSI-active reactants (H<sub>1</sub> containing molecules), such as ethylene and ethane, within the solid sponges, and thus provides insight into mass transport. Furthermore, the obtained data can be used for additional validation of the implemented reactor model. The MRSI experiments for gas-phase reactions were recently developed and conducted in-house by Ulpts et al. [283–285]. The main challenge for MRSI experiments are limitations regarding applicable materials (non-magnetic) and the maximum temperature (about 200 °C for the given setup). Consequently, the hydrogenation of ethylene to ethane was chosen as model reaction because it proceeds at temperatures below 200 °C and does not require a magnetic catalyst material such as nickel, cobalt, or iron.

For the MRSI experiments, two of the 10 ppi sponges were coated as described above (see Section 3.2, p. 61) with an in-house synthesized catalyst, tightly fitted into a glass tube, and inserted into a custom-made glass reactor; the size of the catalyst bed was  $\varnothing 25 \text{ mm} \times 50 \text{ mm}$ . The reactor was heated with a pressurized air flow in the outer shell. In order to measure the axial temperature profile in the center of the catalyst bed and at the wall, two thin glass capillaries ( $\varnothing 0.68 \text{ mm}$ ) were filled with ethylene glycol, and inserted axially in the catalyst bed; the magnetic resonance signals of the ethylene glycol allowed to deduce the temperature within the glass capillaries and thus within the catalyst bed after prior calibration. For experimental details and a description of the MRSI technique see Ulpts et al. [283, 285].

The simulations were performed with the full reactor-scale model using the models of Wallenstein et al. [296] and Dietrich et al. [48] for the radial and axial ETC of the sponges. Because of the much lower temperatures compared to the methanation reaction, thermal radiation was disregarded and the model of Wallenstein et al. [296] was applicable. Again, the measured wall temperature was set as wall boundary condition in the model. Prior to the simulations, a kinetic power-law model for the 1 wt% Pt/Al<sub>2</sub>O<sub>3</sub> during hydrogenation of ethylene was determined (see Ulpts et al. [285]). The numerical procedure was identical to the procedure described in Section 3.3.2, pp. 67 ff. Figure 5.8 shows a comparison of the measured and simulated axial temperature profile (a) and the axial ethane mole fraction profile (b, radially averaged) for a feed of 52 vol%/8 vol%/40 vol% C<sub>2</sub>H<sub>4</sub>/H<sub>2</sub>/Ar at atmospheric pressure and 50 °C. The total flow rate was 0.987 NL min<sup>-1</sup>.

In general, the simulated profiles agree almost perfectly with the measured data for both the axial temperature and average ethane mole fraction profiles. The simulation captures the increase of the temperature from 50 °C to about 140 °C within the first 10 mm of the catalyst ( $\Delta_R H = -137 \text{ kJ mol}^{-1}$  at 298.15 K), as well as the subsequent decrease of the

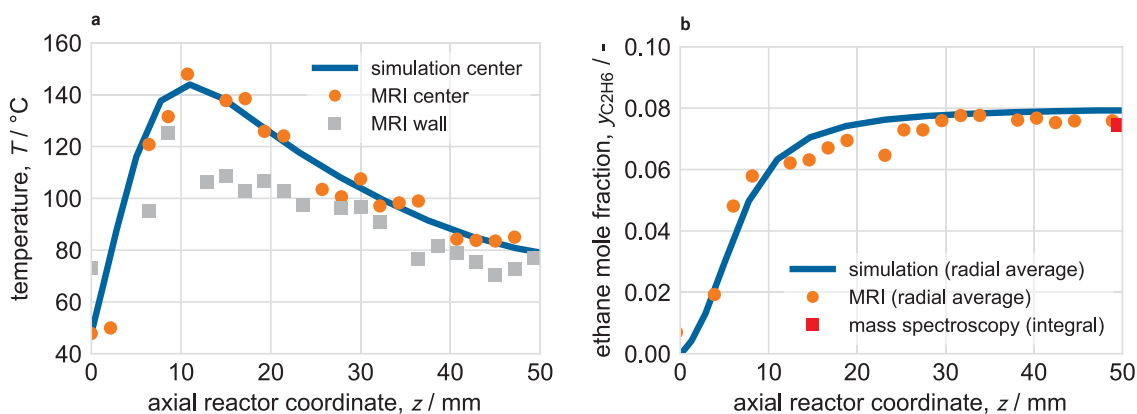


**FIG. 5.8.** Comparison of the measured and simulated axial temperature profile (a) and the radially-averaged ethane mole fraction along the axial reactor coordinate (b). The experimental data was obtained from *operando* MRSI experiments during hydrogenation of ethylene to ethane over a 1 wt% Pt/Al<sub>2</sub>O<sub>3</sub> catalyst supported on the 10 ppi mullite sponges investigated previously in this work. The catalyst bed was  $\varnothing 25$  mm  $\times$  50 mm. The feed was a 52 vol%/8 vol%/40 vol% C<sub>2</sub>H<sub>2</sub>/H<sub>2</sub>/Ar mixture at 50 °C and 1 bar; the total flow rate was 0.987 NL min<sup>-1</sup>. Experimental data extracted from Ulpts et al. [285].

temperature nicely (see Fig. 5.8 a). Also, the increase of the average ethane mole fraction (product) is accurately calculated with the implemented model (see Fig. 5.8 b). As the model uses a pseudo-homogeneous approach, a local comparison of the the ethane concentrations was not possible.

In conclusion, the good match between the model and the MRSI experiments demonstrates that the implemented pseudo-homogeneous multi-scale reactor model can readily be adapted to other gas-phase reactions. Furthermore, it allows predictions not only of temperature profiles, but also of concentration profiles in catalytic sponges with good accuracy, if the boundary conditions are well characterized.

## 5.2 Performance of catalytic sponges during methanation of carbon dioxide at production scale

Based on the successful validation of the implemented reactor model for catalytic sponges at the lab scale, the model was utilized to explore the potential of catalytic sponges at the production scale, which involves much higher flow rates and longer reactor tubes. Prior to an analysis of the tradeoffs regarding the design of solid sponges regarding their porosity and window diameter, and a comparison to conventional packed beds of pellets, a scale-up analysis was conducted to choose suitable operating conditions, coating thicknesses, and an appropriate level of detail in the reactor model.

### 5.2.1 Scale-up analysis of catalytic sponges for CO<sub>2</sub>-methanation

For the scale-up analysis, the approach outlined by Kraushaar-Czarnetzki and Müller [157] for the design of solid catalysts was adopted. Accordingly, a maximal thickness of the catalyst coat and a minimal fluid velocity were selected based on the activity of the chosen catalyst and the interfacial heat and mass transfer rates of solid sponges. Additionally, a runaway analysis was conducted to choose a suitable operating temperature and reactor diameter. Finally, the influence of axial dispersion in catalytic sponges at production scale was investigated.

#### Choice of the methanation catalyst

In order to obtain realistic results of the potential of catalytic sponges for CO<sub>2</sub>-methanation, the kinetic model of Koschany et al. [154] was chosen for all following simulations because it describes the activity of state-of-the-art catalysts for CO<sub>2</sub>-methanation well. Nevertheless, it disregards the formation of carbon monoxide.

Figure 5.9 shows the achievable methane yield depending on the specific flow rate  $\dot{V}_m = \dot{V}/m_{\text{cat}}$  and temperature for the 5 wt% Ni/Al<sub>2</sub>O<sub>3</sub> catalyst synthesized in this work (a) and the one with 20 wt% Ni/Al<sub>2</sub>O<sub>3</sub> investigated by Koschany et al. [154] (b) under ideal

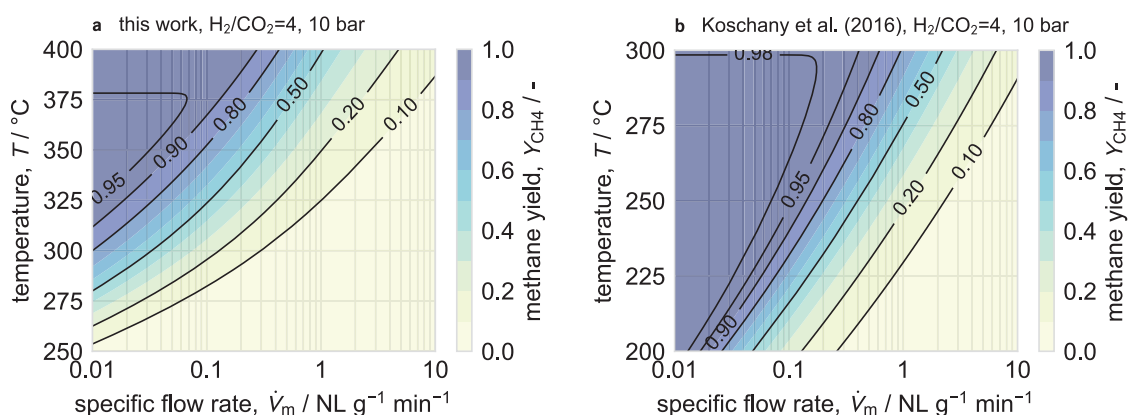


**FIG. 5.9.** Achievable methane yield  $Y_{\text{CH}_4}$  for the catalysts synthesized in this work (a) and the one synthesized by Koschany et al. [154] (b), depending on the specific flow rate  $\dot{V}_m$  and the temperature  $T$  under ideal conditions, i. e., no limitations and no temperature increase were considered. The operating conditions were  $\text{H}_2/\text{CO}_2=4$  and 10 bar. The maps allow to quickly choose the required temperature and specific flow rate for a desired methane yield.

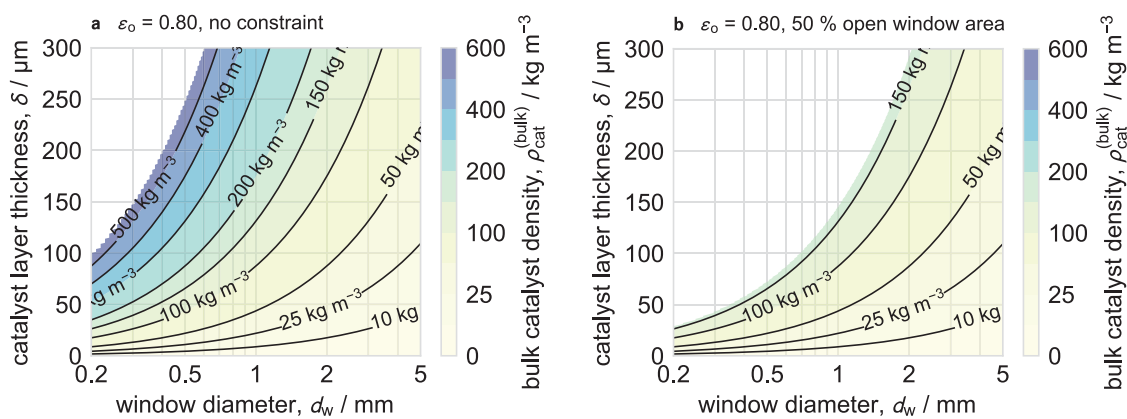


**FIG. 5.10.** Achievable bulk catalyst density, i. e., catalyst mass per unit reactor volume, depending on the window diameter and the thickness of the catalyst coating for solid sponges with an open porosity of 0.8. In the left plot (a), the catalyst coat was allowed to completely close the sponge windows ( $d_w \geq 2\delta$ ). In the right plot (b), the constraint that 50% of the window area had to remain available for fluid flow after the coating was additionally considered. The white regions in both plots indicate parameter combinations that violate the constraints.

conditions, i. e., no limitations and no temperature increase were considered. A pressure of 10 bar and a stoichiometric feed ratio of  $\text{H}_2/\text{CO}_2 = 4$  were chosen as typical feed conditions for the methanation reaction (see for instance Rieke [236] and Schlereth and Hinrichsen [255]). In comparison to the catalyst synthesized in this work, the catalyst of Koschany et al. [154] is much more active, especially at temperatures below 300 °C. The design maps allow to quickly choose a maximal specific flow rate for a given temperature and a required methane yield. For the scale-up analysis of catalytic sponges for  $\text{CO}_2$ -methanation, a temperature of 250 °C and a specific flow rate of  $0.15 \text{ NL g}_{\text{cat}}^{-1} \text{ min}^{-1}$  were chosen to obtain a methane yield of 0.9. The specific flow rate is equivalent to the weight-hourly space velocity (WHSV), however, given in  $\text{NL g}_{\text{cat}}^{-1} \text{ min}^{-1}$  in this work instead of in  $\text{NL g}_{\text{cat}}^{-1} \text{ h}^{-1}$  ( $1 \text{ NL g}_{\text{cat}}^{-1} \text{ min}^{-1} = 60 \text{ NL g}_{\text{cat}}^{-1} \text{ h}^{-1}$ ).

### Internal mass transport limitations

Mass transport in the mesoporous catalyst determines the maximal applicable thickness of the coat. Typically thin coats are applied to ensure effectiveness factors larger 0.9. For high space-time yields, however, a high bulk catalyst density is required. Consequently, the thickest coat possible should be applied, especially in the case of solid sponges because they exhibit high porosities larger 0.7 and thus use only a rather low fraction of the reactor volume for the catalytic material. The bulk catalyst density can be calculated using the specific (volumetric) surface area of the sponge, the thickness of the catalyst coat, and the catalyst properties:

$$\rho_{\text{cat}}^{(\text{bulk})} = S_V \delta (1 - \varepsilon_{\text{cat}}) \rho_{\text{cat}}^{(\text{app})}. \quad (5.1)$$

Figure 5.10 a shows that high bulk catalyst densities up to  $580 \text{ kg}_{\text{cat}} \text{ m}^{-3}$  are achievable with typical solid sponges and coat thicknesses. The white region in the upper left represents infeasible combinations of the coat thickness and the window diameter, i. e., the window is completely blocked by the coating ( $d_w \leq 2\delta$ ). In case of bulk catalyst densities above  $170 \text{ kg}_{\text{cat}} \text{ m}^{-3}$ , however, the window area that remains available for fluid flow after the

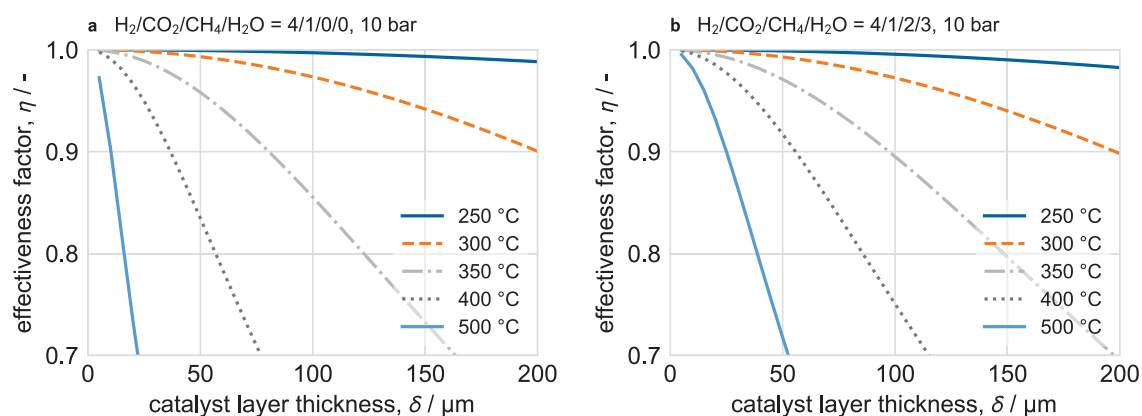


**FIG. 5.11.** Effectiveness factor of the CO<sub>2</sub>-methanation reaction depending on the thickness of the catalyst coat and on the temperature for an undiluted 4:1 H<sub>2</sub>/CO<sub>2</sub>-mixture (a), and a 4:1 H<sub>2</sub>/CO<sub>2</sub>-mixture in 20 vol% methane and 30 vol% water vapor (b). The pressure is 10 bar. Interfacial heat and mass transfer limitations were disregarded in this calculations.

coating decreases significantly. Hence, pressure loss along the catalyst bed would increase drastically during operation. For comparison, Fig. 5.10 b shows that maximal bulk catalyst densities of  $170 \text{ kg}_{\text{cat}} \text{ m}^{-3}$  are achievable, if the window cross-sectional area is not allowed to decrease by more than 50 % of the original uncoated window area. Thus, the change of the window diameter after coating should be considered for realistic estimations of the pressure loss in reactor simulations. In addition, it should be investigated if sponges with small window diameters below 0.5 mm can effectively be coated and which layer thicknesses are obtainable. A promising alternative to the conventional impregnation method concerning small window diameters, are for example sol-gel techniques that were recently applied by Schubert et al. [258] to successfully coat sponge slices with an average pore size of 0.45 mm.

To determine the maximal thickness of the catalyst coat, the catalyst model was solved for different catalyst layer thicknesses, temperatures, and gas mixtures. Interfacial heat and mass transfer limitations were disregarded. For an undiluted 4:1 H<sub>2</sub>/CO<sub>2</sub>-mixture, the effectiveness factor remains above 0.9 up to a temperature of 300 °C and layer thicknesses of 200 μm (see Fig. 5.11 a). For a temperature of 400 °C, a maximal layer thickness of only 40 μm is possible to maintain an effectiveness factor of 0.9. At 500 °C, the effectiveness factor falls below 0.9 for layer thicknesses larger 10 μm. Nevertheless, the calculated effectiveness factors correspond to the feed conditions. Inside the catalyst bed, the composition of the fluid mixture, and thus the reaction rates change. For a 4:1 H<sub>2</sub>/CO<sub>2</sub>-mixture in 20 vol% methane and 30 vol% water vapor, the maximal possible layer thicknesses increase to 60 μm and 25 μm for 400 °C and 500 °C, respectively. Thus, a layer thickness of 50 μm, which is also consistent with the catalyst layers measured in this work (see Section 3.2.2, pp 61 ff.), was chosen for further simulations. In addition, a layer thickness of 50 μm allows bulk catalyst densities of approximately  $300 \text{ kg}_{\text{cat}} \text{ m}^{-3}$  for typical solid sponges (see Fig. 5.10 a).

### Interfacial heat and mass transfer limitations

Interfacial heat and mass transfer limitations between the fluid and the solid catalyst were investigated by solving the catalyst model for a 50 μm thick catalyst coat on a sponge

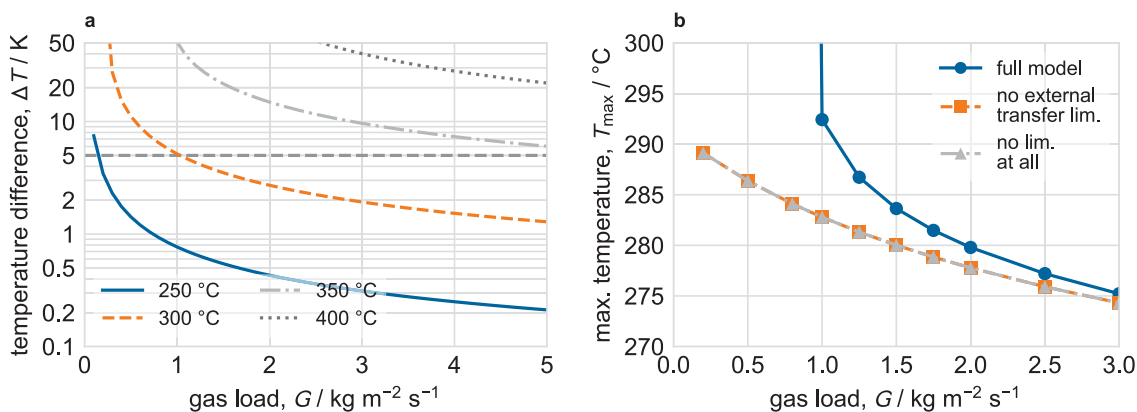


**FIG. 5.12.** Influence of the gas load on the temperature difference between the catalyst coat and the bulk fluid on the catalyst scale (a), and on the maximal temperature on the reactor scale (b). A catalyst layer thickness of  $\delta = 50 \mu\text{m}$  and a strut diameter of 2.2 mm ( $\varepsilon_o = 0.7$ ,  $d_w = 3.0 \text{ mm}$ ), which represents a worst-case scenario, were used for the catalyst-scale simulations. The simulation parameters on the reactor scale were  $\varepsilon_o = 0.75$ ,  $d_w = 0.6 \text{ mm}$ ,  $\lambda_s = 12.5 \text{ W m}^{-1} \text{ K}^{-1}$ ,  $D_t = 25 \text{ mm}$ ,  $V_m = 0.15 \text{ NL g}_{\text{cat}}^{-1} \text{ min}^{-1}$ ,  $T_{\text{in}} = 250 \text{ }^\circ\text{C}$ ,  $p_{\text{in}} = 10 \text{ bar}$ , and  $\text{H}_2/\text{CO}_2 = 4$ .

strut with a diameter of 2.2 mm ( $\varepsilon_o = 0.7$ ,  $d_w = 3 \text{ mm}$ ), which corresponds to a thick strut for solid sponges and thus represents a worst-case scenario. The heat and mass transfer coefficients were calculated with the models of Dietrich [46] and Incera Garrido et al. [129], respectively (see Section 2.3.6, pp. 41 ff.).

For the worst-case scenario described above, high gas loads up to  $5 \text{ kg m}^{-2} \text{ s}^{-1}$  are necessary at a bulk fluid temperature of  $350 \text{ }^\circ\text{C}$  to obtain a temperature difference between the fluid and the solid catalyst of only 5 K (see Fig. 5.12 a). At fluid temperatures of  $300 \text{ }^\circ\text{C}$ , however, the required gas load to reach a 5 K temperature difference between the fluid and the solid catalyst is only  $1 \text{ kg m}^{-2} \text{ s}^{-1}$ . The difference of the  $\text{CO}_2$  molar fraction in the bulk fluid and at the surface of the catalyst is at most 1 vol% for all the considered conditions. Thus, interfacial mass transport limitations can be disregarded.

In addition to the investigation of interfacial heat transfer limitations on the catalyst scale, their effect on the reactor scale was investigated using the simplified reactor model in combination with different variants of the catalyst-scale model (full model, no interfacial transfer limitations, no limitations on the catalyst scale at all). For a typical  $\text{Al}_2\text{O}_3$  sponge with  $\varepsilon_o = 0.75$ ,  $d_w = 0.6 \text{ mm}$ , and  $\lambda_s = 12.5 \text{ W m}^{-1} \text{ K}^{-1}$  at typical methanation operating conditions ( $D_t = 25 \text{ mm}$ ,  $V_m = 0.15 \text{ NL g}_{\text{cat}}^{-1} \text{ min}^{-1}$ ,  $T_{\text{in}} = 250 \text{ }^\circ\text{C}$ ,  $p_{\text{in}} = 10 \text{ bar}$ ,  $\text{H}_2/\text{CO}_2 = 4$ ), the difference of the maximal temperature within the catalyst bed (hot-spot temperature) among the models did not exceed 5 K for gas loads above  $1 \text{ kg m}^{-2} \text{ s}^{-1}$  (see Fig. 5.12 b). Thus, a gas load of  $1.5 \text{ kg m}^{-2} \text{ s}^{-1}$  was chosen in the following simulations to ensure only slight interfacial heat and mass transfer limitations. Nevertheless, if not stated otherwise interfacial heat and mass transfer limitations were explicitly taken into account during the solution of the catalyst-scale model.

### Runaway analysis

Figure 5.13 shows the maximal temperature in the catalyst bed for different inlet temperatures, tube diameters (a), and sponge materials (b) for typical sponge parameters and

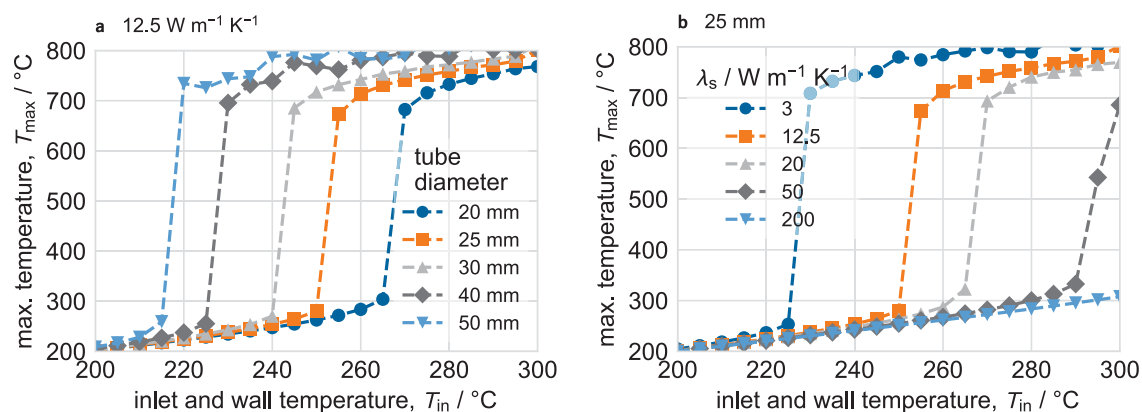


**FIG. 5.13.** Influence of the tube diameter (a) and the solid thermal conductivity (b) on the runaway behavior of catalytic sponges during CO<sub>2</sub>-methanation. The simulation parameters were  $\delta = 50 \mu\text{m}$ ,  $\epsilon_o = 0.75$ ,  $d_w = 0.6 \text{ mm}$ ,  $V_m = 0.15 \text{ NL g}_{\text{cat}}^{-1} \text{ min}^{-1}$ ,  $G = 1.5 \text{ kg m}^{-2} \text{ s}^{-1}$ ,  $T_{\text{in}} = 250 \text{ }^\circ\text{C}$ ,  $p_{\text{in}} = 10 \text{ bar}$ , and  $\text{H}_2/\text{CO}_2 = 4$ .

methanation operating conditions. The simulations were conducted with the simplified reactor model. As expected, runaway, i. e., an abrupt increase of the temperature, occurs at lower inlet temperatures for increasing tube diameters (see Fig. 5.13 a). For the considered Al<sub>2</sub>O<sub>3</sub> sponge ( $\epsilon_o = 0.75$ ,  $d_w = 0.6 \text{ mm}$ ) in a  $\varnothing 25 \text{ mm}$  reactor tube, the chosen temperature of 250 °C is already the maximal temperature before runaway occurs (see Fig. 5.13 b). In case of materials with higher thermal conductivities than Al<sub>2</sub>O<sub>3</sub>, such as SSiC, higher inlet temperatures can be applied before runaway occurs. Nevertheless, even for SSiC inlet temperatures below 290 °C and small tube diameters have to be used in case of the methanation of carbon dioxide.

The runaway plots (see Fig. 5.13) also demonstrate that catalytic sponges in particular, and coated catalysts supports in general, are very sensitive to the inlet temperature, and that runaway occurs abruptly once a certain temperature is reached. In comparison, less

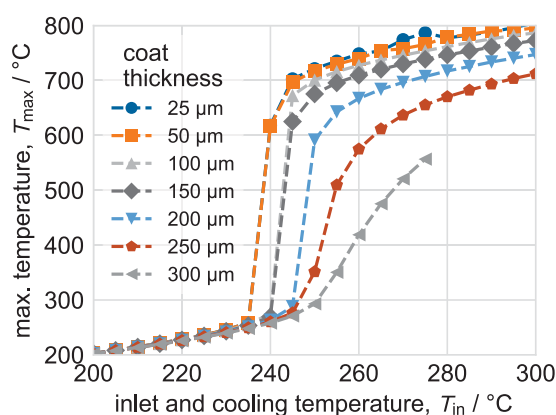


**FIG. 5.14.** Influence of the catalyst coat thickness on the runaway behavior of solid sponges during CO<sub>2</sub>-methanation. For the simulations, the window diameter was adjusted to maintain a constant bulk catalyst density of  $150 \text{ kg}_{\text{cat}} \text{ m}^{-3}$ . The simulation parameters were  $\epsilon_o = 0.75$ ,  $\lambda_s = 12.5 \text{ W m}^{-1} \text{ K}^{-1}$ ,  $D_t = 25 \text{ mm}$ ,  $V_m = 0.15 \text{ NL g}_{\text{cat}}^{-1} \text{ min}^{-1}$ ,  $G = 1.5 \text{ kg m}^{-2} \text{ s}^{-1}$ ,  $p_{\text{in}} = 10 \text{ bar}$ , and  $\text{H}_2/\text{CO}_2 = 4$ .

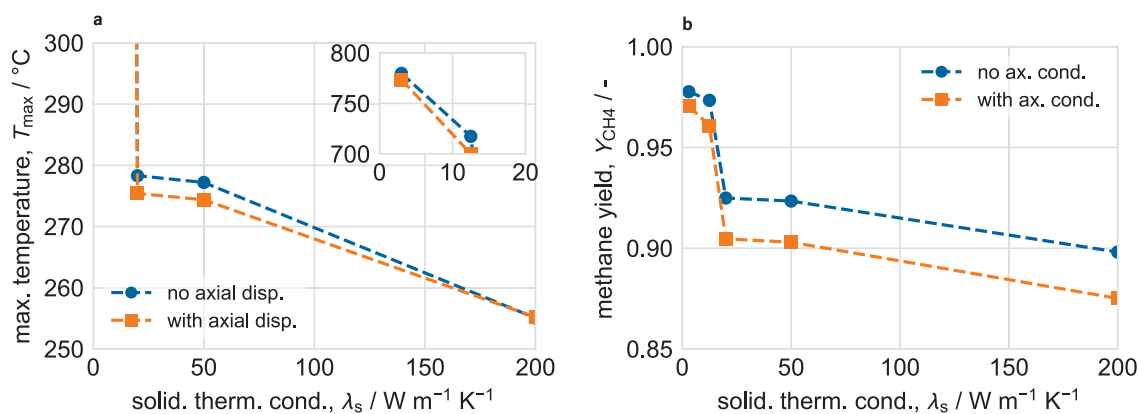


**FIG. 5.15.** Influence of axial dispersion on the maximal temperature (a) and the methane yield at the reactor outlet (b) depending on the solid thermal conductivity. The simulation parameters were  $\delta = 50\ \mu\text{m}$ ,  $\varepsilon_o = 0.75$ ,  $d_w = 0.6\ \text{mm}$ ,  $D_t = 25\ \text{mm}$ ,  $V_m = 0.15\ \text{NL}\ \text{g}_{\text{cat}}^{-1}\ \text{min}^{-1}$ ,  $G = 1.5\ \text{kg}\ \text{m}^{-2}\ \text{s}^{-1}$ ,  $p_{\text{in}} = 10\ \text{bar}$ , and  $\text{H}_2/\text{CO}_2 = 4$ .

abrupt temperature increases are observed if thicker catalyst coats are applied (see Fig. 5.14). For the shown results, the catalyst density was held constant at  $150\ \text{kg}_{\text{cat}}\ \text{m}^{-3}$  by adjusting the window size and thus the specific surface area of the catalytic sponges. For catalyst layers thicker than  $150\ \mu\text{m}$ , runaway occurs at slightly larger temperatures than for the thin catalyst layers. In the case of catalyst layers thicker than  $250\ \mu\text{m}$ , the increase of the maximal temperature in the catalyst bed is not as abrupt as the one for thinner catalyst layers. The reasons for the smoother increase of the maximum temperature are mass transport limitations within the catalyst layer that become limiting at high temperatures and thus dampen the runaway. Consequently, thick catalyst layers can be used to create a more resilient catalytic system that automatically reduces conversion, and thus the release of heat, if the temperature increases, however, at the cost of overall catalyst efficiency.

### Influence of axial dispersive heat and mass transport

For packed beds of pellets, axial dispersive heat transport is usually disregarded in production-scale simulations because of the low contribution of thermal conduction to the axial ETC. For solid sponges, however, thermal conduction in the axial direction can be dominant in *and* against the flow direction because of the continuous solid phase. Thus, the influence of axial dispersion on the temperature profiles and methane yield in catalytic sponges at production scale was analyzed for different solid thermal conductivities. Therefore, the maximum temperature within the catalyst bed and the outlet methane yield were calculated with the full reactor model, which accounts for axial dispersion, and with the simplified reactor model, which disregards axial dispersion, and subsequently compared (see Fig. 5.15 a and b).

Even at high solid thermal conductivities of  $50\ \text{W}\ \text{m}^{-1}\ \text{K}^{-1}$  (SSiC), the difference between the maximum temperatures calculated with the full and the simplified reactor model is below  $5\ \text{K}$  (see Fig. 5.15 a). At higher solid thermal conductivities, axial temperature gradients are probably too low to drive axial thermal conduction because heat removal in the radial direction completely removes the reaction heat. Thus, no hot spots develop. The calculated methane yields only differ by at most  $2\%$ . Thus, axial dispersive transport of

**TAB. 5.2.** Reference parameters used in the simulations for the tradeoff analysis. The parameters were chosen based on the scale-up analysis or set to typical values. If not stated otherwise, the listed parameters were used.

Parameter	Symbol	Value	Reason / Reference
(a) operating conditions			
inlet temperature	$T_{\text{in}}$	250 °C	typical
inlet pressure	$p_{\text{in}}$	10 bar	typical
inlet H <sub>2</sub> /CO <sub>2</sub> -ratio	H <sub>2</sub> /CO <sub>2</sub>	4	stoichiometric
gas load	$G$	1.5 kg m <sup>-2</sup> s <sup>-1</sup>	no external limitations
specific flow rate	$\dot{V}_{\text{m}}$	0.15 NL g <sub>cat</sub> <sup>-1</sup> min <sup>-1</sup>	90 % methane yield
(b) catalyst properties			
kinetic model	-	Koschany et al. [154]	state-of-the-art
apparent catalyst density	$\rho_{\text{cat}}^{(\text{app})}$	3203 kg m <sup>-3</sup>	measurement
coat thermal conductivity	$\lambda_{\text{coat}}$	3.6 W m <sup>-1</sup> K <sup>-1</sup>	Al <sub>2</sub> O <sub>3</sub> data
average pore size	$d_{\text{p}}$	13.8 nm	measurement
catalyst porosity	$\varepsilon_{\text{cat}}$	0.71	measurement
catalyst tortuosity	$\tau_{\text{cat}}$	2	typical
(c) reactor/catalyst design			
tube diameter	$D_{\text{t}}$	25 mm	typical
catalyst coat thickness	$\delta$	50 μm	full efficiency
coat thermal conductivity	$\lambda_{\text{s}}$	50 W m <sup>-1</sup> K <sup>-1</sup>	SSiC

heat and mass can be disregarded in the simulations of production-scale reactors because of the high flow rates and thus dominant convective transport in the axial direction. In addition, the catalyst bed will certainly consist of several segments in the axial direction and will therefore not allow thermal conduction across the boundaries of the individual segments. Nevertheless, the data on axial dispersion in solid sponges is still scarce, and more research is necessary to come to a final conclusion regarding the influence of axial dispersion in catalytic sponge at production scale.

The parameters obtained from the scale-up analysis serve as foundation for the upcoming simulations regarding the tradeoffs in the design of catalytic sponges and the comparison of catalytic sponges and conventional packed beds of pellets at production scale. The chosen parameters are summarized in Tab. 5.2. The solid thermal conductivity was assumed constant (50 W m<sup>-1</sup> K<sup>-1</sup>, SSiC) for the upcoming simulations because of the lack of reliable data for solid sponges and the relatively narrow temperature range of at most 100 K. The use of temperature-dependent and average solid thermal conductivities is given for alumina in Fig. B.1, p.143, in Appendix B. For the considered parameters, the difference of the hot-spot temperature did not exceed 10 K.

## 5.2.2 Analysis of tradeoffs in the design of catalytic sponges

As outlined in the introduction (see Section 1.2, pp. 2 ff.), tradeoffs between high bulk catalyst densities (small windows), low pressure losses (large windows and high porosity), and high effective thermal conductivities (low porosity) limit the design of ideal catalytic sponges. In order to quantify the tradeoffs and deduce design guidelines for catalytic sponges at the production scale, a multi-objective optimization (MOO) problem was set up.

The objectives were to maximize the space-time yield  $STY$  and to simultaneously minimize the pressure loss  $\Delta p$  by finding Pareto-optimal combinations of the window diameter  $d_w$  and the open porosity  $\varepsilon_o$ . In addition, a maximal tolerable temperature increase  $\Delta T_{tol}$  was imposed to avoid solutions that led to thermal runaway of the reactor. Mathematically, the problem is written as:

$$\begin{aligned} & \underset{\varepsilon_o, d_w}{\text{minimize}} && \begin{cases} -STY \\ \Delta p \end{cases} \\ & \text{subject to} && \Delta T_{\max} \leq \Delta T_{\text{tol}}, \\ & && 0.7 \leq \varepsilon_o \leq 0.95, \\ & && 0.2 \text{ mm} \leq d_w \leq 3 \text{ mm}. \end{aligned} \quad (5.2)$$

Here, the negative space-time yield  $STY$  was minimized which is equivalent to maximization. The bounds for the design variables  $d_w$  and  $\varepsilon_o$  were set to typical values (see Fig. 2.5, p. 20).

The multi-objective optimization problem (5.2) was solved using Deb's [43] Non-dominated Sorting Genetic Algorithm (NSGAII) which is widely applied in engineering MOO problems. For the calculations of the space-time yield and the pressure loss, the simplified reactor model that disregards axial dispersion of heat and mass was applied (see Section 5.2.1). On the catalyst scale interfacial transfer limitations and internal mass transport limitations were considered. Moreover, the effective window diameter after the coating procedure  $d_w^{(\text{coat})} = d_w - 2\delta$  was introduced to obtain more realistic results regarding the pressure loss. Although the effect of the coating on the pressure loss seems obvious, especially for small window diameters, it has not yet been systematically investigated and quantified.

If not stated otherwise, the reference parameters obtained from the scale-up analysis (see Tab. 5.2) were used. A population of 50 individuals evolved over 100 generations was sufficient to obtain convergence (see Fig. B.2 in Appendix B, p. 143).

### Influence of the constraint on the maximal temperature increase

The runaway analysis (see Fig. 5.13, p. 107) revealed that catalytic sponges are vulnerable to thermal runaway because the thin catalyst layers do not damp the temperature increase by internal mass transport limitations. Therefore, the MOO problem was solved for different values of the tolerable temperature increase  $\Delta T_{tol}$ , and the resulting temperature profiles for the combinations with the highest  $STY$  were analyzed (see Fig. 5.16). For the simulations, the reference parameters summarized in Tab. 5.2 were used.

For most methanation catalysts, a maximal temperature of 500 °C is usually assumed (see for example Nguyen et al. [199] and Schlereth and Hinrichsen [255]). Although the maximum temperature stays below this limit for all constraints on the maximal temperature increase (see Fig. 5.16), the temperature profiles show the formation of a rather sharp temperature peak for tolerable temperature increases larger than 100 K. The sharp peak might lead to thermal stresses in the catalyst and its support. Consequently, the maximal tolerable temperature increase was set to 100 K in all further optimization calculations.

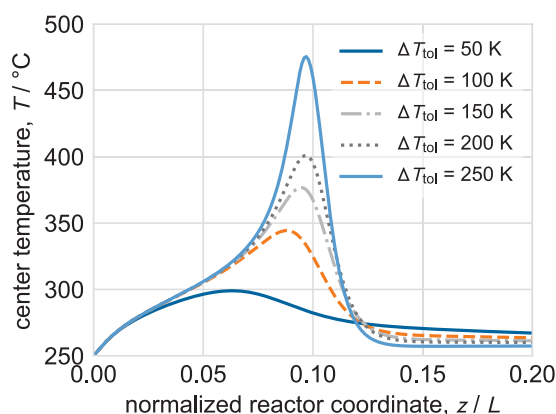


**FIG. 5.16.** Axial temperature profiles for different constraints on the maximal temperature increase  $\Delta T_{\max}$ . For the simulations, the sponge that provided the highest STY from the Pareto-optimal set of solutions was chosen. Other than that, the reference parameters listed in Tab. 5.2, p. 109 were used:  $T_{\text{in}} = 250\text{ }^{\circ}\text{C}$ ,  $p_{\text{in}} = 10\text{ bar}$ ,  $\text{H}_2/\text{CO}_2 = 4$ ,  $G = 1.5\text{ kg m}^{-2}\text{ s}^{-1}$ ,  $\dot{V}_m = 0.15\text{ NL g}_{\text{cat}}^{-1}\text{ min}^{-1}$ ,  $D_t = 25\text{ mm}$ ,  $\delta = 50\text{ }\mu\text{m}$ ,  $\lambda_s = 50\text{ W m}^{-1}\text{ K}^{-1}$  (SSiC).

### Analysis of the Pareto-optimal solutions

Figure 5.17 shows the Pareto-optimal set of solutions, also called Pareto-front, obtained for the MOO problem (5.2). For the simulations, the reference parameters were used (see Tab. 5.2). Pareto-optimal means that the STY cannot be increased without increasing the pressure loss. The small target in the upper left corner represents the utopia point, which indicates the ideal, however, unfeasible operation. The grey area indicates a region of unfeasible performance. Each individual in the population is represented by a point on the Pareto-front. Here, the size of the point indicates the window size (see legend for a scale), and the color indicates the corresponding open porosity (a), temperature increase (b), methane yield (c), and reactor length (d). In addition, the solution that provides the best tradeoff between high space-time yields and low pressure losses, measured by the minimal distance from the utopia point, is highlighted by a star. Furthermore, solutions that lead to a methane yield below 90% or to reactors longer than 10 m are colored grey. The length of the reactor was calculated from the applied gas load, the specific flow rate, and the bulk catalyst density:

$$L_t = \frac{G}{\dot{V}_m \rho_{\text{cat}}^{(\text{bulk})} \rho_f} = v_{\text{sup}} \tau. \quad (5.3)$$

The analysis of the calculated Pareto-optimal set clearly reveals the tradeoff between high space-time yield and low pressure loss. High space-time yields can only be achieved at the cost of considerable pressure losses (see Fig. 5.17 a). Moreover, Fig. 5.17 a shows that high space-time yields are obtained for catalytic sponges with small window diameters because they provide large specific surface areas and thus high bulk catalyst densities. Because of the temperature constraint ( $\Delta T_{\max} \leq 100\text{ K}$ ), however, the porosity has to decrease with decreasing window diameter to increase the effective thermal conductivity of the catalytic sponges. This additionally adds to the pressure loss. For the considered parameters, the best tradeoff with a space-time yield of  $227\text{ kg m}^{-3}\text{ h}^{-1}$  and a pressure loss of 279 mbar is obtained for catalytic sponges with a window diameter of 0.29 mm and an open porosity of

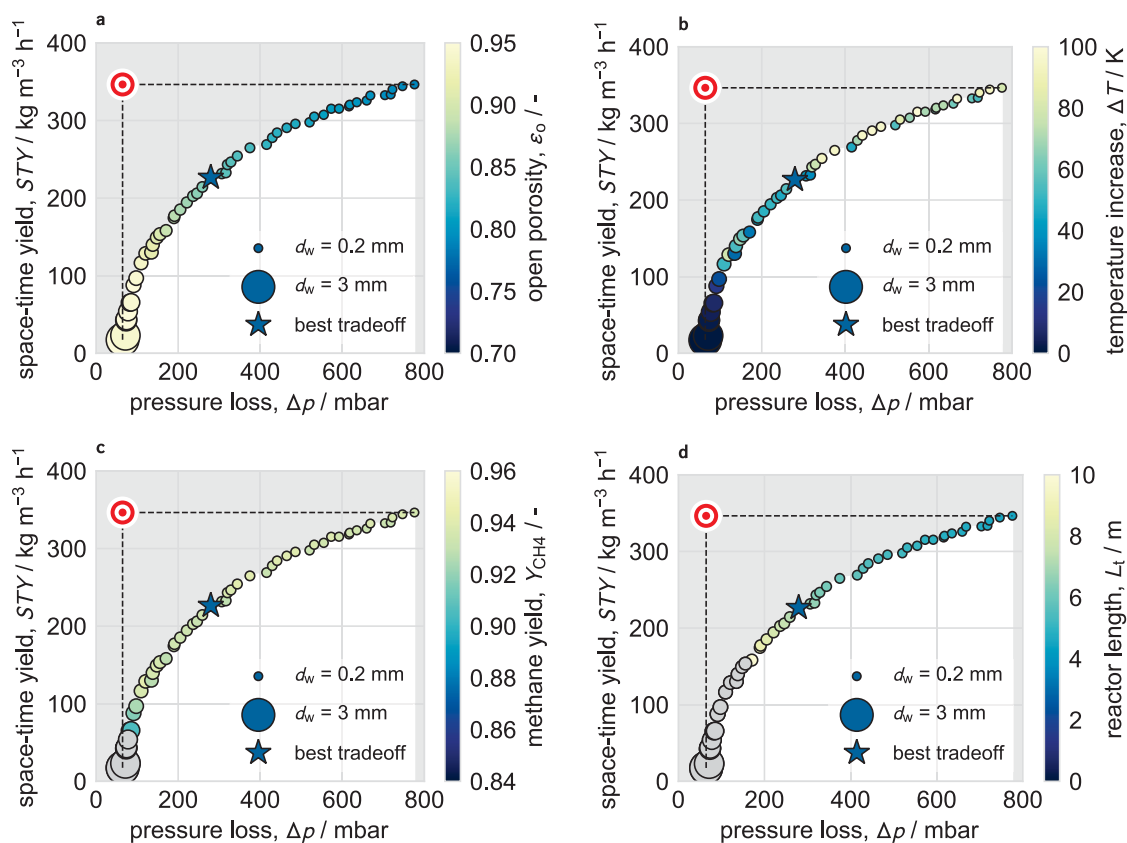


**FIG. 5.17.** Analysis of the set of Pareto-optimal solutions with respect to open porosity (a), temperature increase (b), methane yield (c), and reactor length (d). The small target in the upper left corner indicates the utopia point, while the grey region represents the non-feasible space. The best tradeoff was determined based on the minimal distance from the utopia point. In case of the methane yield (c) and reactor length (d), solutions with a methane yield below 0.9 or a reactor length above 10 m are displayed in grey. For the simulations, the reference parameters listed in Tab. 5.2, p. 109 were used:  $T_{\text{in}} = 250 \text{ }^\circ\text{C}$ ,  $p_{\text{in}} = 10 \text{ bar}$ ,  $\text{H}_2/\text{CO}_2 = 4$ ,  $G = 1.5 \text{ kg m}^{-2} \text{ s}^{-1}$ ,  $\dot{V}_{\text{m}} = 0.15 \text{ NL g}_{\text{cat}}^{-1} \text{ min}^{-1}$ ,  $D_t = 25 \text{ mm}$ ,  $\delta = 50 \text{ } \mu\text{m}$ ,  $\lambda_s = 50 \text{ W m}^{-1} \text{ K}^{-1}$  (SSiC).

0.854. The highest space-time yield of  $347 \text{ kg m}^{-3} \text{ h}^{-1}$ , is obtained for a window diameter of 0.2 mm and an open porosity of 0.789. The corresponding pressure loss is 775 mbar. The pressure loss is only 256 mbar in case of the high space-time yield configuration, and thus three times lower, if the reduction of the window diameter by the coating is disregarded. Based on the investigated samples in literature so far, both sponge design are realistic combinations of the window diameter and the open porosity of ceramic solid sponges (see Fig. 2.5, p. 20).

The influence of the temperature constraint is also visible in Fig. 5.17 b, where the color of the points corresponds to the temperature increase. While the temperature increase is below 50 K for solutions on the left side of the design with the best tradeoff, the temperature increase is repeatedly close to the maximal tolerable temperature increase of 100 K for most of the solutions on the right side of the best tradeoff design. The reason for the higher temperatures for sponges with small window diameters is the higher bulk catalyst density, which leads to higher conversions and thus increased heat production per unit reactor volume.

Figure 5.17 c shows the radially averaged methane yield at the reactor outlet. The methane yield is larger 90 % for most of the solutions in the Pareto-optimal set because the specific flow rate was set to  $0.15 \text{ NL g}_{\text{cat}}^{-1} \text{ min}^{-1}$ , which leads to methane yields of 90 % at 250 °C for the investigated kinetic model. For sponges with large window diameters and high porosities (lower left part of the Pareto-front), however, methane yields below 90 % were obtained because of mass transport limitations on the catalyst scale. These limitations are compensated in polytropic reactors by an increase of the temperature. Thus, methane yields larger than 90 % are achieved for most solutions in the Pareto-optimal set.

Finally, the length of the reactor  $L_t$  is analyzed in Fig. 5.17 d. The required reactor length for methane yields above or equal to 90 % decreases with the window diameter because of the high specific surface areas and thus high bulk catalyst densities. With 4.6 m, the shortest reactor is obtained for catalytic sponges with the smallest window diameter of 0.2 mm for the considered parameters. In case of catalytic sponges with large window diameters and high porosities, the catalyst densities are so low that the reactor length exceeds 10 m (see gray points), which is probably inappropriate for small- to medium-scale PtG units.

Consequently, in order to obtain high space-time yields with catalytic sponges, and thus allow compact PtG units, the window diameter should be as small as possible, and the open porosity should be adjusted to maintain a tolerable temperature increase. Although both measures add to the pressure loss, the latter is still below 1 bar (approx.  $200 \text{ mbar m}^{-1}$ ) for the considered gas load of  $1.5 \text{ kg m}^{-2} \text{ s}^{-1}$  and tube diameter of 25 mm. Hence, the analysis also shows that PtG units equipped with catalytic sponges are realistic from a reactor design point of view.

### **Influence of the material and reactor properties, and of the operating conditions on the Pareto-optimal design of catalytic sponges**

In order to explore the effects of the sponge material, the tube diameter, the inlet temperature, and the gas load, the Pareto-optimal sets are also computed for realistic variations of the above mentioned parameters. Figure 5.18 shows the influence of the sponge material (a), the reactor tube diameter (b), the inlet temperature (c), and the gas load (d) on the Pareto-optimal set of solutions. Except for the varied parameters, the values summarized in Tab. 5.2 were used.

While the porosity decreases with the window diameter to maintain the tolerable temperature increase for SSiC sponges, the open porosity remains high for aluminum sponges because of their high solid thermal conductivity (see Fig. 5.18 a). Hence, a reduction of the open porosity is not necessary to maintain the tolerable temperature increase. Consequently, aluminum sponges provide up to approximately 16 % higher space-time yields than SSiC sponges for the same pressure loss. Metallic sponges, however, require special treatment prior to the washcoating procedure to increase their anchoring surface area, and exhibit an approximately three times larger thermal expansion coefficient which might lead to flake-off of the catalytic layer if varying temperatures need to be handled (see Section 2.3.4, pp. 28 ff.).

The influence of the tube diameter for SSiC sponges is shown in Fig. 5.18 b. For tube diameters of 30 mm, the required open porosity to maintain the tolerable temperature increase is considerably lower than the one required in 25 mm tubes because the reaction

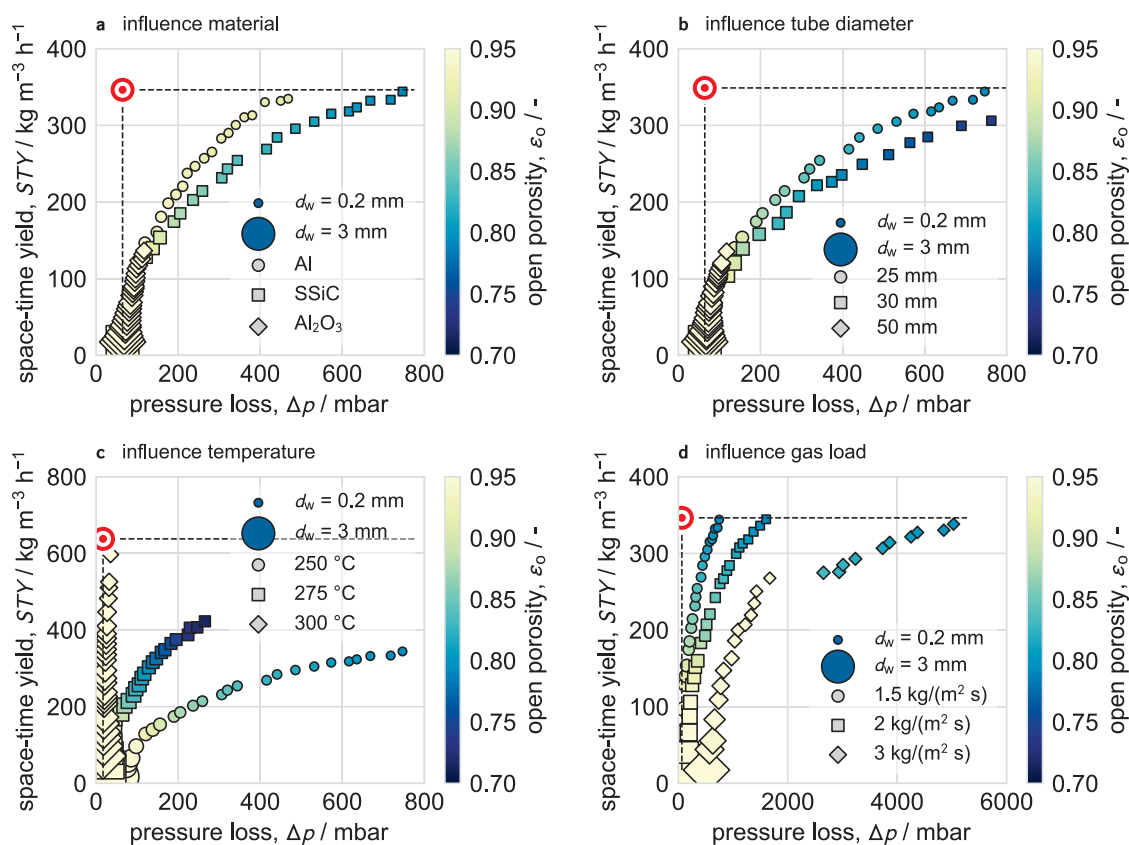


**FIG. 5.18.** Influence of the material (a), tube diameter (b), inlet temperature (c), and gas load (d) on the set of Pareto-optimal designs of catalytic sponges. The small target in the upper left corner indicates the utopia point. If not stated explicitly in the plots, the reference parameters listed in Tab. 5.2, p. 109 were used:  $T_{\text{in}} = 250\text{ }^{\circ}\text{C}$ ,  $p_{\text{in}} = 10\text{ bar}$ ,  $\text{H}_2/\text{CO}_2 = 4$ ,  $G = 1.5\text{ kg m}^{-2}\text{ s}^{-1}$ ,  $\dot{V}_{\text{m}} = 0.15\text{ NL g}_{\text{cat}}^{-1}\text{ min}^{-1}$ ,  $D_{\text{t}} = 25\text{ mm}$ ,  $\delta = 50\text{ }\mu\text{m}$ ,  $\lambda_{\text{s}} = 50\text{ W m}^{-1}\text{ K}^{-1}$  (SSiC). In case of the inlet temperature, the specific flow rate was adjusted to  $0.15\text{ NL g}_{\text{cat}}^{-1}\text{ min}^{-1}$ ,  $0.3\text{ NL g}_{\text{cat}}^{-1}\text{ min}^{-1}$  and  $0.6\text{ NL g}_{\text{cat}}^{-1}\text{ min}^{-1}$  for inlet temperatures of  $250\text{ }^{\circ}\text{C}$ ,  $275\text{ }^{\circ}\text{C}$  and  $300\text{ }^{\circ}\text{C}$ , respectively.

heat has to be transported over a longer distance from the center to the cooled wall. Thus, the pressure loss for a space-time yield of  $300\text{ kg m}^{-3}\text{ h}^{-1}$  increases from approximately 500 mbar in 25 mm tubes to around 700 mbar in 30 mm tubes. In addition, higher flow rates are required for larger tube diameters to maintain a constant gas load and thus prevent interfacial heat and mass transfer limitations. The higher flow rates in turn add to the pressure loss. Consequently, the use of large tube diameters is only beneficial in terms of higher throughputs if the porosity of the catalytic sponges does not have to be decreased significantly in order to ensure a certain temperature limit. Furthermore, the use of large tube diameters requires to increase the flow rate considerably (quadratic dependence of the cross-sectional area on the diameter) to maintain the necessary gas load to prevent interfacial heat and mass transfer limitations. Although the use of large tube diameters is beneficial for steady-state operation because it allows high throughputs with a reduced number of tubes, it sets a lower limit on the throughput and thus determines the minimal flow rate if dynamic gas load have to be handled.

In case of the 50 mm (see diamond-shaped symbols in the lower left corner of the Pareto front), the open porosity is always at its upper bound of 0.95. This can be explained by

the fact, that high porosities result in small strut diameters and thus lead to efficient heat and mass transfer between the fluid and the solid phase. Hence, if the temperature within the reactor increases because of the exothermic reaction, local runaway will occur at a certain temperature. Thus, the optimization algorithm probably tries to prevent local runaway by increasing the open porosity, which reduces the thermal conductivity at the same time. Therefore, high bulk catalyst densities cannot be obtained because of heat transport limitations which results in rather low space-time yields below  $150 \text{ kg m}^{-3} \text{ h}^{-1}$ . In conclusion, the 50 mm tube is too large for SSiC sponges and the considered parameters and operating conditions in order to allow compact PtG reactors.

The highest increases in space-time yield is obtained by increasing the inlet (and cooling) temperature (see Fig. 5.18 c). Compared to the reference inlet temperature of  $250 \text{ }^\circ\text{C}$ , the space-time yield is doubled from  $200 \text{ kg m}^{-3} \text{ h}^{-1}$  to  $400 \text{ kg m}^{-3} \text{ h}^{-1}$  for a pressure loss of 200 mbar and an inlet temperature of  $275 \text{ }^\circ\text{C}$ . The increase of the space-time yield is explained by the higher specific flow rate of  $0.3 \text{ NL g}_{\text{cat}}^{-1} \text{ min}^{-1}$ , which results in shorter reactors. For comparison, the shortest reactor is 4.6 m long in case of an inlet temperature of  $250 \text{ }^\circ\text{C}$  and 3.6 m long in case of an inlet temperature of  $275 \text{ }^\circ\text{C}$ , which allows further down-scaling of methanation reactors.

Even more interesting, however, is the obtained set of Pareto-optimal solutions for an inlet temperature of  $300 \text{ }^\circ\text{C}$ . Again, the open porosity is always at the upper bound of 0.95 to prevent local runaways as a result of interfacial heat transfer limitations. In addition, the specific surface area of solid sponges decreases with increasing porosity which leads to lower bulk catalyst densities. Because of the comparably high specific flow rate of  $0.6 \text{ NL g}_{\text{cat}}^{-1} \text{ min}^{-1}$ , high space-time yields up to  $600 \text{ kg m}^{-3} \text{ h}^{-1}$  are achievable with a window diameter of 0.34 mm and a reactor length of 2.4 m. Nevertheless, it should be further investigated if sponges with such high porosities provide enough mechanical strength for practical handling and application in fixed-bed reactors.

Finally, the increase of the gas load does not allow an increase of the space-time yield because the length of the reactor has to be increased to maintain methane yields of 90 % (see Fig. 5.18 d). In addition, high gas loads lead to a significant increase of the pressure loss because of its quadratic dependency on the fluid velocity. If the gas load is doubled to  $3 \text{ kg m}^{-2} \text{ s}^{-1}$  from the reference gas load of  $1.5 \text{ kg m}^{-2} \text{ s}^{-1}$ , the maximal pressure loss will increase from around 800 mbar to approximately 5000 mbar, which is significant regarding an inlet pressure of 10 bar. Thus, increasing the gas load is not beneficial as long as it is high enough to prevent interfacial heat and mass transfer limitations.

### 5.2.3 Comparison of catalytic sponges and packed beds of pellets for $\text{CO}_2$ -methanation at production scale

In order to assess the applicability of catalytic sponges at the production scale in more detail, a case study based on the results obtained from the tradeoff analysis was conducted. The performance of the catalytic sponges was compared to the the one of conventional packed beds of pellets, and discussed with focus on a small to medium scale methanation unit that has to handle varying feed flow rates. For the simulations of the packed beds of pellets, the established pseudo-homogeneous models by Winterberg et al. [305], which

explicitly consider the radial porosity and fluid velocity distributions in packed beds, were applied. A summary of heat and mass transport in packed beds of pellets was presented by Tsotsas [280, 281]. In case of full (non egg-shell) pellets, the catalyst-scale model could not be solved reliably because of a singularity of the kinetic model of Koschany et al. [154] for  $p_{\text{CO}_2} = 0$  (see Section 4.4.5, pp. 86 ff.). Therefore, Bischoff's general rate approximation with the cure for low Thiele moduli presented in Section 4.4.5, pp. 86 ff. was applied. Consequently, interfacial heat and mass transfer limitations were not considered for the full pellets. In case of the egg-shell pellets, the full catalyst-scale model including heat and mass transfer limitations was solved. The results of the case study are summarized in Tab. 5.3.

As a first case, the catalytic sponge design that provided the best tradeoff between space-time yield and pressure loss in the tradeoff analysis was investigated (see Fig. 5.17 a, p. 112, and case no. 1 in Tab. 5.3). In cases no. 2 and 3, the gas load was subsequently increased from  $1.5 \text{ kg m}^{-2} \text{ s}^{-1}$  to  $2 \text{ kg m}^{-2} \text{ s}^{-1}$  without adjusting the length of the reactor. Accordingly, the space-time yield increases from  $227 \text{ kg m}^{-3} \text{ h}^{-1}$  to  $283 \text{ kg m}^{-3} \text{ h}^{-1}$ , however, the methane yields drops from 0.94 to 0.88. The drop of the methane yield is overcompensated by the higher throughput which thus led to higher space-time yields. The temperature increase also decreases from 74 K to 44 K by 30 K as a result of the lower residence time and the slightly increased radial effective thermal conductivity via hydrodynamic dispersion. If the length of the reactor is simultaneously increased from 6.9 m to 9.2 m to maintain the specific flow rate of  $0.15 \text{ NL g}_{\text{cat}}^{-1} \text{ min}^{-1}$  (case no. 4), the methane yield rises again to 0.93. The space-time yield, however, drops to  $225 \text{ kg m}^{-3} \text{ h}^{-1}$  because of the larger reactor volume. If the gas load is further increased to  $3 \text{ kg m}^{-2} \text{ s}^{-1}$  or even  $4 \text{ kg m}^{-2} \text{ s}^{-1}$  (cases no. 5 and 6), long reactors, which are probably not applicable for small to medium scale methanation units, are required to keep the methane yield above 0.9. The pressure drop also increased significantly to 5026 mbar. Consequently, for the considered case, low bulk catalyst densities set an upper limit for the applicable flow rate.

The performance of the catalytic sponges was compared to that of packed bed of egg-shell-type spherical pellets because the bulk catalyst density can be matched to the one of the catalytic sponges by controlling the depth of the catalytically active layer in the pellets. Thus, the heat transport properties of both catalyst supports could be directly compared. For a given bulk catalyst density  $\rho_{\text{cat}}^{(\text{bulk})}$ , the thickness of the active layer in the egg-shell pellets is

$$\delta_{\text{egg}} = \frac{D_p}{2} \left[ 1 - \left( 1 - \frac{\rho_{\text{cat}}^{(\text{bulk})}}{\rho_{\text{cat,full}}^{(\text{bulk})}} \right)^{1/3} \right] \quad (5.4)$$

with  $\rho_{\text{cat,full}}^{(\text{bulk})}$  being the bulk catalyst density of full-body pellets. Because of the point-wise contact between the individual pellets, the high solid thermal conductivity of the SSiC is not effectively exploited. As a result, high gas loads of  $5 \text{ kg m}^{-2} \text{ s}^{-1}$  have to be applied to increase the radial effective thermal conductivity and maintain a tolerable temperature increase (cases no. 6 and 7). The pressure loss of 9736 mbar, however, is unacceptably high. Consequently, the tube radius was reduced to 20 mm to obtain workable reactor designs (cases no. 8–10). In addition, the pellet diameter was reduced from 3 mm to 2.5 mm to avoid significant wall effects in the packed bed ( $D_t/D_p \geq 8$ ). The direct comparison

**TABLE 5.3.** Results of the case study comparing catalytic sponges, egg-shell pellets, and full body pellets for the methanation of carbon dioxide at production scale. The best tradeoff (a) and the highest STY (b) configurations were considered. If not stated otherwise, the simulation parameters from Tab. 5.2, p. 109 were used:  $T_{in} = 250\text{ }^{\circ}\text{C}$ ,  $p_{in} = 10\text{ bar}$ ,  $\text{H}_2/\text{CO}_2 = 4$ ,  $\dot{V}_{in} = 0.15\text{ NL}_{\text{cat}}\text{ min}^{-1}$ ,  $\lambda_s = 50\text{ W m}^{-1}\text{ K}^{-1}$ .

No.	Support	$\varepsilon_0$	$d_w (D_p)$ mm	$\rho_{\text{cat}}^{(\text{bulk})}$ $\text{kg m}^{-3}$	$D_t$ mm	$L_t$ m	$G$ $\text{kg m}^{-2}\text{ s}^{-1}$	$\dot{V}$ $\text{Nm}^3\text{ h}^{-1}$	$Y_{\text{CH}_4}$ -	STY $\text{kg m}^{-3}\text{ h}^{-1}$	$\Delta p$ mbar	$\Delta p/L_t$ $\text{mbar m}^{-1}$	$\Delta T_{\text{max}}$ K	$\delta$ $\mu\text{m}$
<b>(a) best tradeoff</b>														
1	sponge	0.854	0.29	187	25	6.9	1.5	5.7	0.94	227	279	40	74	50
2	sponge	0.854	0.29	187	25	6.9	1.8	6.8	0.90	262	390	57	49	50
3	sponge	0.854	0.29	187	25	6.9	2	7.6	0.88	283	472	68	44	50
4	sponge	0.854	0.29	187	25	9.2	2	7.6	0.93	225	602	65	45	50
5	sponge	0.854	0.29	187	25	13.8	3	11.4	0.92	223	1891	137	34	50
6	sponge	0.854	0.29	187	25	18.4	4	15.2	0.91	220	5026	273	29	50
6	egg-shell	0.4	3	187	25	18.4	4	15.2	0.98	236	3818	208	410	191
7	egg-shell	0.4	3	187	25	23.0	5	19	0.95	230	9736	423	30	191
8	egg-shell	0.4	2.5	187	20	13.8	3	7.3	0.93	224	2024	147	24	159
9	egg-shell	0.4	2.5	187	20	11.5	2.5	6.1	0.94	225	1125	98	31	159
10	egg-shell	0.4	2.5	187	20	9.2	2	4.9	0.97	234	518	56	343	159
11	full pellet	0.4	3.0	557	25	6.9	4.5	17.1	0.93	668	1735	251	384	3000
12	full pellet	0.4	3.0	557	25	8.5	5.5	20.9	0.90	649	3590	422	240	3000
13	full pellet	0.4	3.0	557	25	9.3	6	22.8	0.88	633	5299	570	168	3000
14	full pellet	0.4	2.5	557	20	6.2	4	9.7	0.92	661	1468	237	241	2500
15	full pellet	0.4	2.5	557	20	7.7	5	12.2	0.89	636	3265	424	109	2500
<b>(b) highest space-time yield</b>														
16	sponge	0.789	0.2	288	25	4.5	1.5	5.7	0.94	347	775	172	80	50
17	sponge	0.789	0.2	288	25	4.5	1.8	6.8	0.90	401	1056	235	61	50
18	sponge	0.789	0.2	288	25	4.5	2	7.6	0.88	435	1267	282	57	50
19	sponge	0.789	0.2	288	25	6.0	2	7.6	0.93	334	1634	272	57	50
20	sponge	0.789	0.2	288	25	9.0	3	11.4	0.91	339	5817	646	47	50
21	sponge	0.789	0.2	288	25	4.5	1	3.8	0.98	242	393	87	352	50
22	sponge <sup>a</sup>	0.789	0.2	288	25	4.5	1	3.8	0.97	239	425	94	51 <sup>a</sup>	50
23	egg-shell	0.4	3	288	25	17.9	6	22.8	0.98	364	9734	544	462	323
24	egg-shell	0.4	2.5	288	20	14.9	5	12.2	0.98	362	7260	487	401	269
25	egg-shell	0.4	2.5	288	20	17.9	6	14.6	0.97	359	9680	541	32	269

<sup>a</sup> external transfer limitations disregarded: infinite heat and mass transfer rates

of catalytic sponges and packed beds of egg-shell pellets (cases no. 5 and 8), shows that identical methane yields, space-time yields, and temperature increases were obtained for both catalyst supports. The catalytic sponges, however, provided a slightly lower pressure loss of 1891 mbar compared to 2024 mbar. Thus, catalytic sponges are a promising alternative to packed beds of egg-shell pellets because they can be operated at a wider range of flow rates as a result of the continuous solid phase and thus dominant heat transport by thermal conduction. Additionally, solid sponges exhibit slightly lower pressure losses at high flow rates.

In comparison to egg-shell pellets, gas loads above  $5.5 \text{ kg m}^{-2} \text{ s}^{-1}$  are required to keep the maximum temperature below  $500 \text{ }^\circ\text{C}$  in case of conventional, fully active pellets because of the high bulk catalyst density of  $557 \text{ kg m}^{-3}$  (see cases 11–13). Despite the high gas loads, the pressure loss is lower in case of the full pellets than in case of the egg-shell pellets because the high bulk catalyst density allows shorter reactors. The full pellets, however, suffer from severe internal mass transport limitations. Consequently, methane yields around 90 % are only possible because of high temperature increases which compensated the mass transport limitations (see cases 12 and 13). For a gas load of  $6 \text{ kg m}^{-2} \text{ s}^{-1}$  (case 13), for instance, the temperature increase and the methane yield are 168 K and 0.88, respectively, while they are 240 K and 0.9 for a gas load of  $5.5 \text{ kg m}^{-2} \text{ s}^{-1}$  (see case 12). If smaller tube diameters were used (cases 14 and 15), lower gas loads are required to maintain a maximum temperature below  $500 \text{ }^\circ\text{C}$  because of the higher surface to volume ratio of the smaller tubes.

As a second case, the sponge design that yields the highest space-time yield was further investigated. Again, the same phenomena as for the best tradeoff case were observed. Increasing the gas load without increasing the reactor length, leads to methane yields below 90 % (see cases 16–18). As a result of the smaller window diameters and the higher bulk catalyst density, however, the space-time yields and the pressure loss are higher. The higher bulk catalyst density also allows an increase of the gas load to  $3 \text{ kg m}^{-2} \text{ s}^{-1}$  without exceeding a reactor length of 10 m (see case 20, 4, and 5). The pressure loss, however, then becomes considerable (5817 mbar).

In cases 21 and 22, the gas load was not increased but decreased to  $1 \text{ kg m}^{-2} \text{ s}^{-1}$  from the reference gas load of  $1.5 \text{ kg m}^{-2} \text{ s}^{-1}$ . For case 22, interfacial heat and mass transfer rates were assumed infinite, and external heat and mass transfer limitations were thus disregarded. While the temperature increase was 352 K for the case that considered interfacial heat and mass transfer limitations (case 21), it was only 51 K in the case that disregarded external heat and mass transfer limitations. The results clearly show, that interfacial heat transfer sets a lower limit on the gas load for catalytic sponges because of excellent heat transport within the catalytic sponges.

Egg-shell pellets do not yield an acceptable reactor design at a bulk catalyst density of  $288 \text{ kg m}^{-3}$  because very high gas loads of  $6 \text{ kg m}^{-2} \text{ s}^{-1}$  are necessary to achieve a tolerable temperature increase. These, however, also lead to unacceptable reactor lengths and thus pressure losses (see cases 23–25). The reason why fully active pellets are manageable although they exhibit an almost twice as high bulk catalyst density, are mass transport limitations that limit the release of heat. In case of egg-shell pellets, mass transport limita-

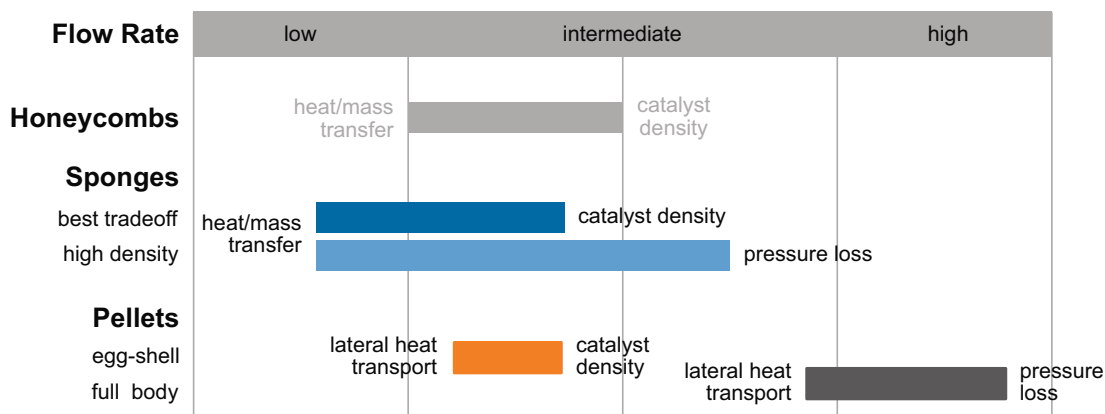


**FIG. 5.19.** Qualitative assessment of honeycombs, sponges, and pellets regarding their application as catalyst support for varying feed flow rates. The colored bars represent the ranges of flow rates in which the catalyst supports can be successfully applied; the annotations indicate the main factors limiting a further decrease or increase of the flow rate. The assessment bases on the results of the conducted case study. Honeycombs were not investigated in this work; the shown results are thus only an estimation.

tions are negligible and the heat transport properties of the packed bed of pellets are not sufficient to remove the released heat.

### Discussion of the case study

The conducted case study on the production-scale methanation of carbon dioxide demonstrates that catalytic sponges provide competitive reactor designs that are technologically feasible. In particular, catalytic sponges could be a replacement for egg-shell pellets because they provide better heat transport properties as a result of their continuous solid phase, which is required for the efficient conversion and thus heat release in thin catalyst coatings. In other words, heat transport within packed beds of pellets is not capable to effectively remove the heat generated in thin catalyst coatings.

Figure 5.19 shows a qualitative comparison of the applicability of honeycombs, catalytic sponges, and pellets in a scenario with varying inlet flow rates, as it is required for PtG units. The assessment bases on the results of the conducted case study. Accordingly, catalytic sponges provide the most flexibility regarding varying inlet flow rates. Because thermal conduction within the solid phase dominates heat transport in catalytic sponges as a result of their continuous solid phase, they can handle low flow rates without violating temperature constraints. The lower bound for the applicable flow rate are heat transfer limitations. If a compromise regarding high bulk catalyst densities, or equivalently, high space-time yields, and low pressure losses is made in the design of the catalytic sponges, low bulk catalyst densities set the upper limit for the flow rate. The result indicates that the development of more active catalyst is an option to enable compact small to medium scale PtG units, if the resulting heat and mass fluxes can still be managed by the catalytic sponges. If catalytic sponges are designed for highest STY, intolerable pressure losses because of the small window diameters after the coating procedure do not allow high flow rates. In this case, the pressure loss per unit reactor length is even comparable to that along packed beds of pellets (see Tab. 5.3).

In comparison to heat transport in catalytic sponges, heat transport in packed beds of pellets is dominated by the hydrodynamic dispersion of heat. Thus, high flow rates are required to meet temperature constraints, and radial heat transport sets the lower limit for the applicable flow rate. As a result of the high bulk catalyst densities of packed beds of pellets, however, compact reactor designs are possible. The upper limit for the applicable flow rate are an unacceptably high pressure loss.

Honeycombs were not considered in the case study. Hence, the assessment is only an estimation. Because of the laminar flow in the channels of the honeycombs, however, heat and mass transfer are not as efficient as in catalytic sponges. Consequently, the minimal required flow rate should be larger than the one for catalytic sponges. On the other side, honeycombs usually exhibit a smaller specific surface area and thus allow not as high bulk catalyst densities as catalytic sponges. Therefore, the upper bound for the applicable flow rate should be lower than the maximal flow rate applicable for catalytic sponges.

Consequently, packed beds of pellets are probably the better choice for large-scale production at constant flow rates because they provide the highest catalyst density and require high gas loads anyways to prevent hot spots. Nevertheless, the situation might change if internal mass transport limitations within the pellets reduce their productivity significantly. If varying flow rates have to be managed, catalytic sponges are probably the better option as they allow stable operation regarding temperature constraints at low to intermediate flow rates, however, at the cost of lower space-time yields.

## 5.3 Catalytic sponges with radially graded porosity

Solid sponges not only allow to tune the specific surface area, the pressure loss, and the effective thermal conductivity by carefully adjusting the window diameter and the porosity, but also enable catalyst supports with spatial porosity gradients. In that way, the solid material can be placed (low porosity) where it is needed to effectively remove the heat of reaction, and reduced (high porosity) in regions where it mostly adds to the pressure loss, but where high effective thermal conductivities are not required. Thus, catalytic sponges with discrete porosity layers in the radial direction are explored in this work to partially resolve the porosity tradeoff in the design of catalytic sponges (see Section 1.2, pp. 2 ff.). Although solid sponges with discrete porosity layers in the radial direction were already manufactured by Faure et al. [67], their design and potential as catalyst support have not been investigated yet. The presented approach in this work also has to be distinguished from the optimal distribution of the active catalytic material, which had been presented in several studies to improve the performance of catalytic processes [38, 120–122, 140–142, 145, 201, 227, 228, 274, 297], because it aims at tuning the heat fluxes and not at diluting the catalyst. The dilution of the active catalytic material with inert material is sometimes applied to reduce the release of heat and thus prevent thermal runaway of reactors. Nevertheless, dilution reduces the bulk catalyst density and thus also the space-time yield. In addition, it renders the development of more active catalysts useless as only more dilution would be required to keep the maximal temperature below a certain threshold. Thus, improving the heat and mass fluxes within the catalyst bed allows to truly intensify catalytic processes.

Only few studies so far investigated porous structures with spatially varying porosity for chemical engineering applications. Zhan et al. [314] and Huang et al. [113] for example predicted optimal porosity profiles for the supportive layer of PEM fuel cells and reported a 20%–30% improved transport of liquid water and also improved oxygen utilization for the optimal porosity distribution in comparison to a uniform distribution. Hüppmeier et al. [114] developed a discontinuously graded membrane to feed oxygen along the reactor axis during autothermal steam reforming of methane. The membrane was designed to feed the right amount of oxygen to a lab-scale fixed-bed membrane reactor (FBMR), and thus allowed almost isothermal operation by carefully balancing the local heat release from the combustion of methane and the local heat demand of the reforming process. Graded catalytic sponges have not been investigated in the scientific literature yet. Therefore, modeling of catalytic sponges with discrete porosity layers in the radial direction is presented in the following section.

### 5.3.1 Modeling graded sponges

In the first step of modeling graded sponges, the cross section is divided in  $n_1$  discrete rings with open porosity  $\varepsilon_{o,i}$ . The window diameter  $d_w$  is assumed constant. In this work,

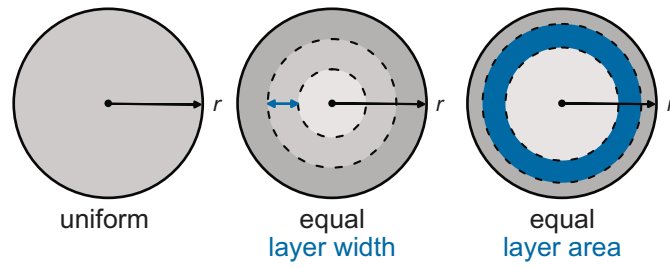


**FIG. 5.20.** Illustration of the investigated equal-thickness and equal-area grading schemes for graded catalytic sponges. Here, three discrete porosity layers are shown.

two different grading schemes are considered: first, rings with equivalent thickness, and second, rings with equal area (see Fig. 5.20). The bounds of the layers are given by

$$r_l^{(\text{bound})} = \begin{cases} \frac{l}{n_1} R_t & \text{if equal thickness} \\ \sqrt{\frac{l}{n_1}} R_t & \text{if equal area} \end{cases}, \quad l = 0, 1, \dots, n_1, \quad (5.5)$$

and the midpoint  $r_l$  of each layer, in which the layer open porosity  $\varepsilon_{o,l}$  is set, is simply the center point between the two bounds:

$$r_l = r_l^{(\text{bound})} + \frac{1}{2} \left( r_{l+1}^{(\text{bound})} - r_l^{(\text{bound})} \right). \quad (5.6)$$

The open porosity at each computational node that lies within one layer is set to the layer porosity  $\varepsilon_{o,l}$ . In addition, all properties that depend on the open porosity, for instance the bulk catalyst density  $\rho_{\text{cat}}^{(\text{bulk})}$ , the radial effective thermal conductivity  $\lambda_{\text{rad}}^{(\text{rad})}$ , and the strut diameter  $d_s$ , are evaluated using the local layer porosity. More complex than the description of the mentioned parameters, however, is the modeling of the superficial fluid velocity in the discrete porosity layers.

### Fluid flow in radially graded sponges

The open porosity significantly influences the permeability of each layer. In the case of discrete porosity layers in the radial direction, each layer represents a different flow resistance. Thus, the system can be modeled in analogy to an electrical circuit with parallel resistors. If Darcy's law is assumed, the pressure loss represents the voltage and the fluid velocity in each layer represents the electric current that goes through the corresponding resistor. Thus, the pressure loss in each layer is the same:

$$\Delta p_l = \frac{\mu_f}{K_l} v_{\text{sup},l} L_t = \text{const.} \quad (5.7)$$

In combination with the overall mass continuity equation,

$$GA = \sum_{l=1}^{n_1} G_l A_l, \quad (5.8)$$

the following flow model for the superficial velocity  $v_{\text{sup},l}$  in the layer  $l$  is derived:

$$v_{\text{sup},l} = v_{\text{sup}} \frac{A_t K_l}{\sum_{l=1}^{n_1} K_l A_l} = v_{\text{sup}} \frac{K_l}{K_{\text{av}}}, \quad l = 1, \dots, n_1 \quad (5.9)$$

Here, density and viscosity variations within the porosity layers as well as convective-dominated flow resistances are disregarded. For the equal-area grading scheme, the weight  $A_l/A$  is equal for all radial layers and the flow distribution is solely influenced by the layer permeability  $K_l$ .

The total pressure loss along graded sponges is calculated using the Darcy-Forchheimer equation with the radially averaged permeability and Forchheimer coefficient:

$$K_{\text{av}} = \frac{\sum_{l=1}^{n_1} K_l A_l}{A_t}, \quad l = 1, \dots, n_1 \quad (5.10a)$$

$$c_{F,\text{av}} = \frac{\sum_{l=1}^{n_1} c_{F,l} A_l}{A_t}, \quad l = 1, \dots, n_1 \quad (5.10b)$$

Similarly, the average open porosity is

$$\varepsilon_{o,\text{av}} = \frac{\sum_{l=1}^{n_1} \varepsilon_{o,l} A_l}{A_t}, \quad l = 1, \dots, n_1. \quad (5.11)$$

In order to verify the derived flow model, Eq. (5.9), it was compared to CFD simulations in a graded sponge. Therefore, the 3-d models obtained from  $\mu\text{CT}$  of the investigated 20 ppi and 40 ppi were cut and combined to create a graded sponge with two equal-thickness layers (inner layer: 40 ppi; outer layer: 20 ppi). Afterwards, the radial superficial velocity profile was extracted (see Appendix D, pp. 149 ff., for a detailed description).

In comparison to the detailed CFD simulations, the simple flow model, Eq. (5.9), describes the radial superficial velocity profile reasonably well (see Fig. 5.21). The absolute magnitude of the velocity matches especially in the outer layer. In the inner layer, the deviations are significantly larger. Nevertheless, the averaged superficial velocities obtained from the CFD simulations are vulnerable to errors in the center of the graded sponge because of

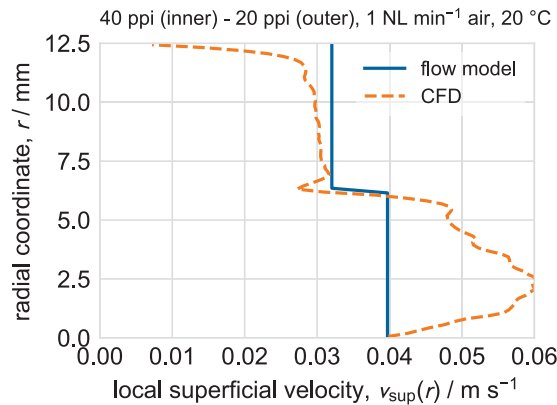


**FIG. 5.21.** Comparison of the modeled superficial velocity distribution in a graded sponge composed of the 40 ppi (inner) and 20 ppi (outer) sponges investigated in this work, to CFD results (see Appendix D, pp. 149 ff.).

the applied procedure to extract the radial velocity profiles. In addition, inertia-dominated flow resistances were disregarded in the simple flow model, which start to become relevant at the applied Reynolds numbers ( $Re_h = \rho_f v_{\text{sup}} d_h / \mu_f$ ) of 8 (40 ppi) to 11 (20 ppi). Thus, the derived flow model is strictly only valid for low fluid velocities. Nevertheless, it allows a first approximation of the flow distribution in graded catalytic sponges.

### 5.3.2 Calculation and analysis of tailored porosity profiles

#### Calculation of tailored porosity profiles

For the calculation of the best radial porosity profile to improve the performance of catalytic sponges during the methanation of carbon dioxide, the same MOO problem as for the analysis of the design tradeoffs of uniform catalytic sponges was used. Instead of the open porosity and the window diameter, however, the open porosity of the inner and of the outer layer,  $\varepsilon_{o,\text{inner}}$  and  $\varepsilon_{o,\text{outer}}$ , were used as design variables. The window diameter was set constant to 0.2 mm, which allows the maximal bulk catalyst density (see Section 5.2.2, p. 109 ff.). The resulting MOO problem is:

$$\begin{aligned} & \underset{\varepsilon_{o,\text{inner}}, \varepsilon_{o,\text{outer}}}{\text{minimize}} && \begin{cases} -STY \\ \Delta p \end{cases} \\ & \text{subject to} && \Delta T_{\text{max}} \leq \Delta T_{\text{tol}}, \\ & && 0.7 \leq \varepsilon_{o,\text{inner}} \leq 0.9, \\ & && 0.7 \leq \varepsilon_{o,\text{outer}} \leq 0.9 \end{aligned} \quad (5.12)$$

In this work, only the porosities of the inner and the outer layer were varied, and a linear relation for the porosities in between the inner and the outer layer was assumed:

$$\varepsilon_o(r_l) = \frac{\varepsilon_{o,\text{outer}} - \varepsilon_{o,\text{inner}}}{r_{l,\text{outer}} - r_{l,\text{inner}}} (r_l - r_{l,\text{inner}}) + \varepsilon_{o,\text{inner}} \quad (5.13)$$

Prior optimization runs, in which the open porosity of every layer was optimized without further restrictions, resulted in disorderly results regarding the radial porosity profile. Thus, the linear relation (5.13) was imposed as an additional constraint in order to obtain comprehensible porosity profiles from which first design guidelines regarding graded catalytic sponges can be deduced. The window size was set to 0.2 mm for all layers. Again, a population size of 50 evolved over 100 generations was used for the optimization runs. In addition, the number of the radial computational nodes was increased to 10 so that every layer was covered by at least one computational node.

Figure 5.22 shows the Pareto-optimal sets obtained for the equal-thickness and equal-area grading schemes with up to five layers. Although more layers are theoretically possible, it has to be checked on which scale the grading of the porosity is feasible from a manufacturing point of view. Hence, only five layers were considered in this study.

In case of the equal-thickness scheme (see Fig. 5.22 a), two layers yield the best tradeoff between high space-time yields and low pressure losses. For the graded sponges, however, the design tradeoffs are limited to a narrow range of space-time yields and pressure losses. In comparison with the uniform sponges (see Tab. 5.3), the highest space-time yield and

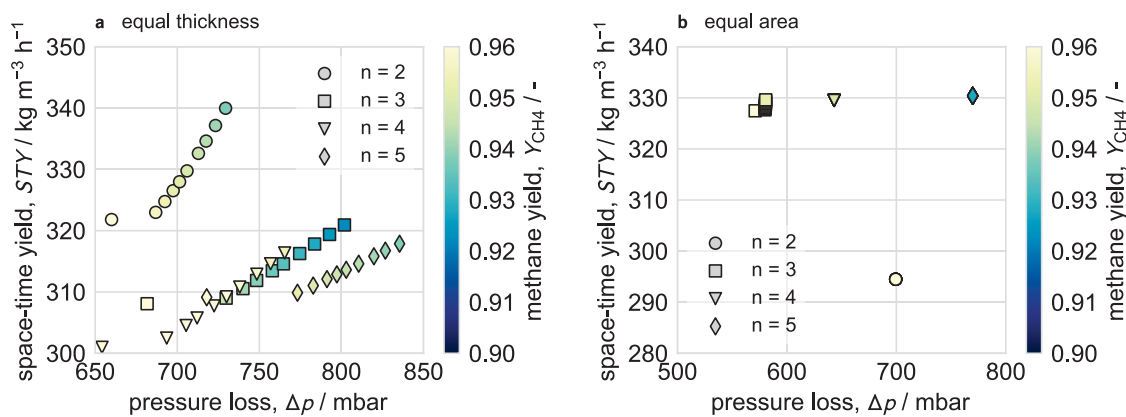


**FIG. 5.22.** Pareto-optimal solutions of graded catalytic sponges obtained for the equal-thickness (a) and equal-area (b) grading schemes and different number of radial porosity layers. The window diameter  $d_w$  was set to 0.2 mm. For the simulations, the reference parameters listed in Tab. 5.2, p. 109 were used:  $T_{in} = 250\text{ }^\circ\text{C}$ ,  $p_{in} = 10\text{ bar}$ ,  $H_2/CO_2 = 4$ ,  $G = 1.5\text{ kg m}^{-2}\text{ s}^{-1}$ ,  $\dot{V}_m = 0.15\text{ NL g}_{cat}^{-1}\text{ min}^{-1}$ ,  $D_t = 25\text{ mm}$ ,  $\delta = 50\text{ }\mu\text{m}$ ,  $\lambda_s = 50\text{ W m}^{-1}\text{ K}^{-1}$  (SSiC).

the corresponding pressure loss for  $n_1 = 2$  are slightly lower ( $340\text{ kg m}^{-3}\text{ h}^{-1}$  compared to  $347\text{ kg m}^{-3}\text{ h}^{-1}$  and  $725\text{ mbar}$  compared to  $775\text{ mbar}$ ). An analysis of the results shows that the inner porosity is always 0.9, while the outer porosity varies between 0.7 and 0.75. Thus, with an increasing number of layers, the porosity in the outer layers increases because of the linear constraint, Eq. (5.13). As a result of the higher weight of the outer layers in the equal-thickness grading scheme, the average porosity increases and hence the bulk catalyst density decreases. Consequently, lower space-time yields are obtained for  $n_1 \geq 3$ . This is also consistent with the slightly higher methane yields (see Fig. 5.22 a) as longer reactor are required. The increase in the methane yield, however, is not enough to compensate the larger reactor volume, which ultimately leads to lower-space time yields.

In case of the equal-area grading scheme (see Fig. 5.22 b), the Pareto front reduces to almost a single point. An analysis of the inner and outer porosities revealed that the inner porosity was always close to 0.9, the upper bound, while the inner porosity was always close to the lower bound of 0.7. Accordingly, the number layers influence the performance more than the radial porosity profile. Here, three layers (square symbols) provide the best tradeoff regarding high space-time yields and low pressure losses. In comparison to the uniform sponges (see Tab. 5.3) and to graded sponges with equally thick layers (see Fig. 5.22 b), the space-time yield is only slightly lower ( $330\text{ kg m}^{-3}\text{ h}^{-1}$ ), however, the pressure loss is considerably lower in case of three layers ( $580\text{ mbar}$  compared to  $775\text{ mbar}$  in case of uniform sponges).

The calculated porosity profile for the best case, i. e., three equal-area layers, is shown in Fig. 5.23. The graded sponge consists of an inner core with high porosity of 0.9 and two layers with low porosities of 0.77 and 0.7 in the outer annulus. Thus, the solid material is taken away from the core and shifted to the wall. A detailed analysis of the effect of the grading on the temperature and yield profiles is presented later after the comparison of the performance of graded and uniform catalytic sponges.

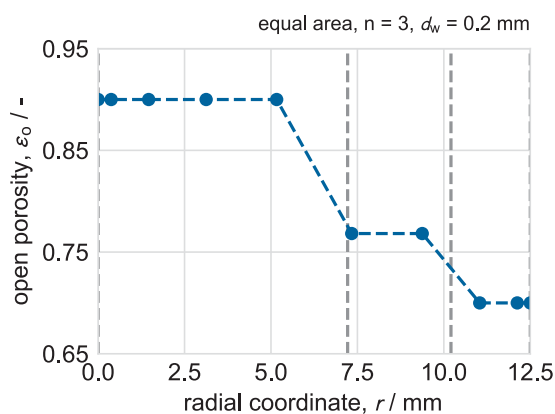


**FIG. 5.23.** Radial porosity profile for three layers and the equal-area grading scheme, which resulted in the best performance. The vertical lines indicate the bounds of the discrete porosity layers. The dots represent the computation nodes in the radial direction that were used in the simulations.

### Evaluation of catalytic sponges with graded porosity

In order to evaluate the potential of graded catalytic sponges, their performance regarding space-time yield, methane yield, pressure loss, and temperature increase was compared to the performance of uniform sponges. Table 5.4 shows a comparison of the best graded sponges with three equal-area layers and an decreasing porosity towards the wall (case 1) to several catalytic sponges with uniform porosity (cases 3–5).

In comparison to a uniform sponge with the average porosity of the graded sponges (cases 3, the same porosity was obtained in the tradeoff analysis in Section 5.2.2, pp. 109 ff.), the graded sponge (case 1) exhibits a slightly lower bulk catalyst density and thus a 5% lower space-time yield because of the high porosities in the core layer. Both, the pressure loss and the temperature increase, however, are reduced considerably by 26% (pressure loss) and 46% (temperature increase) for the graded sponge. The comparison clearly demonstrates that graded sponges are a promising option to partially resolve the porosity tradeoff regarding the design of catalytic sponges. In addition, the graded sponge (case 1) is compared to a graded sponge with the same radial porosity profile, however, with no active catalyst in the core layer (case 2). For the comparison, the same length as for the fully coated

**TAB. 5.4.** Comparison of the performance of graded and uniform catalytic sponges. For the simulations, the reference parameters listed in Tab. 5.2, p. 109 were used:  $T_{\text{in}} = 250\text{ }^{\circ}\text{C}$ ,  $p_{\text{in}} = 10\text{ bar}$ ,  $\text{H}_2/\text{CO}_2 = 4$ ,  $G = 1.5\text{ kg m}^{-2}\text{ s}^{-1}$ ,  $\dot{V}_{\text{m}} = 0.15\text{ NL g}_{\text{cat}}^{-1}\text{ min}^{-1}$ ,  $D_{\text{t}} = 25\text{ mm}$ ,  $\delta = 50\text{ }\mu\text{m}$ ,  $\lambda_{\text{s}} = 50\text{ W m}^{-1}\text{ K}^{-1}$  (SSiC).

No.	Support	$\rho_{\text{cat}}^{(\text{bulk})}$ $\text{kg m}^{-3}$	$L_{\text{t}}$ m	$Y_{\text{CH}_4}$ -	STY $\text{kg m}^{-3}\text{ h}^{-1}$	$\Delta p$ mbar	$\Delta T_{\text{max}}$ K
1	graded (area, $n_1 = 3$ )	269	4.8	0.95	330	580	49
2	graded (area, $n_1 = 3$ ) <sup>a</sup>	193	4.8	0.88	306	637	5
3	uniform ( $\epsilon_0 = 0.789$ ) <sup>b</sup>	288	4.5	0.94	347	770	91
4	uniform ( $\epsilon_0 = 0.7$ )	290	4.5	0.91	340	1326	16
5	uniform ( $\epsilon_0 = 0.9$ )	248	5.2	0.98	312	344	501

<sup>a</sup> no catalyst in the inner layer

<sup>b</sup> average porosity calculated from the graded porosity profile

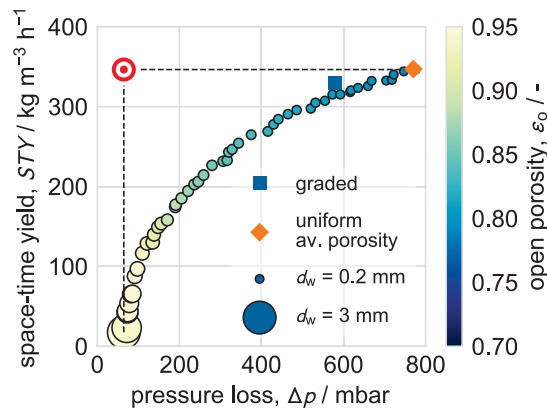


**FIG. 5.24.** Comparison of the graded and uniform catalytic sponges in the  $\Delta p$ - $STY$ -plane including the Pareto optimal set of solutions for uniform SSiC catalytic sponges. The graded sponges allow lower pressure losses and lower hot-spot temperatures while maintaining a comparable space-time yield as the corresponding uniform sponges. (see Tab. 5.4). For the simulations, the reference parameters listed in Tab. 5.2, p. 109 were used:  $T_{in} = 250\text{ }^\circ\text{C}$ ,  $p_{in} = 10\text{ bar}$ ,  $H_2/CO_2 = 4$ ,  $G = 1.5\text{ kg m}^{-2}\text{ s}^{-1}$ ,  $\dot{V}_m = 0.15\text{ NL g}_{cat}^{-1}\text{ min}^{-1}$ ,  $D_t = 25\text{ mm}$ ,  $\delta = 50\text{ }\mu\text{m}$ ,  $\lambda_s = 50\text{ W m}^{-1}\text{ K}^{-1}$  (SSiC).

graded sponge was used to ensure a fair comparison. If the core layer does not contain any catalyst, the methane yield and thus the space time yield are significantly lower. The temperature increase is also much lower because the generated heat is efficiently removed from the outer layers. Consequently, the graded sponge provides a better performance than a tube-in-tube or annulus reactor. Finally, the performance of the graded sponge (case 1) is compared to uniform sponges with extreme porosities of 0.7 (case 4) and 0.9 (case 5). In case of the high uniform porosity (case 5), the effective thermal conductivity is not sufficient to remove the reaction heat and thus thermal runaway of the reactor occurs ( $\Delta T_{max} = 501\text{ K}$ ). Compared to the low uniform porosity (case 4), the graded sponges (case 1) provides a slightly lower space-time yield and a higher temperature increase, however, the pressure loss is reduced by more than 50%. Thus, the graded sponge still provides the best tradeoff between high space-time yields, low pressure losses, and tolerable temperature increases.

The performance of the graded sponge and of the uniform sponge with the average porosity is shown in Fig. 5.24 together with the Pareto-optimal set of uniform sponges, calculated in Section 5.2.2, pp. 109. The design of the uniform sponge with the average porosity is equivalent to the uniform sponge design that provided the highest space-time yield in the calculation of the Pareto-front for uniform sponges. The graded sponge clearly lies in the unfeasible region of the uniform sponges (above the Pareto-front) which demonstrates the potential of graded sponges to resolve the design tradeoffs of catalytic sponges. Moreover, the graded sponge provides a lower temperature increase as uniform sponge designs that yield comparable space-time yields and pressure losses (see Fig. 5.17 b, p. 112).

### Analysis of effect of graded catalytic sponges

In order to understand the effect of the graded porosity profile, the graded sponge design and the uniform sponge design with the average porosity were investigated in more detail.

Figure 5.25 shows the distributions of the temperature (a), the methane yield (b), the local heat generation (c), the local radial heat flux (d), the superficial velocity (e), and the reaction rate (f, log-scale) in the uniform sponge (upper plane) and the graded sponge (lower plane). In case of the graded sponge, the temperature distribution is more uniform (see Fig. 5.25 a). The axial temperature gradients are less steep and the temperature peak is much broader than in case of the uniform sponge. In addition, the temperature peak is

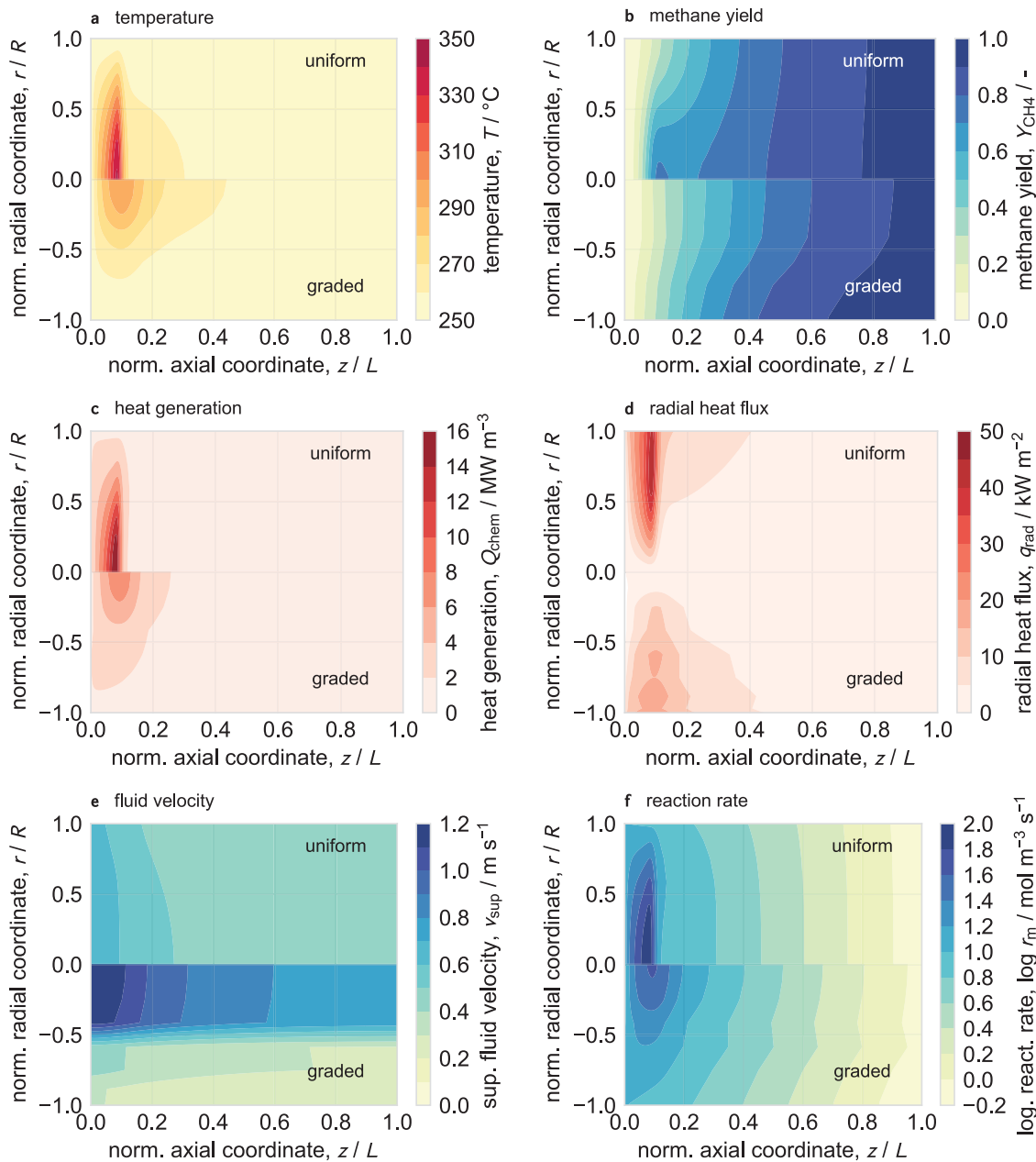


**FIG. 5.25.** Comparison of the temperature (a), methane yield (b), heat generation (c), radial heat flux (d), superficial velocity (e), and reaction rate (f) in the uniform (top, average porosity) and the graded sponge (bottom, three equal-area layers). For the simulations, the reference parameters listed in Tab. 5.2, p. 109 were used:  $T_{\text{in}} = 250^{\circ}\text{C}$ ,  $p_{\text{in}} = 10 \text{ bar}$ ,  $\text{H}_2/\text{CO}_2 = 4$ ,  $G = 1.5 \text{ kg m}^{-2} \text{ s}^{-1}$ ,  $\dot{V}_m = 0.15 \text{ NL g}_{\text{cat}}^{-1} \text{ min}^{-1}$ ,  $D_t = 25 \text{ mm}$ ,  $\delta = 50 \mu\text{m}$ ,  $\lambda_s = 50 \text{ W m}^{-1} \text{ K}^{-1}$  (SSiC).

localized in the core layer because of the low porosities and thus high effective thermal conductivities in the outer layers. The local methane yield also shows a more uniform distribution in the graded sponge than in the uniform sponge (see Fig. 5.25 b). Because of the steep temperature increase in the uniform sponge, the yield also increases steeply in the center of the reactor. In the last half of the reactor, the yield distribution is almost uniform in the radial direction. In the graded sponge, distribution of the methane yield is different. It increases faster along the axial coordinate in the outer layers than in the core layer because of the higher bulk catalyst density and the lower superficial fluid velocity. Nevertheless, high yields above 0.9 are also achieved in the core layer because of the higher temperatures in the center of the graded sponge.

The Figures 5.25 c and d show the local heat generation and the local radial heat flux in the uniform and the graded sponge. Although the analysis of the heat sources and fluxes seems to be the most promising approach to obtain insight into the optimal porosity profile, their evaluation and the identification of cause and effect is difficult because of the two-way coupling of heat generation and heat fluxes with the temperature. Nevertheless, the heat generation in the graded sponge is distributed over a larger region. Moreover, the maximal local heat generation is  $6 \text{ MW m}^{-3}$  compared to  $16 \text{ MW m}^{-3}$  in case of the uniform sponge, although the conversion is comparable in both cases. A similar distribution as the one of the local heat generation rate is obtained for the local radial heat fluxes (see Fig. 5.25 d). Because of the lower temperatures and thus smaller temperature gradients in the graded sponges, however, the comparison to the heat fluxes in the uniform sponge is debatable.

The most striking difference between the uniform and the graded sponge is observed for the distribution of the superficial velocity (see Fig. 5.25 e). While the superficial velocity is almost constant around  $0.6 \text{ m s}^{-1}$  and uniformly distributed over the radius in the uniform sponges, it reaches values of  $0.7 \text{ m s}^{-1}$ – $1.2 \text{ m s}^{-1}$  in the core layer of the graded sponge as a result of the high porosity. In the outer layers, the superficial velocity is only between  $0.2 \text{ m s}^{-1}$ – $0.5 \text{ m s}^{-1}$ . The high velocities in the core layer lead to a small residence time and thus limit the release of heat in the center of the reactor. In addition, they lead to an increased convective transport in the axial direction and thus to a broad and quite smooth temperature peak (see Fig. 5.25 a). The low superficial velocities in the outer layers lead to a long residence time in regions where also the most catalytic material is located. Therefore, high methane yields above 0.9 are possible. Nevertheless, as demonstrated in the evaluation of graded sponges (see Tab. 5.4 cases 1 and 2), the core region also adds to the conversion of carbon dioxide because the reaction rates in the core layer reach similar levels as in the outer regions as a result of the higher temperatures (see Fig. 5.25 a). Thus, the higher temperatures compensate the lower bulk catalyst density.

Finally, it can be concluded that graded sponges do have to potential to resolve the existing design tradeoffs regarding high bulk catalyst densities, low pressure losses, and high effective thermal conductivities. As a first design rule, graded sponges should have a high porosity in the center and low porosities close to the wall. The shift of the solid material from the center of the reactor to the wall reduces the heat release in the center and thus leads to lower hot-spots temperatures. The low porosity and thus high bulk catalyst density at the wall allows efficient conversion of the reactants in regions where the heat

can effectively be removed because of the high effective thermal conductivities in the outer layers. Finally, the low porosities in the outer layers decrease the superficial fluid velocities which causes long residence times and thus high yields. Furthermore, the low superficial velocities in the dense regions allow lower pressure drops than in uniform sponges. Because of the different levels of conversion in the radial porosity layers, however, radial mass transport might influence the performance of graded sponges. Thus, the influence of radial mass transport on the temperature and yield distributions should be further investigated. Also, it should be clarified whether the larger velocity gradients in the radial direction influence dispersive mass and heat transport between the core and the outer layers.

## 6.1 Summary of the current state of catalytic Sponges and monolithic catalyst supports

Because solid sponges combine low pressure losses, large specific surface areas, and excellent heat transport properties, they have been investigated as monolithic catalyst supports for almost 20 years. Considerable progress was made regarding the morphological characterization of solid sponges (for instance by using volume imaging techniques such as MRI and  $\mu$ CT), the calculation of the pressure loss, and the description of the radial effective thermal conductivity using pseudo-homogeneous models. Nevertheless, the accuracy of state-of-the-art pseudo-homogeneous heat transport models (see for example the model of Fishedick et al. [70]) is around  $\pm 30\%$  and thus in the same order of magnitude as the statistical variation of the window and strut diameters of commercial solid sponges. Consequently, pseudo-homogeneous heat transport models have reached their limit regarding accuracy. In contrast to heat transport, interfacial heat transfer between the fluid and the solid phase was only investigated in a handful of studies so far, and the available models suffer from large uncertainties as a result of the limited ranges of the investigated porosities and window diameters, solid and fluid thermal conductivities, and fluid velocities.

In addition to the determination of heat, mass, and momentum transport, solid sponges were applied as monolithic catalyst supports in lab-scale fixed-bed reactors for various chemical processes. Nevertheless, catalytic sponges were compared to conventional packed beds of pellets predominantly at lab scale and thus at low flow rates. Regarding the different governing heat transport mechanisms, i. e., thermal conduction within the solid phase for catalytic sponges and hydrodynamic dispersion in packed beds of pellets, however, the comparison of catalytic sponges to packed beds of pellets is incomplete because flow rates at production scale are much higher than at lab scale. Hence, in most cases catalytic sponges will show better heat transport than packed beds of pellets at the lab scale, unless materials with low thermal conductivities are used. So far only one experimental study investigated fluid velocities higher  $0.5 \text{ m s}^{-1}$  which are typical in production-scale FBRs (see Mülheims and Kraushaar-Czarnetzki [192]). The study confirmed improved heat transport in catalytic SSiC sponges, however, heat transport limitations in the surrounding of the reactor might have influenced the results. Thus, solid sponges are still in a conceptual stage of development with first successful demonstrations at the lab scale.

In this thesis, a 2-d pseudo-homogeneous multi-scale reactor model has been developed and implemented specifically for catalytic sponges. The model explicitly takes into account the interfacial heat and mass transfer between the fluid and the solid phase, and the heat and mass transport within the mesoporous catalyst coat. The required heat and mass transport and transfer models for solid sponges were chosen based on a thorough review of the

current literature. The model was validated against original experiments using a polytropic lab-scale reactor and commercial solid sponges for the methanation of carbon dioxide over an inhouse-synthesized 5 wt% Ni/Al<sub>2</sub>O<sub>3</sub> catalyst. The simulated axial temperature profiles were compared to spatially resolved axial temperature profiles measured during the polytropic experiments. For cases in which the boundary conditions, such as the wall temperature profile, were well characterized, the simulated temperature profiles agreed well with the measured ones. In addition, the measured and simulated carbon dioxide conversions and methane yields were in good agreement. The implemented model thus enables the simulation of realistic temperature profiles and methane yields for catalytic sponges.

Using the validated reactor model, the design tradeoffs of solid sponges with regard to high bulk catalyst densities, low pressure losses, and high effective thermal conductivities were explored by solving a multi-objective optimization problem. The results demonstrated that a tradeoff between high space-time yields and low pressure losses is inevitable, especially if the reduction of the window diameter—as a result of the applied catalyst coat—is taken into account. In order to obtain maximal space-time yields of several 100 kg m<sup>-3</sup> h<sup>-1</sup>, the window diameter of the sponges should be as small as possible (below approximately 0.5 mm) to create a large specific surface area. The open porosity should be as close as possible to an upper limit that still allows sufficient effective thermal conductivities to maintain a certain maximal temperature increase. Because of high porosities of solid sponges above 0.7, however, small window diameters are still applicable at tolerable pressure losses. In addition, as previous studies on catalytic sponges already concluded, the solid thermal conductivity of the sponge material should be high to fully exploit their continuous solid phase. Ultimately, this would lead to the use of metallic sponges. Nevertheless, special treatment is required to create a sufficient anchoring strength of the catalytic coat, and the metal surface might have an influence on the catalytic conversion itself. Furthermore, the thermal extension of metals is approximately three times higher than that of ceramics which might lead to flake-off of the catalyst coat if varying temperature levels are expected during operation.

Following the exploration of the design tradeoffs of catalytic sponges, a case study regarding the production-scale methanation of carbon dioxide has been conducted. Within the case study, the performance of solid sponges was compared to that of packed beds of egg-shell and conventional full-body pellets. The case study demonstrated that the application of catalytic sponges results in feasible reactor designs with tube lengths of several meters at production scale. Moreover, solid sponges provide the most flexibility regarding varying inlet flow rates because their continuous solid phase allows high and stable effective thermal conductivities even at low flow rates. In addition to the early reviews of Carty and Lednor [34] and Twigg and Richardson [282], who stated that catalytic sponges would most probably improve catalytic processes that require high throughputs because of their high porosities, the results of this work demonstrate that catalytic sponges also unfold their potential at low flow rates if temperature constraints in polytropic fixed-bed reactors have to be met. Consequently, catalytic sponges are promising catalyst supports for PtG units that require a high flexibility regarding varying flow rates to follow the fluctuations of

renewable energies. The case study also revealed that, because of the high effective thermal conductivities of solid sponges at low flow rates, interfacial heat transfer between the fluid and the solid phase sets the lower bound for the applicable flow rate, especially if materials with high solid thermal conductivities are used. The upper bound for the applicable flow rate in case of catalytic sponges is either set by low bulk catalyst densities, and thus very long reactor tubes (best tradeoff design), or by intolerable pressure losses as a result of the small window diameters after the coating procedure (design for highest STY). In the latter case, the pressure loss per unit reactor length is comparable to that of packed beds of pellets.

For large-scale production at constant throughputs, however, packed beds of full-body pellets probably provide the best performance because they allow the highest bulk catalyst densities and thus reactor lengths below 10 m even at high fluid velocities. As a result of the shorter reactors, the pressure loss remains acceptable. The drawback of packed beds of pellets, however, are the low catalyst utilization and the higher hot spot temperatures. Consequently, if internal mass transport limitations within the mesoporous pellets are dominant in the whole reactor, the situation might change. In this case, catalytic sponges could also outperform packed beds of pellets for large-scale production because the higher catalyst utilization compensates their lower bulk catalyst density.

Although only the methanation of carbon dioxide was considered in this work, the deduced design guidelines are expected to be also valid for other exo- and endothermic gas-phase reactions such as the synthesis of methanol from carbon dioxide or the reverse water-gas shift reaction. In addition, the guidelines can also serve as a rule of thumb for the design of catalytic sponges for three-phase reactions, e. g., Fischer-Tropsch synthesis. Nevertheless, the presence of a liquid phase might require a change of the design of the sponges.

Finally, tailored graded sponges with discrete porosity layers in the radial direction were predicted in this work and their potential for process intensification was evaluated. The calculated optimal porosity profile led to a 26 % reduction of pressure loss and a 46 % reduction of temperature increase, while the space-time yield dropped only by 5 % compared to a uniform sponge with the same average porosity. Although the results consider only a single case, they clearly demonstrate the potential of graded catalytic sponges to partially resolve the design tradeoffs with regard to high bulk catalyst densities, low pressure losses, and high thermal conductivities by applying tailored porosity profiles.

## 6.2 Outlook on the future of monolithic catalyst supports

The results of this work show that monolithic catalyst supports such as catalytic sponges allow feasible reactor designs at the production scale, and that they provide a high flexibility with regard to varying flow rates. Thus, they are promising catalyst supports for small- to medium-scale PtG units that require stable operation under dynamically changing flow rates. Nevertheless, more research is necessary to bring monolithic catalyst supports from the current conceptual stage at lab scale to first competitive designs at production scale.

Recalling the results of this work, future research on monolithic catalyst supports should focus on the development of pseudo-heterogeneous models and on interfacial heat and mass transfer between the fluid and the solid phase. As mentioned above, pseudo-homogeneous models have reached their limit of accuracy. In addition, they will not provide new insights into heat transport in monolithic catalyst supports because they do not represent the presence of a highly conductive continuous solid phase well. Pseudo-heterogeneous models that treat the solid and the fluid temperature separately are thus inevitable to gain further insights into heat transport in monolithic catalyst supports for two reasons. First, the role of axial conduction in monolithic catalyst supports has to be clarified as it allows significant heat fluxes in *and* against the main flow direction. The influences of thermal conduction in the axial direction should also be investigated in the light of several segmented sponges which would typically be used to make up a catalyst bed of several meters. Second, the role of interfacial heat transfer limitations in the case of monolithic catalyst supports has to be clarified. In pseudo-homogeneous reactor models, the solid temperature is often separately taken into account on the catalyst scale, as in this work, to include the effect of interfacial heat transfer limitations on the temperature distribution. The solid temperatures at neighboring locations, however, do not influence each other in pseudo-homogeneous models. Although this can be assumed for individual pellets with only pointwise contact in a packed bed, it is certainly not true for monolithic catalyst supports with a continuous solid phase. Thus, interfacial heat transfer limitations should be explicitly investigated for monolithic catalyst supports. In addition, more data and reliable models on the heat transfer coefficient in monolithic catalyst structures is required as it sets the lower bound for the applicable flow rate. Therefore, detailed CFD simulations, or *in-silico* experiments, could be conducted as they provide the full distribution of the solid and the fluid temperature and thus allow to accurately deduce heat transfer coefficients. Furthermore, artificial heat sources could be distributed in the solid phase to readily simulate exo- or endothermic chemical reactions, to explore the role of interfacial heat transfer in monolithic catalyst supports. The solution of the resulting conjugate-heat-transfer problem is standard for state-of-the-art CFD codes, however, the creation of a computational mesh for solid sponges is still elaborate. Furthermore, massive computational resources are required to accurately describe the influence of the fluid and solid material, of the window and strut diameter, of the porosity, and of the fluid velocity on the heat transfer coefficient. The solution time of pseudo-heterogeneous models should also be monitored carefully to still allow optimization and tradeoff analyses, as presented in this work, to gain new insights in to the design of monolithic catalyst supports.

In addition to improvements regarding the description and modeling of heat transport, the influence of the catalyst coating should be investigated more systematically to allow more realistic estimations of the pressure loss along catalytic sponges.

Furthermore, experimental studies at the lab and pilot scale are necessary to validate the newly developed models. Special attention should be paid on the accuracy of the temperature measurement within the monolithic catalyst supports and the characterization of the wall temperature profile. Therefore, liquid cooling media such as oil or molten salt baths should be applied depending on the required temperature. Moreover, more research

on the thermal coupling of the monolithic supports and the reactor tube wall is necessary. In particular it should be tested if the approaches applied at the lab scale, for example wrapping of the monolithic supports with carbon foil, are sufficient and applicable also at a larger scale.

Finally, the prediction and evaluation of graded sponges with discrete porosity layers in the radial direction demonstrated the potential of tailored monolithic catalyst supports to resolve design tradeoffs with respect to high catalyst densities, low pressure losses, and high effective thermal conductivities. Consequently, this work represents a first step towards the advanced design of the monolithic catalyst supports which is a necessary prerequisite to utilize the full potential of POCS produced with additive manufacturing techniques (see for example Zhou and Liu [317]). If they can be produced in large numbers at affordable costs, and if the thermal coupling of the monolithic structures to the reactor wall is solved at production scale, undoubtedly the future of monolithic catalyst supports belongs to POCS. They provide full control over the morphology and thus not only allow the design of new unit cells, but also remove most of the statistical variations of geometric features which allows accurate description and modeling of heat and mass transport and interfacial heat and mass transfer. In combination, the advanced design of monolithic catalysts with graded morphological properties presented in this work, and the prospects of additive manufacturing techniques, enable the development of tailored next-generation catalyst supports that are ideally adapted to the process requirements.



## A.1 Verification of the catalyst model

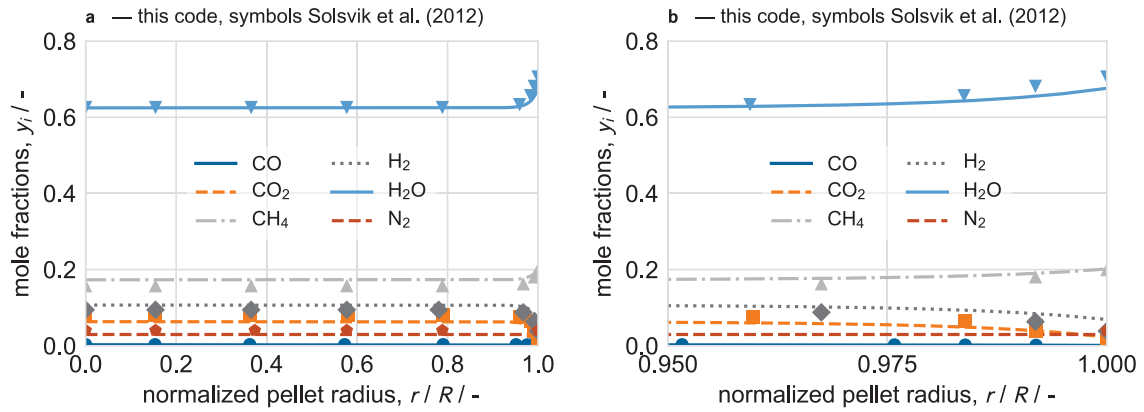


**FIG. A.1.** Comparison of the mole fractions in a  $\varnothing 17.3$  mm spherical  $\text{Al}_2\text{O}_3$  pellet during steam reforming of methane at 800 K and 29 bar calculated with the implemented catalyst-scale model and the values computed by Solsvik et al. [266] (a). The left plot (b) shows the mole fractions in the vicinity of the catalyst surface under the same conditions. The catalyst parameters were:  $d_p = 40$  nm,  $\rho_{\text{cat}}^{(\text{true})} = 2300$  kg m<sup>-3</sup>,  $\lambda_{\text{cat}} = 10$  W m<sup>-1</sup> K<sup>-1</sup>,  $\varepsilon_{\text{cat}} = 0.528$ , and  $\tau_{\text{cat}} = 1.87$ . For the simulations, the original kinetic model of Xu and Froment [308] was used.

## A.2 Influence of the number of axial and radial nodes on the simulation results

**TAB. A.1.** Influence of the number of axial and radial computational nodes,  $n_z$  and  $n_{rad}$ , on the methane yield  $Y_{CH_4}$ , the hot-spot temperature  $T_{max}$ , and the axial hot-spot position  $z_{max}$  for the 10 ppi sponges with feed conditions of 300 °C, 7.5 NL min<sup>-1</sup>, 4 bar, and H<sub>2</sub>/CO<sub>2</sub> = 4. The simulations were performed with the full reactor-scale model including interfacial mass and heat transfer and internal mass and heat transport.

No. axial nodes $n_z$	Quantity	No. radial nodes $n_r$						
		5	6	7	8	9	10	12
10	$Y_{CH_4}$ / -	0.56	0.56	0.56	0.56	0.56	0.56	0.56
	$T_{max}$ / °C	615	615	615	615	615	615	615
	$z_{max}$ / mm	62	61	61	61	61	61	61
12	$Y_{CH_4}$ / -	0.59	0.59	0.59	0.59	0.59	0.59	0.59
	$T_{max}$ / °C	614	614	614	614	614	614	614
	$z_{max}$ / mm	62	62	62	62	62	62	62
15	$Y_{CH_4}$ / -	0.59	0.59	0.59	0.59	0.59	0.59	0.59
	$T_{max}$ / °C	615	615	615	615	615	615	615
	$z_{max}$ / mm	62	62	62	62	62	62	62
18	$Y_{CH_4}$ / -	0.59	0.59	0.59	0.59	0.59	0.59	0.59
	$T_{max}$ / °C	616	616	616	616	616	616	616
	$z_{max}$ / mm	61	61	61	61	61	61	61
20	$Y_{CH_4}$ / -	0.58	0.58	0.58	0.58	0.58	0.58	0.58
	$T_{max}$ / °C	617	617	617	617	617	617	617
	$z_{max}$ / mm	60	60	60	60	60	60	60
25	$Y_{CH_4}$ / -	0.59	0.59	0.59	0.59	0.59	0.59	0.59
	$T_{max}$ / °C	618	619	619	619	619	619	619
	$z_{max}$ / mm	59	59	59	59	59	59	59

## A.3 Accuracy of the temperature measurement with thermocouples

The thermocouples used in the polytropic fixed-bed reactor experiments were enclosed in a cylinder ( $\varnothing 1.5$  mm) made out of a NiCr15Fe alloy (material number 2.4816), also known as alloy 600, or under the trade names Inconel® 600 and Nicrofer® 7216. Thus, not only heat transfer from the fluid to the solid thermocouple case, but also thermal conduction within the thermocouple case might influence the temperature at the tip of the thermocouple where the actual measurement takes place (see Fig. A.2). Recently, Gräf [94] already analyzed the effects in his doctoral thesis, however, he assumed a constant heat transfer coefficient  $\alpha$ , which is not true for different thermocouple diameters  $d_{TC}$ , and considered temperature differences between the wall and the center of the reactor tube up to only 50 K, which were exceeded in the experiments conducted in this work.

In order estimate the measurement error at the tip of the thermocouple, the temperature distribution within the thermocouple case was simulated using the 2-d transient energy balance in a solid cylinder (see Fig. A.2),

$$\rho_{TC} c_{p,TC} \frac{\partial T}{\partial t} = \lambda_{TC} \left( \frac{\partial^2 T}{\partial z^2} + \frac{\partial^2 T}{\partial r^2} + \frac{1}{r} \frac{\partial T}{\partial r} \right), \quad (\text{A.1})$$

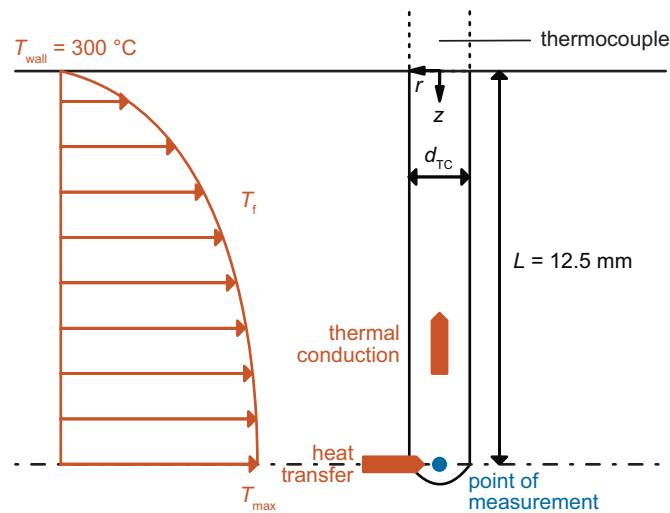


**FIG. A.2.** Illustration of the used model to estimate the effects of heat transfer from the fluid to the thermocouple case and of thermal conduction within the case of the thermocouples on the accuracy of the temperature measurement. The thermocouple is placed at the center of a  $\varnothing 25$  mm tube. The round tip of the thermocouple is assumed flat in the simulations. For the fluid temperature, a parabolic profile with constant wall temperature of  $300\text{ °C}$  and a maximum temperature  $T_{max}$  is assumed.

subject to the following initial and boundary conditions:

$$T(0, z, r) = T_{\text{wall}}, \quad (\text{A.2a})$$

$$T(t, 0, r) = T_{\text{wall}}, \quad (\text{A.2b})$$

$$\left. \frac{\partial T}{\partial z} \right|_{z=L} = 0, \quad (\text{A.2c})$$

$$\left. \frac{\partial T}{\partial r} \right|_{r=0} = 0, \quad (\text{A.2d})$$

$$\left. \frac{\partial T}{\partial r} \right|_{z=R} = \frac{\alpha}{\lambda_{\text{TC}}} [T_{\text{f}} - T(R)]. \quad (\text{A.2e})$$

The thermal properties of the case material were extracted from the Nicrofer® 7216 data sheet<sup>1</sup> provided by VDM metals. Accordingly,  $\rho_{\text{TC}} \approx 8500 \text{ kg m}^{-3}$ ,  $c_{\text{p,TC}} \approx 500 \text{ J kg}^{-1} \text{ K}^{-1}$ , and  $\lambda_{\text{TC}} \approx 20 \text{ W m}^{-1} \text{ K}^{-1}$  for  $300^\circ\text{C} \leq T \leq 500^\circ\text{C}$ . The heat transfer coefficient was calculated at the average fluid temperature,  $\frac{1}{2}(T_{\text{wall}} + T_{\text{max}})$  for a single cylinder in uniform fluid flow (see Gnielinski [89]):

$$Nu = 0.3 + 0.664 Re_1^{1/2} Pr^{1/3}, \quad (\text{A.3})$$

with the dimensionless groups

$$Nu = \frac{\alpha l}{\lambda_{\text{f}}}, \quad Re_1 = \frac{\rho_{\text{f}} v_{\text{sup}} l}{\mu_{\text{f}}}, \quad Pr_1 = \frac{\rho_{\text{f}} \mu_{\text{f}}}{\lambda_{\text{f}}}. \quad (\text{A.4})$$

Herein,  $l = \pi d_{\text{TC}}/2$  is the length of a streamline around the half circumference of the solid cylinder.

For the numerical solution, the same approach as for the solution of the reactor-scale model was applied. Consequently, the spatial derivatives in the axial and radial direction were discretized on a grid of Gauss-Lobatto-Chebyshev nodes using a pseudo-spectral method [71]. Afterwards, the system of semi-discretized equations was integrated along time. Because of the relatively small size of the investigated system, a simulation time  $t_{\text{end}} = 2 \text{ min}$  was sufficient to reach a steady state temperature distribution within the thermocouple case. Finally, the measurement error was calculated as the difference between the maximum fluid temperature and the temperature at the tip of the thermocouple,  $\Delta T_{\text{err}} = T_{\text{max}} - T(z = L, 0)$ .

Figure A.3 shows the determined measurement error over the superficial fluid velocity for various temperature difference between the tube center and the tube wall,  $\Delta T = T_{\text{max}} - T_{\text{wall}}$ , and thermocouples with  $\varnothing 1.5 \text{ mm}$  (a) and  $\varnothing 0.5 \text{ mm}$  (b). In general, the measurement error increases significantly with the temperature difference between the center and the wall of the tube, which is the driving force for thermal conduction in the thermocouple case. Also, the measurement error is higher at low velocities because heat transfer from the fluid to the thermocouple is less effective at low velocities than at high velocities. The sensitivity of the fluid velocity on the measurement error, however, is lower than the one of

<sup>1</sup>Nicrofer® 7216 data sheet by VDM Metals, [http://www.vdm-metals.com/fileadmin/user\\_upload/Downloads/Data\\_Sheets/Datenblatt\\_VDM\\_Alloy\\_600.pdf](http://www.vdm-metals.com/fileadmin/user_upload/Downloads/Data_Sheets/Datenblatt_VDM_Alloy_600.pdf), accessed 2017-07-31.

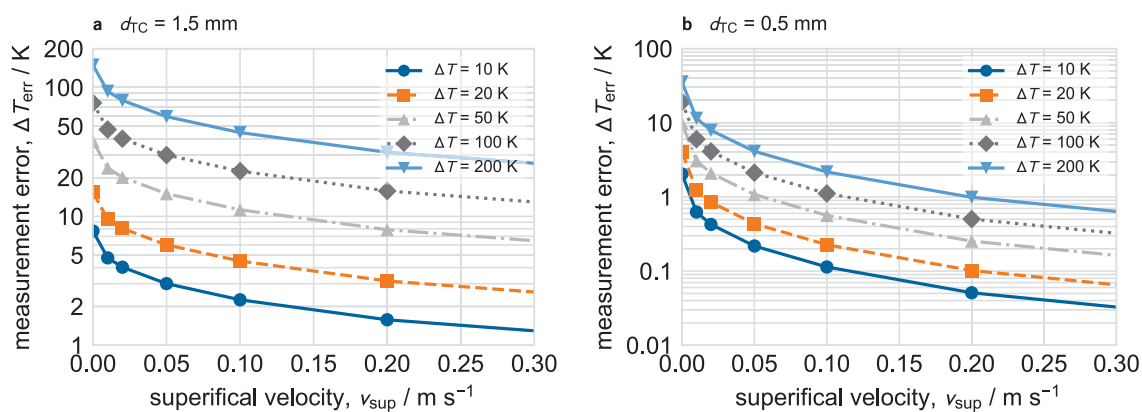


**FIG. A.3.** Estimated error of the temperature measurement using  $\varnothing 1.5$  mm (a) and  $\varnothing 0.5$  mm thermocouples, placed in the center of a plug-flow with velocity  $v_{\text{sup}}$  and parabolic temperature profile with temperature difference  $\Delta T$  between the maximum value and the wall ( $T_{\text{wall}} = 300$  °C). The tube diameter was 25 mm; the fluid was a 4:1  $\text{H}_2/\text{CO}_2$ -mixture at 4 bar.

the temperature difference. In addition, for catalysis experiments the fluid velocity can not arbitrarily be increased to reduce the temperature measurement error because the residence time decreases simultaneously. For the polytropic experiments conducted in this work, the fluid velocity was between  $0.05 \text{ m s}^{-1}$ – $0.15 \text{ m s}^{-1}$  at feed conditions. Consequently, the temperatures were only accurate within approximately 20 K–30 K for a temperature difference of 100 K (see Fig. A.3 a). For comparison, using  $\varnothing 0.5$  mm thermocouples at the same conditions lead to an accuracy of 1 K–2 K (see Fig. A.3 b). Nevertheless, the  $\varnothing 0.5$  mm are less stable and thus more difficult to position accurately in solid sponges. In addition, they can most likely not be inserted in packed beds of pellets as they bend as soon as they hit a pellet. Thus, a compromise between practical handling and measurement accuracy has to be made when designing experiments.

Finally, the calculated values of the measurement error serve only as approximate estimation because heat transfer from the fluid to the thermocouple case might be increased by favorable flow patterns (local acceleration), or decreased by unfavorable flow patterns (dead zones) in the vicinity of the thermocouple.



# Additional Simulation Results

# B

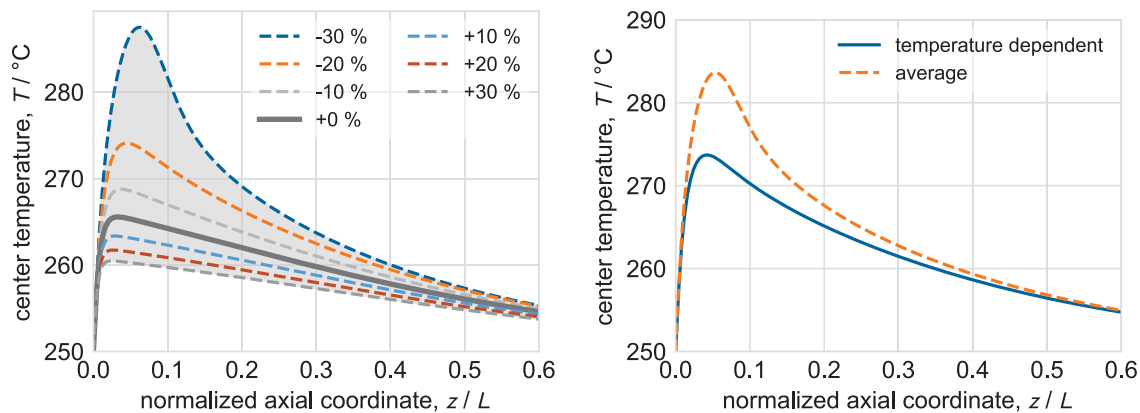


**FIG. B.1.** Influence of the uncertainty of the radial ETC  $\lambda_{\text{rad}}^{(\text{eff})}$  (left plot,  $\varepsilon_o = 0.8$ ,  $d_w = 0.8$  mm), and of the temperature-dependent solid thermal conductivity  $\lambda_s$  (right plot,  $\varepsilon_o = 0.75$ ,  $d_w = 0.6$  mm) on the axial temperature profile in catalytic sponges during methanation of carbon dioxide. The reference parameters (see Tab. 5.2, p.109) were used:  $T_{\text{in}} = 250$  °C,  $p_{\text{in}} = 10$  bar,  $\text{H}_2/\text{CO}_2 = 4$ ,  $G = 1.5$  kg m<sup>-2</sup> s<sup>-1</sup>,  $\dot{V}_m = 0.15$  NL g<sub>cat</sub><sup>-1</sup> min<sup>-1</sup>,  $D_t = 25$  mm,  $\delta = 50$  μm,  $\lambda_s = 12.5$  W m<sup>-1</sup> K<sup>-1</sup> (Al<sub>2</sub>O<sub>3</sub>). For the temperature-dependent solid thermal conductivity of Al<sub>2</sub>O<sub>3</sub>, the data measured by Fishedick et al. [69] was used.

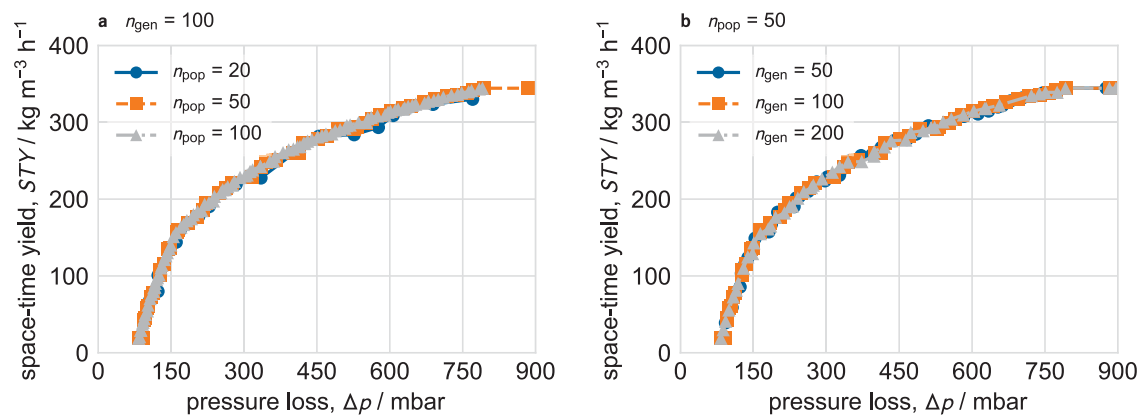


**FIG. B.2.** Influence of the population size (a) and the number of generations (b) in the NSGAI algorithm on the calculated Pareto-optimal sets. For the simulations, the reference parameters (see Tab. 5.2, p.109) were used:  $T_{\text{in}} = 250$  °C,  $p_{\text{in}} = 10$  bar,  $\text{H}_2/\text{CO}_2 = 4$ ,  $G = 1.5$  kg m<sup>-2</sup> s<sup>-1</sup>,  $\dot{V}_m = 0.15$  NL g<sub>cat</sub><sup>-1</sup> min<sup>-1</sup>,  $D_t = 25$  mm,  $\delta = 50$  μm,  $\lambda_s = 50$  W m<sup>-1</sup> K<sup>-1</sup> (SSiC).



# Additional Experimental Details

# C

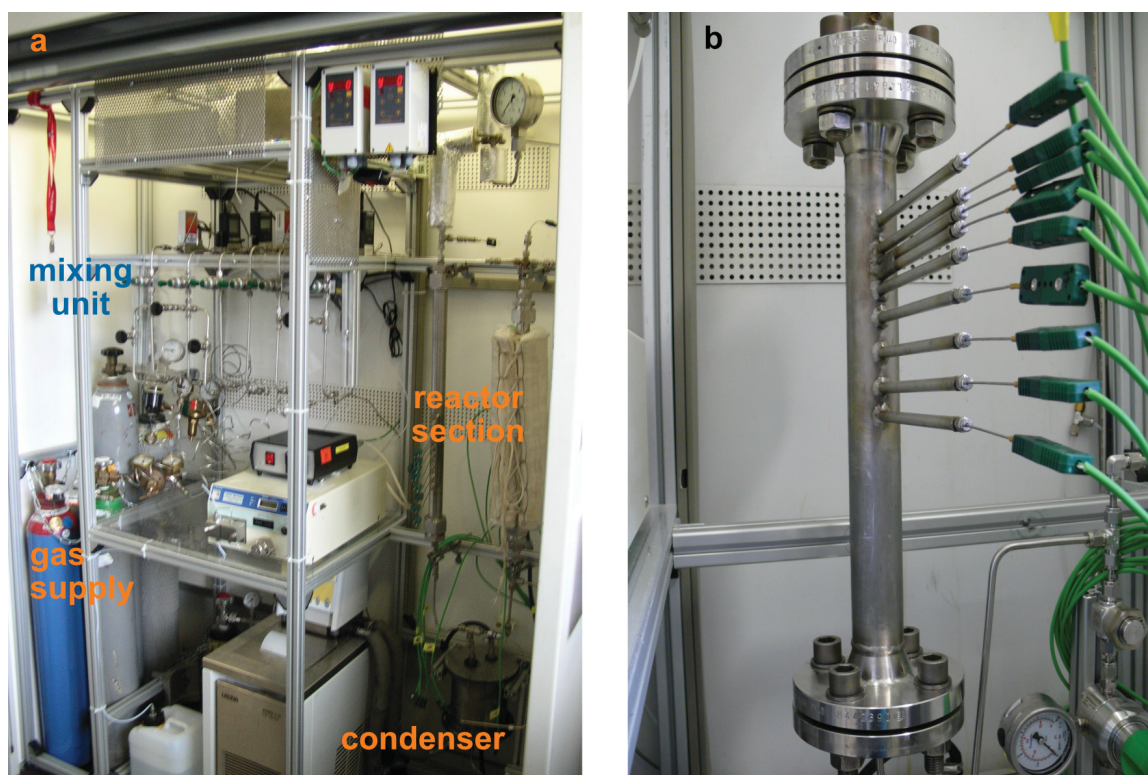


**FIG. C.1.** Photos of the lab-scale methanation setup (a) and the fixed-bed reactor (b). In the left photo, a preliminary fixed-bed reactor is seen in the reactor section. The right photo shows the reactor that was used for the polytropic experiments in this work (heater bands not mounted).

**TAB. C.1.** Measured gas phase compositions for different non-active materials involved in the polytropic experiments. The feed was a 4:1  $H_2/CO_2$ -mixture at 4 bar.

Sample	Temperature <sup>a</sup>	Molar fractions		
	°C	CO mol%	CH <sub>4</sub> mol%	CO <sub>2</sub> mol%
empty reactor tube	300	1.2	0.5	17.9
	400	2.0	0.5	17.9
	500	2.8	0.5	16.1
uncoated sponges	300	1.3	0.5	18.0
	400	1.7	0.5	17.6
	500	2.8	0.5	16.4
carbon foil	300	1.1	0.5	18.3
	400	1.3	0.5	18.4
	500	1.5	0.5	18.6

<sup>a</sup> measured with thermocouple 5 in the middle of the reactor

**TAB. C.2.** Summary of the applied gas chromatography methods for the analysis of the gas composition during the polytropic and kinetic experiments.

	Polytropic experiments	Kinetic experiments	
		front channel	back channel
gas chromatograph column	Hewlett Packard 6890 Supleco Carboxen <sup>TM</sup> PLOT 1010 30 m × 0.53 mm i. d.	Axel Semrau CompactGC Resteck Molsieve 5 Å 15 m × 0.32 mm i. d.	Resteck Q-Bond 30 m × 0.32 mm i. d.
carrier/makeup gas	helium 5.0 (Linde)	helium 5.0 (Linde)	helium 5.0 (Linde)
reference gas	helium 5.0 (Linde)	helium 5.0 (Linde)	helium 5.0 (Linde)
inlet split ratio	1:10	1:10	1:10
inlet split flow	50 Nml min <sup>-1</sup>	10 Nml min <sup>-1</sup>	50 Nml min <sup>-1</sup>
inlet temperature	230 °C	70 °C	70 °C
column pressure	39 kPa	50 kPa	50 kPa
column temperature	50 °C for 3 min to 150 °C in 5 min to 150 °C for 2 min	60 °C	40 °C
detector type	thermal conductivity detector (TCD)	thermal conductivity detector (TCD)	
detector temperature	230 °C	120 °C	120 °C
detector reference flow	30 Nml min <sup>-1</sup>	1 Nml min <sup>-1</sup>	1 Nml min <sup>-1</sup>
detector makeup flow	10 Nml min <sup>-1</sup>	-	-
total run time	10 min	3.5 min	

**TAB. C.3.** Summary of the determined retention times and response factors obtained during calibration of the gas chromatographs.

Quantity	Polytropic experiments		Kinetic experiments			
	Retention time min	Response factor	Retention time min	Response factor	Retention time min	Response factor
Species						
CO	2.68	0.2834	2.34	$0.63 \cdot 10^{-7}$	-	-
CH <sub>4</sub>	4.94	0.1275	2.53	$0.84 \cdot 10^{-7}$	1.94	$3.10 \cdot 10^{-7}$
CO <sub>2</sub>	7.40	0.3853	-	-	2.39	$1.91 \cdot 10^{-7}$

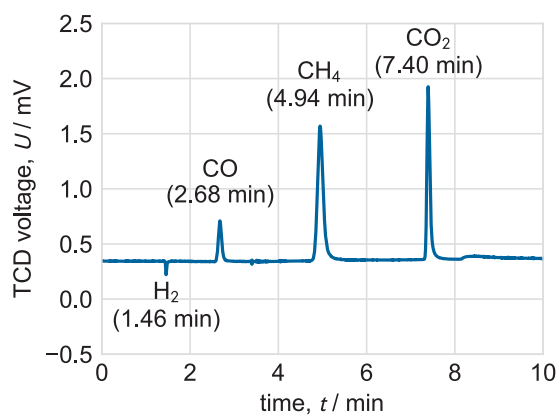


**FIG. C.2.** Example of a chromatogram obtained with the HP6890 during the polytropic experiments.

**TAB. C.4.** Summary of response factors and offsets determined during the calibration of the thermocouples from 20 °C–575 °C.

		Thermocouple									
		1	2	3	4	5	6	7	8	9	10
<b>Position</b>	mm	-	-20	0	10	20	30	50	75	100	120
<b>Response factor</b>	-	0.94	0.97	0.96	0.97	0.97	0.99	0.96	0.97	0.94	1.01
<b>Offset</b>	°C	2.72	1.92	1.98	1.51	0.67	0.58	0.67	0.81	0.75	0.63



# Computational Fluid Dynamics: Velocity distribution in solid sponges

## D.1 Setup of the CFD simulations

Based on the 3-d computer models of the investigated sponges obtained from  $\mu$ CT, Computational Fluid Dynamics (CFD) simulations were conducted to investigate the flow patterns in solid sponges in detail. Although several studies have already made use of CFD to investigate solid sponges (see Section 2.3.8, pp. 46 ff.), the radial velocity distribution and the effect of wall friction have not been analyzed yet.

For the CFD simulations, the 3-d models of the solid sponges were placed in a  $\varnothing 25$  mm tube using conventional CAD software. Subsequently, a computational finite-volume mesh was created. The mesh consisted of 25 mm long entrance section, the 25 mm long sponge, and a 50 mm long outlet section. At the inlet, a paraboloidal laminar velocity profile was set. At the outlet, the pressure was set to a fixed value. The velocity vector at the tube walls and at the surface of the sponge was set to zero (no-slip condition). Finally, laminar, incompressible ( $Ma \leq 0.3$ ), isothermal flow was simulated using OpenFOAM (version 2.4 [276, 302]). As the simulations required grids with several million cells, they were carried out in cooperation with the Center for Applied Space Technology and Microgravity (ZARM) at the University of Bremen, which kindly provided access to its high-performance computing cluster. Air at 20 °C and 1 bar was used as working fluid for all the simulations.

## D.2 Analysis of the radial velocity distribution in solid sponges

### Grid study and validations of the CFD simulations

Initially, a grid study was conducted to determine the required number of cells for the simulations. Therefore, the total pressure loss along the sponges was used as a measure to ensure a grid-independent solution (see Fig. D.1 a). For the 10 ppi, 20 ppi and 30 ppi sponges approximately 3–4 million cells were necessary to obtain a stable pressure loss. In case of the 40 ppi sponges, 5–6 million cells were needed because the smaller windows and thinner struts in the 40 ppi sponge require a higher resolution to be resolved accurately. Nevertheless, the mesh with 9 million cells was chosen for all subsequent simulations so that thin boundary layers at higher flow rates could also be resolved. Using 8 cores of an Intel® Xeon® E5 CPU, led to computational times of approximately 2 h–8 h depending on the inlet velocity.

To validate the CFD simulations, the calculated pressure loss along the sponge was compared to the analytical model of Inayat et al. [126] (see Section 2.3.3, pp. 24 ff.) for different superficial fluid velocities (Fig. D.1 b). The comparison shows a good match between the model and the CFD simulations and thus demonstrates the quality of the

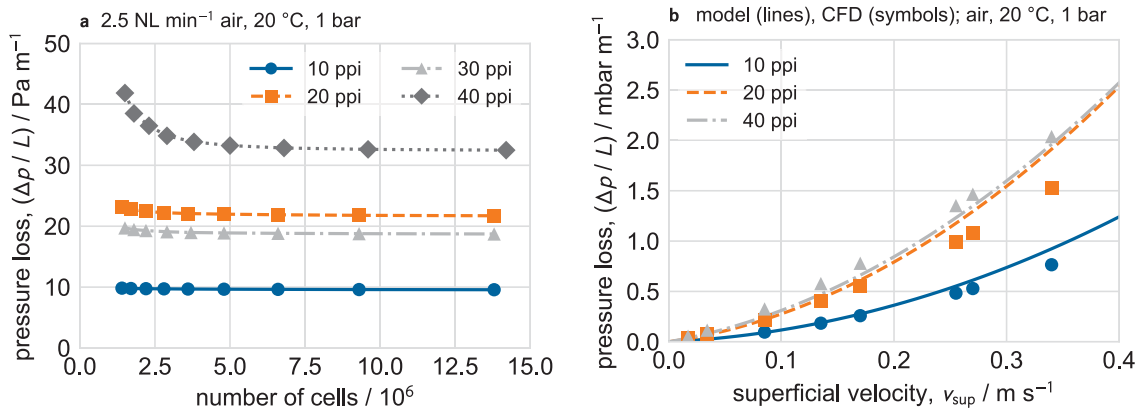


**FIG. D.1.** Influence on the number of computational cells on the pressure loss (a), and comparison of the simulated pressure loss along the investigated solid sponges against the model of Inayat et al. [126] (b). Air at  $20^\circ\text{C}$  and  $1 \text{ bar}$  was used for the CFD computations.

CFD simulations. The calculated pressure losses for the 20 ppi and 40 ppi sponges are quite similar because the influence of the larger windows of the 20 ppi sponge is compensated by the lower open porosity of the 20 ppi sponge.

#### Determination and comparison of the radial velocity profiles

As a result of the irregular 3-d morphology of solid sponges, the analysis and comparison of radial superficial velocity profiles requires intensive post-processing of the 3-d velocity fields. Therefore, the velocity field within the solid sponge was sliced into 25 (axial resolution of  $1 \text{ mm}$ ) circular slices (see Fig. D.2). Afterwards, each slice was divided into 100 rings of equal width. Subsequently, the axial velocity component was averaged over the available area for fluid flow in each of the rings, and multiplied by the average open porosity of the sample to obtain the local radial superficial velocity profile. Finally, the arithmetic average of the radial superficial velocity profiles was calculated, to obtain the average radial superficial velocity profile for a given sponge. The 5 slices adjacent to the beginning and end of the solid sponge were not included in the final averaging process

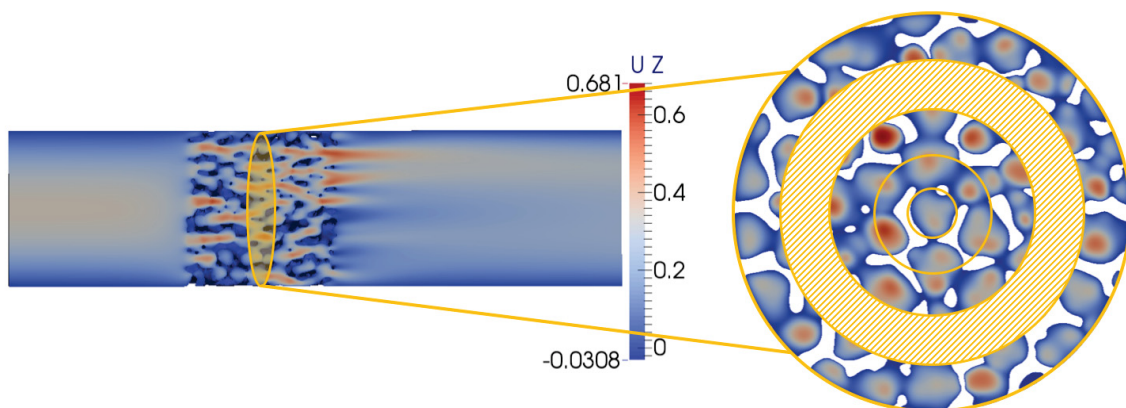


**FIG. D.2.** Map of the velocity distribution in a 20 ppi sponge at  $5 \text{ NL min}^{-1}$  (center-plane, left), and illustration of the averaging procedure to determine the radial superficial velocity profiles from the 3-d CFD computations.

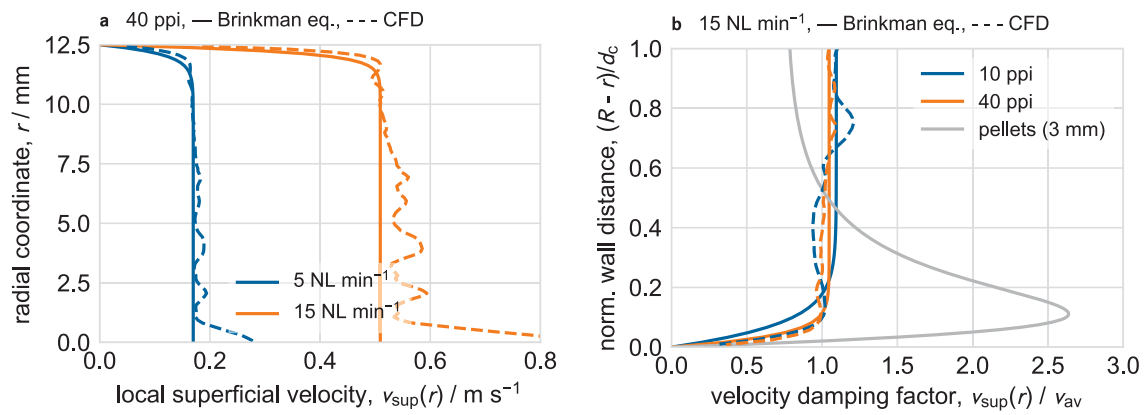


**FIG. D.3.** Comparison of average radial superficial velocity distributions (a) and the velocity damping factor (b) determined from the CFD simulations and from the solution of the extended Brinkmann equations (see Section 4.3.2, pp. 80 f.). For comparison, the velocity damping factor for a packed bed of  $\varnothing 3$  mm spherical pellets is shown (b).

because of in- and outflow effects that would falsify the shape of the average superficial velocity profile.

In Fig. D.3 a, the average superficial velocity profile obtained from the CFD simulations is compared to the solution of the extended Brinkman equation outlined in Section 4.3.2 (pp. 80 f.). Although the model for the effective viscosity required for the solution of the extended Brinkman equation was developed for packed beds of pellets, the modeled velocity profiles match well to the average superficial velocity profile obtained from the CFD simulations for the 40 ppi sample. The superficial velocity is almost uniform over the whole radius, and decreases to zero in the vicinity of the wall. The thickness of the boundary layer is approximately 1.5 mm for the 40 ppi sponge, which roughly corresponds to the average measured window diameter. In addition, the boundary layer seems slightly thinner for higher flow rates. The high oscillations of the average superficial velocity profile in the center were probably caused by the described averaging procedure. Because the inner rings contain only few cells, they are very sensitive to locally high or low porosities. A potential solution is the use of rings with equal area to distribute possible averaging errors equally along the radius of the sponge, however, at the cost of spatial resolution.

Finally, Fig. D.3 b shows the velocity damping factor  $D_v$ , introduced by Gräf et al. [95], for solid sponges and packed beds of pellets along the normalized wall distance. For the sponges, the cell diameter is used in the definition of the normalized wall distance; in case of the pellets, the pellet diameter is used. In contrast to the 40 ppi sponges, the solution of the Brinkman equation overestimates the thickness of the boundary layer for the 10 ppi sponges. Based on the results of the CFD simulations, the thickness of the boundary layer seems to be independent of the pore density. In comparison, the well-known velocity distribution in a packed bed of spherical pellets, here  $\varnothing 3$  mm, exhibits a strong increase in the vicinity of the wall because of the increased open porosity. In addition, the size of the boundary layer is significantly larger for the packed bed of pellets than for the solid sponges. Consequently, for catalytic applications, the sponges offer a much more controlled and predictable flow pattern. Nevertheless, more research is required to fully describe the

influence of the window diameter, the open porosity, and the flow rate on the shape of the velocity distribution in solid sponges, especially as the fluid velocity affects heat and mass transfer between the fluid and the solid phase.

# Calculation of Gas-Phase Equilibria

## Gibbs-free-energy minimization method

The gas-phase equilibrium compositions presented in Section 2.2.2 were calculated with the Gibbs-free-energy minimization method (see for example Gmehling et al. [88, pp. 556 ff.]), which was frequently applied in thermodynamic equilibrium calculations, for instance by Gao et al. [80], Jarungthammachote and Dutta [134], Li et al. [171], Nikoo and Amin [202], and Swapnesh et al. [273]. In contrast to equilibrium methods based on mass-action laws, the Gibbs free energy minimization does not require to specify all desired possible reactions a priori as input and thus allows to calculate general equilibrium compositions.

In order to calculate the gas-phase composition for a given temperature  $T$  and pressure  $p$ , the total Gibbs free energy of the system is minimized subject to the constraint that the number of atoms of each element in the mixture has to be conserved. Mathematically, the minimization problem is written as

$$\text{minimize}_{n_i} \quad G_t(T, p) = \sum_{i=1}^{n_s} n_i \left\{ \Delta_f g_i(T) + R_u T \ln \left[ \frac{n_i p \varphi_i(T, p)}{n_t^{(\text{gas})} p_0} \right] \right\} + n_C \Delta_f g_C(T) \quad (\text{E.1a})$$

$$\text{subject to} \quad \sum_{j=1}^{n_{\text{elem}}} e_{ij} n_i - e_j^0 = 0, \quad \text{conservation of atoms}, \quad (\text{E.1b})$$

$$n_i \geq 0, \quad \text{positive amounts}. \quad (\text{E.1c})$$

Here,  $n_i$  are the molar amounts of the gas-phase species,  $n_t^{(\text{gas})}$  is total molar amount of all gaseous species, and  $n_C$  is the molar amount of solid carbon, which is here additionally considered as only condensed species (see Jess and Wasserscheid [135, pp. 195 ff.]);  $e_{ij}$  is the number of atoms of element  $j$  in a molecule of species  $i$ . Further,  $\varphi_i$  are the fugacity coefficients of species  $i$ , and  $p_0 = 1$  bar is the reference pressure.

The temperature dependent molar Gibbs free energy of formation  $\Delta_f g_i$  of species  $i$  is calculated using

$$\Delta_f g_i(T) = \Delta_f h_i(T) - T \Delta_f s_i(T), \quad (\text{E.2})$$

where the heat and entropy of formation are calculated from

$$\Delta_f h_i(T) = h_i(T) - \sum_{j=1}^{n_{\text{elem}}} e_{ij} h_j(T), \quad (\text{E.3a})$$

$$\Delta_f s_i(T) = s_i(T) - \sum_{j=1}^{n_{\text{elem}}} e_{ij} s_j(T). \quad (\text{E.3b})$$

The molar enthalpy and molar entropy,  $h_i$  and  $s_i$ , are computed from NASA's polynomial equations [184], which are available for more than 2000 species over a large range of temperatures:

$$\frac{h_i(T)}{R_u T} = -a_{i1} \frac{1}{T^2} + a_{i2} \frac{\ln T}{T} + a_{i3} + a_{i4} \frac{T}{2} + a_{i5} \frac{T^2}{3} + a_{i6} \frac{T^3}{4} + a_{i7} \frac{T^4}{5} + \frac{b_{i1}}{T} \quad (\text{E.4a})$$

$$\frac{s_i(T)}{R_u} = -a_{i1} \frac{1}{2T^2} - a_{i2} \frac{1}{T} + a_{i3} \ln T + a_{i4} T + a_{i5} \frac{T^2}{2} + a_{i6} \frac{T^3}{3} + a_{i7} \frac{T^4}{4} + b_{i2} \quad (\text{E.4b})$$

The fugacity coefficients are calculated from either the Soave-Redlich-Kwong (SRK) EOS [263] or from the Peng-Robinson (PR) EOS [216].

### Soave-Redlich-Kwong EOS

The parameters of the SRK-EOS are

$$a_i(T) = 0.42748 \frac{(R_u T_{c,i})^2}{p_{c,i}} \alpha_i(T), \quad (\text{E.5a})$$

$$\alpha_i(T) = \left\{ 1 + \left( 0.48 + 1.574 \omega_i^{(\text{acc})} - 0.176 \omega_i^{(\text{acc})2} \right) \left[ 1 - \left( \frac{T}{T_{c,i}} \right)^{1/2} \right] \right\}^2, \quad (\text{E.5b})$$

$$b_i(T) = 0.08664 \frac{R_u T_{c,i}}{p_{c,i}}, \quad (\text{E.5c})$$

with the critical temperatures  $T_{c,i}$ , the critical pressure  $p_{c,i}$ , and the acentric factors  $\omega_i^{(\text{acc})}$ . All species parameters are tabulated for numerous species in [146].

The fugacity coefficients are calculated from (see Baehr and Kabelac [10, p. 309])

$$\ln \varphi_i = (Z - 1) \frac{b_i}{b_m} - \ln(Z - B) + \frac{A}{B} \ln \left( \frac{Z}{Z + B} \right) \left( \frac{2 \sum_{j=1}^{n_s} y_j a_{ij}}{a_m} - \frac{b_i}{b_m} \right) \quad (\text{E.6})$$

with

$$Z = \frac{v_m p}{R_u T}, \quad A = \frac{a_m p}{(R_u T)^2}, \quad B = \frac{b_m p}{R_u T}. \quad (\text{E.7})$$

### Mixing rules

The mixture parameters  $a_m$  and  $b_m$  are expressed by the following linear mixing rules:

$$a_m = \sum_{i=1}^{n_s} \sum_{j=1}^{n_s} y_i y_j a_{ij}, \quad (\text{E.8a})$$

$$b_m = \sum_{i=1}^{n_s} y_i b_i, \quad (\text{E.8b})$$

$$a_{ij} = \sqrt{a_i a_j}. \quad (\text{E.8c})$$

$$(\text{E.8d})$$

## Peng-Robinson EOS

In case of the PR-EOS, the parameters are

$$a_i(T) = 0.45724 \frac{(R_u T_{c,i})^2}{p_{c,i}} \alpha_i(T), \quad (\text{E.9a})$$

$$\alpha_i(T) = \left\{ 1 + \left( 0.37464 + 1.5422\omega_i^{(\text{acc})} - 0.26992\omega_i^{(\text{acc})^2} \right) \left[ 1 - \left( \frac{T}{T_{c,i}} \right)^{1/2} \right] \right\}^2, \quad (\text{E.9b})$$

$$b_i(T) = 0.0778 \frac{R_u T_c}{p_c}, \quad (\text{E.9c})$$

and the fugacity factors are calculated from (see Peng and Robinson [216])

$$\ln \varphi_i = (Z - 1) \frac{b_i}{b_m} - \ln(Z - B) + \frac{A}{2\sqrt{2}B} \ln \left[ \frac{Z + (1 - \sqrt{2})B}{Z + (1 + \sqrt{2})B} \right] \left( \frac{2 \sum_{j=1}^{n_s} y_j a_{ij}}{a_m} - \frac{b_i}{b_m} \right). \quad (\text{E.10})$$

## Calculation of the equilibrium mole fractions, conversions, and yields

After the minimization of the Gibbs free energy, the mole fractions of the gas-solid system  $z_i$ , the conversion of species  $j$ , and the yield and selectivity of species  $i$  regarding a key species  $j$  are calculated as follows:

$$z_i = \frac{n_i}{n_t}, \quad (\text{E.11a})$$

$$X_j = 1 - \frac{n_j}{n_j^0}, \quad (\text{E.11b})$$

$$Y_i = \frac{n_i - n_i^0 |v_j|}{n_j^0 - n_j v_i}, \quad (\text{E.11c})$$

$$S_{ij} = \frac{Y_i}{X_j}. \quad (\text{E.11d})$$

If multiple chemical reactions are considered, the stoichiometric factors  $v_i$  and  $v_j$  are commonly replaced by the number of carbon atoms in one molecule of the species  $i$  and  $j$ . The minimization problem was implemented in Python [289, version 2.4] solved using a solver developed by Kraft [155].

## Verification of the implementation

In order to verify the implementation of the Gibbs free energy method, the calculations of Gao et al. [80] were repeated and compared to the original values (see Fig. E.1 a to d). The almost perfect match of the results demonstrate that the implemented solver for gas-phase equilibria works flawlessly. The simulation times were between 10 ms–50 ms for each combination of temperature, pressure, and initial composition.

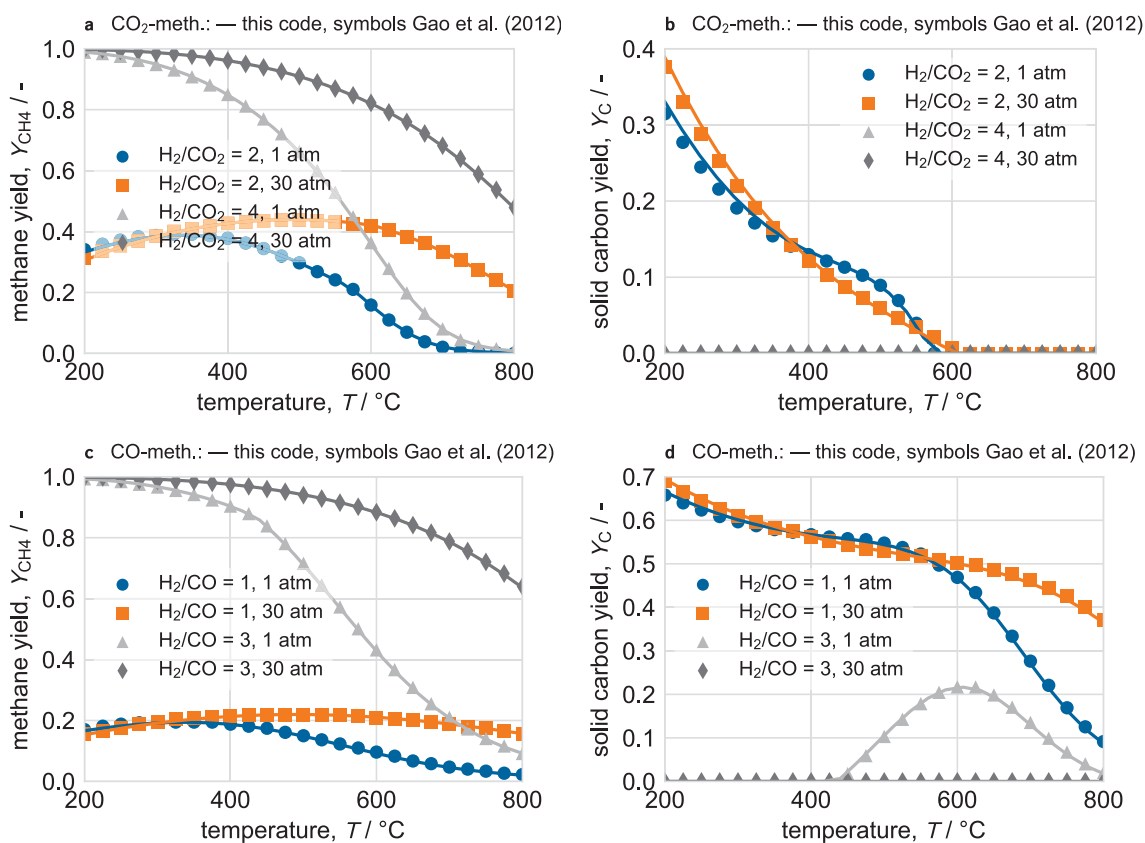


**FIG. E.1.** Comparison of the methane (a and c) and solid carbon equilibrium yields (b and d) calculated with the equilibrium solver implemented in this work (lines) with the results of Gao et al. [80] (symbols) for both, CO<sub>2</sub>-methanation (a and b) and CO-methanation (c and d).

# Calculation of Pure Species, Mixture, and Reaction Properties

## F.1 Calculation of pure species properties

The temperature-dependent viscosity, specific heat, and viscosity of pure species are calculated with the well-established correlations of Kleiber and Joh [146],

$$c_{p,i} \frac{M_i}{R_u} = B_i + (C_i - B_i) \left( \frac{T}{A_i + T} \right)^2 \dots \left\{ 1 - \frac{A_i}{A_i + T} \left[ D_i + E_i \frac{T}{A_i + T} \dots + F_i \left( \frac{T}{A_i + T} \right)^2 + G_i \left( \frac{T}{A_i + T} \right)^2 \right] \right\}, \quad (\text{F.1})$$

$$\mu_i = A_{\mu,i} + B_{\mu,i}T + C_{\mu,i}T^2 + D_{\mu,i}T^3 + E_{\mu,i}T^4, \quad (\text{F.2})$$

$$\lambda_i = A_{\lambda,i} + B_{\lambda,i}T + C_{\lambda,i}T^2 + D_{\lambda,i}T^3 + E_{\lambda,i}T^4. \quad (\text{F.3})$$

The binary diffusion coefficients are estimated using the Chapman-Enskog theory (see Bird et al. [22]),

$$D_{ij} = \frac{3}{16} \frac{1}{N_A \sigma_{ij} \Omega_{ij} p} \left[ \frac{2(R_u T)^3}{\pi} \left( \frac{1}{M_i} + \frac{1}{M_j} \right) \right]^{1/2}, \quad (\text{F.4})$$

with the binary collision diameter

$$\sigma_{ij} = \frac{1}{2} (\sigma_i + \sigma_j) \quad (\text{F.5})$$

and the binary Lennard-Jones parameters

$$\epsilon_{ij} = \sqrt{\epsilon_i \epsilon_j}. \quad (\text{F.6})$$

The collision integral is calculated using the fit of Neufeld et al. [198]:

$$\Omega_{ij} = \frac{1.06036}{T_{ij}^{*0.1561}} + \frac{0.1930}{\exp \left\{ 0.47635 T_{ij}^* \right\}} + \dots + \frac{1.03587}{\exp \left\{ 1.152996 T_{ij}^* \right\}} + \frac{1.76474}{\exp \left\{ 3.89411 T_{ij}^* \right\}} \quad (\text{F.7})$$

where

$$T_{ij}^* = \frac{k_B T}{\epsilon_{ij}}. \quad (\text{F.8})$$

## F.2 Calculation of gas mixture properties

The calculation of the mixture molar weight is trivial using the species molar weights and either the mole or mass fractions,

$$M = \sum_{i=1}^{n_s} y_i M_i = \frac{1}{\sum_{i=1}^{n_s} \frac{\omega_i}{M_i}}. \quad (\text{F.9})$$

With the mixture molar weight the conversion between mole and mass fractions is as follows:

$$y_i = \omega_i \frac{M}{M_i}. \quad (\text{F.10})$$

The mixture specific heat is calculated as sum of the pure species specific heats weighted by the mass fractions:

$$c_{p,f} = \sum_{i=1}^{n_s} \omega_i c_{p,i}. \quad (\text{F.11})$$

For the mixture viscosity, the mixture thermal conductivity, and the molar diffusion coefficient of species  $i$  in the stagnant mixture, Wilke's formula [304] is used:

$$\mu_f = \sum_{i=1}^{n_s} \frac{y_i \mu_i}{\sum_{j=1}^{n_s} y_j \phi_{ij}}, \quad (\text{F.12})$$

$$\lambda_f = \sum_{i=1}^{n_s} \frac{y_i \lambda_i}{\sum_{j=1}^{n_s} y_j \phi_{ij}}, \quad (\text{F.13})$$

and

$$D_{\text{mol},i} = \frac{1 - y_i}{\sum_{j=1, i \neq j}^{n_s} \frac{y_j}{D_{ij}}}, \quad (\text{F.14})$$

with the interaction parameters

$$\phi_{ij} = \frac{1}{\sqrt{8}} \left( 1 + \frac{M_i}{M_j} \right)^{-1/2} \left[ 1 + \left( \frac{\mu_i}{\mu_j} \right)^{1/2} \left( \frac{M_j}{M_i} \right)^{1/4} \right]^2. \quad (\text{F.15})$$

## F.3 Calculation of chemical reaction properties

The temperature-dependent reaction heat is calculated using Kirchhoff's equation,

$$\Delta_R H_j = \Delta_R H_{j,298} + \int_{298.15}^T \Delta_R C_{p,j} dT', \quad (\text{F.16})$$

with

$$\Delta_R C_{p,j} = \sum_{i=1}^{n_s} \nu_{ij} M_i c_{p,i}. \quad (\text{F.17})$$

The equilibrium constants in the kinetic models are calculated using van't Hoff's equation,

$$K_j^{(\text{eq})} = K_{j,298}^{(\text{eq})} \exp \left\{ \int_{298}^T \frac{\Delta_R H_j}{R_u T^2} dT' \right\}, \quad (\text{F.18})$$

with

$$K_{j,298}^{(\text{eq})} = \exp \left\{ -\frac{\Delta_R G_{j,298}}{R_u T_{\text{ref}}} \right\}. \quad (\text{F.19})$$

Both, the integral expressions in Eqns. (F.16) and (F.18), are solved analytically using Eq. (F.1), and hard-coded to allow fast evaluation during the solution of the reactor and catalyst models.



# Collection of Solid Sponge Morphological Properties

# G

**TAB. G.1.** Summary of reported open porosities, window diameters, and specific surface areas of ceramic and metal solid sponges. Metal sponges are listed at the end of the table.

No.	Study	Material	Open porosity -	Window diameter mm	Specific surface area $\text{m}^2 \text{m}^{-3}$
1	Buciuman et al.[33]	$\text{Al}_2\text{O}_3 - \text{SiO}_2$	0.83	1.500	
2		$\text{Al}_2\text{O}_3 - \text{SiO}_2$	0.86	1.550	-
3		$\text{Al}_2\text{O}_3 - \text{SiO}_2$	0.95	1.580	-
4		$\text{Al}_2\text{O}_3 - \text{SiO}_2$	0.80	0.950	-
5		$\text{Al}_2\text{O}_3 - \text{SiO}_2$	0.85	0.950	-
6		$\text{Al}_2\text{O}_3 - \text{SiO}_2$	0.88	0.940	-
7		$\text{Al}_2\text{O}_3 - \text{SiO}_2$	0.90	0.980	-
8		$\text{Al}_2\text{O}_3 - \text{SiO}_2$	0.77	0.580	-
9		$\text{Al}_2\text{O}_3 - \text{SiO}_2$	0.84	0.620	-
10		$\text{Al}_2\text{O}_3 - \text{SiO}_2$	0.84	0.630	-
11		$\text{Al}_2\text{O}_3 - \text{SiO}_2$	0.80	0.340	-
12		$\text{Al}_2\text{O}_3 - \text{SiO}_2$	0.85	0.360	-
13		$\text{Al}_2\text{O}_3 - \text{SiO}_2$	0.87	0.370	-
14		$\text{Al}_2\text{O}_3 - \text{SiO}_2$	0.83	0.210	-
15		$\text{Al}_2\text{O}_3 - \text{SiO}_2$	0.88	0.250	-
16	Richardson et al. [235]	$\text{Al}_2\text{O}_3$	0.82	0.695	-
17	Peng et al. [218]	$\text{Al}_2\text{O}_3$	0.87	0.826	-
18	Patcas et al. [213]	$\text{Al}_2\text{O}_3$	0.74	1.190	-
19		$\text{Al}_2\text{O}_3$	0.75	0.680	-
20	Große et al. [99]	$\text{Al}_2\text{O}_3$	0.76	1.096	1187
21		$\text{Al}_2\text{O}_3$	0.75	1.232	1204
22		$\text{Al}_2\text{O}_3$	0.76	0.745	1917
23	Incera Garrido et al. [129]	$\text{Al}_2\text{O}_3$	0.77	1.933	675
24		$\text{Al}_2\text{O}_3$	0.75	1.192	1187
25		$\text{Al}_2\text{O}_3$	0.77	0.871	1438
26		$\text{Al}_2\text{O}_3$	0.76	0.666	1884
27		$\text{Al}_2\text{O}_3$	0.81	2.252	629
28		$\text{Al}_2\text{O}_3$	0.81	1.131	1109
29		$\text{Al}_2\text{O}_3$	0.81	0.861	1422
30		$\text{Al}_2\text{O}_3$	0.80	0.687	1816
31		$\text{Al}_2\text{O}_3$	0.72	1.069	1290
32	Dietrich et al. [51]	$\text{Al}_2\text{O}_3$	0.69	1.529	1090
33		$\text{Al}_2\text{O}_3$	0.77	2.253	664
34		$\text{Al}_2\text{O}_3$	0.75	1.091	1204

continued on next page

**TAB. G.1.** Summary of reported sponge properties – continued from previous page.

No.	Study	Material	Open porosity -	Window diameter mm	Specific surface area $\text{m}^2 \text{m}^{-3}$
35		$\text{Al}_2\text{O}_3$	0.75	0.884	1402
36		$\text{Al}_2\text{O}_3$	0.76	0.625	1884
37		$\text{Al}_2\text{O}_3$	0.81	1.464	1109
38		$\text{Al}_2\text{O}_3-\text{SiO}_2$	0.74	1.405	1291
39		$\text{Al}_2\text{O}_3-\text{SiO}_2$	0.75	1.127	1395
40		$\text{Al}_2\text{O}_3-\text{SiO}_2$	0.74	0.685	2126
41	Grosse et al. [98]	$\text{Al}_2\text{O}_3$	0.69	1.974	639
42		$\text{Al}_2\text{O}_3$	0.72	1.070	1260
43		$\text{Al}_2\text{O}_3$	0.77	1.796	664
44		$\text{Al}_2\text{O}_3$	0.74	0.955	1204
45		$\text{Al}_2\text{O}_3$	0.75	0.847	1474
46		$\text{Al}_2\text{O}_3$	0.76	0.781	1884
47		$\text{Al}_2\text{O}_3$	0.81	1.952	629
48		$\text{Al}_2\text{O}_3$	0.81	1.137	1109
49		$\text{Al}_2\text{O}_3$	0.79	0.860	1520
50		$\text{Al}_2\text{O}_3$	0.78	0.651	1816
51		SiSiC	0.86	2.181	477
52		SiSiC	0.87	1.603	683
53	Edouard et al. [59]	SSiC	0.88	1.000	-
54	Truong Huu et al. [279]	SSiC	0.90	0.914	-
55		SSiC	0.85	0.895	-
56	Inayat et al. [125]	SSiC	0.85	1.800	732
57		SSiC	0.87	1.297	858
58		SSiC	0.86	1.030	1136
59	Mülheims et al. [192]	$\text{Al}_2\text{O}_3-\text{SiO}_2$	0.76	1.241	1118
60		$\text{Al}_2\text{O}_3-\text{SiO}_2$	0.75	0.970	1610
61		SSiC	0.81	1.249	-
62	Saber et al. [241]	SSiC	0.80	0.480	-
63		SSiC	0.90	0.700	-
64		SSiC	0.92	0.850	-
65		SSiC	0.95	0.140	-
66	Wallenstein et al. [296]	$\text{Al}_2\text{O}_3$	0.81	1.950	630
67		$\text{Al}_2\text{O}_3$	0.81	1.400	970
68		$\text{Al}_2\text{O}_3$	0.79	0.980	1330
69		$\text{Al}_2\text{O}_3$	0.69	1.970	640
70		SiSiC	0.86	2.180	470
71		SiSiC	0.86	1.600	660
72		OBSiC	0.77	2.530	500
73		$\text{Al}_2\text{O}_3-\text{SiO}_2$	0.76	2.020	640
74	this study	$\text{Al}_2\text{O}_3-\text{SiO}_2$	0.77	3.300	521
75		$\text{Al}_2\text{O}_3-\text{SiO}_2$	0.75	2.040	852
76		$\text{Al}_2\text{O}_3-\text{SiO}_2$	0.76	1.900	863

continued on next page

**TAB. G.1.** Summary of reported sponge properties – continued from previous page.

No.	Study	Material	Open porosity -	Window diameter mm	Specific surface area $\text{m}^2 \text{m}^{-3}$
77		$\text{Al}_2\text{O}_3 - \text{SiO}_2$	0.79	1.430	1106
78	Giani et al. [86]	FeCrAlloy®	0.94	4.300	-
79		FeCrAlloy®	0.93	4.700	-
80		FeCrAlloy®	0.94	2.200	-
81		FeCrAlloy®	0.94	2.000	-
82		FeCrAlloy®	0.93	1.700	-
83		Cu	0.91	4.600	-
84	Bianchi et al. [19]	FeCrAlloy®	0.94	2.200	-
85		FeCrAlloy®	0.93	0.860	1450
86		Al	0.89	0.860	936
87		Al	0.90	1.830	649
88		Al	0.94	0.810	-
89	Aghaei et al. [5]	Cu	0.95	0.210	-
90		Cu	0.96	0.340	-
91		FeCrAlloy®	0.90	0.190	-
92		FeCrAlloy®	0.94	0.490	-



# Notation

## A remark on units

SI units were used throughout this work. Thus, if not stated otherwise, all equations have to be evaluated using SI units to obtain correct results. Nevertheless, numerical values were often given in more practical units, such as mm instead of m. In addition, the non-SI units °C and bar were frequently used for temperature and pressure because they not only provide a more practical approach, especially for experimental results and operating conditions, but are also quasi-standard in the chemical engineering community. Moreover, the conversion of °C ( $0\text{ °C} = 273.15\text{ K}$ ,  $\Delta T/\text{K} = \Delta T/\text{°C}$ ) and bar ( $1\text{ bar} = 1 \cdot 10^5\text{ Pa}$ ) to their SI counterparts is trivial. Further, a temperature of 273.15 K and a pressure of 1.013 25 bar are used as normal conditions, also abbreviated NTP.

Symbol	Description	Unit
<i>Roman</i>		
$a_s$	solid/material thermal diffusivity	$\text{m}^2\text{ s}^{-1}$
$b$	weight in plate model	-
$a_i$	cohesion pressure between pure species $i$	$\text{Pa m}^6\text{ mol}^{-2}$
$a_{ij}$	cohesion pressure between species $i$ and $j$	$\text{Pa m}^6\text{ mol}^{-2}$
$b_i$	covolume of pure species $i$	$\text{m}^3\text{ mol}^{-1}$
$a_m$	cohesion pressure in the mixture	$\text{Pa m}^6\text{ mol}^{-2}$
$b_m$	covolume in the mixture	$\text{m}^3\text{ mol}^{-1}$
$a, b, c$	elliptical window axes	mm
$A_A$	CPIM pressure coefficient	$\text{kg}^{1/2}\text{ s}^{-1}\text{ mol}^{-1/2}$
$A_c$	CPIM pressure coefficient (continuum regime)	$\text{kg}^{1/2}\text{ s}^{-1}\text{ mol}^{-1/2}$
$A_{\text{cat,ext}}$	external surface area of catalyst	$\text{m}^2$
$A_{\text{Kn}}$	CPIM pressure coefficient (Knudsen regime)	$\text{kg}^{1/2}\text{ s}^{-1}\text{ mol}^{-1/2}$
$A_l$	cross-sectional area of layer $l$	$\text{m}^2$
$A_t$	tube cross-sectional area	$\text{m}^2$
$c_F$	Forchheimer coefficient	m
$c_{F,\text{av}}$	average Forchheimer coefficient	m
$c_{F,l}$	Forchheimer coefficient of layer $l$	m
$c_{p,i}$	specific heat capacity of pure species $i$	$\text{J kg}^{-1}\text{ K}^{-1}$
$c_{p,f}$	fluid specific heat capacity	$\text{J kg}^{-1}\text{ K}^{-1}$
$c_{p,s}$	solid/material specific heat capacity	$\text{J kg}^{-1}\text{ K}^{-1}$
$c_{p,\text{TC}}$	thermocouple specific heat capacity	$\text{J kg}^{-1}\text{ K}^{-1}$
$C_{\text{geo}}$	empirical coefficient heat and mass transfer	-
$C_h$	empirical coefficient heat transfer	-

continued on next page

continued from previous page

Symbol	Description	Unit
$C_m$	empirical coefficient mass transfer	-
$C_R$	radiation coefficient	-
$C_{Re}$	empirical coefficient heat transfer	-
$C_s, C_S$	coefficients in the tetrakaidecahedral unit cell model	-
$d_c$	cell diameter	mm
$d_{char}$	characteristic diameter	mm
$d_h$	hydraulic diameter	mm
$d_{mix}$	mixing length	mm
$d_p$	average pore diameter in catalyst	nm
$d_s$	strut diameter	mm
$d_{TC}$	diameter of thermocouple	mm
$d_w$	window diameter	mm
$D_p$	spherical/cylindrical pellet diameter	mm
$D_t$	reactor tube diameter	mm
$D_{ik}$	binary diffusion coefficient of species $i$ and $j$	$m^2 s^{-1}$
$D_{mol,i}$	molar diffusion coefficient of species $i$	$m^2 s^{-1}$
$D_i^{(Kn)}$	Knudsen diffusion coefficient of species $i$	$m^2 s^{-1}$
$D_i^{(eff)}$	effective diffusion coefficient of species $i$	$m^2 s^{-1}$
$D_{ax,i}^{(eff)}$	axial effective dispersion coefficient of species $i$	$m^2 s^{-1}$
$D_{rad,i}^{(eff)}$	radial effective dispersion coefficient of species $i$	$m^2 s^{-1}$
$D_{ik}^{(eff)}$	effective binary diffusion coefficient of species $i$ and $j$	$m^2 s^{-1}$
$D_v$	velocity damping factor	-
$e_{ij}$	number of element $i$ in molecule of species $j$	-
$e_j^0$	initial number of element $j$	-
$E_{a,j}$	activation energy of reaction $j$	$kJ mol^{-1}$
$E_R$	Roseland extinction coefficient	$m^{-1}$
$f_L$	coefficient in Lemlich's model	-
$F_1, F_2, F_3$	coefficients in Fishedick's [70] flow model	-
$g$	geometry factor in catalyst-scale model	-
$G$	gas load	$kg m^{-2} s^{-1}$
$G_l$	gas load in layer $l$	$kg m^{-2} s^{-1}$
$G_t$	total Gibbs free energy	J
$h_i$	molar enthalpy of species $i$	$J mol^{-1}$
$j_i$	mass flux of species $i$ in catalyst-scale model	$kg m^{-2} s^{-1}$
$j_{ax,i}$	mass flux of species $i$ in axial direction	$kg m^{-2} s^{-1}$
$j_{rad,i}$	mass flux of species $i$ in radial direction	$kg m^{-2} s^{-1}$
$k_B$	Boltzmann constant ( $1.380 \cdot 10^{-23}$ )	$J K^{-1}$
$k_{m,j}$	specific rate coefficient of reaction $j$	depends
$k_j^{(inf)}$	pre-exponential rate coefficient of reaction $j$	depends
$k_j^{(ref)}$	pre-exponential rate coefficient of reaction $j$ at reference temperature	depends
$K$	permeability	$m^2$
$K_{av}$	average permeability	$m^2$
$K_{ax}$	axial dispersion coefficient	-

continued on next page

continued from previous page

Symbol	Description	Unit
$K_l$	permeability of layer $l$	$\text{m}^2$
$K_{\text{rad}}$	radial dispersion coefficient	-
$K_i$	adsorption coefficient of species $i$	depends
$K_i^{(\text{inf})}$	pre-exponential adsorption coefficient of species $i$	depends
$K_{p,j}^{(\text{eq})}$	equilibrium constant of reaction $j$ (pressure formulation)	depends
$K_j^{(\text{eq})}$	equilibrium constant of reaction $j$	depends
$K_{j,298}^{(\text{eq})}$	equilibrium constant of reaction at 298.15 K $j$	depends
$l_s$	strut length	mm
$l$	length of streamline around thermocouple	mm
$L_t$	length of reactor tube	m
$L_{\text{tot}}$	total length of simulation domain	m
$m_{\text{cat}}$	mass of catalyst	mg
$m_{\text{coat}}$	mass of washcoat	mg
$m_h$	empirical exponent heat transfer	-
$m_m$	empirical exponent mass transfer	-
$m_{\text{sample}}$	mass of a sponge sample	g
$M_i$	molar mass of species $i$	$\text{g mol}^{-1}$
$n_{\text{elem}}$	number of individual elements	-
$n_i$	molar amount of species $i$	mol
$n_i^0$	initial molar amount of species $i$	mol
$n_l$	number of (radial) layers	-
$n_R$	number of reactions	-
$n_s$	number of species	-
$n_t$	total molar amount	mol
$n_t^{(\text{gas})}$	total molar amount in gas phase	mol
$N_A$	Avogadro number ( $6.022 \cdot 10^{23}$ )	$\text{mol}^{-1}$
$p$	pressure	Pa, bar
$p_0$	reference pressure (1)	bar
$p_{c,i}$	critical pressure of species $i$	Pa, bar
$p_i$	partial pressure of species $i$	Pa, bar
$p_i^{(\text{bulk})}$	partial pressure of species $i$ in bulk gas phase	Pa, bar
$p^{(\text{in})}$	pressure at reactor inlet	Pa, bar
$p^{(\text{out})}$	pressure at reactor outlet	Pa, bar
$q_i$	heat flux of species $i$ in catalyst-scale model	$\text{W m}^{-2}$
$q_{\text{ax}}$	heat flux in axial direction	$\text{W m}^{-2}$
$q_{\text{rad}}$	heat flux in radial direction	$\text{W m}^{-2}$
$r$	radial coordinate	mm
$r_l$	midpoint of the $l$ -th radial layer	mm
$r_l^{(\text{bound})}$	bound of the $l$ -th radial layer	mm
$r_{l,\text{inner}}$	midpoint of the innermost radial layer	mm
$r_{l,\text{outer}}$	midpoint of the outermost radial layer	mm
$r_{m,j}$	specific reaction rate of reaction $j$	$\text{mol kg}_{\text{cat}}^{-1} \text{s}^{-1}$
$r_{m,j}^{(\text{av})}$	average specific reaction rate of reaction $j$	$\text{mol kg}_{\text{cat}}^{-1} \text{s}^{-1}$
$r_{m,j}^{(\text{bulk})}$	specific reaction rate of reaction $j$ in bulk gas phase	$\text{mol kg}_{\text{cat}}^{-1} \text{s}^{-1}$

continued on next page

continued from previous page

Symbol	Description	Unit
$R_t$	radius of reactor tube	mm
$R_u$	universal gas constant (8.314)	$\text{J mol}^{-1} \text{K}^{-1}$
$s_i$	molar entropy of species $i$	$\text{J mol}^{-1} \text{K}^{-1}$
$S_{C5+}$	selectivity towards hydrocarbons longer than $C_5$	-
$S_i^{(\text{exp})}$	selectivity of species $i$ in experiments,	-
$S_{T,i}$	total sensitivity index of parameter $i$	-
$STY$	space-time yield	$\text{kg m}^{-3} \text{h}^{-1}$
$S_V$	specific (volumetric) surface area	$\text{m}^2 \text{m}^{-3}$
$t$	time	s
$t_{\text{end}}$	simulation time	s
$T$	temperature	K, °C
$T_{\text{bulk}}$	gas phase bulk temperature	K, °C
$T_{c,i}$	critical temperature of species $i$	K
$T_{\text{in}}$	inlet temperature	K, °C
$T_{\text{max}}$	maximum or hot-spot temperature	K, °C
$T_{\text{ref}}$	reference temperature	K
$T_{\text{wall}}$	wall temperature	K, °C
$v$	interstitial fluid velocity	$\text{m s}^{-1}$
$v_{\text{char}}$	characteristic fluid velocity	$\text{m s}^{-1}$
$v_m$	molar mixture volume	$\text{m}^3 \text{mol}^{-1}$
$v_{\text{sup}}$	superficial fluid velocity	$\text{m s}^{-1}$
$v_{\text{sup},l}$	superficial fluid velocity in layer $l$	$\text{m s}^{-1}$
$v_{\text{sup}}^{(\text{av})}$	radially averaged superficial fluid velocity	$\text{m s}^{-1}$
$V_{\text{app}}$	apparent volume of a sponge	$\text{cm}^3$
$V_{\text{bulk}}$	bulk sample volume of a sponge	$\text{cm}^3$
$V_{\text{cat}}$	catalyst volume	$\text{cm}^3$
$V_{\text{strut-cavities}}$	volume of the cavities inside the struts	$\text{cm}^3$
$\dot{V}$	volumetric flow rate	$\text{NL min}^{-1}$
$\dot{V}_m$	specific volumetric flow rate	$\text{NL g}_{\text{cat}}^{-1} \text{min}^{-1}$
$WHSV$	weight hourly space velocity	$\text{NL g}_{\text{cat}}^{-1} \text{h}^{-1}$
$X_i$	conversion of species $i$	-
$X_i^{(\text{exp})}$	conversion of species $i$ in experiments	-
$X_i^{(\text{mod})}$	simulated conversion of species $i$	-
$y_i^{(\text{dry})}$	mole fraction of species $i$ in a dry gas phase, i. e., without water vapor	-
$Y_i$	yield of species $i$	-
$Y_i^{(\text{exp})}$	yield of species $i$ in experiments	-
$Y_i^{(\text{mod})}$	simulated yield of species $i$	-
$z$	axial coordinate	m
$z_i$	mole fraction of species $i$ in a mixture	-
$z_{\text{max}}$	axial hot-spot position	m
<i>Greek</i>		
$\alpha$	heat transfer coefficient	$\text{W m}^{-2} \text{s}^{-1}$

continued on next page

continued from previous page

Symbol	Description	Unit
$\alpha_i$	cubic EOS parameter of species $i$	-
$\beta_i$	mass transfer coefficient	$\text{m s}^{-1}$
$\delta$	catalyst layer thickness	$\mu\text{m}$
$\Delta H_i$	adsorption enthalpy of species $i$	$\text{kJ mol}^{-1}$
$\Delta_f g_i$	molar Gibbs free energy of formation of species $i$	$\text{J mol}^{-1}$
$\Delta_R G_{j,298}$	Gibbs free energy of reaction $j$ at 298.15 K	$\text{kJ mol}^{-1}$
$\Delta_f h_i$	molar enthalpy of formation of species $i$	$\text{J mol}^{-1}$
$\Delta_R H_j$	reaction enthalpy of reaction $j$	$\text{kJ mol}^{-1}$
$\Delta_R H_{j,298}$	reaction enthalpy of reaction $j$ at 298.15 K	$\text{kJ mol}^{-1}$
$\Delta p$	pressure loss	Pa, mbar
$\Delta_f s_i$	molar entropy of formation of species $i$	$\text{J mol}^{-1} \text{K}^{-1}$
$\Delta T_{\text{max}}$	maximal temperature increase	K
$\Delta T_{\text{tol}}$	tolerable temperature increase	K
$\epsilon_i$	Lennard-Jones parameter of species $i$	J
$\epsilon_{ij}$	binary Lennard-Jones parameter of species $i$ and $j$	J
$\epsilon_{\text{bed}}$	open porosity of packed bed	-
$\epsilon_{\text{cat}}$	catalyst porosity	-
$\epsilon_{\text{n}}$	nominal porosity	-
$\epsilon_{\text{o}}, \epsilon_{\text{h}}$	open or hydrodynamic porosity	-
$\epsilon_{\text{o,av}}$	average open porosity	-
$\epsilon_{\text{o,inner}}$	open porosity of innermost layer	-
$\epsilon_{\text{o,outer}}$	open porosity outermost layer	-
$\epsilon_{\text{t}}$	total porosity	-
$\zeta$	coordinate in catalyst-scale model	$\mu\text{m}, \text{mm}$
$\eta_j$	effectiveness factor of reaction $j$	-
$\theta_{E,j}$	scaled activation energy of reaction $j$	-
$\theta_{k,j}$	scaled pre-exponential rate coefficient of reaction $j$	depends
$\lambda_i$	thermal conductivity of pure species $i$	$\text{W m}^{-1} \text{K}^{-1}$
$\lambda_{\text{coat}}$	thermal conductivity of the catalyst layer	$\text{W m}^{-1} \text{K}^{-1}$
$\lambda_{\text{f}}$	fluid (mixture) thermal conductivity	$\text{W m}^{-1} \text{K}^{-1}$
$\lambda_{\text{s}}$	solid/material thermal conductivity	$\text{W m}^{-1} \text{K}^{-1}$
$\lambda_{\text{TC}}$	thermocouple thermal conductivity	$\text{W m}^{-1} \text{K}^{-1}$
$\lambda_{\text{ax}}^{(\text{eff})}$	axial effective thermal conductivity	$\text{W m}^{-1} \text{K}^{-1}$
$\lambda_{\text{cond}}^{(\text{eff})}$	conductive effective thermal conductivity	$\text{W m}^{-1} \text{K}^{-1}$
$\lambda_{\text{cond}}^{(\text{eff})}$	radiative effective thermal conductivity	$\text{W m}^{-1} \text{K}^{-1}$
$\lambda_{\text{disp,ax}}^{(\text{eff})}$	dispersive axial effective thermal conductivity	$\text{W m}^{-1} \text{K}^{-1}$
$\lambda_{\text{disp,rad}}^{(\text{eff})}$	dispersive radial effective thermal conductivity	$\text{W m}^{-1} \text{K}^{-1}$
$\lambda_{\text{parallel}}^{(\text{eff})}$	parallel effective thermal conductivity	$\text{W m}^{-1} \text{K}^{-1}$
$\lambda_{\text{rad}}^{(\text{eff})}$	radial effective thermal conductivity	$\text{W m}^{-1} \text{K}^{-1}$
$\lambda_{\text{ray}}^{(\text{eff})}$	radiative effective thermal conductivity	$\text{W m}^{-1} \text{K}^{-1}$
$\lambda_{\text{stg}}^{(\text{eff})}$	stagnant effective thermal conductivity	$\text{W m}^{-1} \text{K}^{-1}$
$\lambda_{\text{serial}}^{(\text{eff})}$	serial effective thermal conductivity	$\text{W m}^{-1} \text{K}^{-1}$
$\mu_i$	viscosity of pure species $i$	Pa s
$\mu^{(\text{eff})}$	effective viscosity	Pa s

continued on next page

continued from previous page

Symbol	Description	Unit
$\mu_f$	fluid (mixture) viscosity	Pa s
$\mu_f^{(av)}$	radially averaged fluid (mixture) viscosity	Pa s
$\nu_{ij}$	stoichiometric coefficient of species $i$ in reaction $j$	-
$\rho_{app}$	apparent sponge density	$\text{kg m}^{-3}$
$\rho_{bulk}$	bulk sponge density	$\text{kg m}^{-3}$
$\rho_{env}$	envelope sponge density	$\text{kg m}^{-3}$
$\rho_f$	fluid (mixture) density	$\text{kg m}^{-3}$
$\rho_i$	mass concentration of species $i$	$\text{kg m}^{-3}$
$\rho_s$	solid density	$\text{kg m}^{-3}$
$\rho_{TC}$	thermocouple density	$\text{kg m}^{-3}$
$\rho_{cat}^{(true)}$	true catalyst density	$\text{kg m}^{-3}$
$\rho_{cat}^{(env)}$	envelope catalyst density	$\text{kg m}^{-3}$
$\rho_{cat}^{(bulk)}$	bulk catalyst density	$\text{kg m}^{-3}$
$\rho_f^{(av)}$	radially averaged fluid (mixture) density	$\text{kg m}^{-3}$
$\sigma_B$	Stefan-Boltzman constant ( $5.67 \cdot 10^{-8}$ )	$\text{W m}^{-2} \text{K}^{-4}$
$\sigma_X^{(exp)}$	standard deviations of experimental conversion	-
$\sigma_Y^{(exp)}$	standard deviations of experimental yield	-
$\sigma_i$	molecule diameter of species $i$	nm
$\sigma_{ij}$	binary collision diameter of species $i$ and $j$	nm
$\tau$	residence time	s
$\tau_{cat}$	catalyst tortuosity	-
$\tau_{spg}$	sponge tortuosity	-
$\varphi_i$	fugacity coefficient of species $i$	-
$\phi_{ij}$	interaction parameters between species $i$ and $j$	-
$\omega_i$	mass fraction of species $i$ in the gas phase	-
$\omega_i^{(in)}$	mass fraction of species $i$ at the reactor inlet	-
$\omega_i^{(bulk)}$	mass fraction of species $i$ in bulk gas phase	-
$\omega_i^{(acc)}$	acentric factor of species $i$	-
$\Omega_{ij}$	collision integral	-
<i>Dimensionless groups</i>		
$Nu$	Nusselt number ( $\alpha d_{char} / \lambda_f$ )	-
$Pe$	Peclet number, ( $\rho_f c_{p,f} v_{char} d_{char} / \lambda_f$ )	-
$Pr$	Prandtl number, ( $\mu_f c_{p,f} / \lambda_f$ )	-
$Re$	Reynolds number, ( $\rho_f v_{char} d_{char} / \mu_f$ )	-
$Sc$	Schmidt number, ( $\mu_f / (\rho_f D_{mol,i})$ )	-
$Se$	Semenov number, see Eq. (2.8), p. 17	-
$Sh$	Sherwood number, ( $\beta_i d_{char} / D_{mol,i}$ )	-
$\phi_j$	Thiele modulus of reaction $j$ , see Eq. (4.27), p. 87	-
<i>Abbreviations</i>		
3DFD	3-d fiber deposition	
ABS	acrylonitrile butadiene styrene	
CAD	Computer Aided Design	

continued on next page

continued from previous page

<b>Symbol</b>	<b>Description</b>	<b>Unit</b>
CAS	computer algebra system	
CFD	Computational Fluid Dynamics	
CPIM	cylindrical pore interpolation model	
CSTR	continuously-stirred tank reactor	
$\mu$ CT	X-ray absorption micro Computer Tomography	
DGM	dusty gas model	
EDC	effective diffusion/dispersion coefficient	
EDX	energy-dispersive X-ray spectroscopy	
ETC	effective thermal conductivity	
FBR	fixed-bed reactor	
FBMR	fixed-bed membrane reactor	
GC	gas chromatography	
HPC	high performance computing	
MOO	multi-objective optimization	
MRI	Magnetic Resonance Imaging	
NSGAI	Non-dominated Sorting Algorithm II	
NTP	norm temperature and pressure	
PIV	Particle Image Velocimetry	
POCS	periodic open-cellular structures	
PU	polyurethane	
RSS	residual sum of squares	
SEBM	selective electron beam melting	
SEM	scanning electron microscopy	
SLS	selective laser sintering	
SSA	specific surface area	
STY	space-time yield	
TCD	thermal conductivity detector	
TOS	time on stream	
TRL	Technology Readiness Level	
WHSV	weight-hourly space velocity	
ZSM-5	Zeolite Socony Mobil-5	



## References

- [1] S. Abelló, C. Berruero, and D. Montané. "High-loaded nickel-alumina catalyst for direct CO<sub>2</sub> hydrogenation into synthetic natural gas (SNG)". *Fuel* 113 (2013), pp. 598–609. DOI: 10.1016/j.fuel.2013.06.012.
- [2] T. A. Adams and P. I. Barton. "A dynamic two-dimensional heterogeneous model for water gas shift reactors". *International Journal of Hydrogen Energy* 34 (2009), pp. 8877–8891. DOI: 10.1016/j.ijhydene.2009.08.045.
- [3] J. Adler and G. Standke. "Offenzellige Schaumkeramik, Teil 1". *Keramische Zeitschrift* 55 (2003), pp. 694–703.
- [4] J. Adler and G. Standke. "Offenzellige Schaumkeramik, Teil 2". *Keramische Zeitschrift* 55 (2003), pp. 786–793.
- [5] P. Aghaei, C. G. Visconti, G. Groppi, and E. Tronconi. "Development of a heat transport model for open-cell metal foams with high cell densities". *Chemical Engineering Journal* 321 (2017), pp. 432–446. DOI: 10.1016/j.cej.2017.03.112.
- [6] P. A. Aldana, F. Ocampo, K. Kobl, B. Louis, F. Thibault-Starzyk, M. Daturi, P. Bazin, S. Thomas, and A. C. Roger. "Catalytic CO<sub>2</sub> valorization into CH<sub>4</sub> on Ni-based ceria-zirconia. Reaction mechanism by operando IR spectroscopy". *Catalysis Today* 215 (2013), pp. 201–207. DOI: 10.1016/j.cattod.2013.02.019.
- [7] F. Ausfelder, C. Beilmann, M. Bertau, S. Bräuninger, A. Heinzl, R. Hoer, W. Koch, F. Mahlendorf, A. Metzethin, M. Peuckert, L. Plass, K. Räuchle, M. Reuter, G. Schaub, S. Schiebahn, E. Schwab, F. Schüth, D. Stolten, G. Teßmer, K. Wagemann, and K. F. Ziegahn. "Energiespeicherung als Element einer sicheren Energieversorgung". *Chemie-Ingenieur-Technik* 87 (2015), pp. 17–89. DOI: 10.1002/cite.201400183.
- [8] P. Avila, M. Montes, and E. E. Miró. "Monolithic reactors for environmental applications: A review on preparation technologies". *Chemical Engineering Journal* 109 (2005), pp. 11–36. DOI: 10.1016/j.cej.2005.02.025.
- [9] A. Avril, C. H. Hornung, A. Urban, D. Fraser, M. Horne, J.-P. Veder, J. Tsanaktsidis, T. Rodopoulos, C. Henry, and D. R. Gunasegaram. "Continuous flow hydrogenations using novel catalytic static mixers inside a tubular reactor". *Reaction Chemistry & Engineering* 2 (2017), pp. 180–188. DOI: 10.1039/C6RE00188B.
- [10] H. D. Baehr and S. Kabelac. *Thermodynamik – Grundlagen und technische Anwendungen*. 15th ed. Berlin, Germany: Springer, 2012.
- [11] M. Bai and J. N. Chung. "Analytical and numerical prediction of heat transfer and pressure drop in open-cell metal foams". *International Journal of Thermal Sciences* 50 (2011), pp. 869–880. DOI: 10.1016/j.ijthermalsci.2011.01.007.
- [12] M. Bailera, P. Lisbona, L. M. Romeo, and S. Espatolero. "Power to Gas projects review: Lab, pilot and demo plants for storing renewable energy and CO<sub>2</sub>". *Renewable and Sustainable Energy Reviews* 69 (2017), pp. 292–312. DOI: 10.1016/j.rser.2016.11.130.

- [13] BASF SE. *BASF establishes new Group company to pursue business opportunities in 3D printing [press release]*. 2017. URL: <https://www.basf.com/en/company/news-and-media/news-releases/2017/07/p-17-278.html> (visited on Aug. 8, 2017).
- [14] R. Bauer and E. Schlünder. "Effective radial thermal conductivity of packings in gas flow. Part I. Convective transport coefficient". *International Chemical Engineering* 18 (1978), pp. 181–188.
- [15] M. Belimov, D. Metzger, and P. Pfeifer. "On the temperature control in a microstructured packed bed reactor for methanation of CO/CO<sub>2</sub> mixtures". *AIChE Journal* 63 (2017), pp. 120–129. DOI: 10.1002/aic.15461.
- [16] P. Benz, P. Hütter, and A. Schlegel. "Radiale Stoffdispersionskoeffizienten in durchströmten keramischen Schäumen". *Wärme- und Stoffübertragung* 127 (1993), pp. 125–127.
- [17] A. Bhattacharya, V. Calmidi, and R. Mahajan. "Thermophysical properties of high porosity metal foams". *International Journal of Heat and Mass Transfer* 45 (2002), pp. 1017–1031. DOI: 10.1016/S0017-9310(01)00220-4.
- [18] E. Bianchi, G. Groppi, W. Schwieger, E. Tronconi, and H. Freund. "Numerical simulation of heat transfer in the near-wall region of tubular reactors packed with metal open-cell foams". *Chemical Engineering Journal* 264 (2015), pp. 268–279. DOI: 10.1016/j.cej.2014.11.055.
- [19] E. Bianchi, T. Heidig, C. G. Visconti, G. Groppi, H. Freund, and E. Tronconi. "An appraisal of the heat transfer properties of metallic open-cell foams for strongly exo-/endo-thermic catalytic processes in tubular reactors". *Chemical Engineering Journal* 198-199 (2012), pp. 512–528. DOI: 10.1016/j.cej.2012.05.045.
- [20] E. Bianchi, T. Heidig, C. G. Visconti, G. Groppi, H. Freund, and E. Tronconi. "Heat transfer properties of metal foam supports for structured catalysts: Wall heat transfer coefficient". *Catalysis Today* 216 (2013), pp. 121–134. DOI: 10.1016/j.cattod.2013.06.019.
- [21] E. Bianchi, W. Schwieger, and H. Freund. "Assessment of periodic open cellular structures for enhanced heat conduction in catalytic fixed-bed reactors". *Advanced Engineering Materials* 18 (2015), pp. 608–614. DOI: 10.1002/adem.201500356.
- [22] R. Bird, W. Stewart, and E. Lightfoot. *Transport Phenomena*. 2nd ed. New York, NY, USA: Wiley, 2007.
- [23] F. Biscani, D. Izzo, and C. H. Yam. "A global optimisation toolbox for massively parallel engineering optimisation". *4th International Conference on Astrodynamics Tools and Techniques ICATT 2010* (2010), pp. 1–11.
- [24] K. B. Bischoff. "Effectiveness factors for general reaction rate forms". *AIChE Journal* 11 (1965), pp. 351–355. DOI: 10.1002/aic.690110229.
- [25] K. Boomsma, D. Poulikakos, and Y. Ventikos. "Simulations of flow through open cell metal foams using an idealized periodic cell structure". *International Journal of Heat and Fluid Flow* 24 (2003), pp. 825–834. DOI: 10.1016/j.ijheatfluidflow.2003.08.002.
- [26] K. Boomsma, D. Poulikakos, and F. Zwick. "Metal foams as compact high performance heat exchangers". *Mechanics of Materials* 35 (2003), pp. 1161–1176. DOI: 10.1016/j.mechmat.2003.02.001.
- [27] M. A. Branch, T. F. Coleman, and Y. Li. "A subspace, interior, and conjugate gradient method for large-scale bound-constrained minimization problems". *Society* 21 (1999), pp. 1–23. DOI: 10.1137/S1064827595289108.

- [28] W. M. Brandstädter and B. Kraushaar-Czarnetzki. "Maleic anhydride from mixtures of n-butenes and n-butane: Simulation of a production-scale nonisothermal fixed-bed reactor". *Industrial and Engineering Chemistry Research* 46 (2007), pp. 1475–1484. DOI: 10.1021/ie061142q.
- [29] J. Bremer, K. H. G. Rätze, and K. Sundmacher. "CO<sub>2</sub> methanation: optimal start-up control of a fixed-bed reactor for power-to-gas applications". *AIChE Journal* 63 (2017), pp. 23–31. DOI: 10.1002/aic.15496.
- [30] K. P. Brooks, J. Hu, H. Zhu, and R. J. Kee. "Methanation of carbon dioxide by hydrogen reduction using the Sabatier process in microchannel reactors". *Chemical Engineering Science* 62 (2007), pp. 1161–1170. DOI: 10.1016/j.ces.2006.11.020.
- [31] E. C. Bucharsky, K. G. Schell, P. Habisreuther, R. Oberacker, N. Zarzalis, and M. J. Hoffmann. "Preparation of optically transparent open-celled foams and its morphological characterization employing volume image analysis". *Advanced Engineering Materials* 13 (2011), pp. 1060–1065. DOI: 10.1002/adem.201100024.
- [32] E. C. Bucharsky, K. G. Schell, R. Oberacker, and M. J. Hoffmann. "Preparation of transparent glass sponges via replica method using high-purity silica". *Journal of the American Ceramic Society* 93 (2010), pp. 111–114. DOI: 10.1111/j.1551-2916.2009.03366.x.
- [33] F. C. Buciuman and B. Kraushaar-Czarnetzki. "Ceramic foam monoliths as catalyst carriers. 1. adjustment and description of the morphology". *Industrial & Engineering Chemistry Research* 42 (2003), pp. 1863–1869. DOI: 10.1021/ie0204134.
- [34] W. M. Carty and P. W. Lednor. "Monolithic ceramics and heterogeneous catalysts: Honeycombs and foams". *Current Opinion in Solid State and Materials Science* 1 (1996), pp. 88–95. DOI: 10.1016/S1359-0286(96)80015-5.
- [35] I. Cerri, G. Saracco, and V. Specchia. "Methane combustion over low-emission catalytic foam burners". *Catalysis Today* 60 (2000), pp. 21–32. DOI: 10.1016/S0920-5861(00)00313-8.
- [36] P. Ciambelli, V. Palma, and E. Palo. "Comparison of ceramic honeycomb monolith and foam as Ni catalyst carrier for methane autothermal reforming". *Catalysis Today* 155 (2010), pp. 92–100. DOI: 10.1016/j.cattod.2009.01.021.
- [37] Climeworks AG. *World-first Climeworks plant: Capturing CO<sub>2</sub> from air to boost growing vegetables [press release]*. 2017. URL: <http://www.climeworks.com/world-first-co2-capture-plant/> (visited on June 29, 2017).
- [38] V. Cominos and A. Gavriilidis. "Theoretical investigation of axially non-uniform catalytic monoliths for methane combustion". *Chemical Engineering Science* 56 (2001), pp. 3455–3468. DOI: 10.1016/S0009-2509(01)00031-8.
- [39] S. Couck, J. Lefevre, S. Mullens, L. Protasova, V. Meynen, G. Desmet, G. V. Baron, and J. F. M. Denayer. "CO<sub>2</sub>, CH<sub>4</sub> and N<sub>2</sub> separation with a 3DFD-printed ZSM-5 monolith". *Chemical Engineering Journal* 308 (2017), pp. 719–726. DOI: 10.1016/j.cej.2016.09.046.
- [40] S. Danaci, L. Protasova, J. Lefevre, L. Bedel, R. Guilet, and P. Marty. "Efficient CO<sub>2</sub> methanation over Ni/Al<sub>2</sub>O<sub>3</sub> coated structured catalysts". *Catalysis Today* 273 (2016), pp. 234–243. DOI: 10.1016/j.cattod.2016.04.019.
- [41] S. Das, S. S. Mullick, and P. N. Suganthan. "Recent advances in differential evolution-An updated survey". *Swarm and Evolutionary Computation* 27 (2016), pp. 1–30. DOI: 10.1016/j.swevo.2016.01.004.
- [42] K. P. de Jong. *Synthesis of Solid Catalysts*. Ed. by K. P. de Jong. Weinheim, Germany: Wiley, 2009.

- [43] K. Deb, A. Pratap, S. Agarwal, and T. Meyarivan. "A fast and elitist multiobjective genetic algorithm: NSGA-II". *IEEE Transactions on Evolutionary Computation* 6 (2002), pp. 182–197. DOI: 10.1109/4235.996017.
- [44] J. N. Dew, R. R. White, and C. M. Sliepcevich. "Hydrogenation of carbon dioxide on nickel-kieselguhr catalyst". *Industrial & Engineering Chemistry* 47 (1955), pp. 140–146. DOI: 10.1021/ie50541a044.
- [45] A. Diani, K. K. Bodla, L. Rossetto, and S. V. Garimella. "Numerical analysis of air flow through metal foams". *Energy Procedia* 45 (2014), pp. 645–652. DOI: 10.1016/j.egypro.2014.01.069.
- [46] B. Dietrich. "Heat transfer coefficients for solid ceramic sponges – Experimental results and correlation". *International Journal of Heat and Mass Transfer* 61 (2013), pp. 627–637. DOI: 10.1016/j.ijheatmasstransfer.2013.02.019.
- [47] B. Dietrich, T. Fishedick, S. Heissler, P. G. Weidler, C. Wöll, and M. Kind. "Optical parameters for characterization of thermal radiation in ceramic sponges - Experimental results and correlation". *International Journal of Heat and Mass Transfer* 79 (2014), pp. 655–665. DOI: 10.1016/j.ijheatmasstransfer.2014.08.023.
- [48] B. Dietrich, M. Kind, and H. Martin. "Axial two-phase thermal conductivity of ceramic sponges - Experimental results and correlation". *International Journal of Heat and Mass Transfer* 54 (2011), pp. 2276–2282. DOI: 10.1016/j.ijheatmasstransfer.2011.02.037.
- [49] B. Dietrich, G. Schell, E. Bucharsky, R. Oberacker, M. Hoffmann, W. Schabel, M. Kind, and H. Martin. "Determination of the thermal properties of ceramic sponges". *International Journal of Heat and Mass Transfer* 53 (2010), pp. 198–205. DOI: 10.1016/j.ijheatmasstransfer.2009.09.041.
- [50] B. Dietrich. "Thermische Charakterisierung von keramischen Schwammstrukturen für verfahrenstechnische Apparate". Dissertation. Karlsruhe, Karlsruher Institut für Technologie, 2010.
- [51] B. Dietrich, W. Schabel, M. Kind, and H. Martin. "Pressure drop measurements of ceramic sponges-Determining the hydraulic diameter". *Chemical Engineering Science* 64 (2009), pp. 3633–3640. DOI: 10.1016/j.ces.2009.05.005.
- [52] N. Djordjevic, P. Habisreuther, and N. Zarzalis. "A numerical investigation of the flame stability in porous burners employing various ceramic sponge-like structures". *Chemical Engineering Science* 66 (2011), pp. 682–688. DOI: 10.1016/j.ces.2010.11.012.
- [53] N. Djordjevic, P. Habisreuther, and N. Zarzalis. "Flame stabilization and emissions of a natural gas/air ceramic porous burner". *Advanced Material Research* 47-50 (2008), pp. 105–108. DOI: 10.4028/www.scientific.net/AMR.47-50.105.
- [54] N. Djordjevic, P. Habisreuther, and N. Zarzalis. "Porous burner for application in stationary gas turbines: an experimental investigation of the flame stability, emissions and temperature boundary condition". *Flow, Turbulence and Combustion* 89 (2012), pp. 261–274. DOI: 10.1007/s10494-011-9381-9.
- [55] F. Donsì, S. Cimino, A. di Benedetto, R. Pirone, and G. Russo. "The effect of support morphology on the reaction of oxidative dehydrogenation of ethane to ethylene at short contact times". *Catalysis Today* 105 (2005), pp. 551–559. DOI: 10.1016/j.cattod.2005.06.016.
- [56] J. Ducamp, A. Bengaouer, and P. Baurens. "Modelling and experimental validation of a CO<sub>2</sub> methanation annular cooled fixed-bed reactor exchanger". *The Canadian Journal of Chemical Engineering* 95 (2017), pp. 241–252. DOI: 10.1002/cjce.22706.

- [57] D. Edouard, M. Lacroix, C. P. Huu, and F. Luck. "Pressure drop modeling on SOLID foam: State-of-the art correlation". *Chemical Engineering Journal* 144 (2008), pp. 299–311. DOI: 10.1016/j.cej.2008.06.007.
- [58] D. Edouard, M. Lacroix, C. Pham, M. Mbodji, and C. Pham-Huu. "Experimental measurements and multiphase flow models in solid SiC foam beds". *AIChE Journal* 54 (2008), pp. 2823–2832. DOI: 10.1002/aic.11594.
- [59] D. Edouard, T. Truong Huu, C. Pham Huu, F. Luck, and D. Schweich. "The effective thermal properties of solid foam beds: Experimental and estimated temperature profiles". *International Journal of Heat and Mass Transfer* 53 (2010), pp. 3807–3816. DOI: 10.1016/j.ijheatmasstransfer.2010.04.033.
- [60] A. Eiben and J. Smith. *Introduction to Evolutionary Computing*. Berlin, Germany: Springer Berlin Heidelberg, 2015. DOI: 10.1007/978-3-662-44874-8.
- [61] Y. Elias, P. Rudolf von Rohr, W. Bonrath, J. Medlock, and A. Buss. "A porous structured reactor for hydrogenation reactions". *Chemical Engineering and Processing: Process Intensification* 95 (2015), pp. 175–185. DOI: 10.1016/j.cep.2015.05.012.
- [62] S. Ergun. "Fluid Flow through packed columns". *Chemical Engineering Progress* 48 (1952), pp. 89–94.
- [63] A. Essakhi, A. Löfberg, S. Paul, P. Supiot, B. Mutel, V. Le Courtois, and E. Bordes-Richard. "From materials science to catalysis: Influence of the coating of 2D- and 3D-inserts on the catalytic behaviour of VO<sub>x</sub>/TiO<sub>2</sub> in oxidative dehydrogenation of propane". *Topics in Catalysis* 54 (2011), pp. 698–707. DOI: 10.1007/s11244-011-9676-z.
- [64] European Commission. "G. Technology readiness levels (TRL)". *Horizon 2020 – Work Programme 2014-2015 General Annexes, Extract from Part 19 - Commission Decision C(2014)4995*. (2014).
- [65] A. G. Evans, J. W. Hutchinson, and M. F. Ashby. "Cellular metals". *Current Opinion in Solid State and Materials Science* 3 (1998), pp. 288–303. DOI: 10.1016/S1359-0286(98)80105-8.
- [66] J. L. Falconer and A. E. Zağli. "Adsorption and methanation of carbon dioxide on a nickel/silica catalyst". *Journal of Catalysis* 62 (1980), pp. 280–285. DOI: 10.1016/0021-9517(80)90456-X.
- [67] R. Faure, F. Rossignol, T. Chartier, C. Bonhomme, A. Maître, G. Etchegoyen, P. Del Gallo, and D. Gary. "Alumina foam catalyst supports for industrial steam reforming processes". *Journal of the European Ceramic Society* 31 (2011), pp. 303–312. DOI: 10.1016/j.jeurceramsoc.2010.10.009.
- [68] J. H. Ferziger and M. Peric. *Numerische Strömungsmechanik*. Berlin, Germany: Springer, 2008. DOI: 10.1007/978-3-540-68228-8.
- [69] T. Fishedick, M. Kind, and B. Dietrich. "High temperature two-phase thermal conductivity of ceramic sponges with stagnant fluid - Experimental results and correlation including thermal radiation". *International Journal of Thermal Sciences* 96 (2015), pp. 1–11. DOI: 10.1016/j.ijthermalsci.2015.04.005.
- [70] T. Fishedick, M. Kind, and B. Dietrich. "Radial two-phase thermal conductivity of ceramic sponges up to high temperatures – experimental results and correlation". *International Journal of Thermal Sciences* 114 (2017), pp. 98–113. DOI: 10.1016/j.ijthermalsci.2016.11.020.
- [71] B. Fornberg. *A Practical Guide to Pseudospectral Methods*. Cambridge, UK: Cambridge University Press, 1998.

- [72] M. Frey, D. Édouard, and A.-C. Roger. "Optimization of structured cellular foam-based catalysts for low-temperature carbon dioxide methanation in a platelet milli-reactor". *Comptes Rendus Chimie* 18 (2015), pp. 283–292. DOI: 10.1016/j.crci.2015.01.002.
- [73] M. Frey, T. Romero, A.-C. Roger, and D. Edouard. "Open cell foam catalysts for CO<sub>2</sub> methanation: Presentation of coating procedures and in situ exothermicity reaction study by infrared thermography". *Catalysis Today* 273 (2016), pp. 83–90. DOI: 10.1016/j.cattod.2016.03.016.
- [74] J. Friedland, T. Turek, and R. Güttel. "Investigations on the low temperature methanation with pulse reaction of CO". *Chemie Ingenieur Technik* 88 (2016), pp. 1833–1838. DOI: 10.1002/cite.201600056.
- [75] G. F. Froment, K. B. Bischoff, and J. de Wilde. *Chemical Reactor Analysis and Design*. 3rd ed. Hoboken, NJ, USA: Wiley, 2011, p. 860.
- [76] X. Fu, R. Viskanta, and J. Gore. "Prediction of effective thermal conductivity of cellular ceramics". *International Communications in Heat and Mass Transfer* 25 (1998), pp. 156–160. DOI: 10.1016/S0735-1933(98)00002-5.
- [77] S. Fujita, H. Terunuma, H. Kobayashi, and N. Takezawa. "Methanation of carbon monoxide and carbon dioxide over nickel catalyst under the transient state". *Reaction Kinetics and Catalysis Letters* 33 (1987), pp. 179–184. DOI: 10.1007/BF02066720.
- [78] S.-i. Fujita, M. Nakamura, T. Doi, and N. Takezawa. "Mechanisms of methanation of carbon dioxide and carbon monoxide over nickel/alumina catalysts". *Applied Catalysis A, General* 104 (1993), pp. 87–100. DOI: 10.1016/0926-860X(93)80212-9.
- [79] C. Fukuhara, K. Hayakawa, Y. Suzuki, W. Kawasaki, and R. Watanabe. "A novel nickel-based structured catalyst for CO<sub>2</sub> methanation: a honeycomb-type Ni/CeO<sub>2</sub> catalyst to transform greenhouse gas into useful resources". *Applied Catalysis A: General* 532 (2016), pp. 12–18. DOI: 10.1016/j.apcata.2016.11.036.
- [80] J. Gao, Y. Wang, Y. Ping, D. Hu, G. Xu, F. Gu, and F. Su. "A thermodynamic analysis of methanation reactions of carbon oxides for the production of synthetic natural gas". *RSC Advances* 2 (2012), pp. 2358–2368. DOI: 10.1039/c2ra00632d.
- [81] J. Gascon, J. R. van Ommen, J. A. Moulijn, and F. Kapteijn. "Structuring catalyst and reactor - an inviting avenue to process intensification". *Catalysis Science & Technology* 5 (2015), pp. 807–817. DOI: 10.1039/c4cy01406e.
- [82] I. Ghosh. "Heat transfer correlation for high-porosity open-cell foam". *International Journal of Heat and Mass Transfer* 52 (2009), pp. 1488–1494. DOI: 10.1016/j.ijheatmasstransfer.2008.07.047.
- [83] J. H. Ghouse and T. A. Adams. "A multi-scale dynamic two-dimensional heterogeneous model for catalytic steam methane reforming reactors". *International Journal of Hydrogen Energy* 38 (2013), pp. 9984–9999. DOI: 10.1016/j.ijhydene.2013.05.170.
- [84] L. Giani, C. Cristiani, G. Groppi, and E. Tronconi. "Washcoating method for Pd/Al<sub>2</sub>O<sub>3</sub> deposition on metallic foams". *Applied Catalysis B: Environmental* 62 (2006), pp. 121–131. DOI: 10.1016/j.apcatb.2005.07.003.
- [85] L. Giani, G. Groppi, and E. Tronconi. "Heat transfer characterization of metallic foams". *Industrial and Engineering Chemistry Research* 44 (2005), pp. 9078–9085. DOI: 10.1021/ie050598p.
- [86] L. Giani, G. Groppi, and E. Tronconi. "Mass-transfer characterization of metallic foams as supports for structured catalysts". *Industrial and Engineering Chemistry Research* 44 (2005), pp. 4993–5002. DOI: 10.1021/ie0490886.

- [87] M. Giese, K. Rottschäfer, and D. Vortmeyer. "Measured and modeled superficial flow profiles in packed beds with liquid flow". *AIChE Journal* 44 (1998), pp. 484–490. DOI: 10.1002/aic.690440225.
- [88] J. Gmehling, B. Kolbe, M. Kleiber, and J. Rarey. *Chemical Thermodynamics for Process Simulation*. Weinheim, Germany: Wiley, 2012, p. 735.
- [89] V. Gnielinski. "Querumströmte einzelne Rohre, Drähte und Profilzylinder". In: *VDI-Wärmeatlas*. Ed. by VDI-Gesellschaft für Verfahrenstechnik und Chemieingenieurwesen. 11th ed. Berlin, Germany: Springer, 2013. Chap. G6, pp. 817–818.
- [90] O. Görke, P. Pfeifer, and K. Schubert. "Highly selective methanation by the use of a microchannel reactor". *Catalysis Today* 110 (2005), pp. 132–139. DOI: 10.1016/j.cattod.2005.09.009.
- [91] M. Götz, S. Bajohr, F. Graf, R. Reimert, and T. Kolb. "Einsatz eines Blasensäulenreaktors zur Methansynthese". *Chemie-Ingenieur-Technik* 85 (2013), pp. 1146–1151. DOI: 10.1002/cite.201200212.
- [92] M. Götz, J. Lefebvre, F. Mörs, A. McDaniel Koch, F. Graf, S. Bajohr, R. Reimert, and T. Kolb. "Renewable Power-to-Gas: A technological and economic review". *Renewable Energy* 85 (2016), pp. 1371–1390. DOI: 10.1016/j.renene.2015.07.066.
- [93] S. Govender and H. Friedrich. "Monoliths: A Review of the basics, preparation methods and their relevance to oxidation". *Catalysts* 7 (2017), p. 62. DOI: 10.3390/catal7020062.
- [94] I. Gräf. "Experimentelle Untersuchung und Modellierung des Wärmetransports in katalytischen Schwammpackungen unter polytropen Reaktionsbedingungen". Dissertation. Karlsruhe, Karlsruhe Institut für Technologie (KIT), 2016.
- [95] I. Gräf, G. Ladenburger, and B. Kraushaar-Czarnetzki. "Heat transport in catalytic sponge packings in the presence of an exothermal reaction: Characterization by 2D modeling of experiments". *Chemical Engineering Journal* 287 (2016), pp. 425–435. DOI: 10.1016/j.cej.2015.11.042.
- [96] I. Gräf, A. K. Rühl, and B. Kraushaar-Czarnetzki. "Experimental study of heat transport in catalytic sponge packings by monitoring spatial temperature profiles in a cooled-wall reactor". *Chemical Engineering Journal* 244 (2014), pp. 234–242. DOI: 10.1016/j.cej.2014.01.060.
- [97] G. Groppi, L. Giani, and E. Tronconi. "Generalized correlation for gas/solid mass-transfer coefficients in metallic and ceramic foams". *Industrial and Engineering Chemistry Research* 46 (2007), pp. 3955–3958. DOI: 10.1021/ie061330g.
- [98] J. Grosse, B. Dietrich, G. I. Garrido, P. Habisreuther, N. Zarzalis, H. Martin, M. Kind, and K. C. Bettina. "Morphological characterization of ceramic sponges for applications in chemical engineering". *Industrial and Engineering Chemistry Research* 48 (2009), pp. 10395–10401. DOI: 10.1021/ie900651c.
- [99] J. Große, B. Dietrich, H. Martin, M. Kind, J. Vicente, and E. H. Hardy. "Volume image analysis of ceramic sponges". *Chemical Engineering and Technology* 31 (2008), pp. 307–314. DOI: 10.1002/ceat.200700403.
- [100] J. Grosse and M. Kind. "A contribution to the experimental determination of mass transfer in counter-current flow through ceramic sponges". *Chemical Engineering and Processing: Process Intensification* 55 (2012), pp. 29–39. DOI: 10.1016/j.cep.2012.02.002.
- [101] F. Gutiérrez-Martín and L. M. Rodríguez-Antón. "Power-to-SNG technology for energy storage at large scales". *International Journal of Hydrogen Energy* 1 (2016), pp. -. DOI: <http://dx.doi.org/10.1016/j.ijhydene.2016.07.097>.

- [102] R. Güttel. "Structuring of reactors and catalysts on multiple scales: Potential and limitations for Fischer-Tropsch synthesis". *Chemie-Ingenieur-Technik* 87 (2015), pp. 694–701. DOI: 10.1002/cite.201400107.
- [103] R. Güttel. "Study of unsteady-state operation of methanation by modeling and simulation". *Chemical Engineering and Technology* 36 (2013), pp. 1675–1682. DOI: 10.1002/ceat.201300223.
- [104] R. Güttel and T. Turek. "Improvement of Fischer-Tropsch synthesis through structuring on different scales". *Energy Technology* 4 (2016), pp. 44–54. DOI: 10.1002/ente.201500257.
- [105] P. Habisreuther, N. Djordjevic, and N. Zarzalis. "Statistical distribution of residence time and tortuosity of flow through open-cell foams". *Chemical Engineering Science* 64 (2009), pp. 4943–4954. DOI: 10.1016/j.ces.2009.07.033.
- [106] C. Hackert, J. Ellzey, O. Ezekoye, and M. Hall. "Transverse dispersion at high Peclet numbers in short porous media". *Experiments in Fluids* 21 (1996), pp. 286–290. DOI: 10.1007/BF00190679.
- [107] P. Heinl, C. Körner, and R. F. Singer. "Selective electron beam melting of cellular titanium: Mechanical properties". *Advanced Engineering Materials* 10 (2008), pp. 882–888. DOI: 10.1002/adem.200800137.
- [108] P. Hidnert and H. Krider. "Thermal expansion of aluminum and some aluminum alloys". *Journal of Research of the National Bureau of Standards* 48 (1952), p. 209. DOI: 10.6028/jres.048.030.
- [109] A. C. Hindmarsh, P. N. Brown, K. E. Grant, S. L. Lee, R. Serban, D. E. Shumaker, and C. S. Woodward. "SUNDIALS: Suite of Nonlinear and Differential/Algebraic Equation Solvers". *ACM Transactions on Mathematical Software* 31 (2005), pp. 363–396. DOI: 10.1145/1089014.1089020.
- [110] T. Horneber, C. Rauh, and A. Delgado. "Fluid dynamic characterisation of porous solids in catalytic fixed-bed reactors". *Microporous and Mesoporous Materials* 154 (2012), pp. 170–174. DOI: 10.1016/j.micromeso.2011.12.047.
- [111] T. Horneber, C. Rauh, and A. Delgado. "Numerical simulations of fluid dynamics in carrier structures for catalysis: Characterization and need for optimization". *Chemical Engineering Science* 117 (2014), pp. 229–238. DOI: 10.1016/j.ces.2014.06.036.
- [112] J. Hu, K. P. Brooks, J. D. Holladay, D. T. Howe, and T. M. Simon. "Catalyst development for microchannel reactors for martian in situ propellant production". *Catalysis Today* 125 (2007), pp. 103–110. DOI: 10.1016/j.cattod.2007.01.067.
- [113] Y.-X. Huang, C.-H. Cheng, X.-D. Wang, and J.-Y. Jang. "Effects of porosity gradient in gas diffusion layers on performance of proton exchange membrane fuel cells". *Energy* 35 (2010), pp. 4786–4794. DOI: 10.1016/j.energy.2010.09.011.
- [114] J. Hüppmeier, S. Barg, M. Baune, D. Koch, G. Grathwohl, and J. Thöming. "Oxygen feed membranes in autothermal steam-reformers - A robust temperature control". *Fuel* 89 (2010), pp. 1257–1264. DOI: 10.1016/j.fuel.2009.09.023.
- [115] C. Hutter, C. Allemann, S. Kuhn, and P. Rudolf von Rohr. "Scalar transport in a milli-scale metal foam reactor". *Chemical Engineering Science* 65 (2010), pp. 3169–3178. DOI: 10.1016/j.ces.2010.02.002.
- [116] C. Hutter, D. Büchi, V. Zuber, and P. Rudolf von Rohr. "Heat transfer in metal foams and designed porous media". *Chemical Engineering Science* 66 (2011), pp. 3806–3814. DOI: 10.1016/j.ces.2011.05.005.

- [117] C. Hutter, A. Zenklusen, S. Kuhn, and P. Rudolf von Rohr. "Large eddy simulation of flow through a streamwise-periodic structure". *Chemical Engineering Science* 66 (2011), pp. 519–529. DOI: 10.1016/j.ces.2010.11.015.
- [118] C. Hutter, A. Zenklusen, R. Lang, and P. Rudolf von Rohr. "Axial dispersion in metal foams and streamwise-periodic porous media". *Chemical Engineering Science* 66 (2011), pp. 1132–1141. DOI: 10.1016/j.ces.2010.12.016.
- [119] T. T. Huu, M. Lacroix, C. Pham Huu, D. Schweich, and D. Edouard. "Towards a more realistic modeling of solid foam: Use of the pentagonal dodecahedron geometry". *Chemical Engineering Science* 64 (2009), pp. 5131–5142. DOI: 10.1016/j.ces.2009.08.028.
- [120] S. Hwang, P. Linke, and R. Smith. "Heterogeneous catalytic reactor design with optimum temperature profile II: Application of non-uniform catalyst". *Chemical Engineering Science* 59 (2004), pp. 4245–4260. DOI: 10.1016/j.ces.2004.05.036.
- [121] S. Hwang and R. Smith. "Heterogeneous catalytic reactor design with non-uniform catalyst considering shell-progressive poisoning behavior". *Chemical Engineering and Technology* 31 (2008), pp. 384–397. DOI: 10.1002/ceat.200700398.
- [122] S. Hwang and R. Smith. "Optimum reactor design in methanation processes with nonuniform catalysts". *Chemical Engineering Communications* 196 (2008), pp. 616–642. DOI: 10.1080/00986440802484465.
- [123] M. Iglesias González, H. Eilers, and G. Schaub. "Flexible operation of fixed-bed reactors for a catalytic fuel synthesis – CO<sub>2</sub> hydrogenation as example reaction". *Energy Technology* 4 (2016), pp. 90–103. DOI: 10.1002/ente.201500259.
- [124] A. Inayat, H. Freund, A. Schwab, T. Zeiser, and W. Schwieger. "Predicting the specific surface area and pressure drop of reticulated ceramic foams used as catalyst support". *Advanced Engineering Materials* 13 (2011), pp. 990–995. DOI: 10.1002/adem.201100038.
- [125] A. Inayat, H. Freund, T. Zeiser, and W. Schwieger. "Determining the specific surface area of ceramic foams: The tetrakaidehedra model revisited". *Chemical Engineering Science* 66 (2011), pp. 1179–1188. DOI: 10.1016/j.ces.2010.12.031.
- [126] A. Inayat, M. Klumpp, M. Lämmermann, H. Freund, and W. Schwieger. "Development of a new pressure drop correlation for open-cell foams based completely on theoretical grounds: Taking into account strut shape and geometric tortuosity". *Chemical Engineering Journal* 287 (2016), pp. 704–719. DOI: 10.1016/j.cej.2015.11.050.
- [127] A. Inayat, J. Schwerdtfeger, H. Freund, C. Körner, R. F. Singer, and W. Schwieger. "Periodic open-cell foams: Pressure drop measurements and modeling of an ideal tetrakaidehedra packing". *Chemical Engineering Science* 66 (2011), pp. 2758–2763. DOI: 10.1016/j.ces.2011.03.031.
- [128] G. Incera Garrido and B. Kraushaar-Czarnetzki. "A general correlation for mass transfer in isotropic and anisotropic solid foams". *Chemical Engineering Science* 65 (2010), pp. 2255–2257. DOI: 10.1016/j.ces.2009.12.016.
- [129] G. Incera Garrido, F. C. Patcas, S. Lang, and B. Kraushaar-Czarnetzki. "Mass transfer and pressure drop in ceramic foams: A description for different pore sizes and porosities". *Chemical Engineering Science* 63 (2008), pp. 5202–5217. DOI: 10.1016/j.ces.2008.06.015.
- [130] International Organization for Standardization. *Fine ceramics (advanced ceramics, advanced technical ceramics) – Determination of thermal diffusivity of monolithic ceramics by laser flash method*. 2005. URL: <https://www.iso.org/standard/31901.html>.

- [131] International Organization for Standardization. *Space systems – Definition of the Technology Readiness Levels (TRLs) and their criteria of assessment (ISO 16290:2013)*. 2013. URL: <https://www.iso.org/standard/56064.html>.
- [132] A. Jacob, E. C. Bucharsky, and K. G. Schell. "The application of transparent glass sponges for improvement of light distribution in photobioreactors". *Journal of Bioprocessing & Biotechniques* 2 (2012). DOI: 10.4172/2155-9821.1000113.
- [133] C. Janke, M. S. Duyar, M. Hoskins, and R. Farrauto. "Catalytic and adsorption studies for the hydrogenation of CO<sub>2</sub> to methane". *Applied Catalysis B: Environmental* 152-153 (2014), pp. 184–191. DOI: 10.1016/j.apcatb.2014.01.016.
- [134] S. Jarungthammachote and A. Dutta. "Equilibrium modeling of gasification: Gibbs free energy minimization approach and its application to spouted bed and spout-fluid bed gasifiers". *Energy Conversion and Management* 49 (2008), pp. 1345–1356. DOI: 10.1016/j.enconman.2008.01.006.
- [135] A. Jess and P. Wasserscheid. *Chemical Technology*. Weinheim, Germany: Wiley, 2013.
- [136] L. Jürgensen, E. A. Ehimen, J. Born, and J. B. Holm-Nielsen. "Utilization of surplus electricity from wind power for dynamic biogas upgrading: Northern Germany case study". *Biomass and Bioenergy* 66 (2014), pp. 126–132. DOI: 10.1016/j.biombioe.2014.02.032.
- [137] P. Kaiser, F. Pöhlmann, and A. Jess. "Intrinsic and effective kinetics of cobalt-catalyzed fischer-tropsch synthesis in view of a power-to-liquid process based on renewable energy". *Chemical Engineering and Technology* 37 (2014), pp. 964–972. DOI: 10.1002/ceat.201300815.
- [138] B. Kaskes, D. Vervloet, F. Kapteijn, and J. R. van Ommen. "Numerical optimization of a structured tubular reactor for Fischer-Tropsch synthesis". *Chemical Engineering Journal* 283 (2016), pp. 1465–1483. DOI: 10.1016/j.cej.2015.08.078.
- [139] P. J. A. M. Kerkhof. "A modified Maxwell-Stefan model for transport through inert membranes: the binary friction model". *The Chemical Engineering Journal* 64 (1996), pp. 319–343.
- [140] V. M. Khanaev, E. S. Borisova, L. I. Galkina, and A. S. Noskov. "Improvement of the catalytic monoliths efficiency for CO oxidation using non-uniform active component distribution along the monolith length". *Chemical Engineering Journal* 102 (2004), pp. 35–44. DOI: 10.1016/j.cej.2004.02.003.
- [141] V. M. Khanaev, E. S. Borisova, and A. S. Noskov. "Optimal distribution of the active component in catalytic methane oxidation". *Theoretical Foundations of Chemical Engineering* 39 (2005), pp. 478–486. DOI: 10.1007/s11236-005-0105-5.
- [142] V. M. Khanaev, E. S. Borisova, and A. S. Noskov. "Optimization of the active component distribution through the catalyst bed for the case of adiabatic reactor". *Chemical Engineering Science* 60 (2005), pp. 5792–5802. DOI: 10.1016/j.ces.2005.05.034.
- [143] J. Kierzenka and L. F. Shampine. "A BVP solver based on residual control and the MATLAB PSE". *ACM Transactions on Mathematical Software* 27 (2001), pp. 299–316. DOI: 10.1145/502800.502801.
- [144] L. Kiewidt and J. Thöming. "Predicting optimal temperature profiles in single-stage fixed-bed reactors for CO<sub>2</sub>-methanation". *Chemical Engineering Science* 132 (2015), pp. 59–71. DOI: 10.1016/j.ces.2015.03.068.
- [145] Y. D. Kim, S. J. Jeong, and W. S. Kim. "Optimal design of axial noble metal distribution for improving dual monolithic catalytic converter performance". *Chemical Engineering Science* 64 (2009), pp. 1373–1383. DOI: 10.1016/j.ces.2008.11.020.

- [146] M. Kleiber and R. Joh. "Berechnungsmethoden für Stoffeigenschaften". In: *VDI-Wärmeatlas*. Ed. by VDI-Gesellschaft für Verfahrenstechnik und Chemieingenieurwesen. 11th ed. Berlin, Germany: Springer, 2013. Chap. D1, pp. 117–174.
- [147] J. Klose and M. Baerns. "Kinetics of the methanation of carbon monoxide on an alumina-supported nickel catalyst". *Journal of Catalysis* 85 (1984), pp. 105–116. DOI: 10.1016/0021-9517(84)90114-3.
- [148] M. Klumpp, A. Inayat, J. Schwerdtfeger, C. Körner, R. F. Singer, H. Freund, and W. Schwieger. "Periodic open cellular structures with ideal cubic cell geometry: Effect of porosity and cell orientation on pressure drop behavior". *Chemical Engineering Journal* 242 (2014), pp. 364–378. DOI: 10.1016/j.cej.2013.12.060.
- [149] T. Knorr, P. Heinl, J. Schwerdtfeger, C. Körner, R. F. Singer, and B. J. Etzold. "Process specific catalyst supports—Selective electron beam melted cellular metal structures coated with microporous carbon". *Chemical Engineering Journal* 181-182 (2012), pp. 725–733. DOI: 10.1016/j.cej.2011.10.009.
- [150] S. T. Kolaczkowski, S. Awdry, T. Smith, D. Thomas, L. Torkuhl, and R. Kolvenbach. "Potential for metal foams to act as structured catalyst supports in fixed-bed reactors". *Catalysis Today* 273 (2016), pp. 221–233. DOI: 10.1016/j.cattod.2016.03.047.
- [151] M. Kopp, D. Coleman, C. Stiller, K. Scheffer, J. Aichinger, and B. Scheppat. "Energiepark Mainz: Technical and economic analysis of the worldwide largest Power-to-Gas plant with PEM electrolysis". *International Journal of Hydrogen Energy* 42 (2016), pp. 13311–13320. DOI: 10.1016/j.ijhydene.2016.12.145.
- [152] J. Kopyscinski, T. J. Schildhauer, and S. M. a. Biollaz. "Production of synthetic natural gas (SNG) from coal and dry biomass - A technology review from 1950 to 2009". *Fuel* 89 (2010), pp. 1763–1783. DOI: 10.1016/j.fuel.2010.01.027.
- [153] J. Kopyscinski, T. J. Schildhauer, F. Vogel, S. M. a. Biollaz, and A. Wokaun. "Applying spatially resolved concentration and temperature measurements in a catalytic plate reactor for the kinetic study of CO methanation". *Journal of Catalysis* 271 (2010), pp. 262–279. DOI: 10.1016/j.jcat.2010.02.008.
- [154] F. Koschany, D. Schlereth, and O. Hinrichsen. "On the kinetics of the methanation of carbon dioxide on coprecipitated NiAl(O)<sub>x</sub>". *Applied Catalysis B: Environmental* 181 (2016), pp. 504–516. DOI: 10.1016/j.apcatb.2015.07.026.
- [155] D. Kraft. *A software package for sequential quadratic programming (DFVLR-FB-88-28)*. Tech. rep. Köln, Germany: Institut für Dynamik der Flugsysteme, Deutsche Forschungs- und Versuchsanstalt für Luft- und Raumfahrt (DFVLR), 1988.
- [156] M. Krämer, M. Duisberg, K. Stöwe, and W. F. Maier. "Highly selective CO methanation catalysts for the purification of hydrogen-rich gas mixtures". *Journal of Catalysis* 251 (2007), pp. 410–422. DOI: 10.1016/j.jcat.2007.07.030.
- [157] B. Kraushaar-Czarnetzki and S. P. Müller. "Shaping of solid catalysts". In: *Synthesis of Solid Catalysts*. Ed. by K. P. de Jong. Weinheim, Germany: Wiley, 2009. Chap. 9, pp. 173–199.
- [158] M. T. Kreutzer, F. Kapteijn, and J. A. Moulijn. "Shouldn't catalysts shape up? Structured reactors in general and gas-liquid monolith reactors in particular". *Catalysis Today* 111 (2006), pp. 111–118. DOI: 10.1016/j.cattod.2005.10.014.
- [159] P. Kumar and F. Topin. "Simultaneous determination of intrinsic solid phase conductivity and effective thermal conductivity of Kelvin like foams". *Applied Thermal Engineering* 71 (2014), pp. 536–547. DOI: 10.1016/j.applthermaleng.2014.06.058.

- [160] P. Kumar and F. Topin. "Thermal conductivity correlations of open-cell foams: Extension of Hashin-Shtrikman model and introduction of effective solid phase tortuosity". *International Journal of Heat and Mass Transfer* 92 (2016), pp. 539–549. DOI: 10.1016/j.ijheatmasstransfer.2015.08.085.
- [161] P. Kumar, F. Topin, and J. Vicente. "Determination of effective thermal conductivity from geometrical properties: Application to open cell foams". *International Journal of Thermal Sciences* 81 (2014), pp. 13–28. DOI: 10.1016/j.ijthermalsci.2014.02.005.
- [162] M. Lacroix, L. Dreibine, B. de Tymowski, F. Vigneron, D. Edouard, D. Bégin, P. Nguyen, C. Pham, S. Savin-Poncet, F. Luck, M. J. Ledoux, and C. Pham-Huu. "Silicon carbide foam composite containing cobalt as a highly selective and re-usable Fischer-Tropsch synthesis catalyst". *Applied Catalysis A: General* 397 (2011), pp. 62–72. DOI: 10.1016/j.apcata.2011.02.012.
- [163] M. Lacroix, P. Nguyen, D. Schweich, C. Pham Huu, S. Savin-Poncet, and D. Edouard. "Pressure drop measurements and modeling on SiC foams". *Chemical Engineering Science* 62 (2007), pp. 3259–3267. DOI: 10.1016/j.ces.2007.03.027.
- [164] F. Lali. "Characterization of foam catalysts as packing for tubular reactors". *Chemical Engineering and Processing: Process Intensification* 105 (2016), pp. 1–9. DOI: 10.1016/j.cep.2016.04.001.
- [165] M. Lämmermann, W. Schwieger, and H. Freund. "Experimental investigation of gas-liquid distribution in periodic open cellular structures as potential catalyst supports". *Catalysis Today* 273 (2016), pp. 161–171. DOI: 10.1016/j.cattod.2016.02.049.
- [166] R. Lemlich. "A theory for the limiting conductivity of polyhedral foam at low density". *Journal of Colloid And Interface Science* 64 (1978), pp. 107–110. DOI: 10.1016/0021-9797(78)90339-9.
- [167] D. Lesser, G. Mestl, and T. Turek. "Modeling the dynamic behavior of industrial fixed bed reactors for the manufacture of maleic anhydride". *Chemical Engineering Science* 172 (2017), pp. 559–570. DOI: 10.1016/j.ces.2017.06.049.
- [168] J. Lévêque, R. Philippe, M.-L. L. Zanota, V. Meille, F. Sarrazin, L. Baussaron, and C. de Bellefon. "Hydrodynamics and mass transfer in a tubular reactor containing foam packings for intensification of G-L-S catalytic reactions in co-current up-flow configuration". *Chemical Engineering Research and Design* 109 (2016), pp. 686–697. DOI: 10.1016/j.cherd.2016.03.017.
- [169] Y. Li, Q. Zhang, R. Chai, G. Zhao, F. Cao, Y. Liu, and Y. Lu. "Metal-foam-structured Ni-Al<sub>2</sub>O<sub>3</sub> catalysts: Wet chemical etching preparation and syngas methanation performance". *Applied Catalysis A: General* 510 (2016), pp. 216–226. DOI: 10.1016/j.apcata.2015.11.034.
- [170] Y. Li, Q. Zhang, R. Chai, G. Zhao, Y. Liu, and Y. Lu. "Structured Ni-CeO<sub>2</sub>-Al<sub>2</sub>O<sub>3</sub>/Ni-foam catalyst with enhanced heat transfer for substitute natural gas production by syngas methanation". *ChemCatChem* 7 (2015), pp. 1427–1431. DOI: 10.1002/cctc.201500086.
- [171] Y. Li, Y. Wang, X. Zhang, and Z. Mi. "Thermodynamic analysis of autothermal steam and CO<sub>2</sub> reforming of methane". *International Journal of Hydrogen Energy* 33 (2008), pp. 2507–2514. DOI: 10.1016/j.ijhydene.2008.02.051.
- [172] J. Y. Lim and J. S. Dennis. "Modeling reaction and diffusion in a spherical catalyst pellet using multicomponent flux models". *Industrial and Engineering Chemistry Research* 51 (2012), pp. 15901–15911. DOI: 10.1021/ie302528u.
- [173] J. Y. Lim, J. McGregor, A. J. Sederman, and J. S. Dennis. "Kinetic studies of CO<sub>2</sub> methanation over a Ni/ $\gamma$ -Al<sub>2</sub>O<sub>3</sub> catalyst using a batch reactor". *Chemical Engineering Science* 141 (2016), pp. 28–45. DOI: 10.1016/j.ces.2015.10.026.

- [174] H. Liu, D. Yang, R. Gao, L. Chen, S. Zhang, and X. Wang. "A novel Na<sub>2</sub>WO<sub>4</sub>-Mn/SiC monolithic foam catalyst with improved thermal properties for the oxidative coupling of methane". *Catalysis Communications* 9 (2008), pp. 1302–1306. DOI: 10.1016/j.catcom.2007.11.022.
- [175] J. Liu, C. Li, F. Wang, S. He, H. Chen, Y. Zhao, M. Wei, D. G. Evans, and X. Duan. "Enhanced low-temperature activity of CO<sub>2</sub> methanation over highly-dispersed Ni/TiO<sub>2</sub> catalyst". *Catalysis Science & Technology* 3 (2013), pp. 2627–2633. DOI: 10.1039/c3cy00355h.
- [176] Y. Liu, D. Edouard, L. D. Nguyen, D. Begin, P. Nguyen, C. Pham, and C. Pham-Huu. "High performance structured platelet milli-reactor filled with supported cobalt open cell SiC foam catalyst for the Fischer-Tropsch synthesis". *Chemical Engineering Journal* 222 (2013), pp. 265–273. DOI: 10.1016/j.cej.2013.02.066.
- [177] Z. Liu, B. Chu, X. Zhai, Y. Jin, and Y. Cheng. "Total methanation of syngas to synthetic natural gas over Ni catalyst in a micro-channel reactor". *Fuel* 95 (2012), pp. 599–605. DOI: 10.1016/j.fuel.2011.12.045.
- [178] F. Lucci, A. Della Torre, G. Montenegro, R. Kaufmann, and P. Dimopoulos Eggenschwiler. "Comparison of geometrical, momentum and mass transfer characteristics of real foams to Kelvin cell lattices for catalyst applications". *International Journal of Heat and Mass Transfer* 108 (2017), pp. 341–350. DOI: 10.1016/j.ijheatmasstransfer.2016.11.073.
- [179] P. J. Lunde and F. L. Kester. "Carbon dioxide methanation on a ruthenium catalyst". *Industrial & Engineering Chemistry Process Design and Development* 13 (1974), pp. 27–33. DOI: 10.1021/i260049a005.
- [180] E. Maire, P. Colombo, J. Adrien, L. Babout, and L. Biasetto. "Characterization of the morphology of cellular ceramics by 3D image processing of X-ray tomography". *Journal of the European Ceramic Society* 27 (2007), pp. 1973–1981. DOI: 10.1016/j.jeurceramsoc.2006.05.097.
- [181] F. Manenti, S. Cieri, M. Restelli, and G. Bozzano. "Dynamic modeling of the methanol synthesis fixed-bed reactor". *Computers & Chemical Engineering* 48 (2013), pp. 325–334. DOI: 10.1016/j.compchemeng.2012.09.013.
- [182] M. Martinez Molina, C. Kern, and A. Jess. "Catalytic hydrogenation of carbon dioxide to methane in wall-cooled fixed-bed reactor". *Chemical Engineering & Technology* 39 (2016), pp. 2404–2415. DOI: 10.1002/ceat.201500614.
- [183] S. Matthischke, R. Krüger, S. Rönsch, and R. Güttel. "Unsteady-state methanation of carbon dioxide in a fixed-bed recycle reactor — Experimental results for transient flow rate ramps". *Fuel Processing Technology* 153 (2016), pp. 87–93. DOI: 10.1016/j.fuproc.2016.07.021.
- [184] B. McBride, M. Zehe, and S. Gordon. "NASA Glenn coefficients for calculating thermodynamic properties of individual species". *NASA/TP-2002-211556* (2002).
- [185] S. Meinicke, T. Wetzel, and B. Dietrich. "Scale-resolved CFD modelling of single-phase hydrodynamics and conjugate heat transfer in solid sponges". *International Journal of Heat and Mass Transfer* 108 (2017), pp. 1207–1219. DOI: 10.1016/j.ijheatmasstransfer.2016.12.052.
- [186] M. A. A. Mendes, S. Ray, and D. Trimis. "Evaluation of effective thermal conductivity of porous foams in presence of arbitrary working fluid". *International Journal of Thermal Sciences* 79 (2014), pp. 260–265. DOI: 10.1016/j.ijthermalsci.2014.01.009.
- [187] M. A. Mendes, S. Ray, and D. Trimis. "A simple and efficient method for the evaluation of effective thermal conductivity of open-cell foam-like structures". *International Journal of Heat and Mass Transfer* 66 (2013), pp. 412–422. DOI: 10.1016/j.ijheatmasstransfer.2013.07.032.

- [188] M. A. Mendes, S. Ray, and D. Trimis. "An improved model for the effective thermal conductivity of open-cell porous foams". *International Journal of Heat and Mass Transfer* 75 (2014), pp. 224–230. DOI: 10.1016/j.ijheatmasstransfer.2014.02.076.
- [189] D. Merino, O. Sanz, and M. Montes. "Effect of the thermal conductivity and catalyst layer thickness on the Fischer-Tropsch synthesis selectivity using structured catalysts". *Chemical Engineering Journal* 327 (2017), pp. 1033–1042. DOI: 10.1016/j.cej.2017.07.003.
- [190] B. Miao, S. S. K. Ma, X. Wang, H. Su, and S. H. Chan. "Catalysis mechanisms of CO<sub>2</sub> and CO methanation". *Catalysis Science & Technology* 6 (2016), pp. 4048–4058. DOI: 10.1039/C6CY00478D.
- [191] G. A. Mills and F. W. Steffgen. "Catalytic methanation". *Catalysis Reviews* 8 (1974), pp. 159–210. DOI: 10.1080/01614947408071860.
- [192] P. Mülheims and B. Kraushaar-Czarnetzki. "Temperature profiles and process performances of sponge packings as compared to spherical catalysts in the oxidation of o-xylene to phthalic anhydride". *Industrial & Engineering Chemistry Research* 50 (2011), pp. 9925–9935. DOI: 10.1021/ie201062p.
- [193] P. Mülheims, S. Marz, S. P. Müller, and B. Kraushaar-Czarnetzki. "Einfluss der Einpassung fester Schwämme in ein Reaktionsrohr am Beispiel der partiellen Oxidation von o-Xylol". *Chemie Ingenieur Technik* 83 (2011), pp. 286–294. DOI: 10.1002/cite.201000123.
- [194] P. Mülheims, A. Ritter, A. Reitzmann, and B. Kraushaar-Czarnetzki. "Performance and kinetics of flame-made vanadia/titania catalyst nanoparticles in the partial oxidation of o-xylene". *Industrial & Engineering Chemistry Research* 51 (2012), pp. 13980–13992. DOI: 10.1021/ie301608r.
- [195] R. G. Munro. "Material properties of a sintered  $\alpha$ -SiC". *Journal of Physical and Chemical Reference Data* 26 (1997), pp. 1195–1203. DOI: 10.1063/1.556000.
- [196] H. Muroyama, Y. Tsuda, T. Asakoshi, H. Masitah, T. Okanishi, and T. Matsui. "Carbon dioxide methanation over Ni catalysts supported on various metal oxides". *Journal of Catalysis* 343 (2016), pp. 178–184. DOI: 10.1016/j.jcat.2016.07.018.
- [197] M. Neubert, J. Widzowski, S. Rönsch, P. Treiber, M. Dillig, and J. Karl. "Simulation-based evaluation of a two-stage small-scale methanation unit for decentralized applications". *Energy & Fuels* 31 (2017), pp. 2076–2086. DOI: 10.1021/acs.energyfuels.6b02793.
- [198] P. D. Neufeld, A. R. Janzen, and R. A. Aziz. "Empirical equations to calculate 16 of the transport collision integrals for the Lennard-Jones potential". *The Journal of Chemical Physics* 57 (1972), p. 1100. DOI: 10.1063/1.1678363.
- [199] T. T. M. Nguyen, L. Wissing, and M. S. Skjøth-Rasmussen. "High temperature methanation: Catalyst considerations". *Catalysis Today* 215 (2013), pp. 233–238. DOI: 10.1016/j.cattod.2013.03.035.
- [200] T. T. Nguyen, L. Burel, D. L. Nguyen, C. Pham-Huu, and J. M. M. Millet. "Catalytic performance of MoVTeNbO catalyst supported on SiC foam in oxidative dehydrogenation of ethane and ammoxidation of propane". *Applied Catalysis A: General* 433–434 (2012), pp. 41–48. DOI: 10.1016/j.apcata.2012.04.038.
- [201] Y. Nie, P. M. Witt, A. Agarwal, and L. T. Biegler. "Optimal active catalyst and inert distribution in catalytic packed bed reactors: Ortho-xylene oxidation". *Industrial and Engineering Chemistry Research* 52 (2013), pp. 15311–15320. DOI: 10.1021/ie4005699.

- [202] M. K. Nikoo and N. Amin. "Thermodynamic analysis of carbon dioxide reforming of methane in view of solid carbon formation". *Fuel Processing Technology* 92 (2011), pp. 678–691. DOI: 10.1016/j.fuproc.2010.11.027.
- [203] H. Ohya, J. Fun, H. Kawamura, K. Itoh, H. Ohashi, M. Aihara, S. Tanisho, and Y. Negishi. "Methanation of carbon dioxide by using membrane reactor integrated with water vapor permselective membrane and its analysis". *Journal of Membrane Science* 131 (1997), pp. 237–247. DOI: 10.1016/S0376-7388(97)00055-0.
- [204] K. Osman, T. Götze, and A. Schönrock. "Das e-gas-Projekt am Biogasanlagenstandort in Werlte". *gwf-Gas+Energie* 155 (2014), pp. 304–309.
- [205] J. Paek, B. Kang, S. Kim, and J. Hyun. "Effective thermal conductivity and permeability of aluminum foam materials". *International Journal of Thermophysics* 21 (2000), pp. 453–464. DOI: 10.1023/A:1006643815323.
- [206] V. Palma, D. Pisano, M. Martino, and P. Ciambelli. "Structured catalysts with high thermoconductive properties for the intensification of Water Gas Shift process". *Chemical Engineering Journal* 304 (2016), pp. 544–551. DOI: 10.1016/j.cej.2016.06.117.
- [207] Q. Pan, J. Peng, S. S. Wang, and S. S. Wang. "In situ FTIR spectroscopic study of the CO<sub>2</sub> methanation mechanism on Ni/Ce<sub>0.5</sub>Zr<sub>0.5</sub>O<sub>2</sub>". *Catalysis Science & Technology* 4 (2014), pp. 502–509. DOI: 10.1039/C3CY00868A.
- [208] E. D. Park, D. Lee, and H. C. Lee. "Recent progress in selective CO removal in a H<sub>2</sub>-rich stream". *Catalysis Today* 139 (2009), pp. 280–290. DOI: 10.1016/j.cattod.2008.06.027.
- [209] J. C. Park, N. S. Roh, D. H. Chun, H. Jung, and J. I. Yang. "Cobalt catalyst coated metallic foam and heat-exchanger type reactor for Fischer-Tropsch synthesis". *Fuel Processing Technology* 119 (2014), pp. 60–66. DOI: 10.1016/j.fuproc.2013.10.008.
- [210] W. J. Parker, R. J. Jenkins, C. P. Butler, and G. L. Abbott. "Flash method of determining thermal diffusivity, heat capacity, and thermal conductivity". *Journal of Applied Physics* 32 (1961), pp. 1679–1684. DOI: 10.1063/1.1728417.
- [211] P. Parthasarathy, P. Habisreuther, and N. Zarzalis. "Evaluation of longitudinal dispersion coefficient in open-cell foams using transient direct pore level simulation". *Chemical Engineering Science* 90 (2013), pp. 242–249. DOI: 10.1016/j.ces.2012.12.041.
- [212] F. C. Patcas. "The methanol-to-olefins conversion over zeolite-coated ceramic foams". *Journal of Catalysis* 231 (2005), pp. 194–200. DOI: 10.1016/j.jcat.2005.01.016.
- [213] F. C. Patcas, G. I. Garrido, and B. Kraushaar-Czarnetzki. "CO oxidation over structured carriers: A comparison of ceramic foams, honeycombs and beads". *Chemical Engineering Science* 62 (2007), pp. 3984–3990. DOI: 10.1016/j.ces.2007.04.039.
- [214] D. E. Peebles, D. W. Goodman, and J. M. White. "Methanation of carbon dioxide on nickel(100) and the effects of surface modifiers". *The Journal of Physical Chemistry* 87 (1983), pp. 4378–4387. DOI: 10.1021/j100245a014.
- [215] N. Pegios, G. Schroer, K. Rahimi, R. Palkovits, and K. Simeonov. "Design of modular Ni-foam based catalysts for dry reforming of methane". *Catalysis Science & Technology* 6 (2016), pp. 6372–6380. DOI: 10.1039/C6CY00282J.
- [216] D.-Y. Peng and D. B. Robinson. "A new two-constant equation of state". *Industrial & Engineering Chemistry Fundamentals* 15 (1976), pp. 59–64. DOI: 10.1021/i160057a011.

- [217] W. Peng, M. Xu, X. Li, X. Huai, Z. Liu, and H. Wang. "CFD study on thermal transport in open-cell metal foams with and without a washcoat: Effective thermal conductivity and gas-solid interfacial heat transfer". *Chemical Engineering Science* 161 (2017), pp. 92–108. DOI: 10.1016/j.ces.2016.12.006.
- [218] Y. Peng and J. T. Richardson. "Properties of ceramic foam catalyst supports: One-dimensional and two-dimensional heat transfer correlations". *Applied Catalysis A: General* 266 (2004), pp. 235–244. DOI: 10.1016/j.apcata.2004.02.012.
- [219] J. C. F. Pereira, I. Malico, T. C. Hayashi, and J. Raposo. "Experimental and numerical characterization of the transverse dispersion at the exit of a short ceramic foam inside a pipe". *International Journal of Heat and Mass Transfer* 48 (2005), pp. 1–14. DOI: 10.1016/j.ijheatmasstransfer.2004.08.001.
- [220] J. Petera, L. Nowicki, and S. Ledakowicz. "New numerical algorithm for solving multidimensional heterogeneous model of the fixed bed reactor". *Chemical Engineering Journal* 214 (2013), pp. 237–246. DOI: 10.1016/j.cej.2012.10.020.
- [221] W. Peters, M. Eypasch, T. Frank, J. Schwerdtfeger, C. Körner, A. Bösmann, and P. Wasserscheid. "Efficient hydrogen release from perhydro-N-ethylcarbazole using catalyst-coated metallic structures produced by selective electron beam melting". *Energy & Environmental Science* 8 (2015), pp. 641–649. DOI: 10.1039/C4EE03461A.
- [222] R. Phelan, D. Weaire, and K. Brakke. "Computation of equilibrium foam structures using the Surface Evolver". *Experimental Mathematics* 4 (1995), pp. 181–192. DOI: 10.1080/10586458.1995.10504320.
- [223] R. Philippe, M. Lacroix, L. Dreibine, C. Pham-Huu, D. Edouard, S. Savin, F. Luck, and D. Schweich. "Effect of structure and thermal properties of a Fischer-Tropsch catalyst in a fixed bed". *Catalysis Today* 147 (2009), pp. 305–312. DOI: 10.1016/j.cattod.2009.07.058.
- [224] A. Potdar, L. N. Protasova, L. Thomassen, and S. Kuhn. "Designed porous milli-scale reactors with enhanced interfacial mass transfer in two-phase flows". *Reaction Chemistry & Engineering* 2 (2017), pp. 137–148. DOI: 10.1039/C6RE00185H.
- [225] A. N. Pour, M. R. Housaindokht, and H. Monhemi. "A new LHHW kinetic model for CO<sub>2</sub> hydrogenation over an iron catalyst". *Progress in Reaction Kinetics and Mechanism* 41 (2016), pp. 159–169. DOI: 10.3184/146867816X14628763021337.
- [226] K. V. Price, R. M. Storn, and J. A. Lampinen. *Differential Evolution: A practical approach to global optimization*. New York, NY, USA: Springer, 2005. DOI: 10.1007/3-540-31306-0.
- [227] A. Psyllos and C. Philippopoulos. "Performance of a monolithic catalytic converter used in automotive emission control: the effect of a longitudinal parabolic active metal distribution". *Industrial & Engineering Chemistry Research* 32 (1993), pp. 1555–1559. DOI: 10.1021/ie00020a004.
- [228] R. Rajasree, V. Ravi Kumar, and B. Dattatraya Kulkarni. "Performance enhancement of steam methane reforming using tubular packed-bed microreactors and dilution by adsorbent". *Energy and Fuels* 20 (2006), pp. 463–472. DOI: 10.1021/ef050205z.
- [229] P. Ranut. "On the effective thermal conductivity of aluminum metal foams: Review and improvement of the available empirical and analytical models". *Applied Thermal Engineering* 101 (2016), pp. 496–524. DOI: 10.1016/j.applthermaleng.2015.09.094.
- [230] P. Ranut, E. Nobile, and L. Mancini. "High resolution X-ray microtomography-based CFD simulation for the characterization of flow permeability and effective thermal conductivity of aluminum metal foams". *Experimental Thermal and Fluid Science* 67 (2015), pp. 30–36. DOI: 10.1016/j.expthermflusci.2014.10.018.

- [231] S. Razza, T. Heidig, E. Bianchi, G. Groppi, W. Schwieger, E. Tronconi, and H. Freund. "Heat transfer performance of structured catalytic reactors packed with metal foam supports: Influence of wall coupling". *Catalysis Today* 273 (2016), pp. 187–195. DOI: 10.1016/j.cattod.2016.02.058.
- [232] W. Regulski, J. Szumbariski, L. Laniewski-Wollk, K. Gumowski, J. Skibinski, M. Wichrowski, and T. Wejrzanowski. "Pressure drop in flow across ceramic foams? A numerical and experimental study". *Chemical Engineering Science* 137 (2015), pp. 320–337. DOI: 10.1016/j.ces.2015.06.043.
- [233] A. Reitzmann, A. Bareiss, and B. Kraushaar-Czarnetzki. "Simulation of a reactor for the partial oxidation of o-xylene to phthalic anhydride packed with ceramic foam monoliths". *Oil Gas European Magazine* 32 (2006), pp. 94–98.
- [234] A. Reitzmann, F. C. Patcas, and B. Kraushaar-Czarnetzki. "Keramische Schwämme – Anwendungspotenzial monolithischer Netzstrukturen als katalytische Packungen". *Chemie-Ingenieur-Technik* 78 (2006), pp. 885–898. DOI: 10.1002/cite.200600029.
- [235] J. T. Richardson, M. Garrait, and J. K. Hung. "Carbon dioxide reforming with Rh and Pt-Re catalysts dispersed on ceramic foam supports". *Applied Catalysis A: General* 255 (2003), pp. 69–82. DOI: 10.1016/S0926-860X(03)00645-8.
- [236] S. Rieke. "Erste industrielle Power-to-Gas-Anlage mit 6 Megawatt". *gwf-Gas+Energie* 154 (2013), pp. 661–664.
- [237] S. Rönsch, J. Köchermann, J. Schneider, and S. Matthischke. "Global reaction kinetics of CO and CO<sub>2</sub> methanation for dynamic process modeling". *Chemical Engineering and Technology* 39 (2016), pp. 208–218. DOI: 10.1002/ceat.201500327.
- [238] S. Rönsch, J. Schneider, S. Matthischke, M. Schlüter, M. Götz, J. Lefebvre, P. Prabhakaran, and S. Bajohr. "Review on methanation - From fundamentals to current projects". *Fuel* 166 (2016), pp. 276–296. DOI: 10.1016/j.fuel.2015.10.111.
- [239] P. S. Roy, C. S. Park, A. S. K. Raju, and K. Kim. "Steam-biogas reforming over a metal-foam-coated (Pd-Rh)/(CeZrO<sub>2</sub>-Al<sub>2</sub>O<sub>3</sub>) catalyst compared with pellet type alumina-supported Ru and Ni catalysts". *Journal of CO<sub>2</sub> Utilization* 12 (2015), pp. 12–20. DOI: 10.1016/j.jcou.2015.09.003.
- [240] P. Sabatier and S. J. Baptiste. "New methane synthesis". *Comptes Rendus Hebdomadaires des seances de l'Academie des Sciences* 134 (1902), pp. 514–516.
- [241] M. Saber, C. Pham-Huu, and D. Edouard. "Axial dispersion based on the residence time distribution curves in a millireactor filled with  $\beta$ -SiC foam catalyst". *Industrial and Engineering Chemistry Research* 51 (2012), pp. 15011–15017. DOI: 10.1021/ie3017829.
- [242] H. Salmang and H. Scholze. *Keramik*. Ed. by R. Telle. 7th ed. Berlin, Germany: Springer, 2007.
- [243] A. Saltelli, P. Annoni, I. Azzini, F. Campolongo, M. Ratto, and S. Tarantola. "Variance based sensitivity analysis of model output. Design and estimator for the total sensitivity index". *Computer Physics Communications* 181 (2010), pp. 259–270. DOI: 10.1016/j.cpc.2009.09.018.
- [244] A. Saltelli, S. Tarantola, F. Campolongo, and M. Ratto. *Sensitivity analysis practice: A guide to assessing scientific models*. West Sussex, UK: Wiley, 2004. DOI: 10.1016/j.res.2005.11.014.
- [245] A. Saltelli, M. Ratto, A. Terry, J. Cariboni, Francesca Campolongo, D. Gatelli, M. Saisana, and S. Tarantola. *Global Sensitivity Analysis: The Primer*. West Sussex, UK: Wiley, 2008, p. 304.

- [246] O. Sanz, F. Javier Echave, M. Sánchez, A. Monzón, and M. Montes. "Aluminium foams as structured supports for volatile organic compounds (VOCs) oxidation". *Applied Catalysis A: General* 340 (2008), pp. 125–132. DOI: 10.1016/j.apcata.2008.02.007.
- [247] O. Sanz, I. Velasco, I. Reyero, I. Legorburu, G. Arzamendi, L. M. Gandía, and M. Montes. "Effect of the thermal conductivity of metallic monoliths on methanol steam reforming". *Catalysis Today* 273 (2016), pp. 131–139. DOI: 10.1016/j.cattod.2016.03.008.
- [248] S. Schiebahn, T. Grube, M. Robinius, V. Tietze, B. Kumar, and D. Stolten. "Power to gas: Technological overview, systems analysis and economic assessment for a case study in Germany". *International Journal of Hydrogen Energy* 40 (2015), pp. 4285–4294. DOI: 10.1016/j.ijhydene.2015.01.123.
- [249] W. E. Schiesser and G. W. Griffiths. *A compendium of partial differential equation models: Method of lines analysis with Matlab*. Cambridge: Cambridge University Press, 2009, p. 490. DOI: 10.1017/CBO9780511576270.
- [250] C. Schild and A. Wokaun. "Carbon dioxide hydrogenation over nickel/zirconia catalysts from amorphous precursors : on the mechanism of methane formation". *Journal of Physical Chemistry* 95 (1991), pp. 6341–6346. DOI: 10.1021/j100169a049.
- [251] T. J. Schildhauer, K. Pangarkar, J. R. van Ommen, J. Nijenhuis, J. a. Moulijn, and F. Kapteijn. "Heat transport in structured packings with two-phase co-current downflow". *Chemical Engineering Journal* 185-186 (2012), pp. 250–266. DOI: 10.1016/j.cej.2011.11.054.
- [252] B. Schimmoeller, H. Schulz, S. E. Pratsinis, A. Bareiss, A. Reitzmann, and B. Kraushaar-Czarnetzki. "Ceramic foams directly-coated with flame-made V<sub>2</sub>O<sub>5</sub>/TiO<sub>2</sub> for synthesis of phthalic anhydride". *Journal of Catalysis* 243 (2006), pp. 82–92. DOI: 10.1016/j.jcat.2006.07.007.
- [253] A. Schlegel, P. Benz, and S. Buser. "Wärmeübertragung und Druckabfall in keramischen Schaumstrukturen bei erzwungener Strömung". *Wärme- und Stoffübertragung* 28 (1993), pp. 259–266. DOI: 10.1007/BF01539491.
- [254] D. Schlereth, P. J. Donaubaauer, and O. Hinrichsen. "Metallic honeycombs as catalyst supports for methanation of carbon dioxide". *Chemical Engineering and Technology* 38 (2015), pp. 1845–1852. DOI: 10.1002/ceat.201400717.
- [255] D. Schlereth and O. Hinrichsen. "A fixed-bed reactor modeling study on the methanation of CO<sub>2</sub>". *Chemical Engineering Research and Design* 92 (2014), pp. 702–712. DOI: 10.1016/j.cherd.2013.11.014.
- [256] R. Schlögl. "The Solar Refinery". In: *Chemical Energy Storage*. Ed. by R. Schlögl. Berlin, Germany: De Gruyter, 2013. Chap. 1, pp. 1–34.
- [257] M. Schoder, U. Armbruster, and A. Martin. "Heterogen katalysierte Hydrierung von Kohlendioxid zu Methan unter erhöhten Drücken". *Chemie-Ingenieur-Technik* 85 (2013), pp. 344–352. DOI: 10.1002/cite.201200112.
- [258] M. Schubert, L. Schubert, A. Thomé, L. Kiewidt, C. Rosebrock, J. Thöming, F. Roessner, and M. Bäumer. "Coatings of active and heat-resistant cobalt-aluminium xerogel catalysts". *Journal of Colloid and Interface Science* 477 (2016), pp. 64–73. DOI: 10.1016/j.jcis.2016.05.006.
- [259] F. Schüth. "Energy Storage Strategies". In: *Chemical Energy Storage*. Ed. by R. Schlögl. Berlin, Germany: De Gruyter, 2013. Chap. 2, pp. 35–48.
- [260] K. Schwarzwaldler and V. Somers. "Method of Making Porous Ceramic Articles". *United States Patent 3,090,094 A* (1963), pp. 1–6.

- [261] J. Sehested, J. a. P. Gelten, I. N. Remediakis, H. Benggaard, and J. K. Nørskov. "Sintering of nickel steam-reforming catalysts: Effects of temperature and steam and hydrogen pressures". *Journal of Catalysis* 223 (2004), pp. 432–443. DOI: 10.1016/j.jcat.2004.01.026.
- [262] R. Singh and H. S. Kasana. "Computational aspects of effective thermal conductivity of highly porous metal foams". *Applied Thermal Engineering* 24 (2004), pp. 1841–1849. DOI: 10.1016/j.applthermaleng.2003.12.011.
- [263] G. Soave. "Equilibrium constants from a modified Redlich-Kwong equation of state". *Chemical Engineering Science* 27 (1972), pp. 1197–1203. DOI: 10.1016/0009-2509(72)80096-4.
- [264] J. Solsvik and H. a. Jakobsen. "Modeling of multicomponent mass diffusion in porous spherical pellets: Application to steam methane reforming and methanol synthesis". *Chemical Engineering Science* 66 (2011), pp. 1986–2000. DOI: 10.1016/j.ces.2011.01.060.
- [265] J. Solsvik and H. a. Jakobsen. "Multicomponent mass diffusion in porous pellets: Effects of flux models on the pellet level and impacts on the reactor level. Application to methanol synthesis". *Canadian Journal of Chemical Engineering* 91 (2013), pp. 66–76. DOI: 10.1002/cjce.20680.
- [266] J. Solsvik, S. Tangen, and H. A. Jakobsen. "On the consistent modeling of porous catalyst pellets: Mass and molar formulations". *Industrial and Engineering Chemistry Research* 51 (2012), pp. 8222–8236. DOI: 10.1021/ie3007853.
- [267] A. Sternberg and A. Bardow. "Power-to-What? - Environmental assessment of energy storage systems". *Energy & Environmental Science* 8 (2015), pp. 389–400. DOI: 10.1039/C4EE03051F.
- [268] A. Sternberg and A. Bardow. "Life cycle assessment of Power-to-Gas: Syngas vs methane". *ACS Sustainable Chemistry & Engineering* 4 (2016), pp. 4156–4165. DOI: 10.1021/acssuschemeng.6b00644.
- [269] M. Sterner and I. Stadler. *Energiespeicher - Bedarf, Technologien, Integration*. Berlin, Germany: Springer, 2014. DOI: 10.1007/978-3-642-37380-0.
- [270] A. Stohl, P. Seibert, G. Wotawa, D. Arnold, J. F. Burkhart, S. Eckhardt, C. Tapia, A. Vargas, and T. J. Yasunari. "Xenon-133 and caesium-137 releases into the atmosphere from the Fukushima Dai-ichi nuclear power plant: determination of the source term, atmospheric dispersion, and deposition". *Atmospheric Chemistry and Physics* 12 (2012), pp. 2313–2343. DOI: 10.5194/acp-12-2313-2012.
- [271] A. R. Studart, U. T. Gonzenbach, E. Tervoort, and L. J. Gauckler. "Processing routes to macroporous ceramics: A review". *Journal of the American Ceramic Society* 89 (2006), pp. 1771–1789. DOI: 10.1111/j.1551-2916.2006.01044.x.
- [272] M. Sudiro, A. Bertucco, G. Groppi, and E. Tronconi. "Simulation of a structured catalytic reactor for exothermic methanation reactions producing synthetic natural gas". *Computer Aided Chemical Engineering* 28 (2010), pp. 691–696. DOI: 10.1016/S1570-7946(10)28116-6.
- [273] A. Swapnesh, V. C. Srivastava, and I. D. Mall. "Comparative study on thermodynamic analysis of CO<sub>2</sub> utilization reactions". *Chemical Engineering & Technology* 37 (2014), pp. 1765–1777. DOI: 10.1002/ceat.201400157.
- [274] M. Taniewski, A. Lachowicz, K. Skutil, and D. Czechowicz. "The effect of dilution of the catalyst bed on its heat-transfer characteristics in oxidative coupling of methane". *Chemical Engineering Science* 51 (1996), pp. 4271–4278. DOI: 10.1016/0009-2509(96)00266-7.

- [275] K. R. Thampi, J. Kiwi, and M. Grätzel. "Methanation and photo-methanation of carbon dioxide at room temperature and atmospheric pressure". *Nature* 327 (1987), pp. 506–508. DOI: 10.1038/327506a0.
- [276] The OpenFOAM Foundation. *OpenFOAM*. 2017.
- [277] M. Thema, M. Sterner, T. Lenck, and P. Götz. "Necessity and impact of Power-to-gas on energy transition in Germany". *Energy Procedia* 99 (2016), pp. 392–400. DOI: 10.1016/j.egypro.2016.10.129.
- [278] E. Tronconi, G. Groppi, and C. G. Visconti. "Structured catalysts for non-adiabatic applications". *Current Opinion in Chemical Engineering* 5 (2014), pp. 55–67. DOI: 10.1016/j.coche.2014.04.003.
- [279] T. Truong Huu, R. Philippe, P. Nguyen, D. Edouard, and D. Schweich. "Radial dispersion in liquid upflow through solid SiC foams". *Industrial and Engineering Chemistry Research* 50 (2011), pp. 4329–4334. DOI: 10.1021/ie1017942.
- [280] E. Tsotsas. "Entwicklungsstand und Perspektiven der Modellierung von Transportvorgängen in durchströmten Festbetten". *Chemie Ingenieur Technik* 72 (2000), pp. 313–321. DOI: 10.1002/1522-2640(200004)72:4<313::AID-CITE313>3.0.CO;2-2.
- [281] E. Tsotsas. "Wärmeleitung und Dispersion in durchströmten Schüttungen". In: *VDI-Wärmeatlas*. Ed. by VDI-Gesellschaft für Verfahrenstechnik und Chemieingenieurwesen. 11th ed. Berlin, Germany: Springer, 2013, pp. 1517–1533. DOI: 10.1007/978-3-642-19981-3\_102.
- [282] M. V. Twigg and J. T. Richardson. "Preparation and properties of ceramic foam catalyst supports". *Studies in Surface Science and Catalysis* 91 (1995), pp. 345–359. DOI: 10.1016/S0167-2991(06)81771-4.
- [283] J. Ulpts, W. Dreher, L. Kiewidt, M. Schubert, and J. Thöming. "In situ analysis of gas phase reaction processes within monolithic catalyst supports by applying NMR imaging methods". *Catalysis Today* 273 (2016), pp. 91–98. DOI: 10.1016/j.cattod.2016.02.062.
- [284] J. Ulpts, W. Dreher, M. Klink, and J. Thöming. "NMR imaging of gas phase hydrogenation in a packed bed flow reactor". *Applied Catalysis A: General* 502 (2015), pp. 340–349. DOI: 10.1016/j.apcata.2015.06.011.
- [285] J. Ulpts, L. Kiewidt, W. Dreher, and J. Thöming. "3D characterization of gas phase reactors with regularly and irregularly structured monolithic catalysts by NMR imaging and modeling". *Catalysis Today* in press (2017). DOI: 10.1016/j.cattod.2017.05.009.
- [286] Umweltbundesamt. *Energieziel 2050: 100% Strom aus erneuerbaren Quellen*. 2010. URL: [https://www.umweltbundesamt.de/sites/default/files/medien/378/publikationen/energieziel\\_2050.pdf](https://www.umweltbundesamt.de/sites/default/files/medien/378/publikationen/energieziel_2050.pdf) (visited on Aug. 30, 2017).
- [287] Umweltbundesamt. *Erneuerbare Energien in Deutschland – Daten zur Entwicklung im Jahr 2016*. 2017. URL: [https://www.umweltbundesamt.de/sites/default/files/medien/376/publikationen/erneuerbare\\_energien\\_in\\_deutschland\\_daten\\_zur\\_entwicklung\\_im\\_jahr\\_2016.pdf](https://www.umweltbundesamt.de/sites/default/files/medien/376/publikationen/erneuerbare_energien_in_deutschland_daten_zur_entwicklung_im_jahr_2016.pdf) (visited on Aug. 30, 2017).
- [288] V. Uusitalo, S. Väisänen, E. Inkeri, and R. Soukka. "Potential for greenhouse gas emission reductions using surplus electricity in hydrogen, methane and methanol production via electrolysis". *Energy Conversion and Management* 134 (2017), pp. 125–134. DOI: 10.1016/j.enconman.2016.12.031.
- [289] G. van Rossum. *Python reference manual*. Tech. rep. Amsterdam, NL: Centrum voor Wiskunde en Informatica (CWI), 1995.

- [290] C. K. Vance and C. H. Bartholomew. "Hydrogenation of carbon dioxide on group VIII metals". *Applied Catalysis* 7 (1983), pp. 169–177. DOI: 10.1016/0166-9834(83)80005-0.
- [291] A. Vande Wouwer, P. Saucez, and C. Vilas. *Simulation of ODE/PDE Models with MATLAB®, OCTAVE and SCILAB*. Cham: Springer, 2014. DOI: 10.1007/978-3-319-06790-2.
- [292] D. Vervloet, F. Kapteijn, J. Nijenhuis, and J. R. Van Ommen. "A convection-based single-parameter model for heat transport in multiphase tubular reactors packed with closed cross flow structures". *Chemical Engineering Journal* 233 (2013), pp. 265–273. DOI: 10.1016/j.cej.2013.08.033.
- [293] D. Vervloet, F. Kapteijn, J. Nijenhuis, and J. R. van Ommen. "Process intensification of tubular reactors: Considerations on catalyst hold-up of structured packings". *Catalysis Today* 216 (2013), pp. 111–116. DOI: 10.1016/j.cattod.2013.05.019.
- [294] C. G. Visconti, G. Groppi, and E. Tronconi. "Highly conductive "packed foams": A new concept for the intensification of strongly endo- and exo-thermic catalytic processes in compact tubular reactors". *Catalysis Today* 273 (2016), pp. 178–186. DOI: 10.1016/j.cattod.2016.02.060.
- [295] S. Voltolina, P. Marín, F. V. Díez, and S. Ordóñez. "Open-cell foams as beds in multiphase reactors: Residence time distribution and mass transfer". *Chemical Engineering Journal* 316 (2017), pp. 323–331. DOI: 10.1016/j.cej.2017.01.113.
- [296] M. Wallenstein, M. Kind, and B. Dietrich. "Radial two-phase thermal conductivity and wall heat transfer coefficient of ceramic sponges - Experimental results and correlation". *International Journal of Heat and Mass Transfer* 79 (2014), pp. 486–495. DOI: 10.1016/j.ijheatmasstransfer.2014.08.003.
- [297] G. Wang, F. Wang, L. Li, and G. Zhang. "A study of methanol steam reforming on distributed catalyst bed". *International Journal of Hydrogen Energy* 38 (2013), pp. 10788–10794. DOI: 10.1016/j.ijhydene.2013.02.061.
- [298] G. D. Weatherbee and C. H. Bartholomew. "Hydrogenation of CO<sub>2</sub> on group VIII metals. I. Specific activity of Ni/SiO<sub>2</sub>". *Journal of Catalysis* 68 (1981), pp. 67–76. DOI: 10.1016/0021-9517(81)90040-3.
- [299] G. D. Weatherbee and C. H. Bartholomew. "Hydrogenation of CO<sub>2</sub> on group VIII metals. II. Kinetics and mechanism of CO<sub>2</sub> hydrogenation on nickel". *Journal of Catalysis* 77 (1982), pp. 460–472. DOI: 10.1016/0021-9517(82)90186-5.
- [300] G. D. Wehinger, H. Heitmann, and M. Kraume. "An artificial structure modeler for 3D CFD simulations of catalytic foams". *Chemical Engineering Journal* 284 (2016), pp. 543–556. DOI: 10.1016/j.cej.2015.09.014.
- [301] Q. Wei, G. Yang, Y. Yoneyama, T. Vitidsant, and N. Tsubaki. "Designing a novel Ni-Al<sub>2</sub>O<sub>3</sub>-SiC catalyst with a stereo structure for the combined methane conversion process to effectively produce syngas". *Catalysis Today* 265 (2016), pp. 36–44. DOI: 10.1016/j.cattod.2015.08.029.
- [302] H. G. Weller and G. Tabor. "A tensorial approach to computational continuum mechanics using object-oriented techniques". *Computers in Physics* 12 (1998), pp. 620–631. DOI: 10.1063/1.168744.
- [303] A. Westermann, B. Azambre, M. C. Bacariza, I. Graça, M. F. Ribeiro, J. M. Lopes, and C. Henriques. "Insight into CO<sub>2</sub> methanation mechanism over NiUSY zeolites: An operando IR study". *Applied Catalysis B: Environmental* 174-175 (2015), pp. 120–125. DOI: 10.1016/j.apcatb.2015.02.026.

- [304] C. R. Wilke. "A viscosity equation for gas mixtures". *The Journal of Chemical Physics* 18 (1950), pp. 517–519. DOI: 10.1063/1.1747673.
- [305] M. Winterberg, E. Tsotsas, A. Krischke, and D. Vortmeyer. "A simple and coherent set of coefficients for modelling of heat and mass transport with and without chemical reaction in tubes filled with spheres". *Chemical Engineering Science* 55 (2000), pp. 967–979. DOI: 10.1016/S0009-2509(99)00379-6.
- [306] Wolfram Research Inc. *Mathematica, Version 8.0*. Champaign, IL, USA, 2008.
- [307] S. Woudberg and J. Du Plessis. "An analytical Ergun-type equation for porous foams". *Chemical Engineering Science* 148 (2016), pp. 44–54. DOI: 10.1016/j.ces.2016.03.013.
- [308] J. Xu and G. F. Froment. "Methane steam reforming, methanation and water-gas shift: I. Intrinsic kinetics". *AIChE Journal* 35 (1989), pp. 88–96.
- [309] W. Xu, H. Zhang, Z. Yang, and J. Zhang. "Numerical investigation on the flow characteristics and permeability of three-dimensional reticulated foam materials". *Chemical Engineering Journal* 140 (2008), pp. 562–569. DOI: 10.1016/j.cej.2007.12.010.
- [310] X. H. Yang, J. X. Bai, H. B. Yan, J. J. Kuang, T. J. Lu, and T. Kim. "An analytical unit cell model for the effective thermal conductivity of high porosity open-Cell metal foams". *Transport in Porous Media* 102 (2014), pp. 403–426. DOI: 10.1007/s11242-014-0281-z.
- [311] J. Young and B. Todd. "Modelling of multi-component gas flows in capillaries and porous solids". *International Journal of Heat and Mass Transfer* 48 (2005), pp. 5338–5353. DOI: 10.1016/j.ijheatmasstransfer.2005.07.034.
- [312] M. Zafari, M. Panjepour, M. D. Emami, and M. Meratian. "Microtomography-based numerical simulation of fluid flow and heat transfer in open cell metal foams". *Applied Thermal Engineering* 80 (2015), pp. 347–354. DOI: 10.1016/j.applthermaleng.2015.01.045.
- [313] A. Zenner and D. Edouard. "Revised cubic model for theoretical estimation of effective thermal conductivity of metal foams". *Applied Thermal Engineering* 113 (2017), pp. 1313–1318. DOI: 10.1016/j.applthermaleng.2016.11.129.
- [314] Z. Zhan, J. Xiao, Y. Zhang, M. Pan, and R. Yuan. "Gas diffusion through differently structured gas diffusion layers of PEM fuel cells". *International Journal of Hydrogen Energy* 32 (2007), pp. 4443–4451. DOI: 10.1016/j.ijhydene.2007.03.041.
- [315] J. Zhang, N. Fatah, S. Capela, Y. Kara, O. Guerrini, and A. Y. Khodakov. "Kinetic investigation of carbon monoxide hydrogenation under realistic conditions of methanation of biomass derived syngas". *Fuel* 111 (2013), pp. 845–854. DOI: 10.1016/j.fuel.2013.04.057.
- [316] X. Y. Zhang, M. N. Trame, L. J. Lesko, and S. Schmidt. "Sobol sensitivity analysis : A tool to guide the development and evaluation of systems pharmacology models". *CPT: pharmacometrics & systems pharmacology* 4 (2015), pp. 1–4. DOI: 10.1002/psp4.6.
- [317] X. Zhou and C.-J. Liu. "Three-dimensional printing for catalytic applications: current status and perspectives". *Advanced Functional Materials* 27 (2017), p. 1701134. DOI: 10.1002/adfm.201701134.
- [318] S. Zürcher, M. Hackel, and G. Schaub. "Kinetics of selective catalytic NO<sub>x</sub> reduction in a novel gas-particle filter reactor (catalytic filter element and sponge insert)". *Industrial and Engineering Chemistry Research* 47 (2008), pp. 1435–1442. DOI: 10.1021/ie071091c.
- [319] S. Zürcher, K. Pabst, and G. Schaub. "Ceramic foams as structured catalyst inserts in gas-particle filters for gas reactions-Effect of backmixing". *Applied Catalysis A: General* 357 (2009), pp. 85–92. DOI: 10.1016/j.apcata.2009.01.020.

## Students' Work

In this dissertation, the results from the supervision of the following students' works are included:

Matthias Niemeyer, "Simulation of flow distribution in uniform and graded sponges", *M. Sc. Thesis*, 2016.

Jonas Wentrup, "Comparison of monolithic sponges and pellets as catalyst support for unsteady-state methanation", *B. Sc. Thesis*, 2016.

Philipp Bruck, "Detailed modeling of heat- and mass transport in porous catalysts", *M. Sc. Thesis*, 2015.

Denis Kelm, "Investigation of packed beds and honeycomb-type catalyst carriers for CO<sub>2</sub>-methanation", *M. Sc. Thesis*, 2014.

Michel Kolbe, "Entwicklung einer Testanlage und Validierung eines Simulationsmodells zur Untersuchung katalytischer Reformierungsprozesse", *M. Sc. Thesis*, 2013.



## Colophon

This thesis was typeset with L<sup>A</sup>T<sub>E</sub>X 2 $\epsilon$ . It uses the *Clean Thesis* style developed by Ricardo Langner. The design of the *Clean Thesis* style is inspired by user guide documents from Apple Inc.

Download the *Clean Thesis* style at <http://cleanthesis.der-ric.de/>.